Higher Order Modes and Dampers for the LHC Double Quarter Wave Crab Cavity

James Alexander Mitchell

Department of Engineering

University of Lancaster

A thesis submitted for the degree of Doctor of Philosophy

10th October 2019

Declaration

This thesis has not been submitted in support of an application for another degree at this or any other university. It is the result of my own work and includes nothing that is the outcome of work done in collaboration except where specifically indicated. Many of the ideas in this thesis were the product of discussion with my supervisors G. Burt and R. Calaga.

J. Mitchell
....
James Alexander Mitchell

For my parents.

Abstract

This thesis initially investigates the DQW crab cavity HOM couplers manufactured for tests in the Super Proton Synchrotron (SPS) at CERN and proposed for the HL-LHC upgrade. The coupler's are modelled using equivalent circuit analysis and 'test-boxes' are used to measured each of the six HOM couplers for the SPS test.

The DQW crab cavity's impedance spectra and resulting HOM power generation as a result of excitation by the high-current HL-LHC beam is quantified. Following this, HOM measurements are used to characterise the deviations from the simulated case. Evaluation of the DQW's impedance spectra and stochastic analysis of the foreseeable HOM power generation in the HL-LHC highlights potential issues with the HOMs. To mitigate the issues, a re-design of the HOM coupler is presented; The impedance and HOM power are quantified and benchmarked. In parallel, a new 'quarter wave' rejection filter is designed and evaluated. The operation of the HOM couplers in the presence of the operating electromagnetic field is assessed, quantifying thermal and multipacting behaviour.

Finally, first measurements of crab cavity HOMs with proton bunches are presented and compared with simulations. The measurements are used to evaluate the accuracy of the methods used to calculate impedance and HOM power. Several conclusions feed-back into ancillary design and acceptance criteria for future manufacture.

Acknowledgements

Firstly I would like to express my deepest gratitude to Dr. Graeme Burt and Dr. Rama Calaga for supervising this PhD. The massive amount of time that was set aside for help and advice over the last three years has greatly contributed to the work documented in this thesis, my wider knowledge in the field of RF engineering for accelerator systems and my personal character.

I would like to thank my friendship groups both in the UK and in the Geneva area. The work presented is only possible due to the selfless support received during difficult circumstances.

Finally, I would like to thank CERN. The organisation has provided me with an opportunity to spend three years researching and learning to better my own understanding, whilst contributing to the development of the largest and most reputable machine in high energy physics. The help and support of my section (BE-RF-BR) has allowed my knowledge and skillet to vastly diversify and, specifically, the time and guidance provided by Alexandre Lasheen and Ivan Karpov has greatly contributed to my understanding of RF systems in a particle accelerator environment.

Contents

List of Figures

List of Tables

Chapter 1

Project Introduction

1.1 The Large Hadron Collider

The Large Hadron Collider (LHC) is the world's largest particle collider. Located at the European Organisation for Nuclear Research (CERN), the LHC accelerates protons to extremely high energies in order to generate proton-proton collisions as well as collisions with lead ions.

The driving force behind the construction of the LHC was to create a machine which would allow an investigation into the standard model of particle physics at previously undiscovered energies and collision rates [1]. The LHC would provide a means of searching for the Higgs boson [2, 3].

The proposal for a high energy proton collider, to reside in the 27 km long tunnel built for the Large Electron-Positron (LEP) collider [4], was first made in 1977 [5]. Due to the scale of the project, the design phase of the LHC took place in parallel with the commissioning of the LEP collider. The first proton beam was successfully steered around the LHC in September 2008 [6].

In the following years, the LHC was able to provide record breaking collision energies and, most famously, allowed the independent identification of the Higgs boson by both the ATLAS and CMS experiments [7, 8]. This was presented at a CERN seminar [9] on the 4th July 2012.

The LHC continued to run until 2013 subsequently leading to the start of the first upgrade stage of the LHC, referred to as Long Shut-down One (LS1). The goal of LS1 was to allow the proton-proton collision design energy of 14 TeV to be reached [10]. The main upgrade needed to achieve this was the replacement of over ten thousand high-current interconnections between the superconducting magnets [11].

A 'time line' for past and present events associated with the LHC is available on the CERN website [12].

1.1.1 LHC Operation

A chain of accelerators are used to create a 450 GeV proton beam suitable for injection into the LHC. This chain is composed of four main stages [1]. Firstly, as of the time this thesis was written[1], Linear Accelerator Two (Linac2) allows an energy of 50 MeV to be reached. Following this, a multi-ring booster synchrotron accelerates to 1.4 GeV and this beam is sent into the Proton Synchrotron (PS) where it reaches 26 GeV. Finally, the Super Proton Synchrotron (SPS) is used to accelerate the protons to the LHC injection energy of 450 GeV.

Once the protons are injected into the LHC, the two beams circulate the 27 km circumference, passing through eight interaction regions (IRs). IR1, IR2, IR5 and IR8 are home to the experiments ALICE, ATLAS, CMS, LHCb, LHCf and TOTEM. IR4 is the location of the Radio Frequency (RF) acceleration equipment. IR3 and IR7 house collimation and machine protection equipment and IR6 contains the beam abort system. Figure 1.1 displays the accelerator chain used to provide the 450 GeV protons to the LHC, alongside a schematic detailing the interaction regions and experiment locations.

As stated in the conceptual design report [15], the LHC was designed to reach beam energies of 7 TeV. Thus far, a maximum of 6.5 TeV was achieved in operation.

1.2 The High Luminosity LHC

The three possible upgrade regimes for the LHC include [16] the High-Luminosity upgrade (HL-LHC) [17], the High-Energy upgrade (HE-LHC) [18] and the Electron

---

[1] From 2021, after LS2, all protons at CERN will come from Linac4 [13].

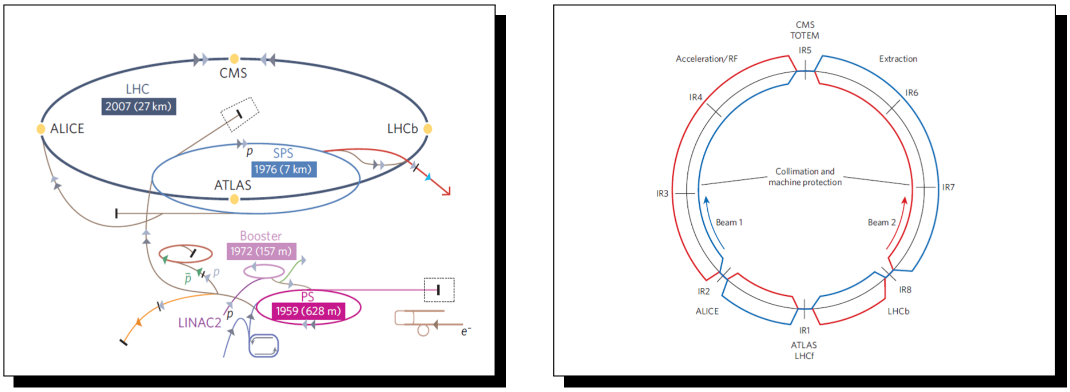

(a) CERN accelerator chain.

(b) LHC layout.

Figure 1.1: CERN accelerator schematics.
Images from [14] and [1].

upgrade (LHeC) [19]. The content of this PhD thesis is concerned with the HL-LHC.

The luminosity of a particle collider is defined as [20] ‘the proportionality factor between the number of events (particle-particle collisions) per second and the cross-section (particle physics definition)’ and has SI units of $m^{-2}s^{-1}$. To assign a figure of merit to the machine performance, this value is often taken over a period of time and termed the ‘integrated luminosity’. The units of m^{-2} are equivalent to the ‘inverse barn’ b^{-1}.

If the design luminosity of 1×10^{34} cm^{-2}s^{-1} is consistently maintained, the corresponding annual integrated luminosity of the LHC will be $40\,\mathrm{fb}^{-1}$. Design margins should allow this luminosity to double in future use of the LHC, as represented in Fig. 1.2, but 2×10^{34} cm^{-2}s^{-1} is the upper limit for the peak luminosity achievable by the collider following Long Shut-down One (LS1). The purpose of the HL-LHC upgrade is to increase the integrated luminosity, allowing significantly more particle-particle collisions and hence increasing the amount of data taken.

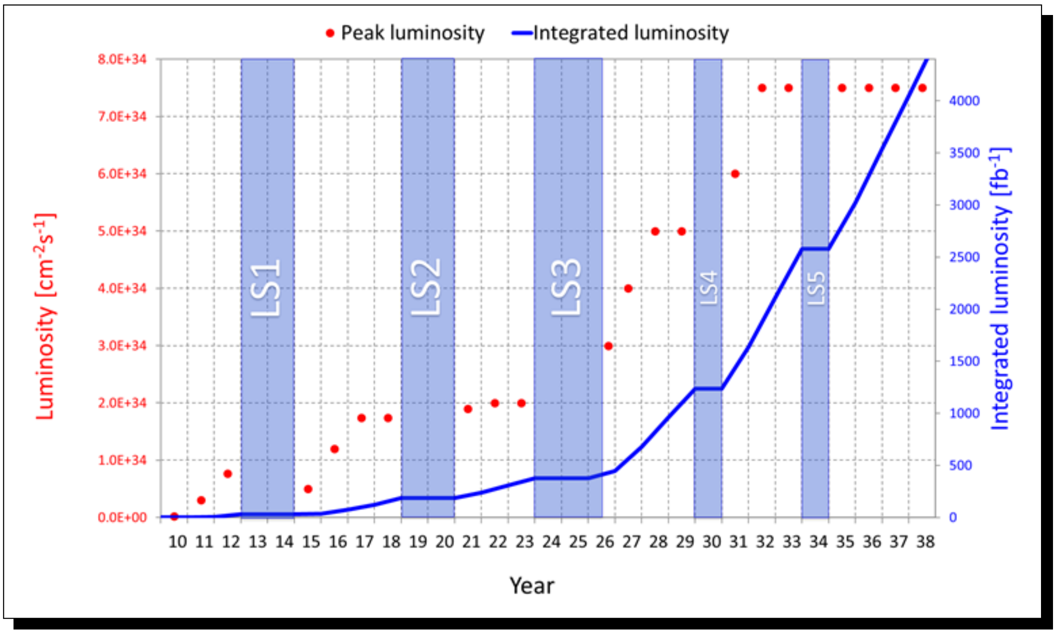

Figure 1.2: Peak and integrated luminosity plan for the LHC from 2010 to 2038. Image from [17, 21].

In order to achieve the higher luminosity, the equation by which it is defined should first be referenced. Assuming beams with perfectly Gaussian profiles and with no RF curvature in the longitudinal plane, the luminosity is denoted as

$$L = \gamma \frac{n_b N^2 f_{rev}}{4\pi \beta^* \epsilon_n} R \tag{1.1}$$

where R is the geometrical reduction factor given by

$$R = \frac{1}{\sqrt{1 + \frac{\theta_c \sigma_z}{2\sigma_{(x,y)}}}}. \tag{1.2}$$

The corresponding nomenclature is shown in Tab. 1.1. At either side of the Interaction Point (IP), there is a region of around 150 m where the counter-rotating charged particle beams circulate in the same vacuum chamber (as opposed to their individual beam pipes). The two beams are physically separated by a defined crossing angle (θ_c). This value is calculated as $\theta_c = 2d\sqrt{\epsilon \beta^*}$, where ϵ is the emittance and β^* is the beta-function at the collision point. The β^* parameter is dependant on the both the transverse beam size and the emittance. The value of the average beam-beam separation from the point where the beams leave their independent beam-pipes to the interaction point (d) is normalised to the transverse beam size. This value is specified as 10.5 σ [22].

Symbol	Description
γ	Proton beam energy in units of rest mass
n_b	Number of proton bunches in the machine
N	Bunch population
f_{rev}	Revolution frequency
β^*	Beam beta function at the collision point
ϵ_n	Transverse normalised emittance
R	Luminosity geometrical reduction factor
θ_c	Full crossing angle between colliding beams
$\sigma_{x,y}$, σ_z	Transverse and longitudinal RMS size

Table 1.1: Nomenclature for Equations 1.1 and 1.2.

To increase the luminosity of the LHC, there are three main options presented by Eq. 1.1. The first two are by increasing either the number of bunches (n_b), or the number protons per bunch (N). The third solution is to decrease the size of the beam at the collision point, i.e. decreasing the value of β^*. The LHC Injectors Upgrade (LIU) project was established to focus on increasing the beam intensity/brightness for proton and ion beams [23, 24]. The HL-LHC project aims to decrease the value of β^*.

The mechanisms employed to reduce the beta function at the collision point (β^*) are detailed in [17]. However, to avoid parasitic collisions, the beams must be separated in the transverse plane by increasing the crossing angle either side of the interaction point. The result of this is an inefficient geometric overlap of the colliding bunches, reducing the geometric reduction factor (R, Eq. 1.2) and hence reducing the luminosity (Eq. 1.1). To counter-act the increased crossing angle, a time-dependant transverse kick is needed before and after the IP, resulting in a rotation of each individual proton bunch. The proposed method of providing the kick is via the use of superconducting RF deflecting cavities (a.k.a. crab cavities).

1.2.1 Crab Cavities: Reducing the Crossing Angle

One method of rotating a charged particle bunch is via the use of an electromagnetic dipole field in an RF cavity, with a wavelength significantly larger than the bunch length, to exert a time varying transverse kick. In this regime, the time at which the kick switches polarity is phased with the centroid of the bunch. This mode of operation is referred to as the crabbing regime.

This concept was first proposed by R. Palmer in 1988 [25]. The reduction in the effective crossing angle leads to a larger geometric overlap of the particle bunches and hence a higher number of particle-particle collisions. A schematic of this process is shown in Fig. 1.3. Additional crab cavities are used to anti-crab after the IP to leave the beam trajectories unperturbed in the rest of the machine [26].

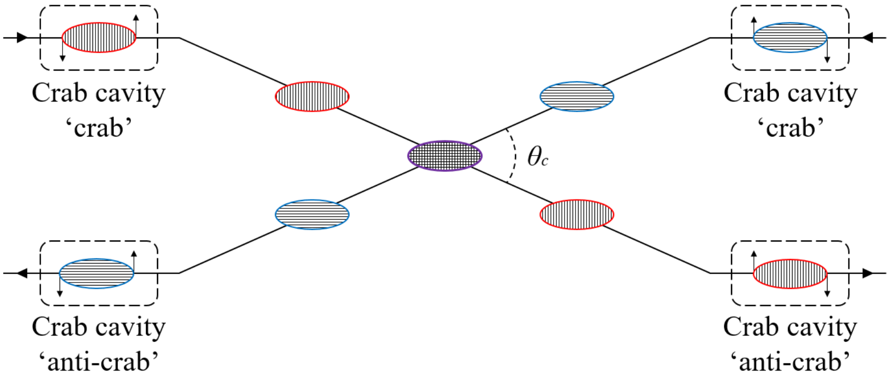

Figure 1.3: Schematic showing the effect of the crab cavities on the bunch orientation at the IP.

As detailed in [27], the transverse kick is given as

$$\Delta p_x = \frac{qV_c}{E_b} sin(\theta_s + kz) \tag{1.3}$$

where q is the particle's charge, V_c the cavity voltage, E_b the beam energy, θ_s the synchronous phase, k the wave number (ω_{RF}/c) and z the offset of the given particle relative to the synchronous particle. The kick results in a transverse displacement of the particle, $x = R_{12}x'$ [28].

The ‘crabbing voltage’ V_c is given as [27, 29]

$$V_c = \frac{2cE_b tan(\theta_r)}{\omega_{RF} R_{12}} \frac{sin(\pi Q)}{cos(\phi^x_{cc\to IP} - \pi Q)} \tag{1.4}$$

where θ_r is the rotation angle, ω_{RF} the RF angular frequency, $R_{12} = \sqrt{\beta_{crab}\beta^*}$ (lattice functions at crab cavity and IP), $\phi^x_{cc\to IP}$ is the phase advance from the cavity to the IP and Q is the synchrotron tune.

The required integrated voltage as a result of the large HL-LHC crossing angle and beam energy is 10–12 MV for full compensation [27]. To produce this deflecting voltage in a limited space ($\sim$ 10 m) and minimise the added impedance to the LHC, superconducting cavities are needed. A transverse deflecting voltage of 3.4 MV per cavity was considered optimum for robust operation well below the quench field limit[1] of Superconducting RF (SRF) cavities [17]. As such, to reach the deflecting voltage requirements, four cavities are required per beam, before and after each interaction point. Hence, 16 vertical (ATLAS) and 16 horizontal (CMS) crab cavities are required.

Alterations to the HL-LHC baseline [17] resulted in a cavity reduction with one ‘two-cavity cryomodule’ per beam, per side at each IP proposed. The use of two cavities per beam, assuming no more than the nominal deflecting voltage is reached, is only capable of providing a partial compensation of the crossing angle [17]. Physical space in the machine will be reserved to allow a second batch of cavities to be installed following LS3 (Fig. 1.2) [17]. The evolution of the crab cavity layout at one IP is shown in Fig. 6, Appendix Sec. 1.

---

[1] The threshold for which the magnetic field is low enough as to not cause a transition from superconducting to normal-conducting operation.

1.3 Thesis Outline

The underlying motivation for the PhD research was to investigate the Double Quarter Wave's (DQW) Higher Order Modes (HOMs); analysing the HOM mitigation methods used, exploring several modelling and measurement techniques and evaluating whether the current infrastructure is suitable for use in the High Luminosity LHC (HL-LHC). The studies and analysis could then be compared with HOM measurements during tests in the Super Proton Synchrotron (SPS), in the world's first use of superconducting crab cavities with protons.

Following the overview of the LHC and HL-LHC project (presented at the start of this chapter), which macroscopically highlights the need for crab cavities and their contribution towards a higher luminosity machine, a stepwise description of both crab cavities and higher order modes is detailed in Chapter 2. RF cavity fundamentals are presented, including examples of monopole and dipole 'modes' and figures of merit used for analysis and benchmarking. Higher order modes in cavity resonators are then detailed, describing the concept of self-excitation, the dangers associated with HOMs and the mitigation methods used; a literature review of HOM damping mechanisms evaluates the advantages and disadvantages of each method.

The HOM mitigation methods (HOM couplers) used for the DQW crab cavity (SPS design) are explored in Chapter 3. An equivalent circuit is initially used to model the HOM couplers. A comparison between the equivalent circuit response and the 3D electromagnetic simulation shows that it is possible to model the couplers very accurately, without the use of complex, time consuming simulations. Parametric sweeps are used to identify tuning methods. Finally, 'test-boxes' are designed, manufactured and used to characterise the physical couplers. Broadband measurements show two areas where the damping is less than predicted.

Chapter 4 characterises the impedance (longitudinal and transverse) and HOM power using eigenmode simulations, analytic calculations and stochastic analysis. HOM parameter deviations were measured during a cryomodule 'cold-test', using liquid helium to cool the structures to the operational temperature of 2 K, resulting in the first mode deviation data-set for cavities with this type of 'exotic geometry'. The deviations are used for stochastic analysis and to quantify inter-cavity ‘spread’. The analysis shows two modes which increased significantly in quality factor and that this increase could have been predicted by the test-box measurements detailed in Chapter 3. One key conclusion resulting from the mode measurements is that a longitudinal mode at 960 MHz could shift in frequency to result in a direct interaction with a bunch spacing harmonic; providing ten times the power threshold.

The main conclusions from Chapter 4 defined an RF optimisation criterion for the couplers. Using the modelling techniques and analysis shown in the previous two chapters, Chapter 5 details the DQW HOM coupler optimisation, allowing the cavity to meet the desired impedance and power requirements. The coupler was also changed to ease several manufacturing processes. A second conceptual design is presented, using a quarter-wave rejection filter, but is shown to be limited by the heat-load on the cavity-coupler copper gasket.

Chapter 6 evaluates three HOM coupler concepts associated with fundamental mode operation; multipoles, multipacting and heating. Simulations and analysis characterise the coupler’s operation in each area.

Finally, Chapter 7 shows the HOM measurements with the SPS proton beam. Measurements with a single bunch and using multiple bunches are compared to simulations and the deviation quantified. Modes are evaluated for ‘coupling ratios’ and problems with cabling and filters are identified and solved. The profile of the proton bunch is measured and the effect of small deviations is shown to be significant on the HOM power. From the analysis, tolerance studies are performed and presented as a necessary part of future predictive analysis.

The thesis is concluded by an overview of all of the work discussed and presents future work for which the research presented in this thesis would act as a foundation.

Chapter 2

RF Crab Cavities and HOMs

Before detailing the RF crab cavities for the HL-LHC upgrade, RF cavity fundamentals are firstly reviewed. Following this, the concept of Higher Order Modes (HOMs) will be discussed and current methods of 'HOM damping' presented.

2.1 RF Cavity Fundamentals

In particle accelerators such as those detailed in the last chapter, charged particle acceleration is achieved via the use of 'resonant cavities'. The Radio Frequency (RF) cavity is an area of empty space in a conductive media, driven by an external RF source. At a resonant frequency, the RF source excites electromagnetic fields in the cavity structure. The geometry of the cavity, for accelerating systems, is designed to provide an electric field in the direction of charged particle propagation, to transfer energy to the particle for acceleration.

2.1.1 Electromagnetic Mode Types and the Pillbox Cavity

It is useful to start with a simple cylindrical geometry often referred to as the 'pillbox cavity' shown in Fig. 2.1.

By solving Maxwell's equations in free space [30–32], the wave equation in

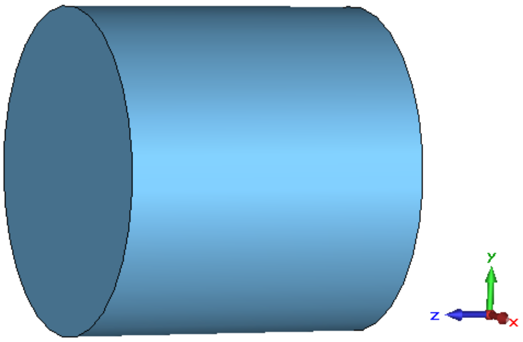

Figure 2.1: The pillbox cavity modeled in CST MWS.

Cartesian coordinates is given as

$$\left(\nabla^2 - \frac{1}{c^2}\frac{\partial^2}{\partial t^2}\right)\begin{Bmatrix}\mathbf{E}\\ \mathbf{B}\end{Bmatrix} = 0. \tag{2.1}$$

By applying boundary conditions to represent the conducting walls at the flat surfaces of the pillbox cavity, two solutions to the wave equation are: Transverse Magnetic (TM) and Transverse Electric (TE). Transverse magnetic modes have an electric field component only in the longitudinal direction. This field can be used to transfer electromagnetic energy to a charged particle beam in the direction of particle propagation. For TE modes, there can only be a magnetic field component along the longitudinal axis. The general expressions for the electric and magnetic field components for both a TM and TE mode in a cylindrical resonator are detailed in Tab. 2.1.

The field is denoted with coefficients m, n and p where m is the number of full period variations of the field components in the azimuthal direction (θ), n is the number of zero point crossings of the longitudinal field along the radial direction (discounting the crossings at the wall) and p is the number of half period variations of the field components in the longitudinal direction (the number of nodes on the z-axis). For a TM mode, the value of m and p can exist as any integer value including zero, whereas the value of n can be any integer apart from zero. For a TE mode, the value of p cannot be zero.

For the field components, J_m refers to a Bessel function of order m[1]. The term

---

[1] It should be noted that the only Bessel functions with non-zero components at $r = 0$ are

Mode	Component	Expression
TM	E_z	$E_0 J_m(k_{mn}r)\cos(m\theta)\cos\left(\frac{p\pi z}{l}\right) exp[j\omega t]$
	E_r	$-\frac{p\pi}{l}\frac{a}{x_{mn}}E_0 J'_m(k_{mn}r)\cos(m\theta)\sin\left(\frac{p\pi z}{l}\right) exp[j\omega t]$
	E_θ	$-\frac{p\pi}{l}\frac{ma^2}{x_{mn}^2 r}E_0 J_m(k_{mn}r)\sin(m\theta)\sin\left(\frac{p\pi z}{l}\right) exp[j\omega t]$
	B_z	0
	B_r	$-j\omega\frac{ma^2}{x_{mn}^2 r c^2}E_0 J_m(k_{mn}r)\sin(m\theta)\cos\left(\frac{p\pi z}{l}\right) exp[j\omega t]$
	B_θ	$-j\omega\frac{a}{x_{mn}c^2}E_0 J'_m(k_{mn}r)\cos(m\theta)\cos\left(\frac{p\pi z}{l}\right) exp[j\omega t]$
TE	E_z	0
	E_r	$j\omega\frac{ma^2}{x'^2_{mn}r}B_0 J_m(k_{mn}r)\sin(m\theta)\sin\left(\frac{p\pi z}{l}\right) exp[j\omega t]$
	E_θ	$j\omega\frac{a}{x'_{mn}}B_0 J'_m(k_{mn}r)\cos(m\theta)\sin\left(\frac{p\pi z}{l}\right) exp[j\omega t]$
	B_z	$B_0 J_m(k_{mn}r)\cos(m\theta)\sin\left(\frac{p\pi z}{l}\right) exp[j\omega t]$
	B_r	$\frac{p\pi}{l}\frac{a}{x'_{mn}}B_0 J'_m(k_{mn}r)\cos(m\theta)\cos\left(\frac{p\pi z}{l}\right) exp[j\omega t]$
	B_θ	$-\frac{p\pi}{l}\frac{ma^2}{x'^2_{mn}r}B_0 J_m(k_{mn}r)\sin(m\theta)\cos\left(\frac{p\pi z}{l}\right) exp[j\omega t]$

Table 2.1: General expressions for TM and TE modes in cylindrical resonators.

k_{mn} is equal to the 'zeros' of the corresponding Bessel function divided by the cavity radius, i.e. $k_{mn} = x_{mn}/a$. The length of the cavity is given by l and ω is the angular frequency.

Modes which have the notation TM_{0np} or TE_{0np} are referred to as monopole modes. The most common monopole mode used in particle acceleration is the TM_{010} mode. When the subscript values are substituted into the field components, the only non-zero elements are

$$E_z = E_0 J_0\left(\frac{2.405r}{a}\right) exp[j\omega t]$$
$$H_\theta = \frac{-j}{Z_0}E_0 J_1\left(\frac{2.405r}{a}\right) exp[j\omega t]$$

noting that the B-field (magnetic flux density) has been written as the H-field (magnetic field strength). Z_0 is the impedance of free space and is equal to the permeability of vacuum multiplied by the speed of light ($Z_0 = \mu_0 c = 377\,\Omega$). From

---

for $m = 0$ (J_0) and the derivative of the $m = 1$ case (J'_1).

the solutions to the equations for the TM_{010} mode, it is clear that the electric field only acts longitudinally and that the magnetic field is perpendicular to this direction at all points. Figure 2.2 demonstrates this mode of operation.

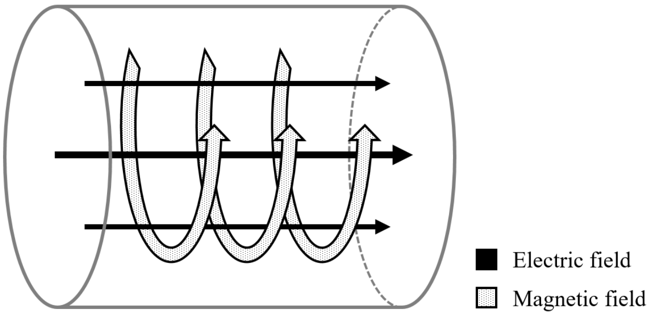

Figure 2.2: Field topology for the TM_{010} mode in a pillbox cavity.

Modes which have the notation TM_{1np} or TE_{1np} are referred to as dipole modes. The field components for the first two dipole modes are defined in Tab. 2.2 and Fig. 2.3 shows the field components of the TM_{110} mode in a pillbox cavity. For m-subscripts of 2–4, the modes are grouped as quadrupoles, sextupoles and octupoles respectively.

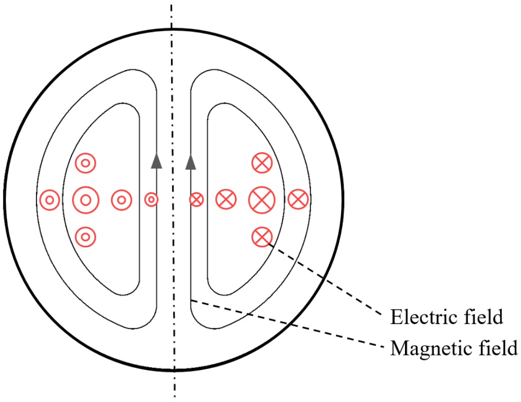

Figure 2.3: Field topology for the TM_{110} mode in a pillbox cavity.

As well as TM and TE fields, there are also transverse electromagnetic (TEM) fields. Generally TEM mode structures are used for low and medium velocity beams and are based around two main designs; the key difference being whether the electrical length is $\lambda/2$ or $\lambda/4$ [31].

Mode	Component	Expression
TM$_{110}$	E_z	$E_0 J_1(k_{11}r)\cos(\theta) exp[j\omega t]$
	E_r	0
	E_θ	0
	B_z	0
	B_r	$-j\omega \frac{a^2}{x_{11}^2 r c^2} E_0 J_1(k_{11}r)\sin(\theta) exp[j\omega t]$
	B_θ	$-j\omega \frac{1}{x_{11} c^2} E_0 J_1'(k_{11}r)\cos(\theta) exp[j\omega t]$
TE$_{111}$	E_z	0
	E_r	$j\omega \frac{1a^2}{x_{11}'^2 r} B_0 J_1(k_{11}r)\sin(\theta)\sin\left(\frac{\pi z}{l}\right) exp[j\omega t]$
	E_θ	$j\omega \frac{1}{x_1'} B_0 J_1'(k_{11}r)\cos(\theta)\sin\left(\frac{\pi z}{l}\right) exp[j\omega t]$
	B_z	$B_0 J_1(k_{11}r)\cos(\theta)\sin\left(\frac{\pi z}{l}\right) exp[j\omega t]$
	B_r	$\frac{\pi}{l}\frac{a}{x_{11}'} B_0 J_1'(k_{11}r)\cos(\theta)\cos\left(\frac{\pi z}{l}\right) exp[j\omega t]$
	B_θ	$-\frac{\pi}{l}\frac{a^2}{x_{11}'^2 r} B_0 J_1(k_{11}r)\sin(\theta)\cos\left(\frac{\pi z}{l}\right) exp[j\omega t]$

Table 2.2: General expressions for TM$_{110}$ and TE$_{111}$ modes in cylindrical resonators.

2.1.2 Parameters used for RF cavity analysis

When using RF cavities in particle accelerators, there are a multitude of parameters, referred to as *figures of merit*, which allow their operation and performance to be defined quantitatively, in terms of accelerator related quantities. This section details some fundamental figures of merit for RF cavity analysis and presents several parameters and nomenclature used throughout this thesis.

A commonly used figure of merit in RF cavity design is the *shunt impedance*

$$r_s = \frac{|V_0|^2}{2P_d} \tag{2.2}$$

which is a measure of the cavity's ability to produce a longitudinal voltage (V$_0$) for a given power dissipated (P$_d$). It is independent of the excitation level of the cavity and often denoted per unit length for structure bench-marking and comparison. It should be noted here that two definitions of the shunt impedance are defined in literature and are referred to as the 'linac' and 'circuit' definitions. Equation 2.2 shows the circuit definition, where the linac definition is this value multiplied by two.

Another commonly used figure of merit is the *quality factor* ('intrinsic' or 'unloaded')

$$Q_0 = \frac{\omega_0}{\Delta\omega} = \frac{\omega_0 U_{st}}{P_d} \tag{2.3}$$

which like the shunt impedance, is defined for a given mode in a cavity at a discrete frequency. It is defined as the ratio of the mode's resonant frequency (ω_0) to its bandwidth ($\Delta\omega$). The mode's bandwidth is equivalent to the ratio between the power dissipated per RF cycle (P_d) and the stored energy (U_{st}).

This definition only takes into account power lost due to losses on the cavity walls. In reality, with the addition of beam pipes, couplers and measurement probes, there is also a power flux to an external load. The quality factor of the cavity is hence reduced to the *loaded quality factor*

$$\frac{1}{Q_l} = \frac{1}{Q_0} + \frac{1}{Q_e} \tag{2.4}$$

where Q_e is the *external quality factor* which represents the power flux away from the cavity (P_e, assuming there is no input RF power) and is hence given as

$$Q_e = \frac{\omega_0 U_{st}}{P_e}. \tag{2.5}$$

In addition to the shunt impedance detailed in Eq. 2.2, which is used for characterising the impedance of electromagnetic modes with a high on-axis voltage, the impedance of higher order terms (i.e. dipole, quadrupole, sextupole etc.) can be quantified. The interaction of the beam with the specific cavity mode is characterised by the *loss factor* or by the *r/Q* value. The loss factor is defined [33] as the square of the *longitudinal voltage*

$$V_{\parallel}^{(m)}(r) = \int_{-l/2}^{l/2} E_z^{(m)}(r,z) exp[-j\omega t]\ dz \tag{2.6}$$

divided by four times the *stored energy*

$$U^{(m)} = \frac{\epsilon_0}{2} \int d^3r \left| E^{(m)} \right|^2 \tag{2.7}$$

and is hence given by

$$k^{(m)}(r) = \frac{\left|V_{\parallel}^{(m)}(r)\right|^2}{4U^{(m)}} \tag{2.8}$$

where m is the mode order and m = 0, 1, 2 corresponds to a monopole, dipole and quadrupole mode respectively. The r/Q value is the ratio of the shunt impedance to the quality factor and can hence be written with respect to the loss factor and normalised to a radial beam offset

$$\left(\frac{r}{Q}\right)^{(m)} = \frac{1}{r^{2m}}\frac{2k^{(m)}(r)}{\omega_0}. \tag{2.9}$$

The r/Q parameter has the units $[\Omega]$, $[\Omega/m^2]$ and $[\Omega/m^4]$ for m = 0, 1 and 2 respectively. For the accelerating mode, i.e. a monopole mode (m = 0), this results in the simple relationship $r/Q = V_{\parallel}^2/2\omega_0 U$. It should be noted that this parameter, like the shunt impedance, has more than one definition where the 'linac' definition is double that of the circuit definition presented. From this value, the mode impedance is calculated as

$$Z_{\parallel}^{(m)} = \left(\frac{r}{Q}\right)^{(m)} Q_l \tag{2.10}$$

showing that the impedance is proportional to the loaded quality factor. Equation 2.4 shows that the value of Q_l will increase with the unloaded and external quality factors and is hence proportional to the conductivity of the cavity wall material and inversely proportional to the power flux to the external load (Eq. 2.5). In a condition where there is no means for power to escape the cavity, the loaded quality factor would be equal to that of the unloaded quality factor. However, this scenario is generally not the case for three main reasons. The first is that there needs to be a way to provide power to the cavity, be it through a waveguide or coaxial coupler. This means that there will be some power, albeit minimal due to the narrow bandwidth of the input coupling mechanism, which escapes through this device. Secondly, for RF cavities to transfer electromagnetic energy to charged particles, the particles must have a means of entry and exit to and from the cavity. Usually, cylindrical beam pipes, with a radius 'a', are used for which cut-off frequencies of the TE_{11} and TM_{01} modes are defined as

$$f_c\ (TE_{11}) = \frac{1.841c}{2\pi a} \tag{2.11}$$

and

$$f_c\ (TM_{01}) = \frac{2.405c}{2\pi a}. \tag{2.12}$$

Beyond these frequencies, field propagation is feasible and hence power dissipation away from the cavity resonator will occur. Finally, as discussed, some power will be dissipated on the cavity walls. These losses are thus material dependant and scale inversely with the electrical conductivity of the material.

It is possible however for $\mathrm{Q}_l \approx \mathrm{Q}_e$. This condition is true if the value of Q_0 is very large, meaning $1/\mathrm{Q}_0 \ll 1/\mathrm{Q}_e$ and is only possible if the losses on the cavity walls are negligible due to a very small resistivity. This is the case for superconducting cavities, which operate below the critical temperature of the wall material (usually Niobium), resulting in incredibly large intrinsic quality factors in the order of 10^{10} for frequencies below 1 GHz.

2.1.3 Transverse Impedance and the Panofsky Wenzel Theorum

In addition to characterising the impedance of monopole modes with the 'longitudinal impedance', the 'transverse impedance' of dipole modes is used to characterise the operational mode of a deflecting cavity (i.e. RF cavities used to impart a transverse kick on charged particles).

For high energies, the transverse voltage equivalence is calculated from the transverse E and H-field

$$V_{\perp}(r) = \int_{-l/2}^{l/2} (E_{\perp} - Z_0 H_{\perp}) exp[-j\omega z/c]\ dz \tag{2.13}$$

hence the transverse r/Q is given by

$$\left(\frac{r}{Q}\right)_{\perp} = \frac{|V_{\perp}|^2}{2\omega_0 U}. \tag{2.14}$$

The transverse voltage can also be defined by the relationship between the longitudinal and transverse voltages as defined by the Panofsky-Wenzel theorum [34]. To derive this relationship, one should first look at the force exerted on a moving charged particle by both the electric and magnetic fields. This is described by the Lorentz Force

$$F = q(\vec{E} + \vec{v} \times \vec{B}) \tag{2.15}$$

where q is the charge and $\vec{v}$ the velocity. The electric and magnetic fields in terms of their scalar and vector potentials are given as

$$\vec{E} = -\nabla\Theta - \frac{\partial \vec{A}}{\partial t} \tag{2.16}$$

and

$$\vec{B} = \nabla \times \vec{A}. \tag{2.17}$$

where Θ is the electric scalar potential and $\vec{A}$ is the magnetic vector potential. If the cross product term in the Lorentz Force equation (Eq. 2.15) is firstly assessed, by rearranging the definition of the gradient of a scalar product and taking only the longitudinal component of the velocity, i.e. $\vec{v} = v_0\hat{z}$, it can be shown that

$$\vec{v} \times \vec{B} = v_0 \left[\nabla(\hat{z}\cdot\vec{A}) - \cancelto{0}{\vec{A} \times (\nabla \times \hat{z})} - \cancelto{0}{(\vec{A}\cdot\nabla)\hat{z}} - (\hat{z}\cdot\nabla)\vec{A}\right] = v_0\left[\nabla(A_z) - \frac{\partial \vec{A}}{\partial z}\right]$$

where two terms go to zero due to differentiation of the unit vector $\hat{z}$. Hence, the Lorentz force equation shown in Eq. 2.15 can be written using this equivalency as well as the $\vec{E}$ definition shown in Eq. 2.16. This gives the definition

$$F = q\left(-\nabla\Theta - \frac{\partial \vec{A}}{\partial t} + v_0\left[\nabla(A_z) - \frac{\partial \vec{A}}{\partial z}\right]\right) = q\left(-\nabla\Theta + v_0\nabla A_z - v_0\frac{dA}{dz}\right).$$

From the definition

$$\vec{V} = \frac{1}{q}\int \vec{F}\cdot dz \tag{2.18}$$

the voltage can be written as

$$\vec{V} = \int -\nabla\Theta + v_0\nabla A_z - v_0\frac{dA}{dz}\cdot dz = \nabla\int -\Theta + v_0\nabla A_z - v_0\cdot dz - \cancelto{0}{\int\frac{dA}{dz}\cdot dz}$$

where the integral of dA/dz is zero due to the absence of magnetic field at the integration limits (before and after the cavity). As the right hand side of the equation shows the gradient function applied to the integral term, the curl of this expression is zero

$$i\left(\frac{\partial V_z}{\partial y} - \frac{\partial V_y}{\partial z}\right) - j\left(\frac{\partial V_z}{\partial x} - \frac{\partial V_x}{\partial z}\right) + k\left(\frac{\partial V_y}{\partial x} - \frac{\partial V_x}{\partial y}\right) = 0$$

and hence, the transverse to longitudinal relationships can be written

$$\left.\begin{array}{ccc}\dfrac{\partial V_z}{\partial x} = \dfrac{\partial V_x}{\partial z} & \text{and} & \dfrac{\partial V_z}{\partial y} = \dfrac{\partial V_y}{\partial z}\end{array}\right\} \quad \nabla_\perp V_z = \frac{\partial \vec{V}_\perp}{\partial z}$$

A direct relationship between the transverse and longitudinal voltages can be expressed

$$\nabla_\perp V_z = \frac{\partial t}{\partial z}\frac{\partial}{\partial t}\vec{V}_\perp = \frac{1}{c}\frac{\partial}{\partial t}\vec{V}_\perp = \frac{j\omega}{c}\vec{V}_\perp$$

resulting in the common representation of the Panofsky-Wenzel theorem

$$\boxed{\vec{V}_\perp = -\frac{jc}{\omega}\nabla_\perp V_z} \tag{2.19}$$

where c is the speed of light. For the first term of the Taylor expansion, the transverse voltage can be written as

$$V_{\perp} = -\frac{jc}{\omega}\frac{V_z}{r} \tag{2.20}$$

where r is the radial offset. The transverse r/Q, referring to Eq. 2.14, is hence given by

$$\boxed{\left(\frac{r}{Q}\right)_{\perp} = \frac{1}{2\omega_0 U}\left(\frac{c}{\omega}\left|\frac{dV_z}{dr}\right|\right)^2} \tag{2.21}$$

and the transverse impedance by

$$\boxed{Z_{\perp} = \frac{\omega}{c}\left(\frac{r}{Q}\right)_{\perp} Q_l.} \tag{2.22}$$

2.1.4 RF Superconductivity

As mentioned in Sec. 1.2, the crab cavities operate in the superconducting regime. The assumption that $Q_l \approx Q_e$ for resonant modes in a superconducting cavity was presented in Sec. 2.1.2. To develop on this concept, the principles of RF superconductivity are introduced here.

For a selection of materials, if connected to a DC source, it is possible to observe zero electrical resistance and the expulsion of magnetic flux when cooled below a certain (critical) temperature. This phenomenon is called superconductivity and was discovered by Heike Kamerlingh Onnes in 1911 [35, 36]. The discovery was twinned with the discovery of the superfluid transition of helium at 2.2 K. Like superconductivity, it is a zero-resistance phenomena, but rather than zero opposition to electron flow, superfluidity is the frictionless flow of liquid through a channel [37, 38].

The resistance to currents which result from a time varying electromagnetic field however, are non-zero even in the superconducting regime. To quantify this, the BCS[1] RF surface resistance is typically written as

$$R_s = A(1/T)f^2 exp\left(-\Delta(T)/kT\right) + R_0 \tag{2.23}$$

where A is a constant dependant on material parameters, T is the temperature, f is the frequency, k is Boltzman's constant and R_0 is the residual resistance. The energy gap of the superconductor 2Δ is the energy gain necessary for two electrons to form a 'Cooper Pair' [39]. The constant A is dependant on the coherence length, Fermi velocity, mean free path and London penetration depth (depth that the magnetic field penetrates). The coherence length is the propagation distance for which the wave can be defined as coherent, i.e. where the phase of the wave can be accurately predicted. The Fermi velocity is the velocity due to only the Fermi energy [40]. The residual resistance is a fixed value for the material sample, its value generally depends on surface impurities and trapped flux.

Generally, for superconductors below L-band (1–2 GHz), the BCS surface resistance is in the order of a few nano-Ohms. For niobium, depending on the material quality, the value at 2 K is usually between 1 and 100 nΩ. The low resistance gives rise to incredibly high intrinsic quality factors (Q_0) in the order of 10^{10} for frequencies less than 1 GHz. For the fundamental mode in an RF cavity, this is advantageous in terms of efficiency, as a very low amount of power is dissipated on the cavity walls. However, the increased quality factor is also the case for any other resonant modes in the cavity and acts to increase the impedance of these modes.

2.2 Compact Crab Cavities for the HL-LHC

After detailing RF cavity fundamentals, going into further detail with respect to transverse mode characterisation and superconducting cavities, the RF crab cavities proposed for the HL-LHC are presented hereafter.

Crab cavities can be defined as deflecting cavities phased such that the charged particle bunch is phased with the zero crossing. Early examples of RF deflectors

---

[1] A 'conventional' theory for superconductivity, detailed in [39] and expanded upon in Appendix section 2.

are that of CERN's radio frequency particle separator [41] and CBAF's 'Highly-Effective Deflecting Structure' [42].

The first superconducting resonant deflecting cavity used in the crabbing regime was that of the 'KEKB B-Factory' at KEK, Japan [43, 44]. The cavity has a 'race-track' geometry and operates using the first dipole. This means that there is a mode (TM_{010}) lower in frequency than the operational mode. The cavity was installed to reduce beam-beam instabilities (betatron oscillations) and to compensate for luminosity reduction as a result of inefficient bunch overlap at the interaction point. The crab cavities were installed in February 2007 and operated successfully until the accelerator was shut down.

Examples of superconducting crab cavities proposed for the future are that of the Advanced Photon Source (APS) [45–47], the International Linear Collider (ILC) [48, 49] and the Argonne National Lab (ANL) Emittance Exchange Experiment [50].

With reference to crab cavities for the HL-LHC, like the current (KEKB) and proposed superconducting crab cavities detailed, elliptical designs could be used to achieve proton bunch crabbing. Due to the cavity's transverse size at an operating mode frequency of 400 MHz (radius $\sim$ 600 mm) being larger than the beam pipe separation (194 mm), the two initial crab cavity proposals for the HL-LHC upgrade were two-cell and single-cell 800 MHz superconducting elliptical cavity designs [51, 52].

The transverse size of the 800 MHz elliptical cavities (radius $\sim$ 300 mm) is still large compared with the beam-pipe separation. Additionally, due to the long proton bunches in the HL-LHC, RF non-linearity effects are observed at 800 MHz [53], resulting in the conclusion that a crabbing frequency of 400 MHz would be most suitable.

Hence, to reduce the transverse size of the cavities and to operate at the more favourable frequency, compact superconducting crab cavities were designed and proposed for the HL-LHC. The final two cavities put forward for vertical (IR1-ATLAS) and horizontal (IR5 - CMS) crabbing were the Double Quarter Wave (DQW) [54] and Radio Frequency Dipole (RFD) [55, 56] respectively. The two cavities are to be tested initially in the Super Proton Synchrotron (SPS) at CERN [17]. The bare Niobium cavity designs are shown in Fig. 2.4.

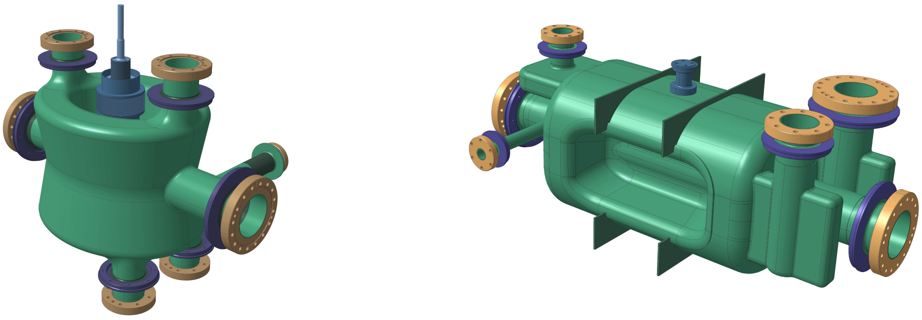

(a) DQW - vertical. (b) RFD - horizontal.

Figure 2.4: Crab cavities for the SPS tests (2018).

With respect to the fundamental ‘crabbing’ mode, the vertical crab cavity (DQW) is a ‘TEM-like’ mode structure that has two quarter wave resonators which share a load capacitor. The electric field acts between the two resonators and the magnetic field ‘loops’ around them at the base of the cavity, perpendicular to the E-field.

The horizontal crab cavity (RFD) uses a ‘TE_{11}-like’ mode (evolving from a ‘ridged waveguide’) to provide the transverse voltage used to crab the proton bunch. The electric field is maximum between the ‘double ridges’, contributing to the majority of the deflecting kick.

The high capacitive loading of the dipole mode, due to the parallel plates of the two resonators, decreases its frequency for a given geometry. This is advantageous for two main reasons. Firstly, it allows the cavity size to be smaller than that of an elliptical cavity by around one third in the horizontal plane (where the beam-pipe separation imposes a geometric limit) for the same mode frequency. Secondly, the capacitive loading reduces the frequency of the dipole mode to below that of the monopole modes and hence the cavities operate at the lowest frequency mode[1].

Although termed as the ‘dipole mode’, due to the cavity’s complex geometries the fundamental modes are not pure dipole modes and as such have longitudinal accelerating components. Both cavities have been designed to minimise the accelerating component of the fundamental mode, hence minimising non-linearities

---

[1] The frequency of different mode types is detailed in the coming sections, but the concept for the HL-LHC crab cavities is presented here as it heavily contributed to their designs.

of the deflecting voltage. Additionally, the effect of each of the multipole components [57][1] on the beam have been assessed and the cavities have been optimised to defined thresholds. Key figures of merit for the two cavities are detailed in Tab. 2.3.

Parameter	Unit	DQW	RFD
Frequency, f_0	MHz	400.52	400.79
Deflecting Voltage, $V_\perp$	MV	3.34	3.34
$r/Q_\perp$	Ω/m	433	431
Peak Surface Electric Field, E_{pk}	MV/m	36	35
Peak Surface Magnetic Field, B_{pk}	mT	71	55.1
Accelerating Voltage, $V_\parallel$	kV	14.5	1.8
Stored Energy	J	10.2	10.3
$\Re\{b_3\}$	mT/m^2	496	475
Cavity Transverse Envelope, (x, y)	mm	(410, 511)	(375, 408)
Cavity Length, l	mm	660	919

Table 2.3: Key figures of merit for the two crab cavities proposed for the HL-LHC upgrade at the time of the pre-validation tests in the SPS.

2.3 Higher Order Modes

Due to the high current HL-LHC beams [58] ($\sim 1.1\,\mathrm{A}$) and high quality factors associated with superconducting cavity modes (Sec. 2.1.4), the crab cavity Higher Order Modes (HOMs) could have a detrimental effect on the HL-LHC beam and surrounding infrastructure. As such, the concept of HOMs and ‘damping’ is detailed hereafter.

2.3.1 HOMs and Consequences

Referring back to Sec. 2.1.1, Higher Order Modes (HOMs) can be defined as modes which have higher coefficient values (m, n and p). Generally as the coefficients increase, so does the frequency. However this is not always the case and, especially with deflecting cavities with exotic geometries, the operational (or ‘fundamental’)

---

[1] Again, the concept of multipoles is detailed in the coming chapters, but was a key parameter in the crab cavity design requirements.

mode can be of a higher order than another mode with a higher frequency. As such, it is common practice to define HOMs simply as all of the modes above the fundamental mode frequency and any modes lower than this frequency as 'Lower Order Modes' (LOMs). This terminology will be used to categorise electromagnetic modes with respect to the fundamental mode throughout this thesis.

As with the fundamental mode, the field configuration, frequency, r/Q, Q_0 and impedance of the HOMs are all dependent on the geometry of the cavity.

For a pillbox cavity (Sec. 2.1.1), the resonant frequencies of the TM and TE modes are given by [59]

$$\omega_{mnp} = \frac{1}{\sqrt{\mu_0 \epsilon_0}} \sqrt{\left(\frac{p_{mn}}{r}\right)^2 + \left(\frac{p\pi}{l}\right)^2} \qquad \text{(TM)} \tag{2.24}$$

and

$$\omega_{mnp} = \frac{1}{\sqrt{\mu_0 \epsilon_0}} \sqrt{\left(\frac{p'_{mn}}{r}\right)^2 + \left(\frac{p\pi}{l}\right)^2} \qquad \text{(TE)} \tag{2.25}$$

where μ_0 is the relative permeability, ϵ_0 the relative permittivity and p_{mn} is the nth zero crossing of the mth order Bessel function. The geometric parameters r and l are the cavity radius and length.

If a pillbox cavity with a radius of 150 mm and a length of 450 mm is used as an example, the mode frequencies correspond to those shown in Fig. 2.5.

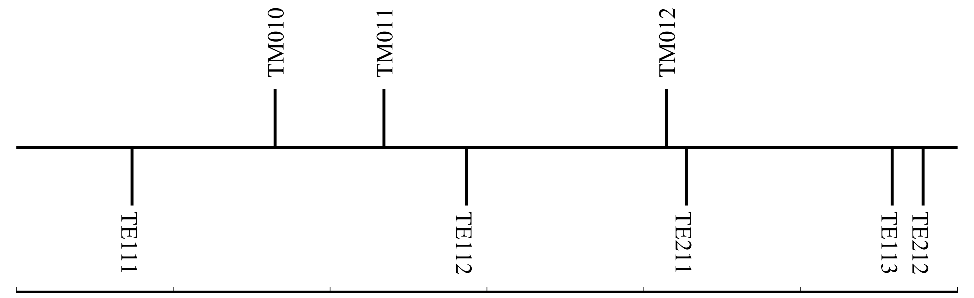

Figure 2.5: Mode frequencies in a pillbox cavity with a radius of 150 mm and a length of 450 mm.

For this geometry, the lowest frequency mode is that of the TE_{111}. The frequency of this mode increases linearly with the square of the ratio of the cavity's radius to its length $(r/l)^2$. However, the frequency of the TM_{010} mode is only determined by the cavity radius. As such, the frequency of the TE_{111} surpasses that of the TM_{010} at $\sim (r/l)^2 = 0.25$, highlighting the nomenclature issues detailed at the start of this section. The mode frequencies as a function of pillbox cavity geometry are detailed in [59, p. 95].

As discussed in Sec. 2.1.1, when referring to higher order modes in cylindrical resonators, it is common to refer to them by the number of full period field variations in the azimuth, i.e. the value of m, referring to the values of m = 0, 1, 2, 3 ... as 'monopole', 'dipole', 'quadrupole', 'sextupole' and so on. Examples of mode types up to the octopole are shown in Fig. 2.6.

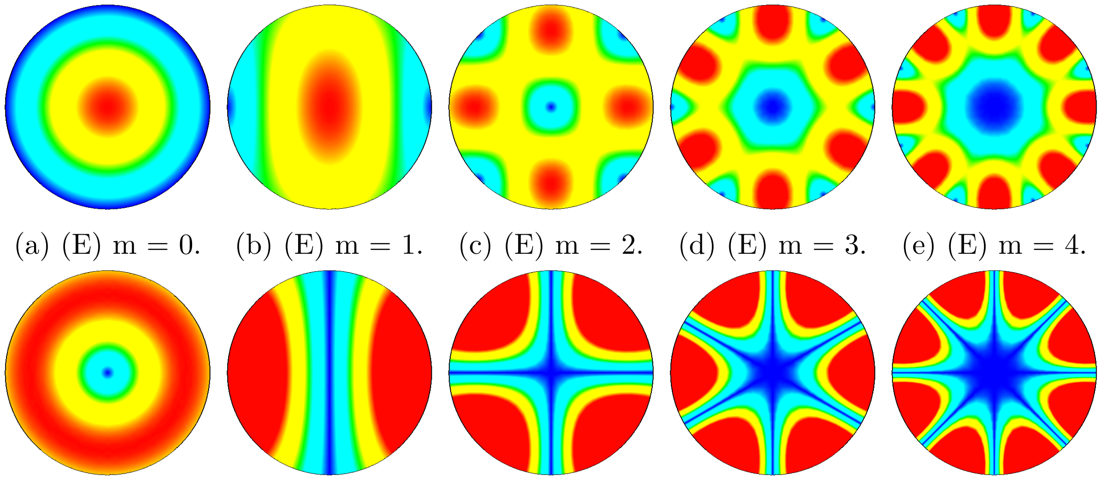
(a) (E) m = 0. (b) (E) m = 1. (c) (E) m = 2. (d) (E) m = 3. (e) (E) m = 4.

(f) (H) m = 0. (g) (H) m = 1. (h) (H) m = 2. (i) (H) m = 3. (j) (H) m = 4.

Figure 2.6: Field configurations (magnitude) in a pillbox cavity corresponding to various values of m. Note, it is neither TE or TM modes that are selected but rather modes which best illustrate the periodic azimuthal variation.

If excited, the higher order modes of a cavity resonator in a particle accelerator can have detrimental effects on the beam. These effects can be grouped into two main categories [60, 61]:

1. Beam instabilities and related effects.

2. Power generation (heating).

The first point can be split into the effect seen by longitudinal (monopole) and transverse (dipole) modes. Longitudinal modes can cause longitudinal emittance growth and energy spread whereas transverse modes can cause transverse emittance growth and instabilities in beam motion.

Power generation is generally as a result of longitudinal modes as they have a large on-axis impedance and hence store energy taken from the propagating beam. Power losses in the walls of the cavity result from this. Hence, this concept is important for superconducting cavities as the 'heat load' is dissipated into the helium bath. If the heat load becomes too large, the temperature gradient between the inner surface of the cavity and the liquid helium will increase. If the inner wall temperature exceeds that of the superconductor's critical temperature, the cavity becomes normal conducting. Power generation as a result of HOMs is usually associated with high current machines such as B-factories, synchrotrons and electron cooling.

2.3.2 HOM Excitation and the Wakefield

The excitation source for HOMs is the charged particle beam itself, which acts as a broadband current source. Assuming ultra-relativistic particles, as a charged particle enters a cavity, the cross-section 'seen' by the particle changes geometry as it traverses the beam-pipe to cavity transition. As a result of this, the space charge field surrounding the particle expands. Hence, the image charge which results from the charged particle has a longer path and, as it cannot travel faster than the speed of light, falls behind in the direction of propagation. This results in a deposition of energy behind the charged particle and this energy is termed the 'wakefield'.

The energy is deposited in HOMs with an electric field on the axis of particle propagation, defined by the loss factor and r/Q in Sec. 2.1.2, which can in-turn impart energy on trailing charged particles. For example if two charges, q_1 and q_2, are propagating through a pillbox cavity with a spacing of 's' as shown in Fig. 2.7, the wakefield from the leading particle will have an effect on the trailing particle.

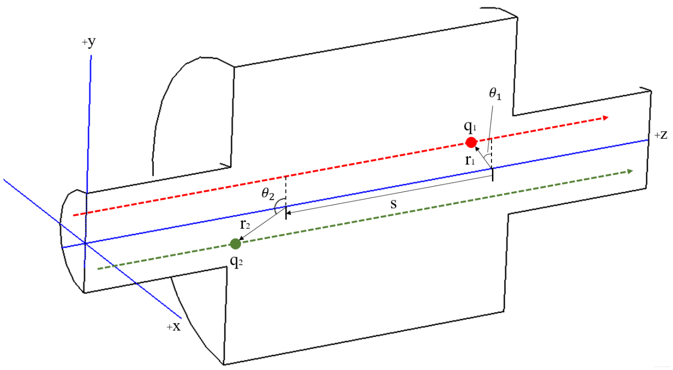

Figure 2.7: Schematic showing two charged particles propagating through an RF cavity [33].

This concept is characterised by the Lorentz force such that

$$F = q_2\left(\vec{E} + c\vec{e}_z \times \vec{B}\right) \tag{2.26}$$

where $\vec{E}$ is the electric field, c is the speed of light and B is the magnetic flux density.

To quantify the time for which an excited HOM will act, therefore assessing its impact on a trailing charged particle, the decay constant can be calculated. A HOM can be modelled as its equivalent RLC (resistor-inductor-capacitor) circuit[1] with the beam modelled as a current source as shown in Fig. 2.8.

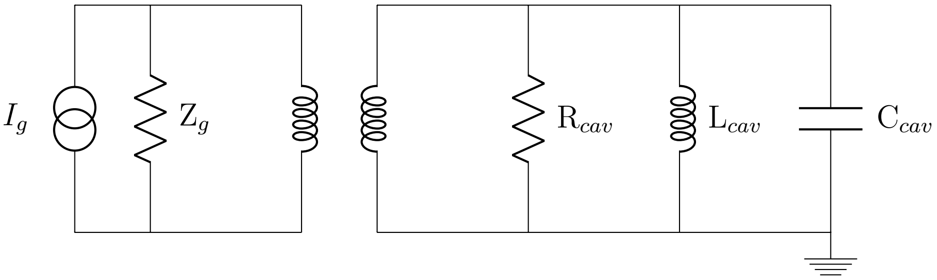

Figure 2.8: Circuit representation of coupling a power source to a cavity.

---

[1] In the main body of the thesis, the excitation of HOMs and the wakefield are presented with reference to an equivalent circuit. The equations for the wake impedance, from the wake function, are detailed in [62]

In this case, the stored energy in the reactive elements is given by

$$U_e = \frac{1}{2}C|V_0|^2 \tag{2.27}$$

$$U_h = \frac{1}{2}L|I_L|^2 = \frac{1}{2}|V_0|^2\frac{1}{{\omega_0}^2} \tag{2.28}$$

and hence, from Eq. 2.3, the unloaded quality factor can be written as

$$Q_0 = \omega_0\frac{U_e}{P_d} = \omega_0 CR = \frac{R}{\omega_0 L}. \tag{2.29}$$

Using Kirchoff's Current Law (KCL), the current in the parallel RLC circuit can be written as

$$I(t) = \underbrace{\frac{V(t)}{R}}_{I_R(t)} + \underbrace{\frac{1}{L}\int V(t)\cdot dt}_{I_L(t)} + \underbrace{C\cdot\frac{dV(t)}{dt}}_{I_C(t)} \tag{2.30}$$

Since there are two reactive elements in this equation, taking the derivative results in a second order differential equation. Assuming that at $t = 0$ all of the energy is stored in the capacitor, the trial solution $V(t) = V_0\exp(-\alpha t)$ can be used to calculate the voltage

$$V_C(t) = V_0\exp\left(-\frac{\omega_0}{2Q_0}t \pm j\omega_0 t\sqrt{1-\frac{1}{4{Q_0}^2}}\right) \tag{2.31}$$

and the energy, referring back to Eq. 2.27, can be written as

$$U_C(t) = \frac{1}{2}\frac{Q_0}{\omega_0 R}{V_0}^2\exp\left(-\frac{\omega_0}{Q_0}t\right) \tag{2.32}$$

The energy damping term is hence given by

$$\boxed{\tau = Q_0/\omega_0.} \tag{2.33}$$

The energy decay time is proportional to the unloaded quality factor which, referring back to Sec. 2.1.4, is larger for a superconducting cavity compared to a normal conducting cavity. For example, a HOM at 3 GHz with a Q_0 of 1.0×10^9 will have a decay time (to 1/e of the initial energy) of 53.0 ms, hence meaning that, assuming relativistic energies, the corresponding decay length is $\sim 1.6 \times 10^4$ km. The excitation of a very high-Q HOM will therefore effect the trailing charged particle bunches. To reduce the energy damping term, as shown in Eq. 2.4, the mode must be 'damped' (i.e. the loaded Q must be reduced) by adding a power flux to an external load. For example if a structure capable of coupling to the mode in question is added and the Q_e value is 6.0×10^4, then the loaded quality factor is

$$Q_l = \frac{Q_e Q_0}{Q_0 + Q_e} = \frac{6 \times 10^{13}}{1.00006 \times 10^9} = 6.0 \times 10^4$$

resulting in a decay constant of $\tau = 3.2\,\mu\mathrm{s}$ and a length of less than 1 km. Therefore if the r/Q of a given HOM is high, the quality factor of the mode must be 'damped' by providing an external power flux to reduce its effect on trailing particles. This concept is also shown by the dependence of the impedance of a mode on the quality factor as shown in Sections 2.1.2 and 2.1.3. Furthermore it should be noted that, due to the very high value of Q_0, the values of Q_l and Q_e are approximately equal.

2.3.3 Coupling to Fields and HOM Damping

In order to provide a power flux to or from a cavity resonator, a coupling mechanism to the field of the given resonant mode is needed. To illustrate this concept, the mechanisms associated with driving the cavity's fundamental mode are presented.

The fundamental mode of the RF cavity resonator is driven by an external excitation source. Examples of RF power sources [63] are modulators, klystrons, gridded tubes, magnetrons and solid state amplifiers [64–68]

Regardless of the excitation source, a power flux needs to be provided to the cavity and a means of coupling to the desired cavity resonance provided. This can be represented by a transmission line [69] and a mutual inductance as shown in in Fig. 2.9.

Common methods of transferring the power, and hence acting as the transmis-

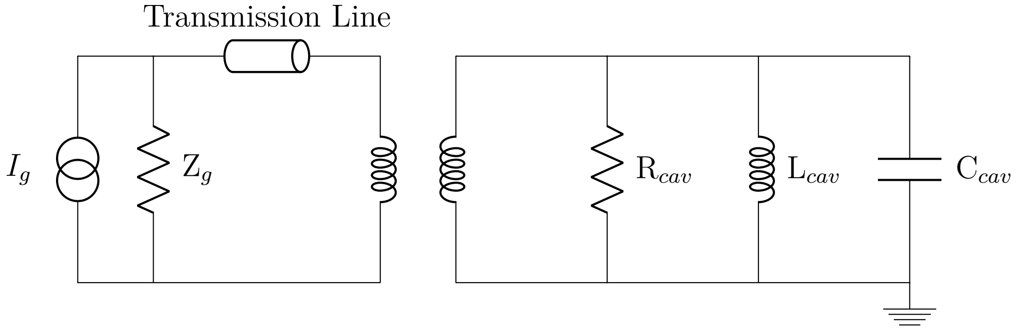

Figure 2.9: Circuit representation of coupling a power source to a cavity resonator.

sion line and coupling mechanism in the equivalent circuit, are waveguide couplers and coaxial couplers. Waveguides couple to the resonant field via a slot in the cavity wall. The field in the waveguide couples to the electric and/or magnetic field in the cavity, depending on the configuration. Coaxial couplers couple to the field via an antenna. The antenna geometry determines the type of coupling.

If coaxial couplers are used as an example, the mutual inductance is analogous to a case where the inner conductor is bent into a loop shape and connected to ground (outer wall of the cavity). Operationally, if the geometry of the loop is small compared to the wavelength, a pertubative approach can be used to represent the coupling [69]. The loop excites a magnetic dipole $\vec{M}_{loop}$, the magnitude of which is proportional to the loop area and input power. This magnetic dipole is the mechanism for coupling power into the cavity and as such the amplitude of the resonant mode is proportional to the scalar product of the magnetic dipole and magnetic field of the cavity mode $\left(\vec{M}_{loop} \cdot \vec{H}_{cavity}\right)$. It is clear that the vectors must be non-zero and non-orthogonal and that a deviation from the angle of maximum coupling, where the loop is perpendicular to the cavity flux, will act to reduce the amplitude of the resonant mode.

In addition to magnetic coupling with a loop, it is also possible to electrically couple with a probe. The mutual inductance shown in Fig. 2.9 is replaced by a capacitance to model this as a circuit equivalence, as it is the surface electric current which couples with the electric field of the cavity resonance. In a similar fashion to the loop, a pertubative approach can be used as long as the probe geometry is small compared to the wavelength. The probe excites an electric dipole $\vec{P}_{probe}$ for which the moment is proportional to the probe's surface current density. Similarly to the loop, the amplitude of the resonant mode is proportional to the scalar product of the excited dipole and cavity field $\left(\vec{P}_{probe} \cdot \vec{E}_{cavity}\right)$.

Both antenna types excite a dipole which acts as a coupling mechanism between the coaxial line and cavity field. The dipole is the source of field into the cavity until the resonant field increases and the field is radiated back to the transmission line. Taking this into account, there is a clear equilibrium between the incident power, reverse power and power dissipated on the cavity walls. A detailed breakdown of the complex and frequency dependant mode amplitudes can be found in [70].

To visually represent the antenna coupling types presented, the two fundamental shapes are displayed in Fig. 2.10. These geometries, referred to as 'probe' and 'loop'-type coupling elements, represent electric and magnetic coupling mechanisms respectively. The dominant coupling field and circuit equivalence is also shown in the figure to highlight the operational differences between the two antenna types.

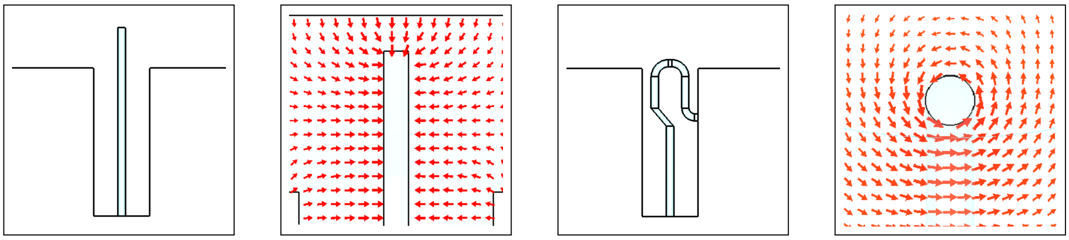

(a) Probe schematic. (b) Probe E-field. (c) Loop Schematic. (d) Loop H-field.

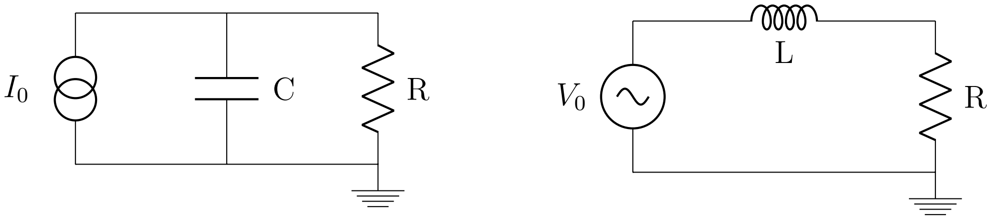

(e) Electric coupling. (f) Magnetic coupling.

Figure 2.10: Basic antenna coupling mechanisms.

Referring back to the equivalent circuit (Fig. 2.9) and the formula defined in

Sec. 2.1.2, the loaded quality factor can be defined as

$$Q_l = \frac{\omega_0 U_{st}}{P_T} = \frac{\omega_0 U}{P_{cav} + P_{ext}} \tag{2.34}$$

where ω_0 is the resonant angular frequency of the mode, U_{st} is the stored energy, P_{cav} is the power dissipated in the cavity walls and P_{ext} is the power dissipated to the matched load of the RF excitation source (with no input RF power). The coupling coefficient is defined as the ratio of P_{ext} to P_{cav} which can be denoted with respect to the values of Q_0 and Q_e

$$\beta = \frac{P_{ext}}{P_{cav}} = \frac{Q_0}{Q_e} \tag{2.35}$$

and hence

$$Q_l = \frac{Q_0}{1+\beta}. \tag{2.36}$$

If β is less than one, the coupling is ‘undercoupled’ and if it is greater than one the coupling is ‘overcoupled’. The coupling coefficient can be calculated as

$$\beta = \frac{1 + \left|S_{11(f_0)}\right|}{1 - \left|S_{11(f_0)}\right|} \qquad \text{(Overcoupled)} \tag{2.37}$$

$$\beta = \frac{1 - \left|S_{11(f_0)}\right|}{1 + \left|S_{11(f_0)}\right|} \qquad \text{(Undercoupled)} \tag{2.38}$$

where $S_{11(f_0)}$ is the reflection coefficient [69] at the resonance.

Generally, for driving a resonant mode, a ‘critically coupled’ scenario is most favourable as this represents the equilibrium steady-state operation where there is no reflected power to the generator. Figure. 2.11a shows a simple pillbox with a loop type coupler. At a given insertion depth into the cavity, the loop was rotated, hence varying the magnetic dipole $\vec{M}_{loop}$ and altering the coupling. Plots of the reflection coefficient S_{11} for three angles are shown in Figs. 2.11b and 2.11c to demonstrate overcoupling, undercoupling and critical coupling.

Whilst for the fundamental mode the input coupler is designed to achieve critical coupling, if a structure is connected to the cavity to provide a power flux

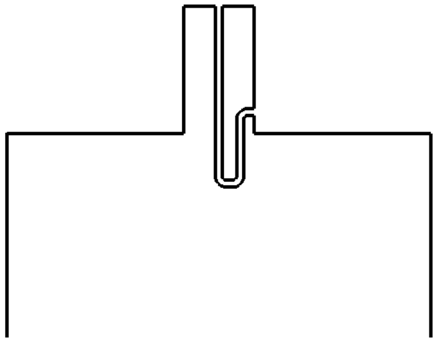

(a) Schematic of loop coupler on cavity.

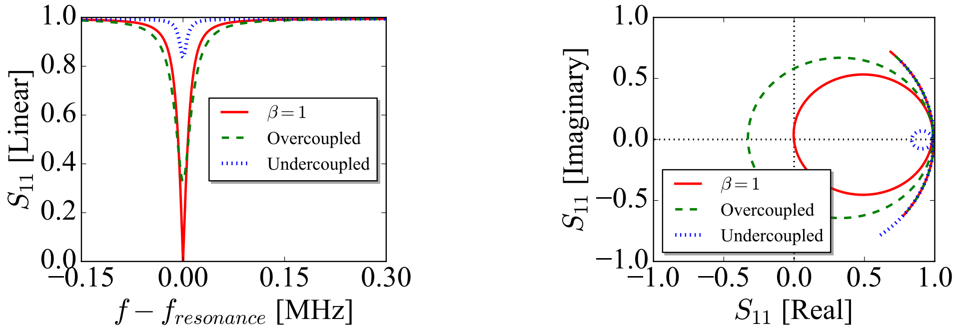

(b) Linear S_{11}.

(c) Real/Imaginary S_{11}.

Figure 2.11: S_{11} plots for three rotations of a loop type coupler mounted onto a pillbox cavity operating in the TM_{010} mode. The plots represent scenarios where β is less than, equal to and greater than one.

for the HOMs (with no input power), i.e. for damping, it is clear that it is the overcoupled case which is preferred, as the purpose is to decrease the HOM's external quality factor. Therefore the ideal scenario for HOM damping is a transmission line which is strongly coupled to the higher order modes, providing a transmission path to an external load, but which does not provide a power flux to the fundamental mode.

2.3.4 Damping Mechanisms

After detailing the theory associated with HOM damping, examples of 'in-use' damping mechanisms should be referenced.

From literature [61, 71–73], the methods of damping HOMs in superconducting

RF cavities can be split into three main categories.

The first two categories are based on the coupling mechanisms detailed in Sec. 2.3.3. They are coaxial dampers and waveguide dampers. Operationally, these structures are used to couple to modes with lower frequencies than the cut-off frequency of the beam-pipes. Coaxial dampers, referring back to Sec. 2.3.3, have different geometries and orientations to best couple to the high impedance modes of interest. These geometries are often categorised as 'probe', 'loop' and 'hook'-types. Where a 'hook' is simply a loop type coupler without an inductive conection to ground, providing a predominantly magnetic coupling but with no weld to the outer conductor. The advantage of coaxial HOM dampers is that they are generally compact in nature compared to alternative options (at frequencies below S-band) and rarely add additional length to the overall cryomodule in the direction of beam propagation. Additionally, they can often be accessed from outside the helium vessel, meaning post installation access is possible in case of problems or upgrades.

To analyse the use of coaxial geometries to damp Higher Order Modes, i.e. 'HOM couplers', the equivalent circuits detailed in Fig. 2.10 for the probe and loop coupling mechanisms should first be referenced. The circuits, arrived at using Thevenin's theorum, represent that of 'non-resonant coupling'. For the probe-type coupling mechanism, the current (I_0) is the displacement current which ends on the surface of the probe. For the loop, the voltage (V_0) is induced by the magnetic field 'flowing' through the loop. The resistance (R) is the terminating resistance (nominally 25, 50 or 75 Ω due to standardised RF components) of a transmission line with a characteristic impedance of $Z_t = R$. As detailed with examples in [74] and [75], the power extracted from a given mode in this case is

$$P_{probe} = \frac{1}{2} I_0^2 \Re\{Z\} = \frac{1}{2} I_0^2 \frac{1}{Y_t} \cdot \frac{Y_t^2}{Y_t^2 + (\omega C)^2} \tag{2.39}$$

$$P_{loop} = \frac{1}{2} V_0^2 \Re\{Y\} = \frac{1}{2} V_0^2 \frac{1}{Z_t} \cdot \frac{Z_t^2}{Z_t^2 + (\omega L)^2} \tag{2.40}$$

where Z is the impedance as seen by the current source and Y the admittance seen by the voltage source. The angular frequency is given by ω and C and L represent the capacitance and inductance respectively.

To increase the power flux away from the cavity (i.e. decreasing the external quality factor as shown in Eq. 2.5) either the generator current or voltage (dependant on coupling mechanism) should be increased or the value of Z_t (loop) or Y_t (probe) should be decreased.

Using the example of a loop coupler, if the radius of the loop is increased, the induced voltage is also increased but the real part of the admittance is decreased as a result of the larger loop inductance ($(\omega L)^2$ term in Eq. 2.40). The same issue is presented in the case of the probe coupler with the trade-off between the real part of the impedance and the term $(\omega C)^2$. For both coupling mechanisms there is hence a lower limit to the external quality factor in the non-resonant case.

However, it is possible to compensate the coupler's reactive elements to reduce the generator loss over the probe/loop, hence decreasing the minimum obtainable external quality factor. Adding a series capacitor to the loop inductance and a parallel inductance to the probe capacitance results in the equivalent circuits shown in Fig. 2.12.

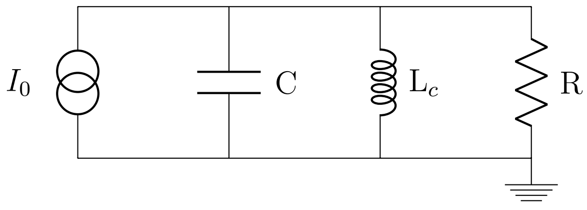

(a) Probe.

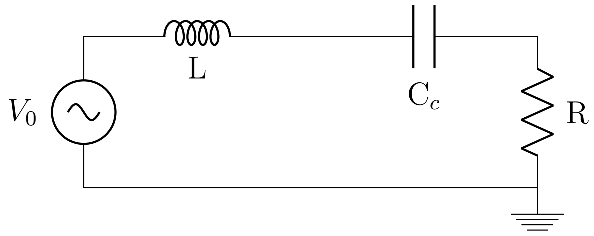

(b) Loop.

Figure 2.12: Compensated coupling equivalences.

The effect of the reactive compensation on the extracted power can be quantified as

$$P_{probe} = \frac{1}{2} I_0^2 \Re\{Z\} = \frac{1}{2} I_0^2 \frac{1}{Y_t} \cdot \frac{Y_t^2}{Y_t^2 + \left(\omega C - \dfrac{1}{\omega L_c}\right)^2} \tag{2.41}$$

$$P_{loop} = \frac{1}{2} V_0^2 \Re\{Y\} = \frac{1}{2} V_0^2 \frac{1}{Z_t} \cdot \frac{Z_t^2}{Z_t^2 + \left(\omega L - \dfrac{1}{\omega C_c}\right)^2} \tag{2.42}$$

and using this compensation to change the generator loss is referred to as 'resonant coupling'.

The bandwidth of the circuit (Eq. 2.29) is defined by

$$Q_{probe} = \frac{f_0}{\Delta f} = \frac{\omega_0 U}{P_d} = \frac{\omega_0 C}{Y_t} \tag{2.43}$$

$$Q_{loop} = \frac{f_0}{\Delta f} = \frac{\omega_0 U}{P_d} = \frac{\omega_0 L}{Z_t} \tag{2.44}$$

and is hence determined by the ratio of the admittance to the capacitance for a probe and by the ratio of the impedance to the inductance for a loop type coupling mechanism. The damping at a given frequency can therefore be increased, but at the cost of a reduced bandwidth.

As previously discussed, it is also possible to increase the power flux away from the cavity by decreasing the value of Z_t (loop) or Y_t (probe). This can be done with 'RF transformers', i.e. reactive elements or $\lambda/4$-transformers [69, 74]. As with the reactive compensation however, employing this mechanism results in higher circuit quality factors and hence smaller bandwidths. The two transformer types are shown in Fig. 2.13.

The circuit quality factor[1] for both cases changes with the 'impedance transformation factor' (t). If the quarter-wave transformer is used, then t is given by

$$t = \frac{R_2}{R_1} = \frac{R_2^2}{Z_t^2} = \frac{Z_t^2}{R_1^2} \tag{2.45}$$

---

[1] Not to be confused with the quality factor of a resonant mode.

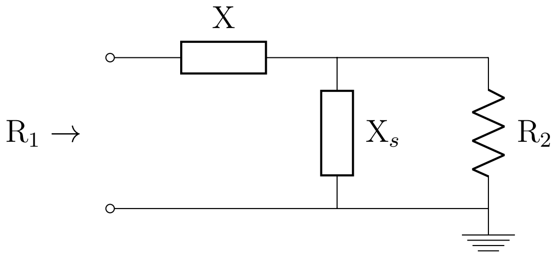

(a) Reactive elements.

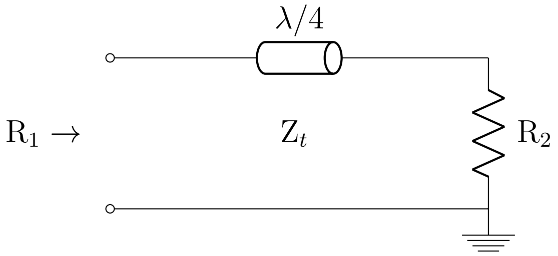

(b) Quarter-wave transformer.

Figure 2.13: RF transformer options.

and the new circuit quality factor is

$$Q_{new} = tQ_0 + Q_t \tag{2.46}$$

where the transformer quality factor (Q_t) for the quarter wave transformer is

$$Q_t = \frac{1}{2\left|1 - \frac{2}{\pi}\arctan\left(\sqrt{t-2}\right)\right|}. \tag{2.47}$$

A detailed work through of these formula for both types of RF transformer detailed is presented in [74].

To provide a broadband transmission profile, multiple RF transformers can be used, where element optimisation allows the peak power flux to be situated near to the most detrimental HOMs. The damping at the frequency of the coupler resonance can be increased, but at the expense of bandwidth.

In addition to damping the HOMs, as discussed in Sec. 2.3.3, the ideal HOM coupler should provide short circuit response at the frequency of the fundamental mode. A common mechanism used to ‘reject’ the fundamental mode is the ‘band-stop filter’ (or ‘notch-filter’). The equivalent circuit for the band-stop filter is shown in Fig. 2.14.

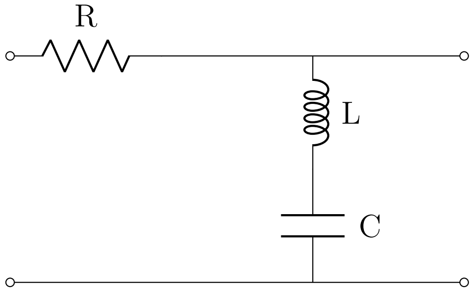

Figure 2.14: Band-stop filter.

The band-stop filter is often implemented as a stub connected to the central conductor of the coaxial coupler and terminates capacitively to ground (outer wall). The centre frequency of the resulting stop-band is calculated as $f_{sb} = 1/\sqrt{LC}$.

Other methods of achieving the rejection are by using quarter wave resonances and high-pass filters.

Following the operational analysis of ‘the HOM coupler’, an overview of several existing designs is shown in Fig. 2.15.

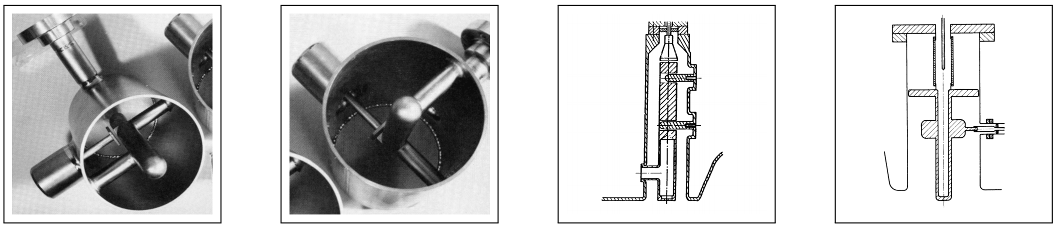

(a) HERA: ‘TE’ [76]

(b) HERA: ‘TM’ [76]

(c) CEA: ‘Probe’ [77]

(d) CERN: ‘Type-I’ [78]

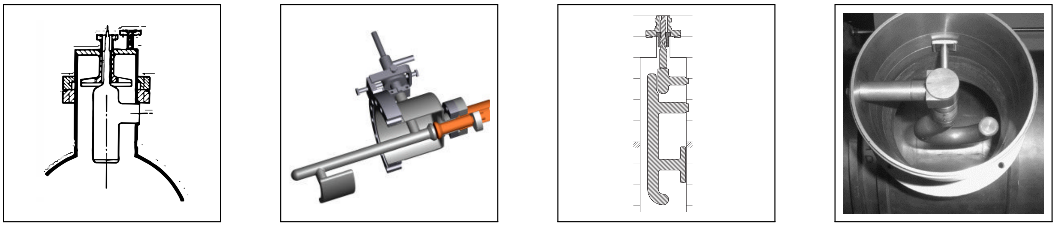

(e) CERN: ‘Type-III’ [78]

(f) LHC: ‘Broadband’ [79]

(g) SPL: ‘3 stage’ [80]

(h) Soleil: ‘L-type’ [81]

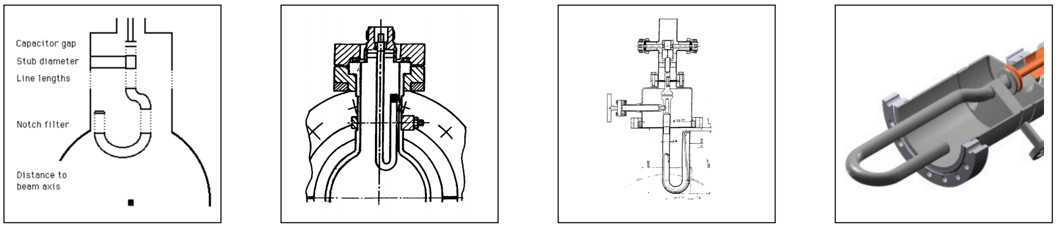

(i) Soleil: ‘D-Type’ [81]

(j) CEA: ‘Hook’ [77]

(k) LEP-II [82]

(l) LHC: ‘Narrowband’ [79]

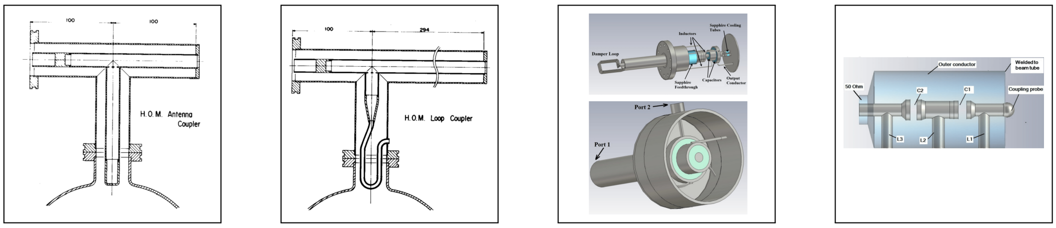

(m) KEK: ‘Probe’ [83]

(n) KEK: ‘Loop’ [83]

(o) RHIC: ‘High-Pass’ [84]

(p) eRHIC: ‘Coaxial’ [85]

Figure 2.15: Superconducting HOM coupler ‘styles’.

The HOM couplers each have geometries which:

- Provide coupling to the HOM's electromagnetic field.
- Provide a rejection at the fundmantal mode frequency.
- Determine the high frequency transformation network.

The different mechanisms of providing each of the operational criterion are detailed hereafter, with reference to the existing HOM couplers shown in Fig. 2.15.

Coupling

Referring to the mechanisms used to couple to the HOMs, examples of probe-type coupling are shown in Figs. 2.15a–2.15g and hook-type coupling in Figs. 2.15i–2.15l. Loop-type coupling mechanisms are used for the KEK and RHIC designs shown in Figs. 2.15n and 2.15o.

Although there are advantages for the probe type coupling in terms of manufacturing ease, the choice of coupling element is generally determined by the field topology and HOM coupler mounting position on the cavity resonator. Therefore, the first choice is generally between probe and hook/loop-type coupling elements. If magnetic coupling is preferenced, a hook-type coupler would be chosen if some electric coupling is beneficial or if the couplers need to be de-mounted. Loop-type coupling is used for a case where a strong magnetic coupling is requred. The latter also allows better cooling to the high H-field region on the coupler, resulting from the fundamental mode field.

Fundamental mode rejection - LC filters

As discussed, the rejection of the fundamental mode is often achieved using an inductive-capacitive (LC) 'notch' filter. The filter is commonly included as either:

1. An additional length to a hook-type coupling element, for which the resonant frequency of the inductance and capacitance (between the hook and wall) is designed to be equal to the frequency of the fundamental mode.

2. A parallel inducance and capacitance between the central concuctor and outer wall.

Examples of incorperating the notch filter into the coupling hook are shown in Figs. 2.15i–2.15l. Using the hook geometry as the notch is advantageous as it reduces the number of physical elements for machining. However, to achieve the capacitances necessary, the distance between the hook and the wall is often very small and sensitive to tolerances. Furthermore, the small distance risks a 'short-circuit' with coupler misalignment (from transport or assembly damage) and as such failure of the HOM coupler.

The parallel LC connection between the central conductor and outer wall is shown in Figs. 2.15a–2.15h. If the coupler is demountable, an important distinction is whether the filter is above or below the cavity-coupler seal. Having the filter above the cavity gasket is advantageous because it allows 'tuning' of the notch frequency. However, as the electromagnetic field is shorted after the gasket location, the dynamic heat-load on the normal-conducting material can be significant.

To increase the bandwidth of the notch filter, decreasing its sensitivity to manufacturing tolerances, a 'double-notch' can be incorperated. An example a HOM coupler that uses a double-notch is that of the SPL HOM coupler shown in Fig. 2.15g. The inner conductor has parallel LC connections to ground (outer wall) before and after the gasket location. The two filters act to increase the rejection at the fundamental mode frequency and also to broaden the bandwidth of the stop-band. If one of the filters is slightly detuned, the rejection will still be suffiecient. It should be noted that although the effect of the notch filters 'sum', detuning of the filter below the gasket location will lead to an increased dynamic heat load on the gasket.

Fundamental mode rejection - other methods

In addition to the use of LC notch filters, two other methods of fundamental mode rejection are:

1. Quarter wave rejection.

2. Ladder filters.

Figures 2.15m and 2.15n show HOM couplers which use quarter-wave rejection filters, i.e. lengths of $\lambda/4$, to reject the fundamental mode frequency. The coupler acts as a broad-band transmission line for the HOMs. This design removes the need for a band-stop filter, reducing the manufacturing complexity of the coupler. A disadvantage is the quarter-wave harmonics which create additional stop-bands at higher frequencies. If the harmonic frequencies are lower than the cut-off frequency of the beam-pipes there will be no damping of any HOMs at the harmonics.

The final two couplers shown in Fig. 2.15 use Chebyshev filtering. The HOM coupler shown in Fig. 2.15o is used on the 56 MHz superconducting Quarter Wave Resonator (QWR) [86] used for the Relativistic Heavy Ion Collider (RHIC) [87] at Brookhaven National Laboratory (BNL). Here, the ground connection of the loop-type coupling mechanism is not the outer wall of the port connected to the cavity, but is a 'sleeve' which is electrically connected to ground via the flange; this allows the loop-type coupler to be 'de-mountable'. The filter is a three stage, high-pass Chebyshev filter [69, p. 400] providing a short to low frequencies, and high transmission to high frequencies. The frequency of the transition from low to high transmission is placed after the fundamental mode frequency but before the first HOM. The Chebyshev filter has a sharp transition but has some ripple on the stop-band and pass-band. The ripple decreases with stages (LC networks of the fiter 'ladder'). Compared to the Chebyshev filter, a Butterworth filter has less ripple for the same number of stages, however the transition from the stop-band to the pass-band is broad in the frequency domain. The transition can be made sharper with the use of more filters.

High frequency filtering:

Referring back to the couplers which use LC band-stop filters, these couplers often employ 'multi-stage' (or 'coupled resonance') filtering. This concept was presented prior to the review of existing HOM couplers. The main conclusion given was that the use of coupler resonances can increase the damping at a given frequency, but at the expense of damping bandwidth. To evaluate this concept, and the choice of the number of stages, the HOM couplers for the LHC accelerating cavities shown in Figs. 2.15f and 2.15l are referenced.

With reference to the RF transformer options detailed in Fig. 2.13, ‘the broadband coupler’ uses three resonant circuits to provide a damping to modes which are far from one another in the frequency domain (776 and 1200 MHz). This allows high damping at the frequency of the modes, but results in a low transmission between the coupler resonances. The ‘narrowband LHC HOM coupler’ uses two coupled series resonant circuits since the two modes to be damped are much closer to one another (500 MHz and 535 MHz). The transmission characteristics for the two couplers are detailed in [74, p. 61].

The RF filtering network is hence dependant on the cavity HOMs and damping requirements set by the accelerator’s operational criterion.

Removable or welded:

The final important distinguishing feature between the HOM couplers shown, is whether the coupler is ‘de-mountable’ or not. This choice can have significant implications on the cryogenic heat-load, assembly and re-assembly complexities and cavity performance. Referring to couplers welded to the cavity geometry, such as the HERA couplers shown in Figs. 2.15a and 2.15a (which influenced the couplers used on the TESLA cavities [88]), advantages are:

- No risk of contamination from installation of the couplers onto a processed cavity.
- No gasket, removing issues associated with vacuum leaks and dynamic heat loads.
- The inner components can be ‘cooled’ via the inductive stub’s connection to the the liquid helium bath.
- Chemical processing and installation of the cavities and couplers as a single unit reduces the steps needed to reach an operational structure. This is beneficial for large scale projects [89].

Disadvantages of the welded couplers are:

- Although chemical processing of only one structure is required with the couplers mounted, this can add complexities to the chemistry as opposed to processing the cavities and couplers individually.
- Mounted couplers can not be replaced/accessed in the event of an operational failure.

Generally, the ability to remove and re-install the HOM couplers in case of failure or operational problem has the largest influence on the design in this respect.

After detailing the first category of HOM dampers (coaxial couplers) the second category (waveguide couplers) should be referenced.

Using these structures both reduces the complexity of manufacture and does not suffer from the inductive heating issues related to hook and loop type couplers. Waveguide dampers are broadband with a 'natural' rejection of the fundamental mode due to the structure's cut-off frequency. The waveguides lead to an absorber (often made from ferrite and other lossy RF materials).

Disadvantages of waveguide dampers are that they are often 'bulky' for low frequency applications and can also be problematic with respect to 'heat leaks'.

An example of a superconducting cavity with waveguide dampers is that of the 1.5 GHz high-current five-cell structure developed at Jefferson Laboratory (JLAB) for future Energy Recovery Linacs (ERLs) and Free Electron Lasers (FELs) [90]. A CAD render and prototype cavity are shown in Fig. 2.16.

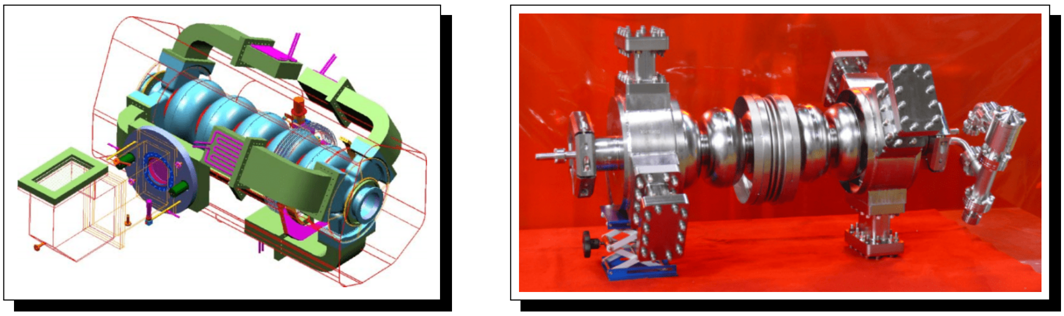

(a) CAD showing waveguide dampers.

(b) Manufactured prototype.

Figure 2.16: 1.5 GHz high-current five-cell waveguide damped structure (JLAB). Images from [90, 91].

Each cavity has six waveguide dampers for which one also acts as the Fundamental Power Coupler (FPC). From literature [72], the HOM power capability was verified up to 4 kW per waveguide (20 kW per cavity).

The third damping mechanism is via the use of Beam Line Absorbers (BLAs). These structures damp modes which have frequencies above that of the beam-pipe cut-off frequency. Generally, they are employed in cases where the beam pipe radius is large enough to allow the lowest frequency HOM to propagate away from the cavity. The RF absorbers are made from 'unbiased ferrites' or 'lossy dielectrics'. In order to interact with magnetic fields, the permeability of the material must be complex and as such, an unbiased ferrite must be used [92]. One example of the use of beam line absorbers is for the Cornell Electron Storage Ring (CESR) B-cell cavity. The BLA used [92] is shown in Fig. 2.17a.

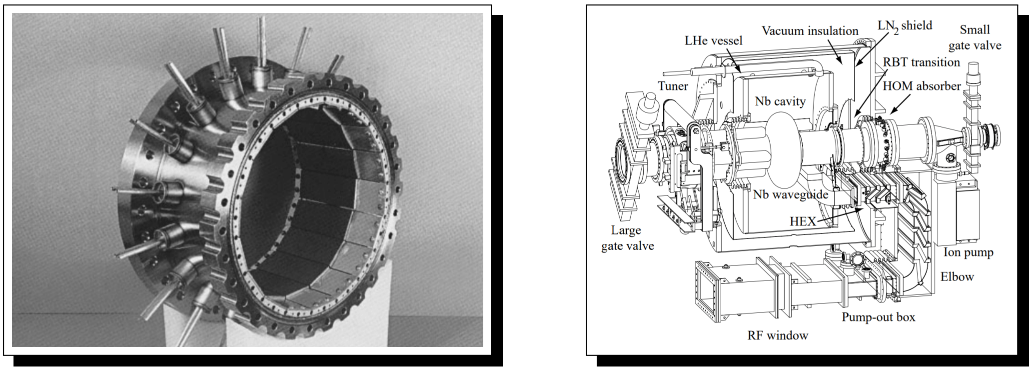

(a) Beam Line Absorber (BLA).

(b) B-Cell cryomdule.

Figure 2.17: HOM damping infrastructure used on the Cornell Electron Storage Ring.
Images from [92]

In addition to the absorbers, the cavity also employs ‘waveguide flutes’. These are ridges in the cavity beam-pipe in the direction of charged particle propagation. These ridges act to decrease the cut-off frequency for the two lowest dipole modes whilst keeping the monopole cut-off the same as the ‘non-fluted’ case. It is important that the flute position on the azimuth match the polarisation of the low frequency HOMs. The waveguide flutes are located on the opposite side to that of the BLA and are visible in Fig. 2.17b.

The main drawback of BLAs is space constraints in the direction of beam propagation. Additional disadvantages are the potential for contamination and the build up of electrostatic charge in the ferrite which can result in deflecting fields.

For the three damping categories detailed (coaxial couplers, waveguide couplers and beam line absorbers), a sub-category for the first two is that of on-cell dampers. In some cases, it is not possible to damp one or more HOMs sufficiently by coupling to the field at the cavity beam-pipe. On-cell damping is used for cases where there are high impedance modes that need to be damped, but for which sufficient coupling to meet the damping requirements is not possible from the beam port.

On-cell damping is predominantly used in normal conducing cavity systems. Like the beam pipe damping structures, these are comprised of coaxial and waveguide couplers which couple to the HOMs and provide a power flux to an external load.

Referring to Normal Conducting (NC) operation, accelerating cavities are designed to maximise the shunt impedance (Eq. 2.2) of the fundamental mode; This is achieved by using small aperture beam pipes and 'nose-cones' [31, 93] to increase the on-axis E-field (and hence r/Q. This minimises the power required for a given accelerating gradient (E_{acc} in MV/m) and hence reduces the heat load and cooling requirements.

It is clear that the gradient in a normal conducting cavity will never reach that of a superconducting (SC) cavity, however there is a trade off between the two in terms of operational efficiency and hence cost [73, 93]. The choice between NC and SC cavity is decided with respect to operational criterion such as beam energy, beam current, RF duty factor and impedance thresholds. One case where normal conducting single-cell cavities are viable over superconducting, is for storage rings at medium beam energies. As discussed, the cavities used in such facilities have 'nose cones' to maximise the gradient. However, by raising the shunt impedance of the fundamental mode, the r/Q for the HOMs also increases. The result of this is high HOM impedance which, with beam energies in the hundreds of milliamps, could result in high heat loads and instabilities. As such, the HOMs need to be 'heavily damped' and require 'direct' HOM damping by coupling to the field in the cavity structure rather than from the beampipe.

An example of a machine which uses on-cell beam-pipe damping is that of PEP-II [94]. The normal conducting cavity [95] has a fundamental mode frequency of 352 MHz and an operational voltage of 800 kV [96]. It has three waveguides which couple to the cavity HOMs via coupling slots on the cavity wall itself [97, 98] and lead to Aluminum nitride RF loads [94]. The waveguides are spaced by 120° to allow damping of all HOMs up to the sextupole (m = 3). Additionally, this maintains symmetry and hence higher order multipole components of the fundamental mode are minimised. An image of the PEP-II cavity is shown in Fig. 2.18.

The limitation of on-cell dampers on superconducting cavities is the enhancement of peak fields at the location of the HOM couplers when compared to the

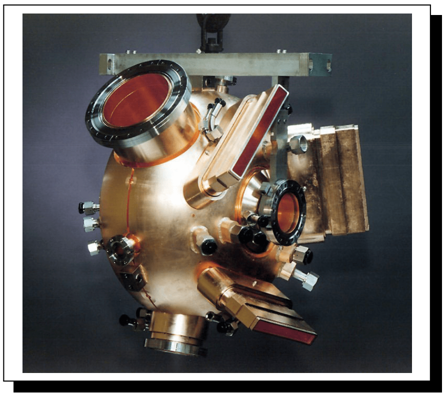

Figure 2.18: PEP-II cavity.
Image from [99].

normal conducting case. Specifically, the increase in the peak magnetic flux density B_{pk} with the addition of coupling slots to the cavity walls acts to reduce the quench field limit, i.e. the field level at which the cavity transitions from superconducting to normal conducting. There are some cases however, where on-cell damping is used for superconducting cavities.

An example of a superconducting on-cell coaxial HOM coupler is that of the loop-type coupler used on the 56 MHz superconducting Quarter Wave Resonator (QWR) [86] used for the Relativistic Heavy Ion Collider (RHIC) [87] at Brookhaven National Laboratory (BNL). This coupler was already detailed in Sec. 2.3.4 and is shown in Fig. 2.15o.

An example of a superconducting on-cell waveguide damper is that of the single cell deflecting cavity [100] designed for the Advanced Photon Source. This cavity is shown in Fig. 2.19.

To conclude on HOM damping mechanisms, the main types are coaxial dampers, waveguide dampers and beam line absorbers (often coupled with altering the cut-off frequency of the beam pipe for specific mode types and polarisations). The type of damping mechanism employed is specific to the particle accelerator system and operational impedance thresholds defined. Generally, the first two damping mechanisms (coaxial and waveguide) are placed on the beam-pipes of a superconducting cavity. However, if a higher damping is required, on-cell dampers can be used but there are risks associated with the significant increase in peak electric

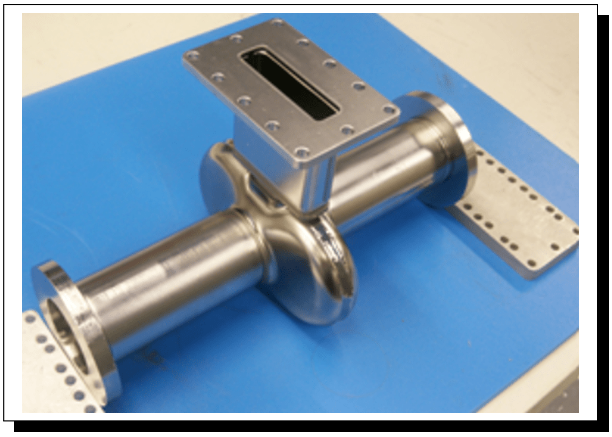

Figure 2.19: On-cell wavguide damped deflecting cavity prototype for the Advanced Photon Source.
Image from [100].

and magnetic fields, especially in the case of superconducting cavities.

2.4 Dressed Compact Crab Cavities for the HL-LHC

After detailing the use of coaxial couplers to both provide power to the fundamental mode and damp the HOMs, the dressed crab cavities for the SPS test[1] (Sec. 2.2) are shown in Fig. 2.20.

The Double Quarter Wave (DQW) cavity uses three on-cell, coaxial, superconducting (internally cooled) HOM couplers to damp the HOMs. They have an L-C band-stop filter centred at 400 MHz to reject any power from the fundamental mode and use transmission line lengths to allow an increased damping at specific frequencies (i.e. those of detrimental HOMs) at the expense of bandwidth (Sec. 2.3.4). The capacitive output gives a high-pass filter response, further rejecting the fundamental mode but allowing transmission at the HOM frequencies. The fundamental mode pick-up of the DQW also acts as a HOM coupler for some high frequency modes.

---

[1] Before installation in the LHC, the crab cavities are scheduled for tests in the SPS (CERN's 7 km synchrotron).

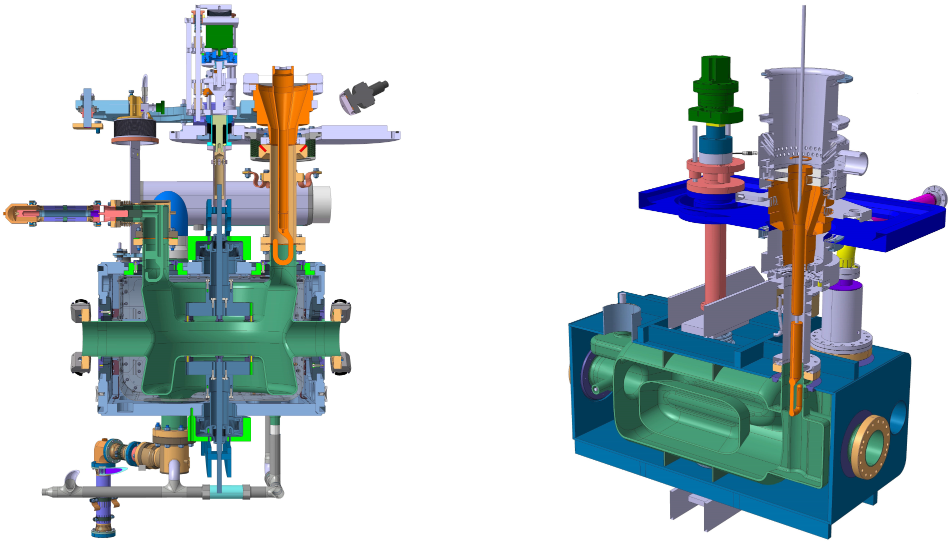

(a) DQW - vertical.

(b) RFD - horizontal.

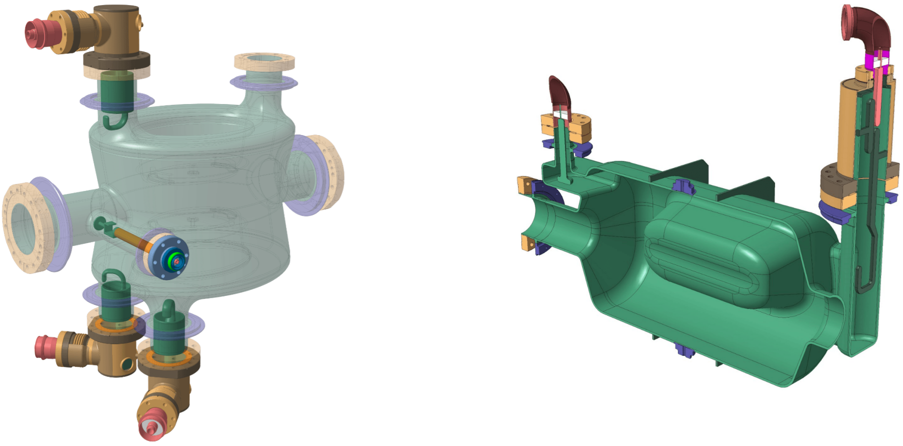

(c) DQW showing HOM couplers.

(d) RFD showing HOM couplers.

Figure 2.20: Dressed crab cavities proposed for the HL-LHC. Designs are those proposed for the verification tests in the Super Proton Synchrotron (SPS).

The RFD cavity has two HOM couplers of differing geometries. The location of the couplers are chosen to damp the vertical and horizontal HOMs independently [101].

The ‘horizontal HOM coupler’ is located in a ‘wave-guide stub’ connected to one cavity end plate. The ‘hook-type’ coupling element, which couples to horizontal and accelerating HOMs[1], is connected to a high-pass filter which rejects the operating mode, but has a high transmission at higher frequencies.

The second 'vertical HOM coupler' is placed in a wave-guide stub on the other end-plate. The wave-guide stub is in different plane to the one for the horizontal mode damping. Due to the fundamental mode's polarity and symmetry, the location of the wave-guide stub gives a 'natural' rejection, meaning that there is no need for a rejection filter. The coupler uses a 'probe-type' coupling element to couple to the vertical and accelerating HOMs.

---

[1] The crab cavity HOM 'categories' used are detailed in the coming chapters.

Chapter 3

SPS DQW HOM Coupler

As superconducting crab cavities had never before been used with protons, prototype tests in the Super Proton Sychrotron[1] (SPS) were scheduled. The aim of the tests was to identify any unforeseen risks and to demonstrate operational reliability, machine protection and cavity transparency [17].

The first test scheduled was for that of the Double Quarter Wave (DQW) crab cavity. A two-cavity cryomodule was scheduled for testing in the final quarter of 2018.

The HOM coupler designed for the SPS DQW crab cavity test is presented in this chapter. Firstly, the choice of HOM coupler design along with the RF performance is evaluated with the use of equivalent circuit analysis. The circuit response is then compared to that of 3D electromagnetic simulation software; Parametric analysis is applied.

Finally, 'test-boxes' are designed and used to measure the manufactured coupler response, comparing this to simulations to qualify that the transmission response of each coupler is as expected.

3.1 Design

The DQW HOM coupler evolved from the '4-Rod' crab cavity HOM coupler design shown in [102]. The annotated vacuum cross-section for the DQW HOM coupler

---

[1] CERN's 7 km proton synchrotron.

is shown in Fig. 3.1 alongside photographs of the manufactured coupler.

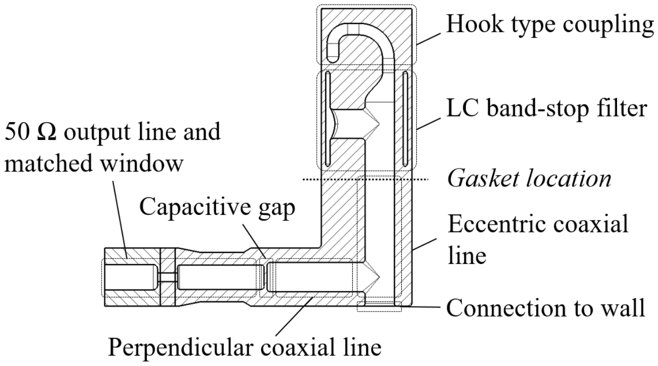

(a) Two dimensional schematic of the SPS DQW HOM coupler's vacuum geometry.

(b) Manufactured assembly. (c) Manufactured pieces.

Figure 3.1: HOM Coupler for the SPS DQW crab cavity.

The structure is an 'on-cell', niobium HOM coupler which is internally cooled by liquid helium to 2 K and operates in the superconducting regime. If the couplers were not superconducting they would not support the cavity's high magnetic field and would significantly reduce the Q_0 of the cavity.

The locations at which the HOM couplers are installed onto the cavity is shown in Chapter 2, Sec. 2.4. To evaluate why these locations were chosen, the modes for which damping is most important was evaluated. The bare cavity model, alongside the r/Q values for the HOMs under 1 GHz[1], is detailed in Fig. 3.2. The r/Q values

---

[1] Due to the profile of the proton bunch, the HOM excitation is inversely proportional to the frequency with a 'Gaussian-like' dependence. Hence, low frequency HOMs generally have a stronger excitation.

are separated into ‘transverse vertical’, ‘transverse horizontal’ and ‘longitudinal’. For the crab cavities proposed for the HL-LHC upgrade, each of the HOMs is classified as ‘vertical (v)’, ‘horizontal (h)’, ‘longitudinal (l)’ or ‘hybrid (hy)’, as it is difficult to assign them to pillbox equivalences due to the complex field topologies of the ‘exotic’ structures.

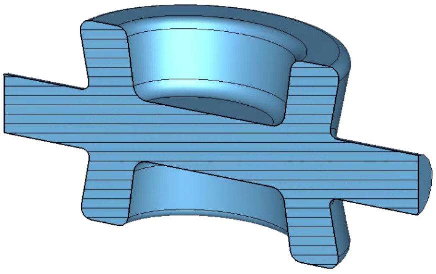

(a) Bare cavity model.

f [MHz]	r/Q_v [Ω/m]	r/Q_h [Ω/m]	r/Q_l [Ω]
592.5	0.3	0.3	$\boxed{55.2}$
689.2	0.0	$\boxed{34.7}$	0.0
715.6	$\boxed{1.2}$	0.2	$\boxed{7.7}$
755.9	$\boxed{21.1}$	0.0	0.0
934.4	0.0	$\boxed{17.3}$	0.0
969.4	0.2	0.1	$\boxed{9.7}$

(b) r/Q values for the low frequency modes.

Figure 3.2: SPS DQW bare crab cavity detrimental mode evaluation.

The field topology for the three modes with the highest r/Q values in each respective plane was evaluated to assess the best location to install the HOM couplers. As it was not possible to install ancillaries onto the side of the cavity structure, due to the transverse dimension restrictions arising from the second beam pipe in the LHC, the HOM couplers could only be installed on the top and bottom of the cavity. As such, the field topology was evaluated in this location specifically. The electric and magnetic fields for the three modes are shown as contour plots in Fig. 3.3 and as vector plots in Appendix Sec. 3, Fig. 8. The longitudinal mode at a frequency of 969 MHz is also shown. This is because, as a result of the filling schemes used in the LHC, modes close to multiples of the bunch spacing harmonic frequencies[1] (multiples of 40.08 MHz) can be very detrimental for HOM power generation.

---

[1] This concept will be expanded upon in the coming chapters but, for reference, it ‘flags’ this mode as dangerous for HOM power generation.

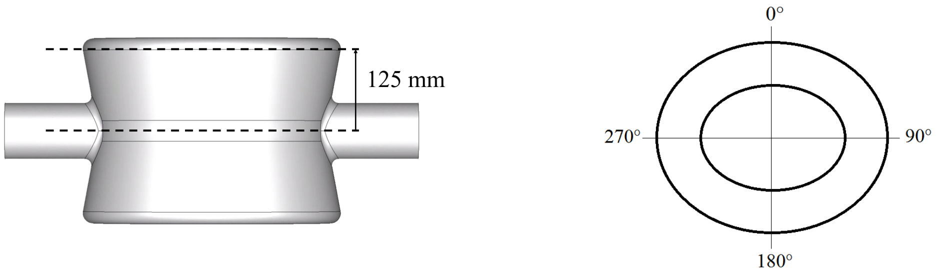

(a) Plane used for field contour plots. (b) Field evaluation plane.

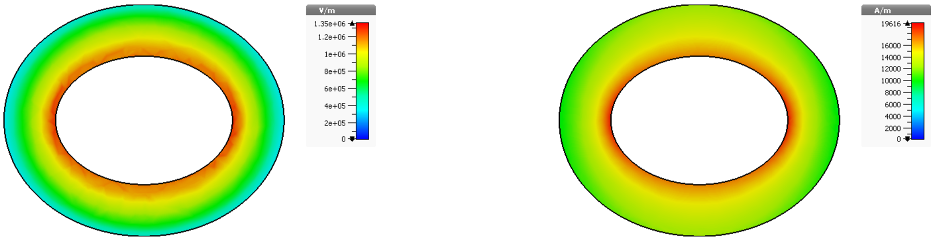

(c) 593 MHz - E-Field. (d) 593 MHz - H-Field.

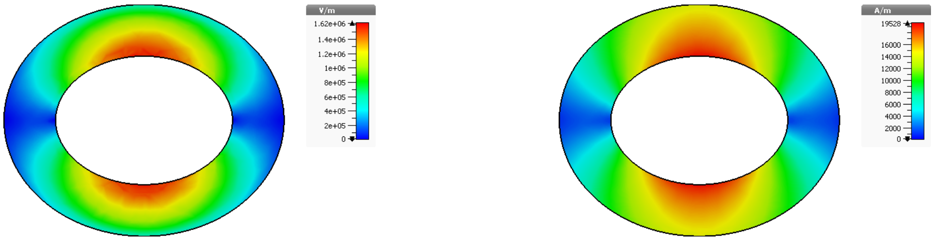

(e) 689 MHz - E-Field. (f) 689 MHz - H-Field.

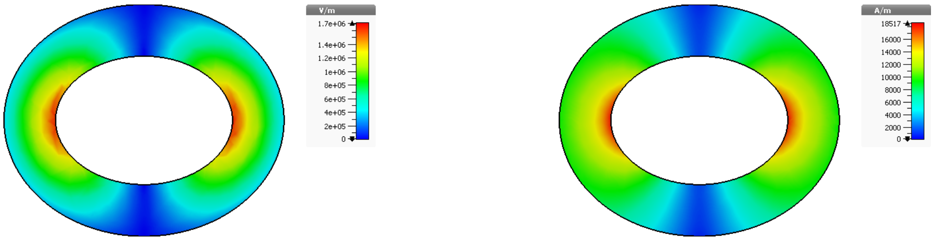

(g) 756 MHz - E-Field. (h) 756 MHz - H-Field.

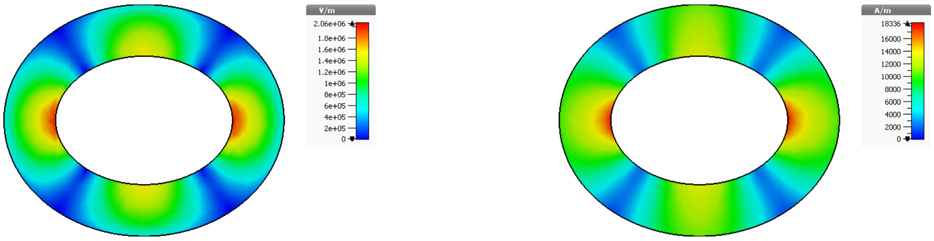

(i) 969 MHz - E-Field. (j) 969 MHz - H-Field.

Figure 3.3: Field profiles for low frequency ($< 1\,\text{GHz}$), high impedance higher order modes in the bare SPS DQW crab cavity. The fields correspond to a stored energy of 1 J.

The electric field of each mode acts between the inner quarter wave resonator and the outer wall and the the magnetic field 'flows' around the central conductor; The field profiles in this plane are similar to that of a coaxial line. As there is a high magnetic field at the location shown for each of the modes, the DQW HOM coupler's hook-type coupling mechanism was chosen to couple magnetically, but to also allow the couplers to be 'de-mountable'. Electric coupling wasn't chosen as, although there is an electric field component, for most HOMs the E-field is small at the coupler port area compared the central cavity region. Therefore adequate coupling would require a large coupling element to provide a significant area perpendicular to the electric field lines. Additionally, the axial electric field could be perturbed, contributing to larger multipole components of the fundamental mode [57].

Although it is difficult to exactly match any of the modes to those of a perfect cylindrical resonator (i.e. the 'pillbox cavity'), the field 'poles' in this plane are clear. Referring to the contour plots (Fig. 3.3), for the 593 MHz mode, the angle at which the HOM coupler ports are placed does not matter since there are no defining poles and hence a uniform field distribution around the elliptical path. For the next two modes shown however, 689 and 756 MHz, there are two poles where both the electric and magnetic fields are enhanced. The planes of these two poles are perpendicular to one another, hence meaning that choosing HOM coupler port locations (Fig. 3.3b) at only 90° and 270° or at 0° and 180°, would only allow sufficient coupling to one of these modes. Hence, coupler ports in both planes should be used, or at angles in-between them (i.e. 45°, 135°, 225°, 315°. The 969 MHz mode has four poles which align with the planes of the previous two modes.

Originally, for the Proof-of-Principle (POP) design [54], one Fundamental Power Coupler[1] (FPC) port and one HOM coupler port were included on the top side of the cavity at 270° and 90° respectively. On the bottom of the cavity, four HOM coupler ports were included at 45°, 135°, 225° and 315°. This allowed coupling to all of the pole configurations shown in Fig. 3.3. Additionally, it allowed the LHC's

---

[1] Device which couples power into the cavity. For the DQW this structure also uses a hook-type coupling element.

second beam pipe to pass if the cavity was used in the horizontal kicking scheme[1].

Evolving from the PoP design to the SPS DQW crab cavity, two HOM couplers were removed from the bottom to reduce the number of cavity ancillaries. In terms of coupling to the HOM fields, one was left in the 45/225° plane and one in the 135/315° plane.

The HOM couplers are installed on each port with the hook orientated perpendicular to the magnetic field, in order to provide maximum coupling; this angle is equal to that of the port, i.e. 45° and 135° for the bottom couplers and 90° for the top HOM coupler. For reference, the dressed DQW crab cavity is shown again in Fig. 3.4.

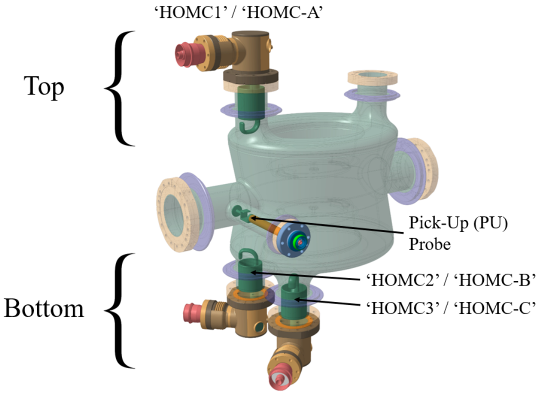

Figure 3.4: DQW crab cavity dressed with HOM couplers and pick-up probe.

3.2 Modelling as an Equivalent Circuit

To analyse the transmission response and hence geometry choice of the HOM coupler, it is possible to model the geometries using electronic circuit equivalences. This form of analysis allows rapid modelling and optimisation of coaxial couplers and is hence a good starting point for assessing key geometries and provides a tool for future optimisation and tuning.

---

[1] The feasibility of changing the 'kicking plane' was investigated for both the DQW and RFD crab cavities during the cryomodule proposal stage.

3.2.1 Modelling the hook

As discussed, the coupling section of the HOM coupler is a hook which preferentially couples to the magnetic fields of the HOMs. Magnetic coupling is modelled by a series voltage across an inductor. The lumped element equivalence for the hook is shown in Fig. 3.5. The capacitance is provided by the distance between the hook and the outer wall.

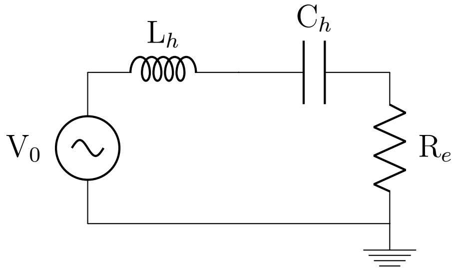

Figure 3.5: Equivalent circuit for the coupling hook.

The resonant frequency is defined by

$$\omega_0 = \sqrt{\frac{1}{L_h C_h}} \tag{3.1}$$

where, if assuming a parallel plate scenario, the capacitance can be expressed as

$$C_h = \frac{\epsilon A}{d} \tag{3.2}$$

where ϵ is the permittivity, A is the overlap area of the plates and d the distance between them. When using the coupler's geometry, this results in a C$_h$ value of 0.386 pF. This was calculated using the average distance of the hook from the outer wall of the coupler which varied due to the elliptical cross section of the hook (employed to spread the magnetic flux and increase coupling).

To evaluate the inductance of the hook, two methods can be used. The first is to assume that the hook is a perfect loop. The inductance in this case is given by [103]

$$L_h = \mu_0 \mu_r \frac{D}{2} \left[ln \left(\frac{8D}{d} \right) - 2 \right] \tag{3.3}$$

where μ_0 and μ_r are the vacuum and relative permeabilities respectively, D is the diameter of the loop and d the cross-sectional diameter. As the hook is not a perfect loop, some approximations are necessary. Figure. 3.6 shows the hook cross-section in two planes for the estimation of D and d.

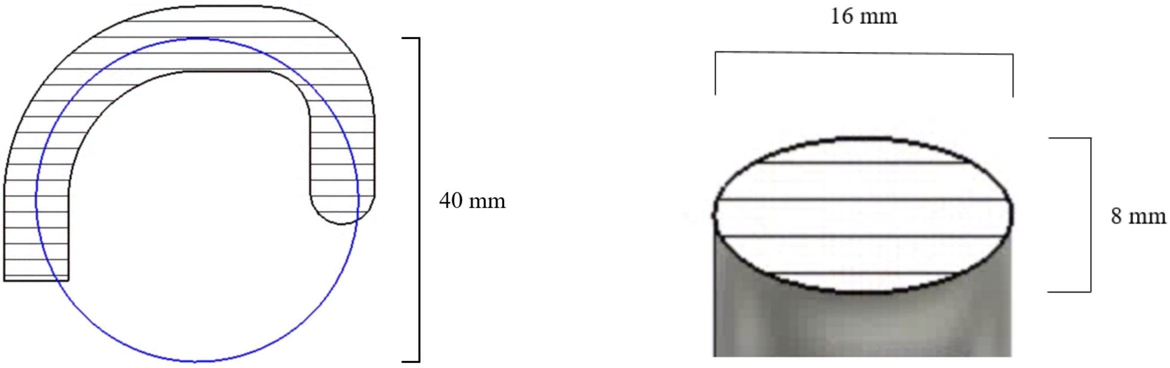

(a) 'D' estimation
Loop area.

(b) 'd' estimation
Elliptical bar geometries.

Figure 3.6: Hook cross-sections for loop equivalence estimations.

The coupling loop diameter D can hence be seen to be around 40 mm and the cross-section diameter d between 8 and 16 mm. Since the hook only covers half of the circumference of the loop, the diameter for the equation was halved to 20 mm. To evaluate the spread of the loop inductance due to the uncertainty in the parameter values, a plot of the inductance as a function of loop diameter for the major and minor diameters of the ellipse was produced. This is shown in Fig. 3.7.

The highlighted area on the plot shows the loop inductance range that appropriately models the hook of the SPS DQW HOM coupler.

The second method of calculating the inductance is to model the hook in 3D electromagnetic simulation software and return the resonant frequency. The 3D code CST Microwave Studio [104] gave the resonant frequency of the SPS DQW HOM coupler's hook as 2836 MHz. Hence, using Eq. 3.1 with the capacitance calculated, the value of L_h was calculated as 8.16 nH. This value is annotated on the plot shown in Fig. 3.7 and is within the analytic range highlighted (within 10% of the average value). Since the analytic calculation makes many assumptions as

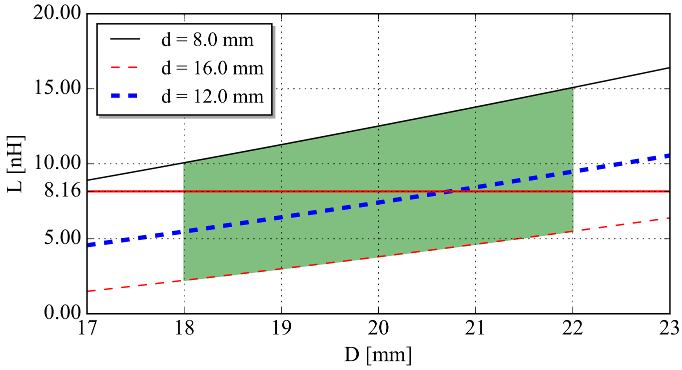

Figure 3.7: Loop inductance as a function of loop diameter D for the major, minor and average diameters of the elliptical cross-section.

it actually represents that of an ideal loop, the result from the electromagnetic simulation was used and hence a value of 8.16 nH was assigned to L_h.

3.2.2 Adding a Notch

With respect to the direction of the power flux from the cavity, the hook is connected via a coaxial transmission line to a band-stop filter. The purpose of this filter is to reject any power at the fundamental mode. This means the couplers will have a high external quality factor for this mode. It should be noted that the filter is placed before the location of the copper gasket to reduce the field from the fundamental mode at this location. For a case where the cross-section of the transmission line connecting the hook to the filter is two concentric circles, the impedance can be calculated using the formula for coaxial lines

$$Z_0 = 138 \times log_{10}\left(D/d \times 1/\sqrt{\epsilon_r}\right) \tag{3.4}$$

where D and d are the outer and inner diameters respectively and ϵ_r is the relative permittivity. However, as the transmission line to the band-stop filter is not coaxial and has an impedance which varies with cross-section, due to the tapered line and surrounding capacitive jacket, this method is not directly applicable. To obtain an accurate value for equivalent circuit analysis, it is possible to model the transmission line with its coaxial equivalence. To do this, the impedance along the line was computed in CST MWS. This, alongside the cross-section of the line, is shown in Fig. 3.8.

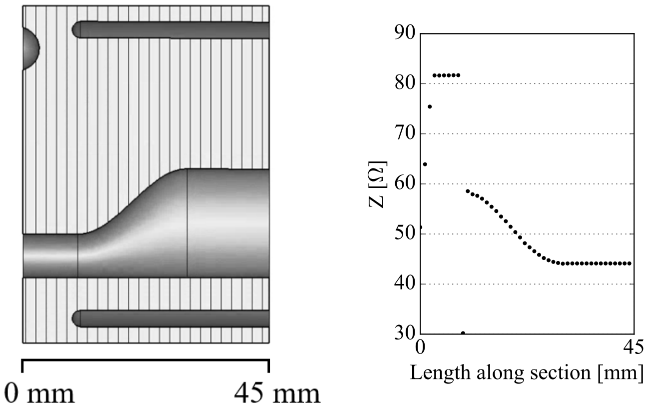

(a) Model cross-section. (b) Impedance variation.

Figure 3.8: Impedance modelling of the transmission line from the hook to the band-stop filter.

The final impedance along the line was used (44 Ω). The coaxial line formula was rearranged to give $D/d = 2.1$.

This D/d value can be used to model the line as its coaxial equivalence. Referring to Fig. 3.8a, the transmission line (TL_{h-bs}) length was set to 45 mm.

The band-stop filter elements are calculated in the same way as they were for the hook. The capacitive jacket was modelled using a parallel plate approximation, resulting in a capacitance value of $C_{bs} = 35.5\,\mathrm{pF}$. As the frequency is defined by the fundamental mode of the cavity (400 MHz), the corresponding inductance for a frequency of 400 MHz is $L_{bs} = 4.46\,\mathrm{nH}$ (Eq. 3.1). The equivalent circuit up to the band-stop filter is shown in Fig. 3.9 alongside the current response through the external resistor over a 3 GHz frequency range.

3.2.3 Modelling the Output Line

Following the band-stop filter, the next section of the coupler allows transmission at higher frequencies to provide a power flux to the HOMs (i.e. reducing their external quality factor). It is possible to model this section using lumped element analysis in a similar fashion to the modelling done for the hook and band-stop

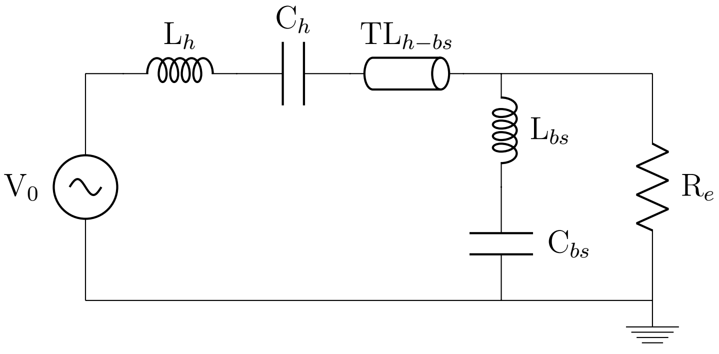

(a) Equivalent circuit.

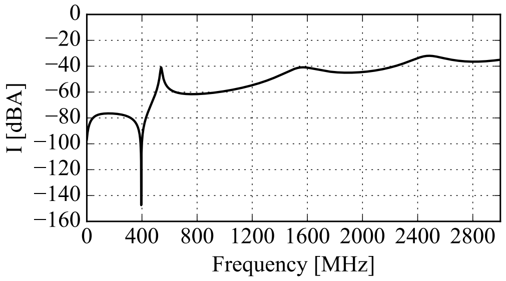

(b) Current response through the external 50 Ω resistor (R_e).

Figure 3.9: Coupler response up to the band-stop filter.

filter. However, like the section which connects the hook to the band-stop filter, transmission line modelling can also be used. The full equivalent circuit, to the 50 Ω output line, is shown in Fig. 3.10a. As the ‘hook-type’ coupling element is not purely magnetic, the configuration for electric coupling is also shown (Fig. 3.10b).

Following the band-stop filter, composed of C_{bs} and L_{bs}, the central shaft of the coupler from the band-stop filter to the bend section is modelled as the transmission line TL$_{bs-b}$ with a physical length of $\sim$ 105 mm. Again, the inner and outer conductors of this transmission line are not concentric and hence the eccentricity was accounted for by modelling the line impedance in CST MWS and calculating the corresponding outer to inner conductor diameter ratio for an ideal coaxial line. The shaft then splits into two lines which can be modelled by a parallel circuit. One line connects to the outer can of the HOM coupler and hence this is represented by an $\sim$ 18 mm transmission line to ground. The other line has a 90 ° bend, terminating as an open after a length of $\sim$ 77 mm. This line couples capacitively

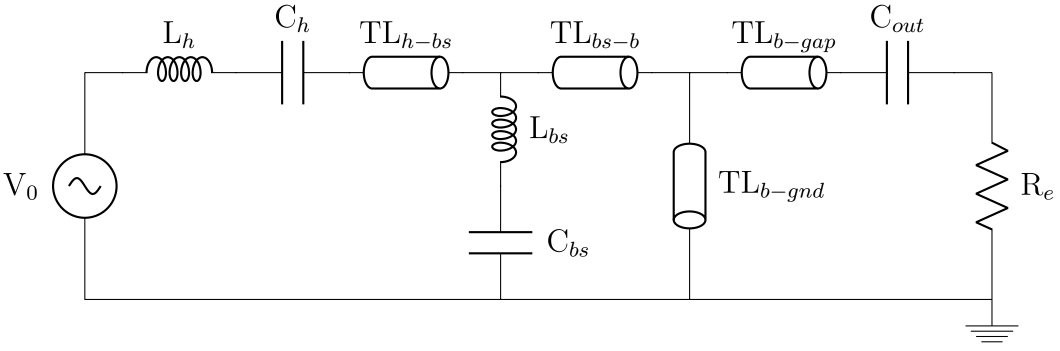

(a) Magnetic coupling.

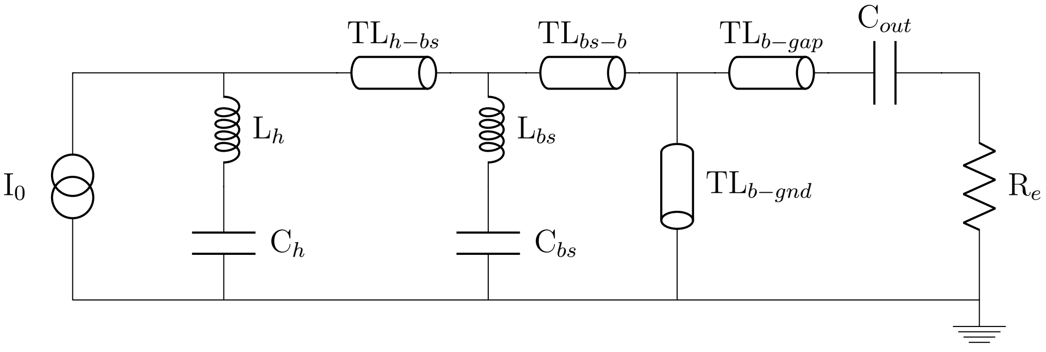

(b) Electric Coupling.

Figure 3.10: Equivalent circuits for the SPS DQW HOM coupler.

to the 50 Ω output line via a capacitance (C_{out}). The value of this capacitance, again using a parallel plate approximation, was calculated as 0.934 pF. All of the calculated values used for modelling the equivalent circuit are shown in Tab. 3.1. The current across the external load is shown in Fig. 3.11.

Component	Value	Component	Value
L$_h$	8.91 nH	TL$_{bs-b}$	D/d = 2.78, l = 105 mm
C$_h$	0.386 pF	TL$_{b-gnd}$	D/d = 2.78, l = 18.0 mm
TL$_{h-bs}$	D/d = 2.1, l = 45 mm	TL$_{b-gap}$	D/d = 1.98, l = 77.0 mm
L$_{bs}$	4.46 nH	C$_{out}$	0.934 pF
C$_{bs}$	35.5 pF	R$_e$	50 Ω

Table 3.1: Lumped element and transmission line values used for equivalent circuit.

In addition to the stop-band at the fundamental mode frequency, the final response shows multiple resonances at frequencies above 400 MHz at which there

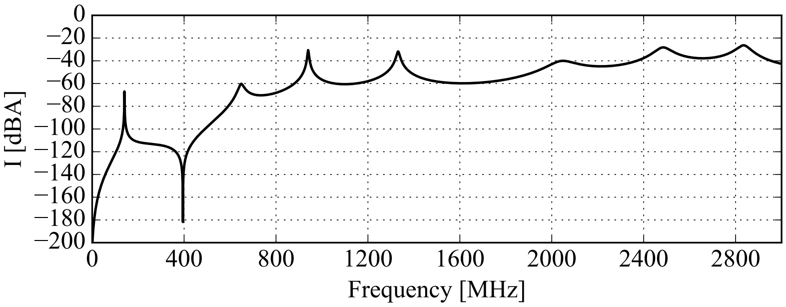

Figure 3.11: Current response over the external resistance ($R_e = 50\,\Omega$) for the circuit shown in Fig. 3.10 using the calculated values shown in Tab. 3.1.

is a relatively high transmission along the coupler. Operationally, for maximum damping, these resonances (or 'pass-bands') should be moved in frequency and optimised to provide the largest transmission to the most detrimental HOMs. The frequency and bandwidth of the pass-bands are determined by the transmission line characteristics. This is detailed in Chapter 2, Sec. 2.3.4.

3.3 Modelling using 3D Electromagnetic Simulation Software

To validate the response of the equivalent circuit model, it was compared to that of the HOM coupler modelled in 3D electromagnetic software. Although the couplers can be represented by equivalent circuit modelling of the most dominant geometries, the complex axially asymmetric features are in reality a massive array of lumped elements which are impossible to model in their entirety. Additionally, the physical lengths measured on the coupler do not necessarily correspond to their electrical lengths when subjected to RF, and the equivalent circuit model does not correctly model the superposition of the forward and reflected waves.

The coupler was hence modelled in the frequency domain in CST Microwave Studio [104]. The waveguide ports for the simulation were placed at the 50 Ω coaxial line output and at the open cylindrical waveguide above the hook. The resulting S_{21} response is shown in Fig. 3.12 for cases where the waveguide mode on the open vacuum port (port 1) is either the TM_{01} or TE_{11}.

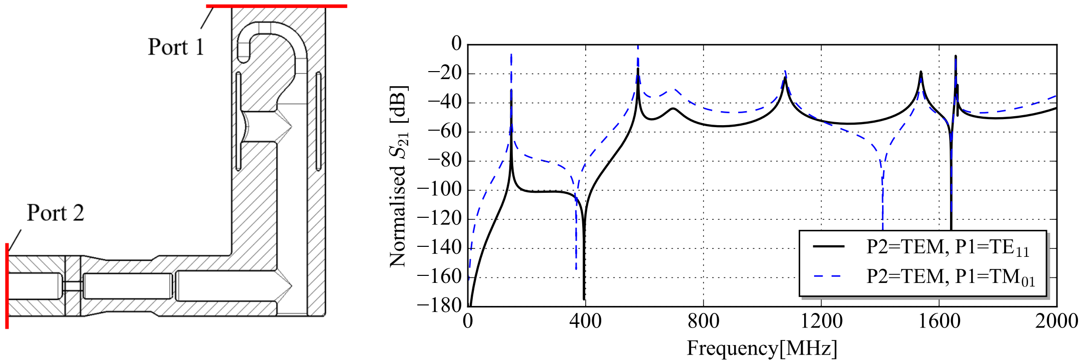

(a) Vacuum geometry with port locations.

(b) S_{21} response.

Figure 3.12: SPS DQW HOM coupler transmission response.

The form of the S_{21} plot is similar to that of the equivalent circuit response shown in Fig. 3.11, showing the stop-band at the fundamental mode frequency, rise to high transmission at $\sim$ 600 MHz the two transmission line pass-bands over 800 MHz seen in the equivalent circuit model. Rejection-bands are seen at $\sim$ 1.4 GHz (in TM_{01} case) and 1.6 GHz where the first is the coaxial cut-off frequency of the TM_{01} mode (lower in frequency due to lumped element interference) and the second is a TE-resonance between the outer conductor and capacitive jacket.

It should be noted that the amplitude of the S_{21} response is an arbitrary value which is a function of the distance from the hook to the open waveguide port (Port 1 in Fig. 3.12a). The relative amplitude is valid however, and hence for comparison and evaluation of geometric changes, the same distance from the hook to the open vacuum waveguide port should always be used. The results are generally normalised for easier comparison and visualisation.

As the equivalent circuit model shows three pass-bands before 2 GHz whereas the 3D simulation shows four, the effect of each of the transmission line lengths on the current response was evaluated. The discrepency was found to be a result of the transmission line TL_{h-bs}. This line represents the length between the hook and band-stop filter sections. Changing the length from 45 mm to 110 mm decreased the frequency of the pass-band most effected by this geometry and hence ‘split’ it from another pass-band at the same frequency. This brings the form of the current response very close to that of the simulated S_{21} response in CST MWS. The large increase in length required for this parameter is due to the difficulty in representing the complex tapered section connecting the hook to the band-stop filter as an equivalent transmission line. The increase needed shows that the transmission line length is not just the section shown in Fig. 3.8a but is in reality made up of this section, some of the hook length and some of the inductive stub length. These three lengths added together are ~ 100 mm.

The current through the external load for the circuit values detailed in Tab. 3.1, but with a change in the length of the transmission line TL_{h-bs} from 45 to 110 mm, is shown in Fig. 3.13.

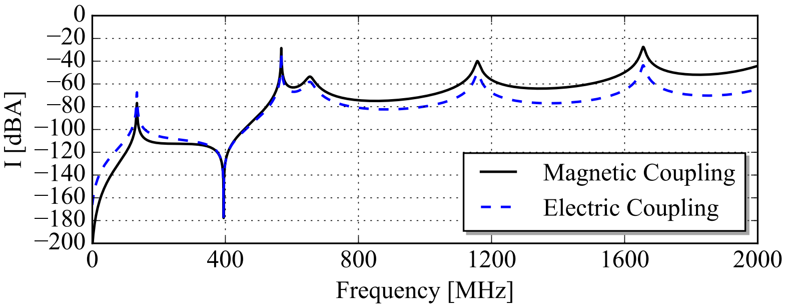

Figure 3.13: Changing the length of TL_{h-bs} to 110 mm.

The form of the equivalent circuit is now the same of that of the 3D simulation.

3.3.1 Tuning

The equivalent circuit parameters were approximate and measured from the coupler lengths. The lengths do not exactly represent that of the coupler’s circuit equivalences, as it is difficult to predict the start and end points of each transmission line. As such, the circuit was tuned to best represent that of the CST MWS response shown in Fig. 3.12b.

To identify the parameters which had the greatest affect on the coupler's transmission features, each equivalent circuit element was altered by ±10%. The deviation in the transmission response showed which features the given element strongly affected. The results from the study are shown in Fig. 3.14: For reference, Fig. 3.14a shows the equivalent circuit. Figure 3.14b shows a cross-section of the HOM coupler with the circuit equivalences highlighted and Fig. 3.14c shows the transmission response annotated with the equivalent circuit elements which most strongly affect each feature.

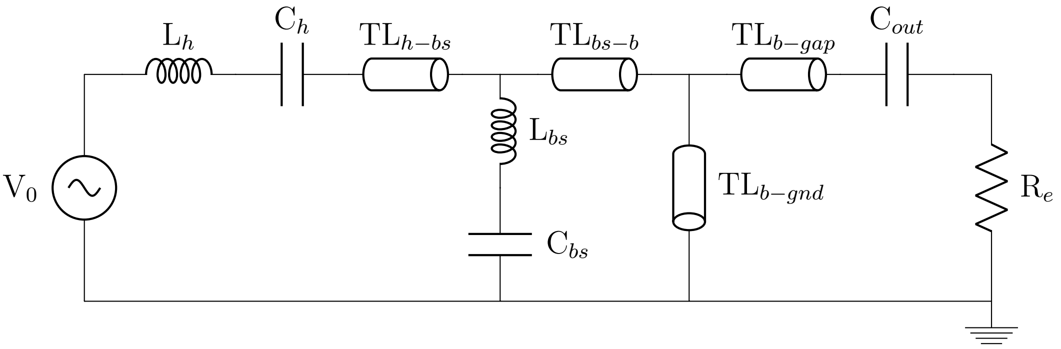

(a) Equivalent circuit.

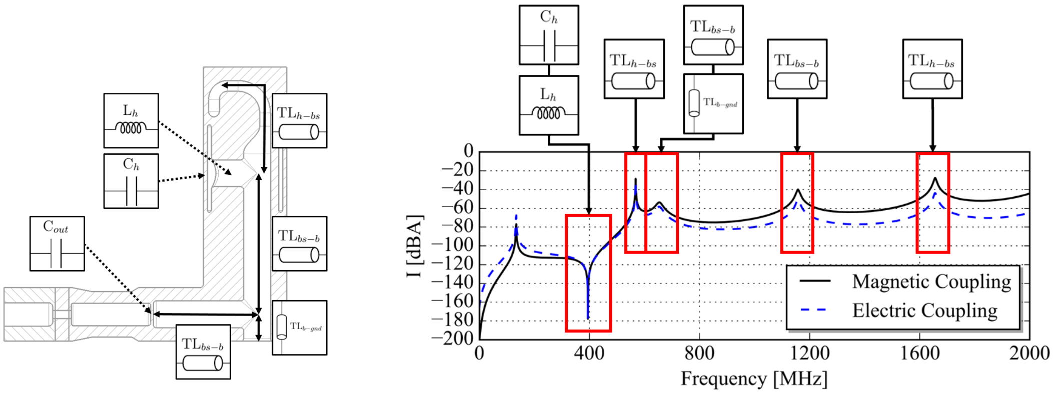

(b) Schematic.

(c) Stop-band and pass-bands annotated with the coupler equivalences which most strongly influence them.

Figure 3.14: Coupler schematic detailing transmission line equivalences and the corresponding pass-bands.

The frequencies and bandwidths of the pass-bands result from the transmission line characteristics. In most cases, the resonances are most strongly affected by one transmission line, however one is the result of the coupling between two transmission lines.

To visualise the pass-band resonances, the electric and magnetic fields at the frequencies of each of the pass-bands were generated in CST MWS (frequency domain, 1 W RMS input). The resulting contour plots are shown in Fig. 3.15.

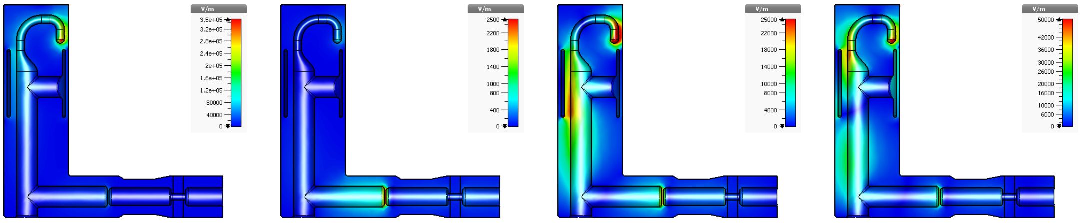

(a) 578 MHz (E) (b) 697 MHz (E) (c) 1077 MHz (E) (d) 1538 MHz (E)

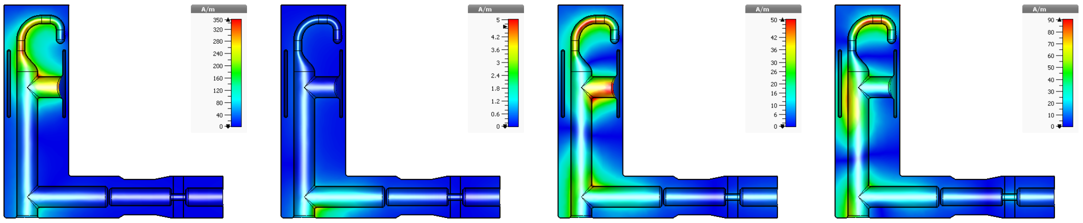

(e) 578 MHz (H) (f) 697 MHz (H) (g) 1077 MHz (H) (h) 1538 MHz (H)

Figure 3.15: Electromagnetic fields at the frequencies of the coupler pass-bands.

The field profiles show the geometries across which the coupler resonances act. The areas with the highest field correspond to the equivalent circuit features which most strongly affect the pass-band. It is also clear however, that the pass-bands are influenced by multiple geometries and are actually the result of the coupling between multiple circuit elements.

Knowing which circuit equivlance controlled which pass-band, the equivalent circuit was tuned to match that of the CST MWS response. The two transmission curves are displayed in Fig. 3.16 and the corresponding circuit parameters are detailed in Tab. 3.2.

The first three pass-bands were tuned to within 5 MHz of that shown for the 3D model. For the pass-band at 1538 MHz in the CST simulations, it was difficult to get the frequency lower than 1640 MHz without perturbing the other peaks in the

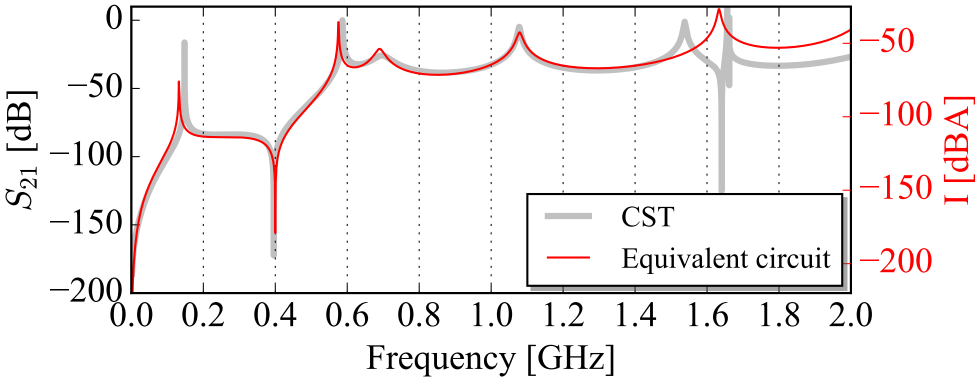

Figure 3.16: Tuned response.

Component	Value	Component	Value
L_h	8.91 nH	TL_{bs-b}	D/d = 2.78, l = 120 mm
C_h	0.386 pF	TL_{b-gnd}	D/d = 2.78, l = 18.0 mm
TL_{h-bs}	D/d = 2.1, l = 109 mm	TL_{b-gap}	D/d = 1.98, l = 70.0 mm
L_{bs}	4.46 nH	C_{out}	0.934 pF
C_{bs}	35.5 pF	R_e	50 Ω

Table 3.2: Tuned lumped element and transmission line values.

equivalent circuit response. Three main assumptions explain this. The first is that the effect of smaller geometries becomes more significant at higher frequencies. For example at 600 MHz the corresponding quarter wavelength is ∼ 125 mm whereas at 1.5 GHz it is ∼ 50 mm. The smaller geometries need to be modelled as circuit elements to get a more accurate response. Generally, this is the effect of several inductances associated with the blended and bend sections.

Secondly, the location at which the field couples to the hook differs with frequency. This means that the first transmission line length (TL_{h-bs}) varies as a function of frequency. This transmission line strongly affects two coupler resonances (see Fig. 3.14c - at ∼ 600 and 1600 MHz). As such, the static value was chosen to best represent the first peak of the coupler modelled on it's own. However, when the coupler is installed onto the cavity, the field topology (and hence location of coupling), will vary with each HOM. Each HOM could be modelled as a separate RLC circuit coupled to the HOM couplers equivalent circuit, but this process would be very arduous and time consuming.

Thirdly, as discussed, the TE-resonance between the outer conductor and capacitive jacket results in a stop-band at 1.6 GHz. This resonance is not modelled in the equivalent circuit and as such, the resulting perturbation on the pass-band at a similar frequency is not represented.

Since the general response of the equivalent circuit gave an accurate representation of the coupler's response in 3D electromagnetic simulation software, no further changes were made, as the goal of the modelling was to provide a means for parametric analysis and rapid optimisation.

3.3.2 Parametric Studies

After tuning the circuit response, parametric studies were performed to provide information on how to alter the coupler's transmission response in the frequency domain. Each value was varied from 0.8 – 1.2 times its original value in five steps. The responses are displayed in Fig. 3.17.

Referring back to the analysis of which circuit parameters most strongly effected which transmission features (Fig. 3.14c), the parametric studies display these relationships, but also show that other elements can still have a significant effect on a given pass-band.

The studies, with simulation times of less than ten seconds, detail the methods available to alter the HOM coupler's response in the case of new specifications, new cavities or unforeseen issues.

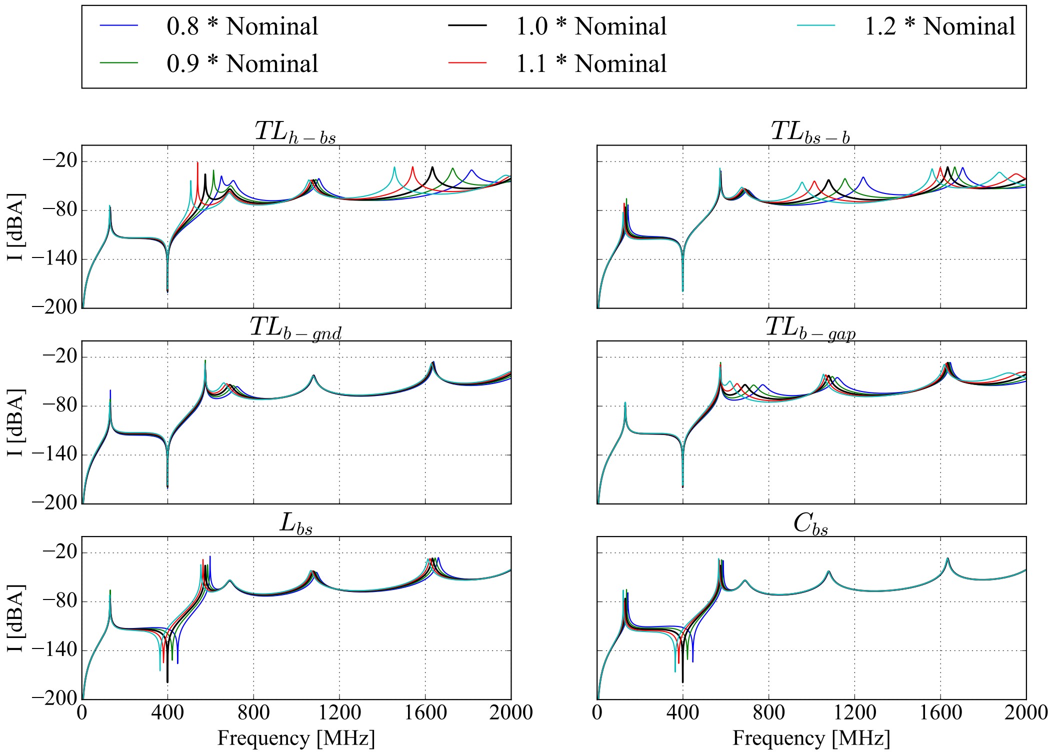

Figure 3.17: Spectral variations with equivalent circuit parameter changes.

3.4 HOM Coupler Test Boxes

HOM coupler test-boxes were designed to measure the HOM coupler transmission response at warm (room temperature), before installation onto the cavity. Any deviations from the simulated case would signify a fabrication error. The change in the band-stop filter frequency response would be quantified and higher frequency deviations analysed to see for which modes the damping would vary.

Additionally, the feasibility of having a ‘dual-coupler’ system for pre-installation RF conditioning was to be investigated.

3.4.1 Design

Conceptually, a circular wave guide was used, allowing two HOM couplers to be mounted on either side. Pick-up ports were installed onto the structure near to the location of the HOM coupler hooks.

As analysis of the HOM couplers was required over a large frequency range, a magnetically coupled pick-up, inductively connected to the outer wall of the cavity, was used. Using pick-ups with capacitances to ground resulted in resonances which would perturb the high frequency response. A 3D render of the test box, with two HOM couplers installed, is shown in Fig. 3.18 and the annotated vacuum model in Fig. 3.19.

The length of the pick-up ports has an effect on the most predominant waveguide mode measured. As such, the length of this port was kept minimal in order to measure the TE_{11} response.

The HOM coupler response compared to that of the test box is shown in Fig. 3.20. The general form of the spectral response is well replicated by the test-box measurement. Note, as the coupler was modelled with a waveguide port at an arbitrary distance from the coupling hook, the amplitude of the coupler response is arbitrary.

3.4.2 Single Coupler - Band-Stop Filter Frequency

Each of the HOM couplers were mounted onto one side of the test box, with the other side blocked with an aluminium plate to provide an electrical short. The

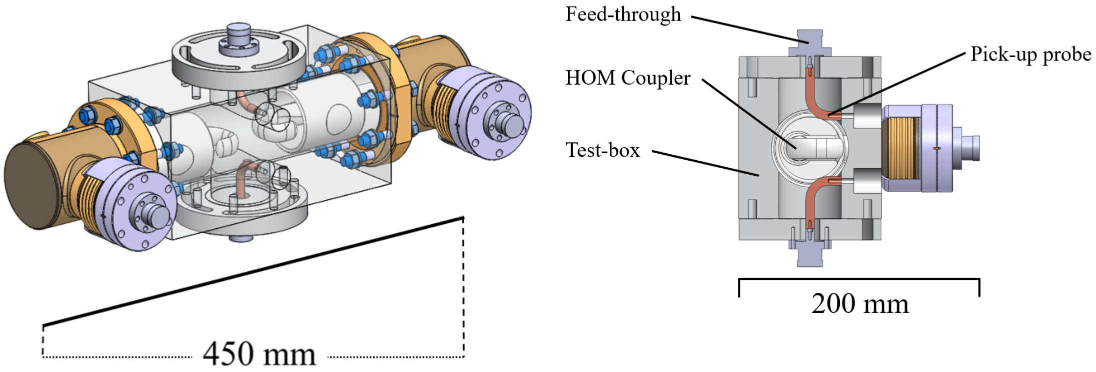

(a) Assembly.

(b) Cross-section detailing inductive pick-ups.

Figure 3.18: Low power HOM coupler test box (CAD) with two HOM couplers mounted.

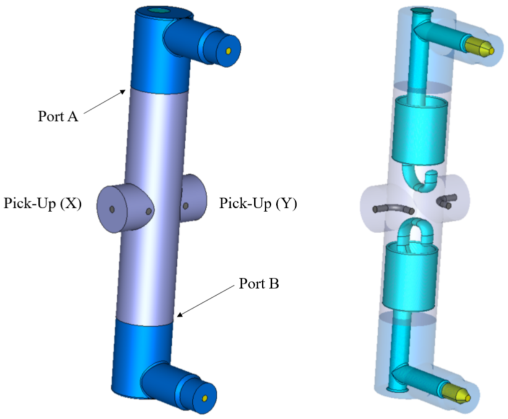

Figure 3.19: Annotated test box vacuum model.

set-up is displayed in Fig. 3.21.

The stop-band frequency was measured for each coupler. The results are shown in Fig. 3.22 and a tolerance study to show the effect of several parameters on the stop-band frequency is shown in Tab. 3.3

Comparing the measurements on side A and side B of the test box (Fig. 3.19), there is an offset between the two data-sets of $\sim 3\,\mathrm{MHz}$. The systematic nature of the offset suggests this is due to an error in the test box geometry. Referring to the tolerance table (Tab. 3.3), a deviation of $3\,\mathrm{MHz}$ is too large to be caused by any single error, but could be a combined effect of alignment, rotational and test

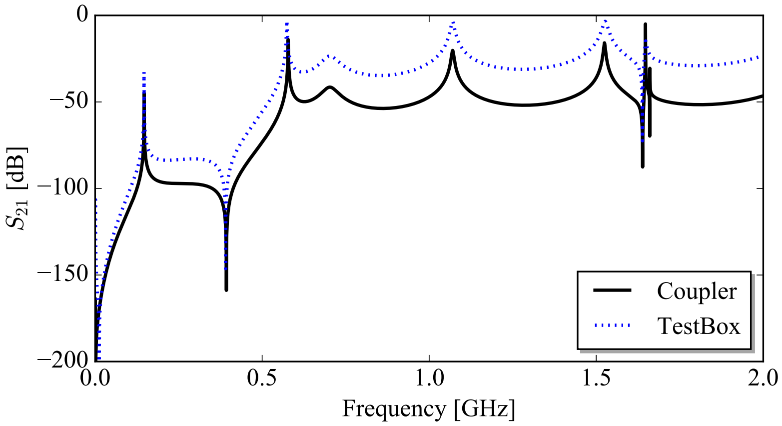

Figure 3.20: Simulated coupler response (arbitrary amplitude) compared to the simulated test box response. The simulations reflect measurement conditions, i.e. using air as the background medium and with 300 K geometries.

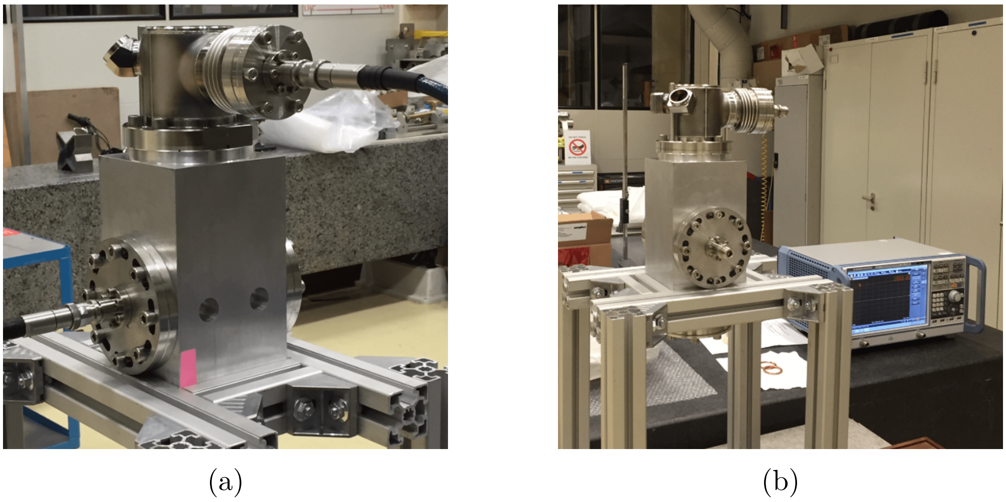
(a)

(b)

Figure 3.21: Single HOM coupler on test-box.

box length errors.

The errorbars on each of the measurements represent ± one standard deviation of the stop-band frequency measurements taken on both pick-up probes. The error bar represents an axial misalignment of the HOM coupler.

The main conclusion from the stop-band measurements is that, although the frequency value of the stop-band is not accurate due to errors on the test box

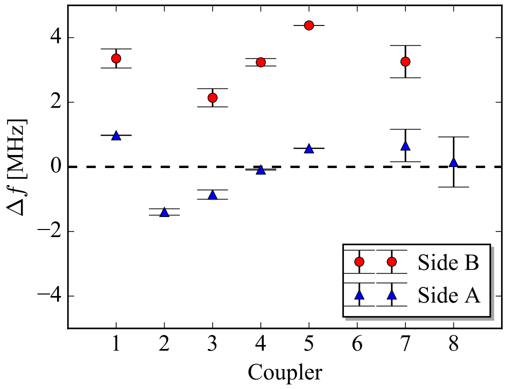

Figure 3.22: Stop-band frequency measurements. The frequency is plotted as the difference from the nominal simulated test-box value (Δf).

Tolerance	Unit	Δf per 1 unit [kHz/unit]
Coupler axial allignment	Degrees	28
Coupler rotation	Degrees	122
Coupler insertion	mm	324
Difference between pick-up probe signals (X and Y) with coupler rotation	Degrees	244
Pick-up probe diameter	mm	21
Pick-up probe length	mm	316

Table 3.3: Stop-band frequency error analysis.

made clear by the differing results from mounting the couplers on the two sides, the 2.4 MHz spread between the couplers is representative.

3.4.3 Single Coupler - Broadband Frequency

In addition to measurements of the stop-band frequency, the broadband transmission was also measured. The transmission response between the coupler and pick-up ‘X’ is shown in Fig. 3.23. Unlike the stop-band measurements, the high frequency section of the spectral transmission response, i.e. after 600 MHz, does not change with the test box or pick-up probe geometry. The high frequency section is determined by the transmission line lengths and as such any deviations from the simulated response is a result of HOM coupler geometric deviations, rather than errors on of the test-box geometry.

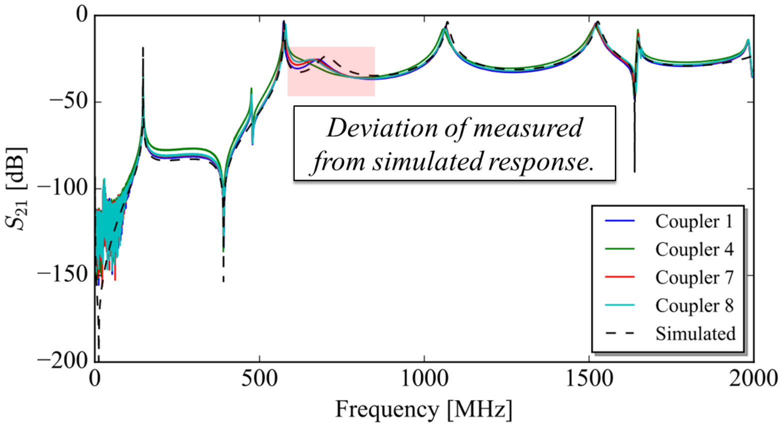

Figure 3.23: Test box transmission measurements. Four couplers are shown as the responses for couplers 2, 3, 5 and 6 were perturbed by a calibration error.

For each coupler, the measured profile matches the simulated very well apart from in the region around 700 MHz. The pass-band which deviates from the simulation is strongly effected by the equivalent circuit transmission line TL_{b-gap} and TL_{b-gnd} (Sec. 3.2). As such, the frequency decrease is most likely due to extra length on the coupler's output line before the capacitive gap or an additional distance from the bend to the wall-connection.

The difference between the measured and simulated response ($\Delta S_{21} = S_{21:meas} - S_{21:sim}$) is shown in Fig. 3.24. The frequencies of the four low frequency DQW cavity modes detailed in Sec. 3.1 are annotated. A negative ΔS_{21} indicates less damping than designed.

There are two under-damped frequency bands when comparing the measured transmission responses to the simulated. The first is a broadband under damping centred at 710 MHz and is a result of the frequency increase of the pass-band frequency most strongly effected by the distance between the bend and output capacitance.

The second area, at around 1070 MHz is of similar amplitude to the first, but has a smaller bandwidth. Referring to Fig. 3.14c, this is from a relative lengthening

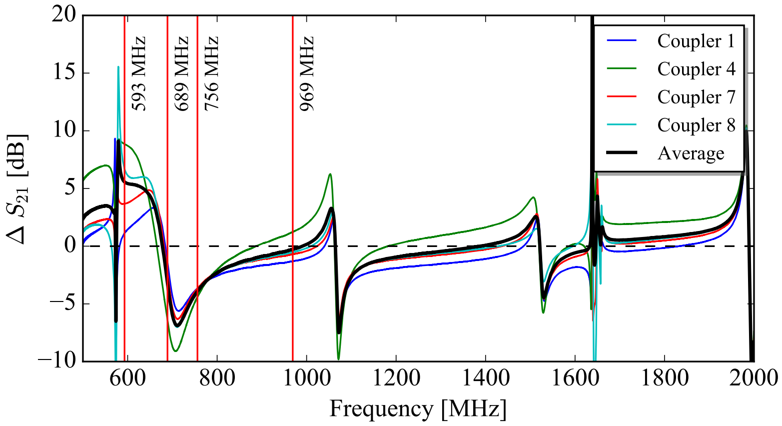

Figure 3.24: Difference between the simulated and measured traces shown in Fig. 3.23.

of the transmission line TL_{bs-b}, i.e. the length of the inner conductor of the coupler between the LC band-stop filter and bend section.

Additionally, the high frequency section, from $\sim$ 1700–2000 MHz, generally has a higher transmission than that of the simulations.

This information can be used to predict the change in HOM damping (i.e. the ratio of the measured to simulated cavity mode quality factor $Q_{e:meas}/Q_{e:sim}$). To verify this, the simulated mode parameters of the dressed cavity should firstly be assessed. Following this, the ratio of the measured to simulated mode quality factors should be compared to the deviation in damping predicted by the test-box measurements.

3.4.4 Dual Coupler Measurements

In addition to the single coupler measurements, dual coupler transmission measurements allowed the feasibility of transmitting RF power through the structures to 'pre-condition' the couplers before cavity installation, in a similar way to the procedure applied to the Fundamental Power Couplers (FPCs) [105]. A photograph of this set-up is shown in Fig. 3.25 and the measured response is shown in Fig. 3.25.

It is possible to transmit more than 40% of the power at three of the trans-

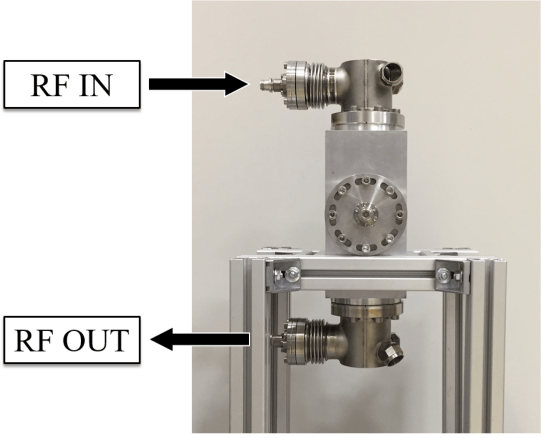

Figure 3.25: Dual coupler test-box measurement set-up.

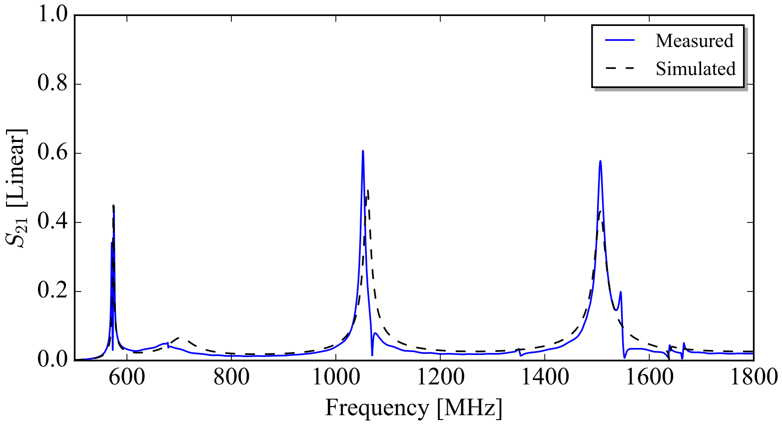

Figure 3.26: Simulated and measured transmission response from one HOM coupler to another.

mission line resonant frequencies. The amplitude of the S_{21} is slightly higher in measurements than in simulation for the second two transmission regions but is lower for the first. This is due to the intra-coupler frequency difference of the first narrowband pass-band. This could also happen for the other pass-bands, but the effect would be much less due to their larger bandwidths. Conditioning with such a structure should be done at 1050 or 1510 MHz. A circulator would be needed to protect the amplifier against the reflected power in the order of 20% of the input signal (around 20% 'losses' in the Niobium).

3.5 Conclusions

3.5.1 SPS DQW HOM Coupler

The HOM coupler that was designed and built for the SPS DQW crab cavity was evaluated in detail.

Firstly, the choice of HOM coupler location was analysed with respect to design restrictions and efficient coupling to the high r/Q HOMs.

The performance of the HOM coupler was then evaluated. For a detailed understanding and to provide a model for fast optimisation and tuning, an equivalent circuit model was used. The coupling element, band-stop filter and transmission line RF transformer section were modelled. The response of the equivalent circuit was compared to that of 3D electromagnetic simulations. It was found that one of the transmission line lengths modelled in the equivalent circuit (TL_{h-bs}) was underestimated by a factor of 2. Changing the length of this section in the equivalent circuit and tuning the structure gave a response very close to that of the 3D model. For reference, the responses are shown in Fig. 3.27.

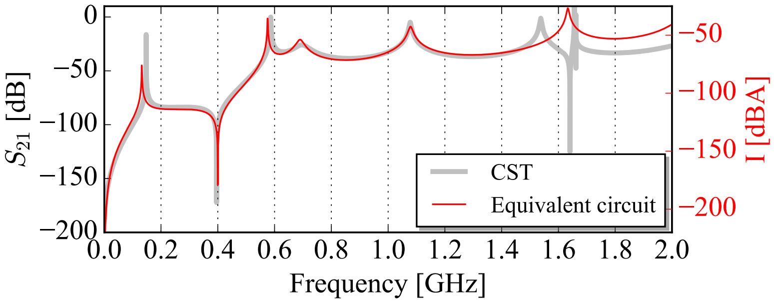

Figure 3.27: Tuned response.

Discrepancies in the pass-band at ~ 1.6 GHz were as a result of:

- The effect of smaller geometries becoming more significant at high frequencies.
- The coupling location of the field to the hook changing with frequency, acting to change transmission line lengths.

- The TE-resonance associated with the outer wall and capacitive jacket adds a perturbation not modelled in the equivalent circuit.

Since the responses were very close and the idea was not to reproduce the complexities of the 3D model, but to provide a model for fast optimisation and tuning, the equivalent circuit resulting in the response shown in Fig. 3.27 was kept. Parametric studies were carried out to evaluate the effect of each geometry on the transmission response of the coupler. This information can be used in the case of any necessary HOM damping changes needed.

3.5.2 Test Box Conclusions

To characterise the transmission response of the couplers, a ‘test-box’ was designed and manufactured and the response of each HOM coupler built for the SPS DQW was measured.

The test box measurements were split into two main measurement campaigns. The first measured the frequency of the stop-band and the second characterised the high frequency transmission response.

Difficulties with accurately measuring the stop-band frequency were observed as a result of errors imposed by the test-box geometry. This result suggests the same might be true with installation on the crab cavity and that the effect of the 3 MHz difference in stop-band frequency should be evaluated. Regardless of the error, the test-box allowed the intra-coupler stop-band frequency spread to be quantified.

The high frequency transmission analysis is not perturbed with any significance by the test-box or pick-up geometry because it is a function of the coupler’s transmission line lengths and as such insertion or rotational errors have a negligible effect on the transmission response. The deviation of the manufactured HOM coupler’s high frequency response from that of the simulated was quantified (ΔS_{21}) showing two frequency bands of decreased damping:

1) 710 MHz → broadband.
2) 1070 MHz → narrowband.

The use of these measurements to assess the ability to predict deviations in HOM damping from simulations to measurements should be verified. To do this, the simulated dressed cavity mode parameters should be compared to the measured and the resulting ratios in quality factor compared to the test-box measurements.

Chapter 4

Impedance and Power Calculations

Following the analysis of the SPS DQW HOM coupler's equivalent circuit operation, the impedance spectra of the cavity with three HOM couplers mounted was evaluated, assessing the ability of the HOM couplers to damp the HOMs within given thresholds.

In Chapter 3, the HOMs in the DQW crab cavity were characterised as 'vertical', 'horizontal' and 'longitudinal' depending on there r/Q values. The same nomenclature will be used hereafter, but with reference to the HOM impedances, i.e. taking into account their quality factors.

As a result of the HL-LHC's high beam current, high HOM powers as a result of the interaction with longitudinal HOMs is feasible. As such, after evaluating the longitudinal impedance, the HOM power was calculated and evaluated statistically, using measured deviation values, to assess the worst-case.

4.1 Impedance Calculations

As discussed in Chapter 2, an important parameter used to quantify the effect of the higher order modes on the charged particle beam is the impedance. Impedance simulations are generally carried out using either wakefield or Eigenmode solvers. Wakefield simulations return the impedance as a function of frequency, whilst the

Eigenmode simulations generate the mode parameters and field topology from the solutions of the eigenvalue problem [106]. In Eigenmode simulations, the impedance is calculated for the respective resonant modes.

The wakefield simulations are limited by the computationally intensive calculations that are needed for high-Q cavities. As such, using the mathematics detailed in Chapter 3, the Eigenmode solver in CST MWS [104] was used for the impedance simulations. The 'non-linear Eigenmode solver' with tetrahedral meshing was used for the calculations. The non-linear solver avoided problems with 'Q-switching' (where the quality factors are mistakenly assigned to adjacent modes) often seen with the standard Eigenmode solver for broadband simulations. For this reason and for general accuracy, this solver was recommended by the software developers [107]. Figure 4.1 shows the dressed SPS DQW crab cavity, annotated with the coupler nomenclature used throughout this thesis, alongside the vacuum model used for simulations.

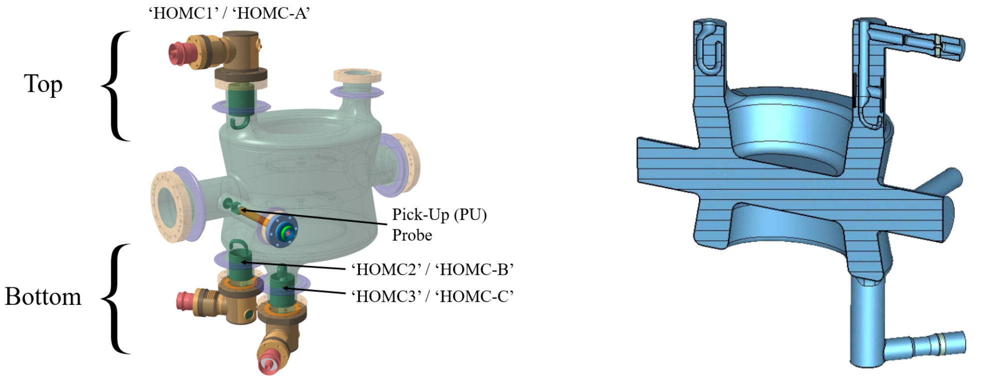

(a) HOM coupler nomenclature. (b) Vacuum model in CST MWS [104].

Figure 4.1: Dressed SPS DQW crab cavity.

The longitudinal and transverse impedance was calculated for the dressed SPS DQW crab cavity[1]. The transverse impedance was calculated in the vertical and horizontal planes where a linear voltage relationship with radial position was assumed, modelling each mode as if it were a pure dipole. To account for the bandwidth of each mode, and since it was the resistive part of the losses (i.e. power

---

[1] The design for preliminary tests in the Super Proton Synchrotron (SPS) at CERN before installing the cavities into the LHC as part of the HL-LHC upgrade.

loss) for evaluation, the real part of the resonator model

$$Z(f) = \frac{Z_n}{1 + Q_e^2(x/f - f/x)^2} \tag{4.1}$$

was applied over a frequency range up to the beam-pipe cut-off frequency of 2.1 GHz. Here, Z_n is the impedance at the resonant frequency f, Q_e is the external quality factor and x is the frequency array.

For an ‘exotic’ cavity geometry such as that of the DQW crab cavity, some HOMs have significant $r/Q_{\parallel}$ and $r/Q_{\perp}$ values. As such, the longitudinal and transverse impedance was calculated for every HOM up to the beam-pipe cut-off frequency. The resulting impedance spectra are shown in Fig. 4.2.

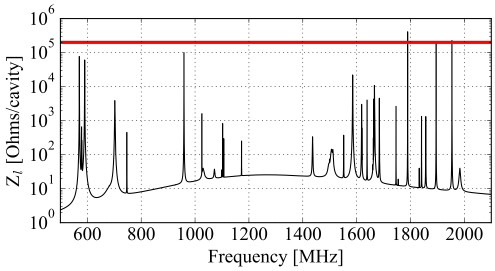

(a) Longitudinal.

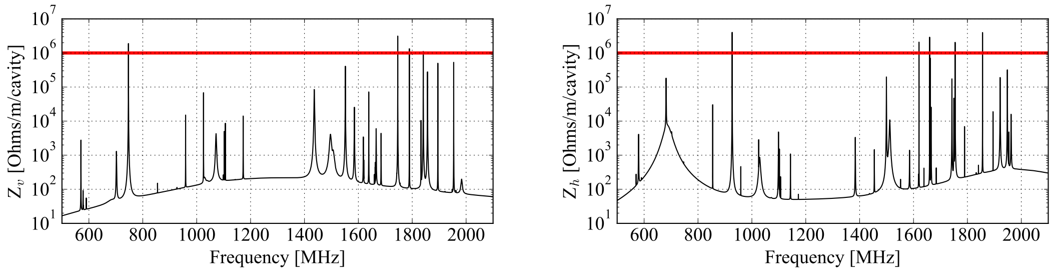

(b) Vertical.

(c) Horizontal.

Figure 4.2: Impedance spectra in each plane for the dressed SPS DQW crab cavity.

The design limits for the LHC DQW[1], shown as red lines in Fig. 4.2, are 200 kΩ/cavity and 1 MΩ/m/cavity for the longitudinal and transverse impedance respectively [108]. For the SPS DQW, this criteria was not met for all modes.

---

[1] The vertial crabbing structure for installation into the LHC as part of the HL-LHC upgrade.

This was because of a space constraint associated with the cryomodule in the SPS which limited the size of the couplers.

Modes above the impedance threshold as well as low frequency[1] (i.e. $< 1\,\text{GHz}$), high impedance modes are detailed in Tab. 4.1.

Frequency [MHz]	Q_e	R_v $[k\Omega/m]$[a]	R_h $[k\Omega/m]$	R_l $[k\Omega]$[b]
570.36	3080	3	0	77
590.14	1920	0	0	61
681.62	1160	0	175	0
746.67	6160	$\boxed{1889}$	0	0
926.80	12600	0	$\boxed{4020}$	0
958.87	10300	15	0	100
1620.25	187670	1	$\boxed{2187}$	1
1659.75	106680	0	$\boxed{2911}$	0
1662.25	3377420	2	$\boxed{4542}$	2
1746.23	35440	$\boxed{3132}$	0	3
1754.42[c]	23520	0	$\boxed{2047}$	0
1789.31	104020	$\boxed{1339}$	7	$\boxed{413}$
1840.93	16630	$\boxed{1108}$	0	1
1856.09	126610	1	$\boxed{4013}$	0
1953.89	57330	530	4	$\boxed{227}$

Table 4.1: Modes which are higher in impedance than the design limit (boxed) and low frequency, high impedance modes.

---

[a] Transverse threshold: $1\,\text{M}\Omega/\text{m}/\text{cavity}$

[b] Longitudinal threshold: $200\,\text{k}\Omega/\text{cavity}$

[c] Damped by the pick-up probe on the cavity beam-pipe.

Referring to the modes detailed in Tab. 4.1, three points of interest were noted from the impedance simulations:

- **Lowest frequency mode 'split'**: With the addition of the HOM couplers to the cavity, the lowest frequency HOM was 'split' into two modes. This is a result of the HOM coupler's transmission line resonance from the hook to the band-stop filter geometry. The resonance has a high amplitude within

---

[1] Due to the profile of the proton bunch, the HOM excitation is inversely proportional to the frequency with a 'Gaussian-like' dependence.

the bandwidth of the first HOM, but has a much lower bandwidth than the HOM.

- **Many horizontal modes are over the impedance threshold**: There are six modes for which the horizontal impedance is over the impedance threshold. Furthermore, they are all more than a factor of two higher than the design threshold and one is low frequency. This is a result of the general field topology of the horizontal modes. Whereas the highest impedance vertical modes generally have a high magnetic flux around the central resonators at the cavity base, which couples well to the hook type HOM couplers positioned at 90° to this flux, the high impedance horizontal modes do not necessarily have the highest magnetic field at this location.
- **The mode which is damped by the pick-up probe is over the impedance threshold**: The mode (1754 MHz) has a high field area on the upper surface of the cavity, but it is concentrated in a plane which the HOM couplers cannot efficiently couple to. There is also a high field area on the beam-pipe blend. It is hence damped by the Pick-Up (PU) probe, which uses a 'mushroom-like' geometry to coupler to the electric field at the beam-pipe. The mode's field topology is shown in Fig. 4.3 alongside a 3D model of the pick-up probe.

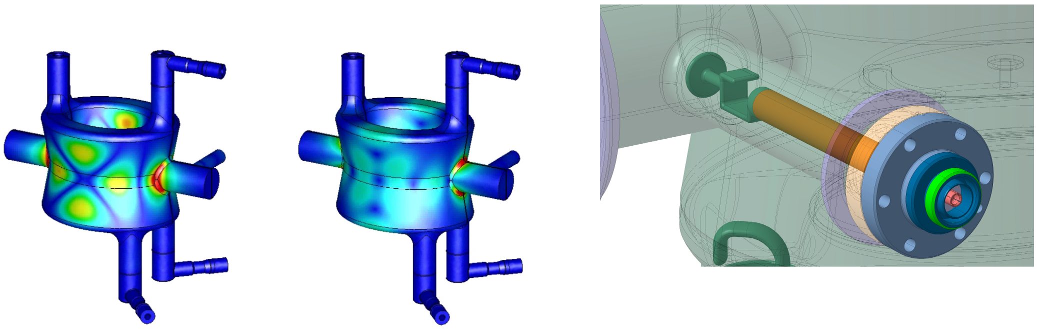

(a) Electric (left) and magnetic (right) field topology of the 1.75 GHz mode (arbitrary units).

(b) Pick-up probe used for sampling the fundamental mode and damping the 1754 MHz mode.

Figure 4.3: Horizontal mode damped by the beam-pipe pick-up probe.

4.2 Power Calculations

As discussed, the large HL-LHC beam current could result in a high HOM power from interactions with longitudinal HOMs. For reference, an example of a machine with problems from high HOM power is that of the Spallation Neutron Source (SNS) [109].

4.2.1 Nominal Power Spectra

Firstly, the 'nominal' HOM power, i.e. the power assuming that there is no deviation in mode parameters from that of the simulated case, was calculated for the dressed SPS DQW crab cavity in the HL-LHC. The HOM power is given by

$$P_{\|} = J_A^2 \sum_{-\infty}^{\infty} Re\left\{Z_{\|}(k\omega_0)\right\} |J_k|^2 \tag{4.2}$$

where J_A is the average beam current, k the integer value representing the revolution harmonic, ω_0 the angular revolution frequency and J_k[1] the normalised Fourier harmonic of the beam current. As the longitudinal impedance is known (Fig. 4.2a), it is only the beam components (J_A and J_k) that are unknown. The Beam parameters for HL-LHC are shown in Tab. 4.2.

Parameter	**Value**
Machine	HL-LHC
Number of bunches, M	2748
Particles per bunch, N_p	2.2×10^{11}
Harmonic number, h	35640
RF frequency, f_{RF}	400.8 MHz
Bunch length, σ_t	1.2 ns
Bunch spacing, t_{bb}	24.95 ns

Table 4.2: Parameters for HL-LHC beam.

The average beam current is the charge, i.e. the number of protons ($M \times Np$) multiplied by the proton charge ($+eC$), multiplied by the revolution frequency ($f_0 \sim 11\,\text{kHz}$ for the LHC). The resulting value for the HL-LHC is $\sim 1.1\,\text{A}$.

---

[1] In literature, J_k is also referred to as the 'time structure' of the beam.

To calculate the normalised Fourier harmonic of the beam current (J_k), the bunch pattern and filling scheme can be generated in the time-domain and Fourier transformed into the frequency domain. It can also be computed directly in the frequency domain, which is far less demanding computationally. From [110], the normalised Fourier harmonic of the beam current is given by

$$J_k = \underbrace{\frac{sin(n_{tr}\pi k f_0 t_{tt})}{n_{tr} sin(\pi k f_0 t_{tt})} e^{j(n_{tr}-1)\pi k f_0 t_{tt}}}_{\text{number of trains}} \times \underbrace{\frac{sin(M\pi k f_0 t_{bb})}{M sin(\pi k f_0 t_{bb})} e^{j(M-1)\pi k f_0 t_{bb}}}_{\text{number of bunches}} \times \underbrace{S(kf_0)}_{\text{bunch profile}} \tag{4.3}$$

where n_{tr} is the number of trains, k is the integer value representing the revolution harmonic, f_0 is the revolution frequency, t_{tt} is the spacing between the trains, M is the number of bunches, t_{bb} is the spacing between the bunches and $S(kf_0)$ is the bunch profile 'envelope'. For example, if a Gaussian profile was used, this function would be represented by $exp\left(-2(\pi k f_0 \sigma)^2\right)$.

The equation is split into three terms (annotations shown in Eq. 4.3). The first term represents a modulation due to the number of bunch trains, the second shows the modulation due to the number of bunches in each train and the third, as mentioned, represents the form of the bunches.

The value of J_k as a function of frequency is shown in Fig. 4.4 for a single bunch and for multiple bunches in the same train. J_k is only non-zero at multiples of f_0.

The two parameters which effect the modulation of the multibunch train are the bunch spacing t_{bb} and the number of bunches M:

- Figure 4.4c shows the bunch spacing harmonics at multiples of $1/t_{bb}$.
    - The largest excitation in a multibunch regime is at the bunch spacing harmonic frequencies and as such it could be very detrimental to have a HOM frequency allign with a multiple of $1/t_{bb}$.
- Figure 4.4d shows the 15^{th} bunch spacing harmonic over a narrower frequency range and details the modulation as a result of the number of bunches M.

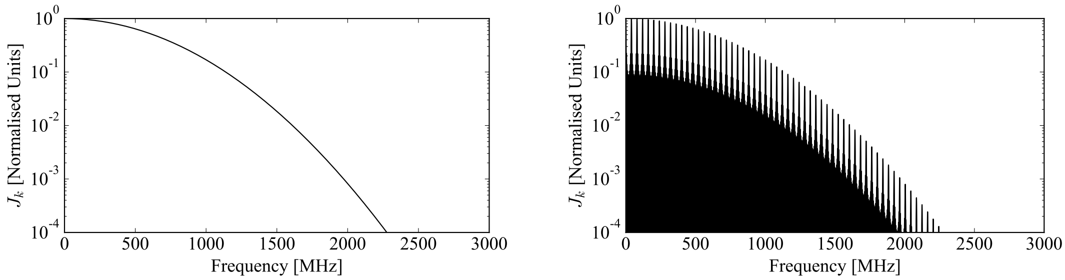

(a) Single bunch. (b) 12 bunches.

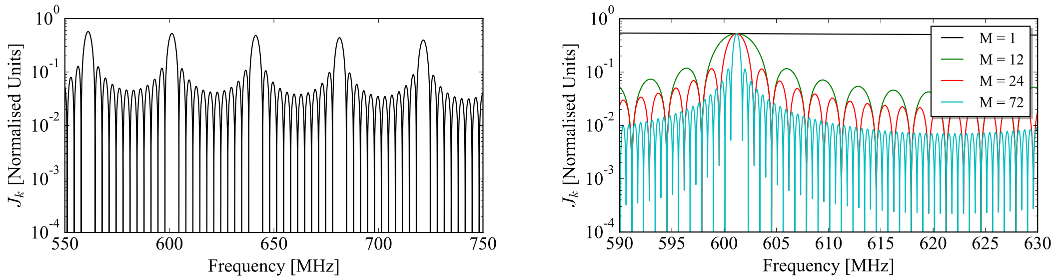

(c) 12 bunches, narrow frequency range. (d) Modulation with bunch number (M).

Figure 4.4: J_k as a function of frequency. The bunch parameters shown in Tab. 4.2 were used apart from the number of bunches (varied). A Gaussian bunch profile is used.

- Even though the intensity increases with bunch number, the value of J_k at a discrete frequency could decrease as the number of bunches is increased. As such, HOM power does not necessarily increase with the number of bunches.

In addition to the modulation as a result of the number of bunches and their spacing, the number of trains also modulates the form of J_k as a function of frequency. Due to kicker rise times and the need for 'abort gaps', the bunches are arranged using a pre-defined 'filling scheme'. The filling scheme for the HL-LHC is shown in Fig. 4.5.

The majority of the trains in the filling scheme consist of 72 bunches. To evaluate the modulation effect of the trains and the filling scheme detailed in Fig. 4.5, J_k as a function of frequency was generated for:

1. A single train of 2748 bunches.

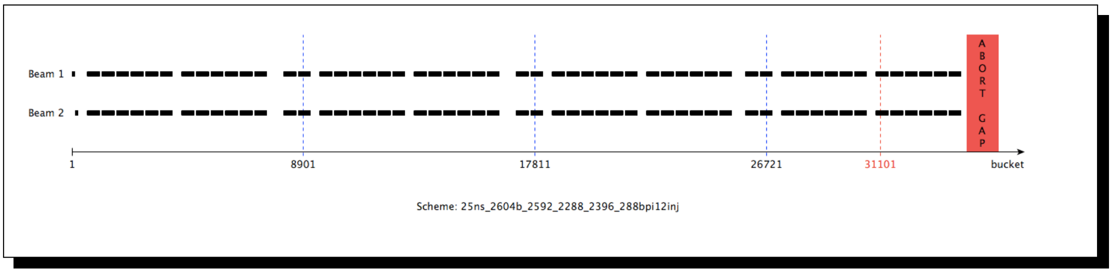

Figure 4.5: HL-LHC filling scheme. Image from [111].

2. 39 trains of 72 bunches with a train spacing of 80 RF buckets[1].

3. The HL-LHC filling scheme.

For the filling scheme, the bunches were firstly generated in the time domain and transformed into the frequency domain with a Fast Fourier Transform[2] (FFT). The comparison is shown in Fig. 4.6.

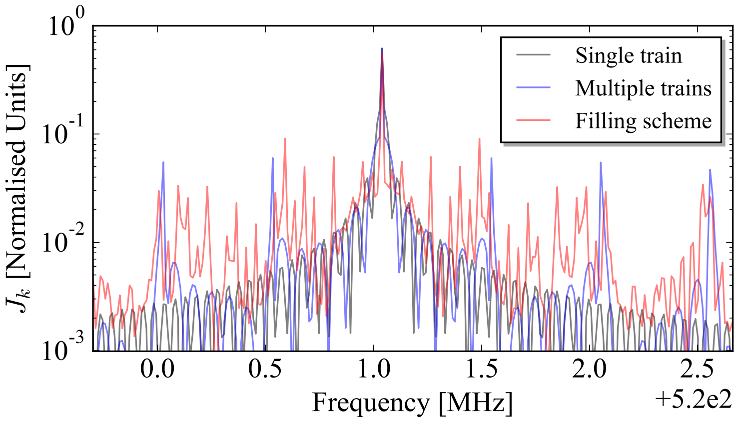

Figure 4.6: J_k as a function of frequency for three filling schemes. The frequency range is chosen to highlight one of the bunch spacing harmonics.

The train spacing harmonics, spaced at $\sim 0.5\,\text{MHz}$ from one another, are visible from the plot of the multiple trains with the additional modulation due to the various train lengths and abort gap shown as a result of the HL-LHC filling scheme.

---

[1] The RF bucket size for the LHC is $1/f_{rf} = 1/(400.8 \times 10^6) \approx 2.495\,\text{ns}$.

[2] Computationally expensive at high frequencies.

In all cases however, the highest value of J_k is at the frequency of the bunch spacing harmonics and is the same amplitude for each of the filling schemes presented. The value of J_k at a multiple of $1/t_{bb}$ is around an order of magnitude higher than the side-bands which result from the train spacing and abort gap modulation.

The resulting power spectra (Eq. 4.2) was calculated for each of the three filling schemes and is shown in Fig. 4.7.

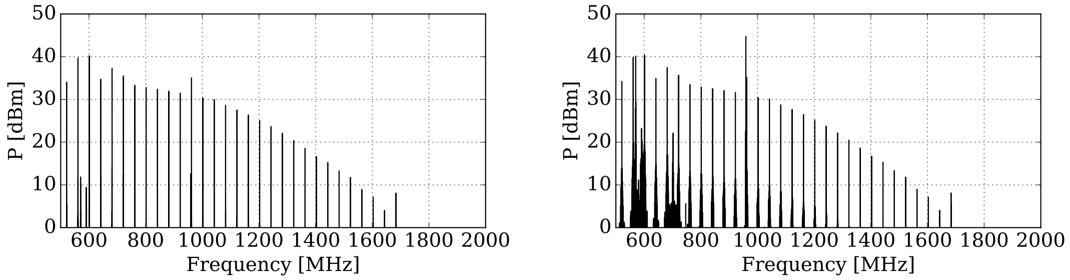

(a) One train of 2748 bunches.

(b) 39 trains of 72 bunches.

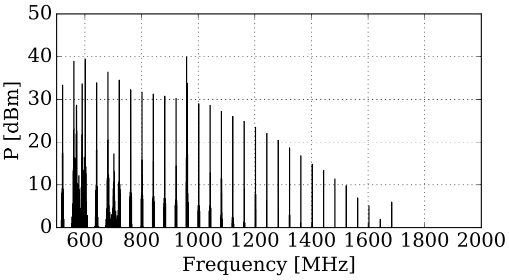

(c) Using HL-LHC filling scheme.

Figure 4.7: HOM power from the SPS DQW crab cavity in the HL-LHC with the three filling schemes detailed.

In each of the three cases, the main contribution to the HOM power, referring to the longitudinal impedance spectra and values detailed in Fig. 4.2a and Tab. 4.1 respectively, comes from the first HOMs and the longitudinal mode at 960 MHz. Whilst the first frequency band of HOM power is consistent for the three filling schemes, interaction with the 960 MHz mode changes significantly. The parameters for this mode are shown in Tab. 4.3.

The power calculations show that for the simulated design, the nominal summed

Frequency [MHz]	Q_e	R_v $[k\Omega/m]$[a]	R_h $[k\Omega/m]$	R_l $[k\Omega]$[b]
958.87	10300	15	0	100

Table 4.3: Parameters for the longitudinal mode at 960 MHz.

---

[a] Transverse threshold: 1 MΩ/m/cavity

[b] Longitudinal threshold: 200 kΩ/cavity

power up to the beam pipe cut-off frequency is less than 100 W. This represents a factor of ten less than the design limit of 1 kW defined in [108]. However, due to manufacturing tolerances, the cavity and coupler geometry, and hence the mode frequencies and quality factors, will not be exactly that of the simulated values. Therefore, it is important to evaluate the effect of mode parameter shifts from that of the nominal simulated values.

4.2.2 HOM Measurements - Cryomodule Test Stand

To gain insight into the magnitude and direction of HOM frequency and quality factor shifts as a result of manufacturing errors, the SPS DQW dressed cavity HOM parameters were measured.

Prior to installation in the SPS, the cryomodule was tested in a purpose built concrete bunker (named M7) at CERN's cryogenic test facility, SM18 [112]. The bunker with the cryomodule is shown in Fig. 4.8.

The test motivation was to validate cryomodule performance through the cool down and at the fixed operational temperature of 2 K. RF performance tests included: fundamental mode characterisation, HOM measurements, mode tracking with environment fluctuations, tuner validation and the effect of the tuner on the HOMs.

To quantify the HOM characteristics, S_{21} measurements were taken from 0–2 GHz using several port configurations as to identify the maximum number of modes measurable. Figure 4.9 displays the broadband measurements taken on the CERN-DQW-001 and CERN-DQW-002 cavities, for four ancillary configurations. The dressed cavity schematic shown in Sec. 4.1 (Fig. 4.1a) details the coupler nomenclature used. Note, the Fundamental Power Coupler (FPC) port was not

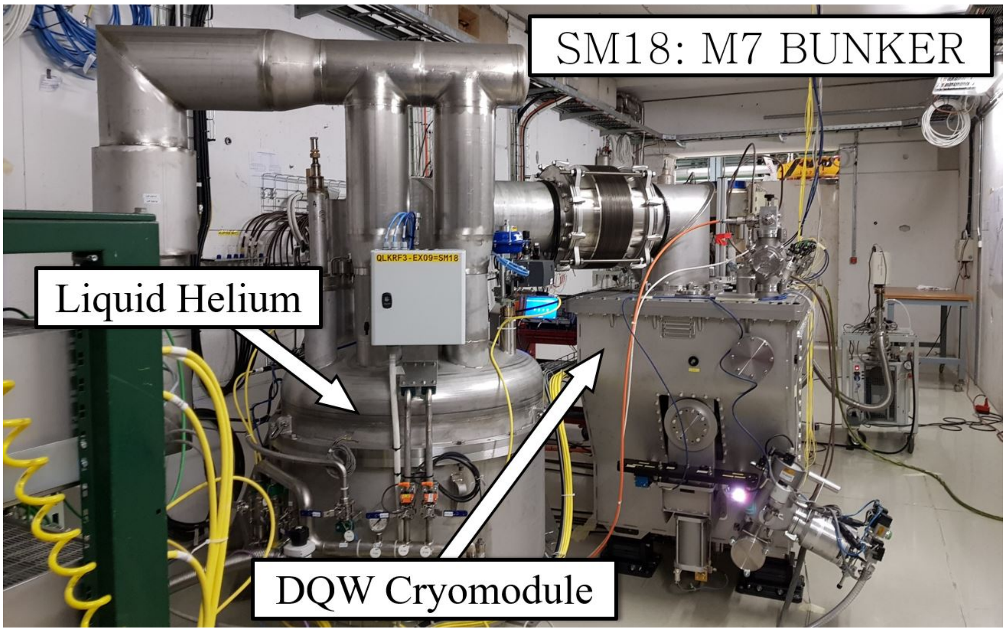

Figure 4.8: SPS DQW cryomodule in CERN's SM18 cold test faciltiy - concrete bunker 'M7'.

used due to the 400 MHz circulator installed on both cavities[1].

As the electromagnetic field profile differs from mode to mode, the different ancillaries can have different coupling coefficients for a given mode. Hence, it is possible to measure some modes via only one of the transmission configurations. An example of this is the mode at a measured frequency of $\sim$ 860 MHz. From Fig. 4.9, this is only observed in the HOMC2-HOMC3 transmission measurement. This suggests that the high field area for this mode is located at the bottom of the cavity, or that the top HOM coupler is located at a field 'node'.

From the transmission measurements, the mode frequencies were noted for each coupler configuration. Following this, all modes were measured in transmission over a frequency span no larger than five times the 3 dB bandwidth. A resonator fit was used and the centre frequency and loaded-Q was established. In most cases, multiple measurements of the same mode were taken. In these cases, the average of the measured frequency and loaded-Q were calculated. The standard deviation between the measurements hence gave an idea of the measurement error.

---

[1] Perturbing the broadband response.

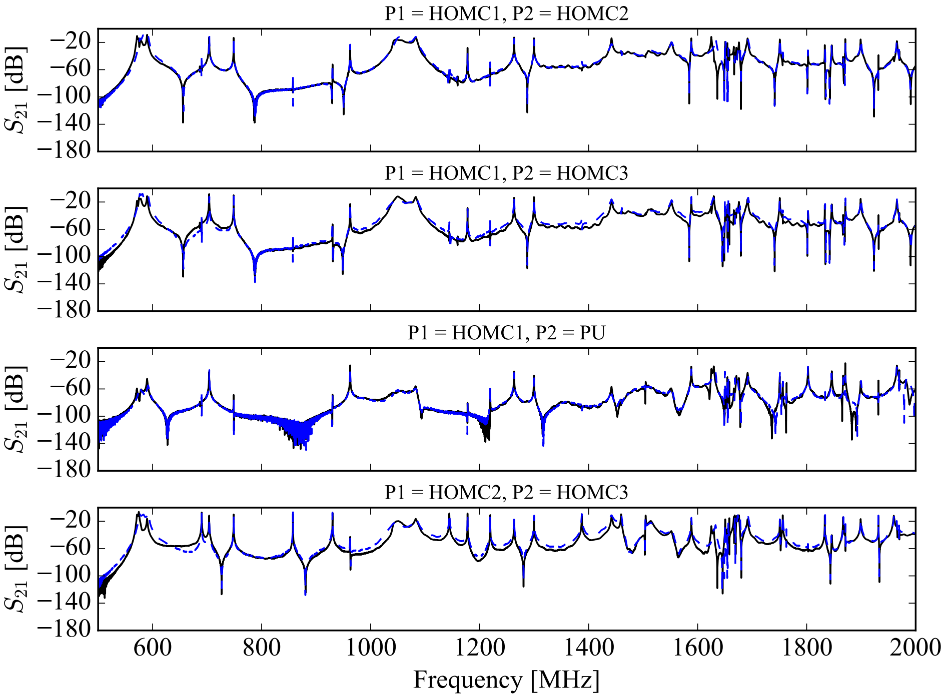

Figure 4.9: S_{21} measurements for each DQW crab cavity with corresponding port configurations. Cavity one is represented by the continuous black lines and cavity two by the dashed blue lines.

This error could be because one orientation was weakly coupled to the mode and hence susceptible to interference from noise, or because a strongly coupled mode close in frequency perturbed the resonance. Figure 4.10 shows the quality factors against frequency for both cavities. The mode parameters were measured during 2 K operation and hence, as discussed in Chapter 2, it is assumed that $Q_l = Q_e$ as the value of Q_0 is very large compared to Q_e.

It should be noted here that there was a manufacturing non-conformity on both DQW crab cavities for the SPS [113]. This non-conformity meant that each of the HOM coupler ports were 5 mm longer than that of the design. To accurately compare simulations to measurements, the cavity with the HOM couplers retracted by 5 mm was simulated and it is this data-set used in Fig. 4.10.

Apart from the first four HOMs, the mode parameters are close to the simulated at low frequencies, but deviate more as the frequency increases. This may be

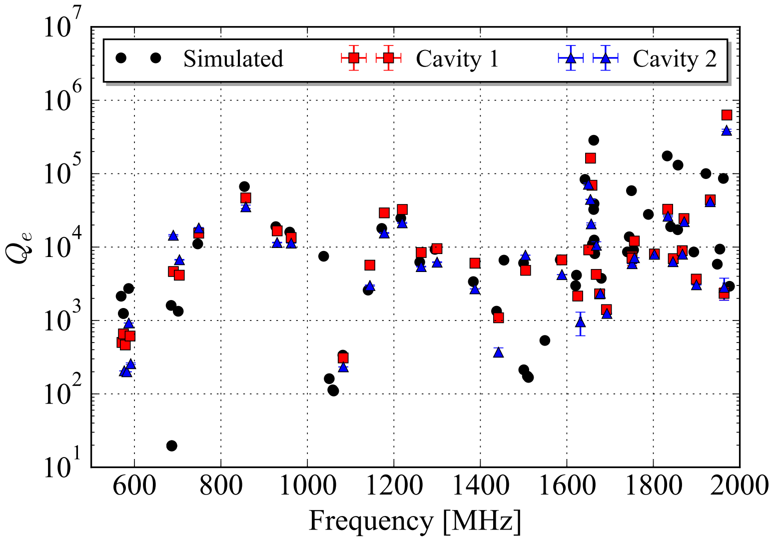

Figure 4.10: External quality factor against frequency.

because at higher frequencies the effect of smaller geometric deviations becomes more prevalent on the mode parameters.

4.2.3 Comparing Measurements to Simulations: Broadband

The measured modes were compared to the simulated modes with an automated script which 'looked' for the simulated mode with the closest frequency to that of the measured. It should be noted that it is assumed that the frequency shift of the modes (from simulated to measured) is lower than the frequency spacing to the adjacent mode. This may not be true in all cases.

The deviation of the cavity mode parameters from the simulated case is displayed in Fig. 4.11 with the average and standard deviation shown in each plot.

Referring to the frequency deviations, the HOM frequency in both cavities was higher than that of the simulations. The average increase in frequency from the entire data-set was 1.5 times larger in cavity two than cavity one. However this is significantly perturbed by the first four modes and if these are removed, the average increases in frequency become 0.27% and 0.31% for cavity one and two

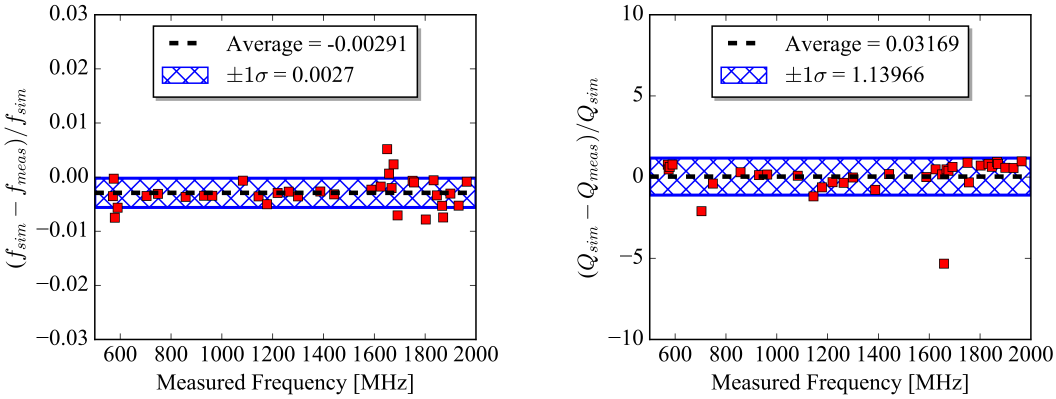

(a) Cavity 1 - Frequency.

(b) Cavity 1 - Q_L.

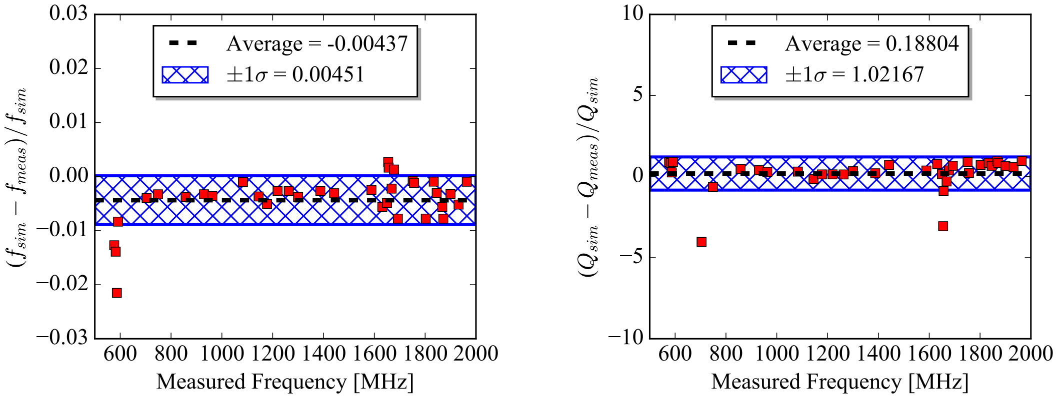

(c) Cavity 2 - Frequency.

(d) Cavity 2 - Q_L.

Figure 4.11: Deviation of the the measured mode parameters from the simulated. Average and standard deviations are presented in each measurement set.

respectively.

In both measurement sets, there are three modes which are outside the standard deviation at ~ 1.65 GHz. There are many modes at this frequency which strongly depend on the coupler geometry. In some cases, the measured mode could have been compared to the incorrect simulated mode.

This notion is strengthened by the quality factor deviation plots. In both cases there is a large increase in quality factor for one of the modes at ~ 1.65 GHz. There is also a large increase in quality factor for the mode at ~ 704 MHz in both cavities.

On average, the mode quality factors have slightly decreased from that of the simulations by about 3 and 2% for each cavity. However, the standard deviation shows that it is possible for the quality factor, and hence impedance, to double.

Three measured modes were not included in the comparative data-sets shown as they were 'flagged' for manual analysis as a result of the quality factor shift being ten times larger than the simulated quality factor. The three modes that were discounted are shown in Tab. 4.4. The simulated mode used for comparison is underlined and the manually assigned mode is 'boxed'.

Simulated Modes		Measured Modes				
		Cavity 1		Cavity 2		
f [MHz]	Qe	f [MHz]	Qe	f [MHz]	Qe	
$\boxed{684.84}$	1604	690.02	4644	689.82	14471	'F1'
686.16	20					
686.22	19					
$\underline{686.31}$	20					
701.22	1335					
$\boxed{1499.92}$	6061	1504.55	4822	1504.20	7753	'F2'
$\underline{1500.40}$	213					
1508.71	174					
1511.24	167					
1641.90	83568	1658.05	69524	1656.37	20699	'F3'
$\boxed{\underline{1659.12}}$ *	10981					
1662.01	32510					
1662.19	285289					
1662.93	39046					
1663.16	12471					
1664.57	8127					
1679.66	3755					

Table 4.4: Modes for which the Q deviation was over a factor of ten in at least one cavity. The closest simulated mode is underlined and a box is placed around the manually chosen mode.

*There is already a mode compared to 1641.90 MHz.

Of the three 'flagged' modes (at 690, 1504 and 1657 MHz and denoted as 'F1', 'F2' and 'F3' as shown in the table) the second 'F2' is now within the frequency and quality factor standard deviation shown in Fig. 4.11.

For the first mode 'F1', although the frequency is outside the standard deviation for cavity one but inside for cavity two (shifts of +0.76% and +0.73% with respect to the simulated mode), the frequency shifts are reasonable. The quality factor has increased by a factor of 2.9 and 9.2 respectively for each cavity. This is still far outside the standard deviation in both cases.

For the third mode 'F3', because of the large number of simulated modes which are close in both frequency and quality factor, it is difficult to compare the measured mode to a simulated one with much confidence. If the mode is compared to the one 'boxed' in Tab. 4.4, the frequency shifts are within the standard deviation, but the quality factors have increased by factors of 6.3 and 1.9 respectively.

Comparing all the measured modes to the simulated modes (manually changed for two modes), the new shift values were calculated and are shown in Tab. 4.5.

Cavity	$(f_{sim} - f_{meas})/f_{sim}$		$(Q_{sim} - Q_{meas})/Q_{sim}$	
	Average	Standard Deviation	Average	Standard Deviation
1	-0.0032	0.0028	-0.0422	1.1468
2	-0.0047	0.0043	0.0488	1.5853

Table 4.5: Corrected shifts between the measurements and simulations.

From the broadband measurements, the mode's which deviate significantly from the simulated values are:

- **Frequency**: First HOMs and some modes ∼ 1.65 GHz (although difficult to compare the correct measured and simulated modes).
- **Quality factor**: 685 MHz (horizontal mode) and 701 MHz (hybrid mode: similar longitudinal, vertical and horizontal impedance).

Referring back to the test-box measurements detailed in Chapter 3, Sec 3.4, these modes both lie in the frequency range highlighted as 'under-damped'.

4.2.4 Comparing Measurements to Simulations: Detrimental Modes

Referring to the first HOMs, these four have have moved in frequency significantly compared to the simulated case. The simulated and measured frequencies of these modes are detailed in Tab. 4.6.

Mode type[a]	**Mode Frequency [MHz]**		
	Simulated	**Cavity 1 (Deviation)**	**Cavity 2 (Deviation)**
l	569.16	571.16 (+ 2.00)	576.39 (+ 7.23)
l	574.34	574.51 (+ 0.17)	582.32 (+ 7.98)
h	574.47	578.78 (+ 4.31)	586.84 (+ 12.37)
l	586.51	589.82 (+ 3.32)	591.40 (+ 4.89)

Table 4.6: Simulated and measured frequencies for the first HOMs.

---

[a] v: vertical, h: horizontal, l: longitudinal, hy: hybrid

In all cases, each of the first HOMs has increased in frequency compared to that of the simulated and the modes in cavity two have increased by a larger amount. In both cavities, the largest frequency increase is shown by the mode at 574 MHz (simulated frequency). The frequency shift can become detrimental if it alters the mode's frequency to a multiple of the bunch spacing harmonic frequency. At an RF frequency of 400.8 MHz, filling every tenth RF bucket results in a t_{bb} value of 24.95 ns and hence a bunch spacing harmonic frequency of 40.08 MHz. Therefore, the two detrimental frequencies near to the first HOMs are at $40.08 \times 14 = 561.12$ MHz and $40.08 \times 15 = 601.20$ MHz. Hence, the first mode has moved further away from the 14^{th} bunch spacing harmonic and the final mode has moved closer to the 15^{th} bunch spacing harmonic. However, even for the largest deviation seen for this mode (cavity two, + 4.89 MHz), the mode is 9.8 MHz away from the bunch spacing harmonic, a factor of two larger than the mode frequency shift. Strong excitation of any of the first HOMs by a bunch spacing harmonic is therefore unforeseen. Additionally, the Q_e for every mode has reduced compared to that of the simulations. The larger bandwidth increases the power at the frequencies of the bunch spacing harmonics, but decreases the 'worst-case' power feasible as a result of HOM-harmonic alignment.

In addition to the first modes, the deviation of the low frequency, high impedance modes (Sec. 4.1, Tab. 4.1) are of interest. The simulated and measured mode parameters for these modes are shown in Tab. 4.7. The 1754 MHz mode is also included as it is only damped by the pick-up antenna and therefore of interest.

As discussed in the broadband comparisons, the first two modes in the table (684.84 and 701.22 MHz) have significantly increased in quality factor compared

Mode type[a]	**Simulation**		**Cavity 1**		**Cavity 2**	
	f [MHz]	Q_e	**f [MHz]**	Q_e	**f [MHz]**	Q_e
h	684.84	1604	690.02	4644	689.82	14471
hy: v,h,l	701.22	1335	703.66	4137	704.01	6719
v	746.32	11051	748.63	15468	748.77	18237
v	926.88	18982	930.07	16634	929.92	11520
l	959.06	15994	962.37	13471	962.53	11315
h	1754.33	9121	1756.07	12085	1756.36	7156

Table 4.7: Simulated and measured mode parameters for low frequency, high impedance modes. The 1754 MHz mode is also included.

---

[a] v: vertical, h: horizontal, l: longitudinal, hy: hybrid

to the simulated values by average factors of 6 and 4 respectively.

4.2.5 Frequency Spread and Harmonic Interaction Risk

Generally, the HOM frequencies have increased by similar amounts in cavity one and two and hence the inter-cavity frequency spread is low. If the HOMs in the two cavities overlap, the impedance effectively doubles and hence a spread between the cavities acts to reduce the maximum of the summed impedance for the cryomodule. The inter-cavity spread was evaluated for all modes and is shown in Fig. 4.12.

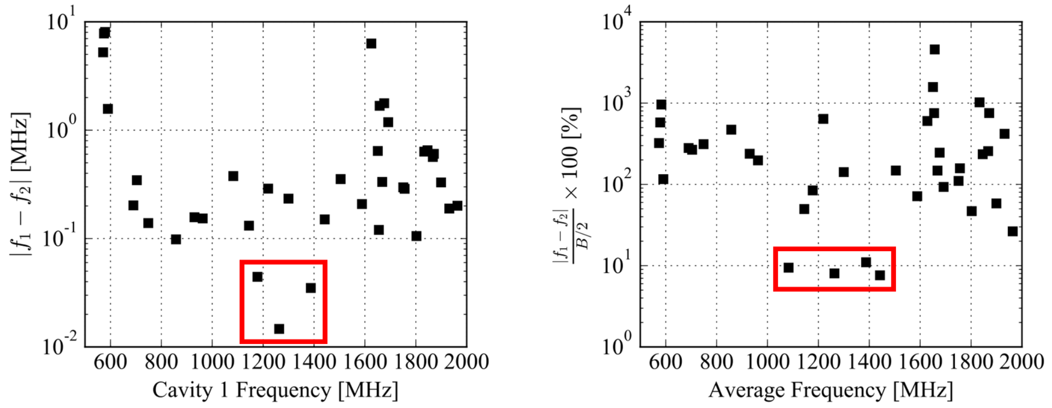

(a) Inter-cavity frequency spread.

(b) Inter-cavity spread as a percentage of 3 dB bandwidth.

Figure 4.12: Mode frequency analysis.

The plot of frequency spread (in MHz) is shown in Fig. 4.12a. The first HOMs are far in frequency from the same modes in the other cavity, decreasing the maximum impedance but increasing the effective bandwidth. The majority of the modes are above 100 kHz apart from one another, excluding three. To assess whether these modes, or any other HOMs, will destructively overlap, the second plot in Fig. 4.12b shows the frequency separation as a percentage of the modes average measured 3 dB bandwidth. Lower values represent a stronger interaction between the two cavity modes. Four modes are shown to have values at around 10%. None of the four modes have impedance values greater than half that of the thresholds and as such the overlap is not problematic (assuming the mode impedances match the simulated values).

To evaluate the modes which are at risk of causing high HOM power, the mode distances from the multiples of the bunch spacing harmonic frequencies were evaluated. This is shown in Fig. 4.13 for all modes measured. Modes which are close in frequency to a harmonic are labelled with the mode's longitudinal impedance and the HOM power as a result of mode-harmonic alignment with HL-LHC beam parameters.

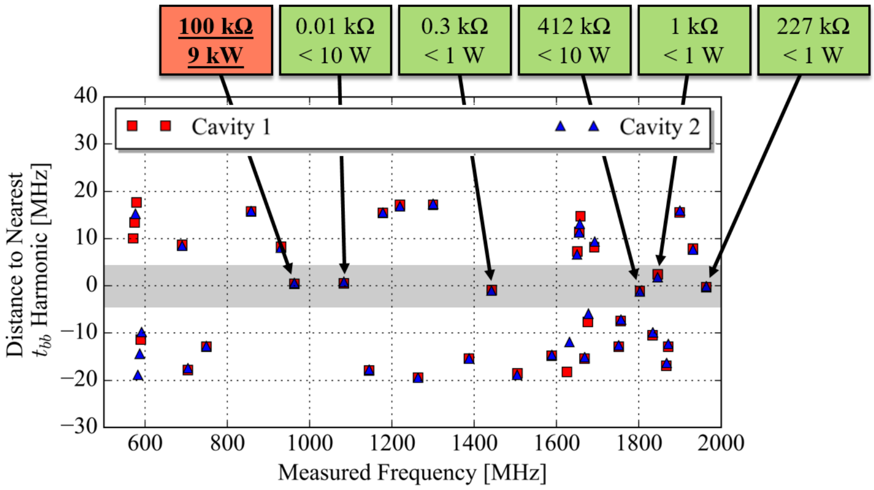

Figure 4.13: Frequency deviation of each mode from the nearest bunch spacing harmonic. The longitudinal impedance and 'alignment power' is annotated for modes close to a harmonic.

If the same cavity and HOM coupler designs are used in the HL-LHC and the frequency shifts are simular to the SPS DQW crab cavities, there is a risk of a HOM power of 9 times the threshold as a result of the longitudinal mode at around 960 MHz, interacting with the 24^{th} bunch spacing harmonic of the HL-LHC beam.

4.2.6 Comparison with Test Box Measurements

The transmission characteristics of the HOM couplers were measured using 'test-boxes'. These measurements are presented in Chapter 3, Sec. 3.4. The difference between the simulated and measured response was quantified in each case (ΔS_{21}).

To evaluate whether the deviation in the mode quality factor (simulated to measured) could be predicted using the pre-installation coupler measurements, the ΔS_{21} from the test-box measurements was compared to the Q-shift from the cryomodule measurements detailed in Sec. 4.2.2. This is shown in Fig 4.14.

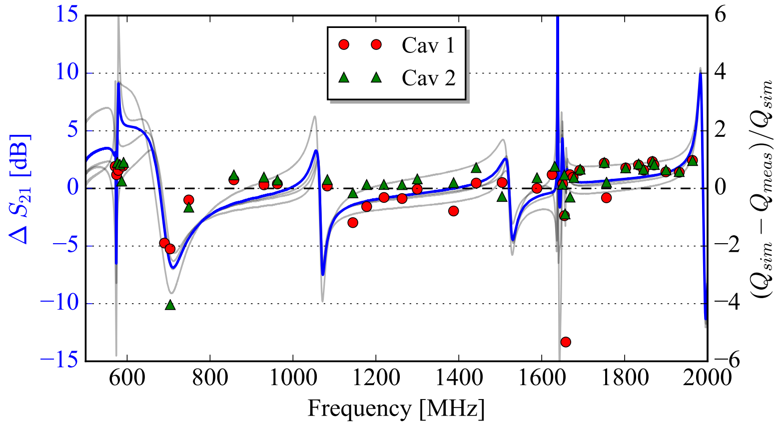

Figure 4.14: A plot of the coupler transmission deviations (from the simulated response) quantified with the test box measurements overlaid with the SPS DQW HOM quality factor shifts (from the simulated values). Note, the transmission difference (ΔS_{21}) is plotted here as the simulated response subtracted from the measured. The measurements for the four couplers are shown in grey and the average is shown by the thick blue line.

The deviation in quality factor correlates well with the average deviation between the simulated and measured text-box responses. Specifically, the main quality factor increases (at ∼ 700, 1100 and 1600 MHz) are predicted from pre-installation analysis of the HOM couplers. The two modes found to have the highest quality factor deviations in Sec. 4.2.4 were those at 685 and 701 MHz. Broadband under-damping in this frequency range is predicted by the test-box measurements.

To evaluate whether the magnitude of the quality factor deviations can be predicted, Table 4.8 details the gain predicted from the average of the coupler measurements and that measured from the quality factor deviations.

	ΔS_{21} [Linear Gain]		$Q_e(meas.)/Q_e(sim.)$	
Mode Frequency [MHz]	Minimum	Maximum	Cavity 1	Cavity 2
685	1.07	3.54	2.90	9.02
704	3.15	7.98	3.10	5.03

Table 4.8: Predicted and measured quality factor shifts for the outliers.

Although predicting the modes which will significantly change in quality factor, the coupler measurements are not able to predict the exact quality factor. To allow a more accurate prediction of the quality factor of each HOM in the two cavities:

- The data for every HOM coupler is needed. Currently two HOM couplers are missing due to a calibration error on the broad-band measurements.

- The information regarding which HOM coupler is installed on which port on the cavity is needed. This was not logged in the assembly stages.

- The mode dependant coupling would need to be quantified. For example, if a given HOM only couples to one of the HOM couplers, any transmission change of a different coupler will have no effect on the HOM parameters.

However, as a proof-of-principle, the test-boxes give a strong indication as to which modes will receive less damping than expected. This information could be used as an acceptance criteria for the HOM couplers and could also allow ‘coupler location optimisation’. For example, if a high impedance mode only couples to one coupler, the coupler with the highest transmission at this frequency should be assigned to this port location.

4.2.7 Applying Measured Tolerances

The data presented in Sec. 4.2.3 allowed tolerances to be applied to the cavity's HOM parameters. The effect of these tolerances on HOM power (with the HL-LHC beam parameters) was assessed. Referring to the HOM power, the worst case power for a mode is a result of the interaction with a bunch spacing harmonic. To identify modes which could produce a large HOM power as a result of this interaction, a global frequency shift was applied to the HOM table and the HOM power calculated as a function of the shift. A continuous train of bunches was used since, for the SPS DQW HOM longitudinal impedances, it is only the interaction of a HOM with the bunch spacing harmonics which could generate a power larger than the 1 kW threshold.

The summed power as a function of the shift is displayed in Fig. 4.15. It should be noted that the step in $\Delta f/f$ should be small enough to take into account the bandwidth of a mode with the highest quality factor at the highest frequency of interest.

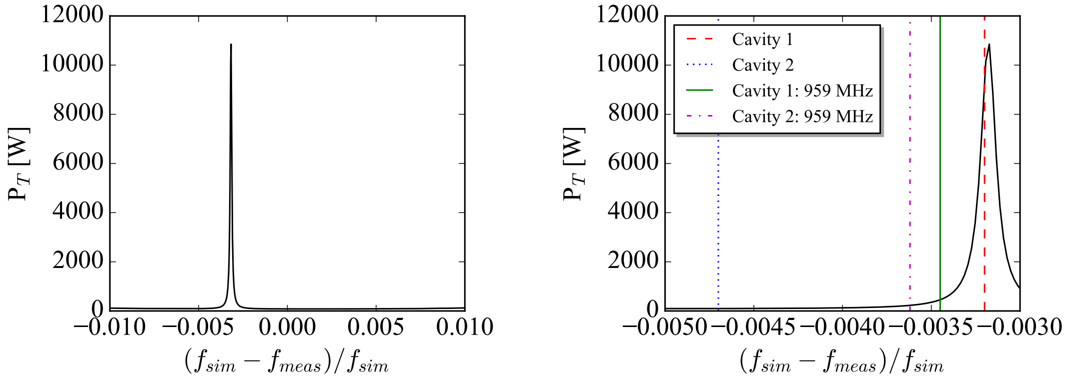

(a) Full range. (b) Zoom with markers at measured shifts.

Figure 4.15: Total power as a function of a global frequency shift applied to every mode in the simulated data-set. The frequency shift range used encapsulates the measured range.

The sweep shows a distinctive peak at a global mode frequency shift of +0.32%. If the power spectra is plotted as a function of frequency at this global mode frequency shift, the high power is shown to be a result of the interaction between the longitudinal mode at ∼ 960 MHz and the 24^{th} bunch spacing harmonic, resulting in a total power of ∼ 11 kW. The mode was identified as a potential risk in Sec. 4.2.5. For reference, the plot in Fig. 4.15b is annotated with the frequency shifts measured for the 960 MHz mode alongside the average shifts for each cavity. Figure 4.16 shows the spectral power at the detrimental frequency shift alongside the difference from the nominal case.

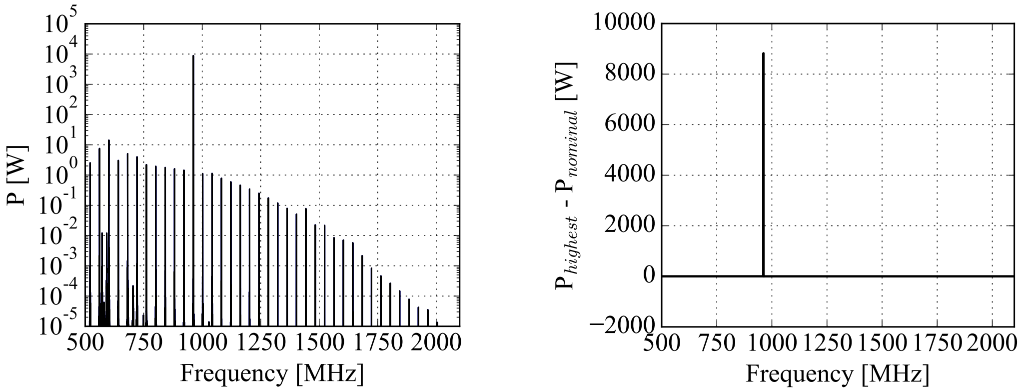

(a) At the most detrimental mode frequency shift.

(b) Difference between the detrimental and nominal spectra.

Figure 4.16: Evaluation of the power spectra with a +0.32% global mode frequency shift.

For the HL-LHC DQW crab cavities, it is essential that the longitudinal impedance of the mode at 960 MHz is reduced, or that the frequency is shifted to beyond the specified limits.

To evaluate the worst case for the HOM power, the frequency and quality factor deviations measured were applied stochastically to each mode.

The frequency was varied from the *lowest average shift value minus the largest standard devitation* to the *highest shift value plus the highest standard deviation.* This corresponded to shifts of −0.9% → +1.1%, hence varying over a 2.4σ range. The random samples were generated as a 'random-uniform' distribution to avoid unrealistic peak powers from the 'tails' of the Gaussian function.

Since the quality factors shifted in oposite directions in each cavity, the stochastic range was set from the cavity two average shift minus one standard deviation, to the cavity one shift plus one standard deviation. The resulting range was 50% → 200%.

The average and maximum power were recorded for various sample sizes (to evaluate convergence) and are displayed in Fig. 4.17. The plot is annotated with the power that would result from every HOM moving by the average frequency shift measured in both cavities. The analysis shows that the average and maximum values for the total HOM power are $\sim 250\,\mathrm{W}$ and $11\,\mathrm{kW}$. The maximum power feasible is mainly caused by the 960 MHz mode ($> 90\%$).

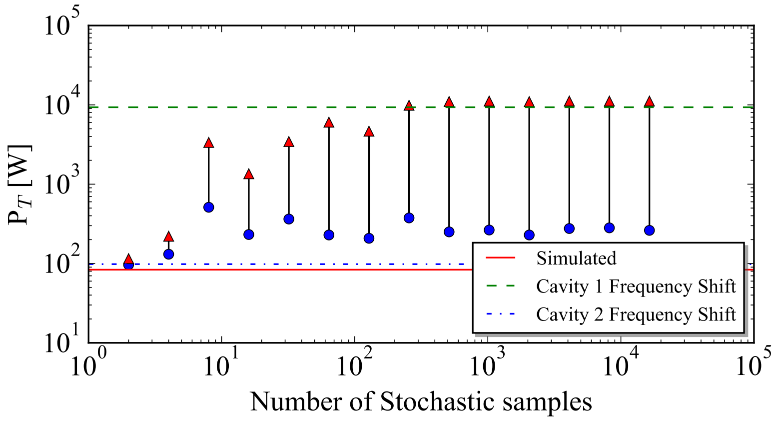

Figure 4.17: Total power as a function of stochastic deviation samples. The blue circles represent the average and the red triangles are the maximum.

4.3 Conclusions

Evaluation of the SPS DQW crab cavity impedance and HOM power (with HL-LHC beam parameters) had four main stages:

Impedance calculations

- The longitudinal and transverse impedance was calculated for every mode up to the beam-pipe cut-off frequency of 2.1 GHz. Modes with impedances above the HL-LHC threshold were identified.

Nominal power calculations

- The HOM power resulting from the HL-LHC beam and SPS DQW crab cavity longitudinal impedance spectra was calculated.
- It was shown that the highest power is seen at multiples of the bunch spacing harmonic frequency, i.e. multiples of $1/t_{bb}$.
- The nominal integrated power was over ten times less than the threshold of 1 kW.
- The main contributions to the power were the first HOMs and the longitudinal mode at 960 MHz.

Measurements

- The HOM characteristics were measured during the SPS DQW cryomodule test.
- The deviation of the measured frequency and quality factor of the HOMs from their simulated values was quantified.
- The frequencies of the modes which deviated with significance from their simulated values are shown in Tab. 4.9.

Frequency deviation
First four HOMs: 569, 574.3, 574.5, 587 MHz
HOMs at $\sim$ 1.65 GHz

Quality factor deviation
685 MHz (Factors: 2.9 & 9.0)
701 MHz (Factors: 3.1 & 5.0)

Table 4.9: HOMs which deviated with significance from the simulated case.

- The inter-cavity frequency spread and risk of a mode interacting with a bunch spacing harmonic was evaluated.
- Interaction of the HL-LHC beam and the longitudinal mode at 960 MHz was evaluated as feasible and capable of generating a HOM power of nine times the threshold.

Test-boxes

- Chapter 3 detailed the transmission characterisation of the HOM couplers using the 'test-box'.
- Comparison of these measurements with the HOM quality factor measurements showed that it is possible to predict the modes which will significantly shift from the simulated case. Exact prediction of the HOM quality factors needs more information.
- HOM coupler qualification and port-location optimisation was proposed.

Worst-case HOM power

- The measured frequency and quality factor shifts were applied to the HOM power calculations.
- The maximum power feasible was 11 times that of the threshold and mainly a result of the interaction of $\underline{\text{longitudinal mode at } 960\,\text{MHz}}$ with the 24^{th} bunch spacing harmonic of the HL-LHC beam.

The simulations, measurements and analysis provide information on how the SPS DQW crab cavities will interact with the HL-LHC beam and by how much the HOM characteristics can shift from the expected. A recurring feature throughout the analysis was the possibility of high HOM power as a result of the longitudinal HOM at 960 MHz. Even though this mode is within the impedance threshold, it's quality factor should be reduced or it's frequency moved further from the 24^{th} bunch spacing harmonic (assuming $t_{bb} = 25\,\text{ns}$) for installation as part of the HL-LHC upgrade.

Chapter 5

HL-LHC DQW HOM Coupler

With respect to cavity impedance and HOM power, the analyis shown in Chapter 4 highlighted areas for which the SPS DQW crab cavity[1] is not suitable for the HL-LHC upgrade.

Furthermore, after experience gained from manufacturing the HOM couplers for the SPS tests, geometric changes were necessary to increase the simplicity of the machining and welding processes.

5.1 Design Goals

The first RF design goal was to reduce the impedance of all HOMs to below 200 kΩ/cavity and 1 MΩ/m/cavity respectively for longitudinal and transverse modes [108]. In addition to these thresholds, the longitudinal mode at 959 MHz (simulated frequency) needs to be damped further due to its high longitudinal impedance and proximity to the 24^{th} bunch spacing harmonic of a HL-LHC beam with 25 ns bunch spacing. The frequency, quality factor and impedance of this mode are detailed in Tab. 5.1.

As discussed in Chapter 4, for a total bunch length of 1.2 ns (Tab. 4.2) the normalised Fourier harmonic amplitude (J_k) at the 24th harmonic is ~ 0.2. The maximum longitudinal impedance (to produce 1 kW) is 10.33 kΩ. Assuming the

---

[1] The vertical crab cavity and ancillary design used for preliminary validation in the Super Proton Synchrotron (SPS).

Frequency [MHz]	Q_e	R_v $[k\Omega/m]^a$	R_h $[k\Omega/m]$	R_l $[k\Omega]^b$
570.36	3080	3	0	$\boxed{77}$
590.14	1920	0	0	$\boxed{61}$
958.87^c	10300	15	0	$\boxed{100}$

Table 5.1: Parameters for the longitudinal mode at 960 MHz.

---

[a] Transverse threshold: 1 MΩ/m/cavity

[b] Longitudinal threshold: 200 kΩ/cavity

[c] Close to 24^{th} bunch spacing harmonic.

r/Q_l does not change significantly with coupler geometry, this means the Q_e should be reduced by at least a factor of 10 to below 1000. As seen from the HOM measurements shown in Chapter 4, Sec. 4.2.3, the quality factors of the manufactured cavity can deviate from the simulated value by up to a factor of 2. Although this was not the case for the 959 MHz mode, a 'safety factor' of two was used for this mode. As such, a longitudinal impedance limit of 5 kΩ was specified for the 959 MHz mode.

Finally, the maximum integrated HOM power (taking into account mode frequency and quality factor shifts) must be kept lower than 1 kW.

As an indication as to which other modes could produce a high HOM power, a plot of the maximum mode power feasible as a function of it's distance from the closest spectral harmonic was plotted and is shown in Fig. 5.1.

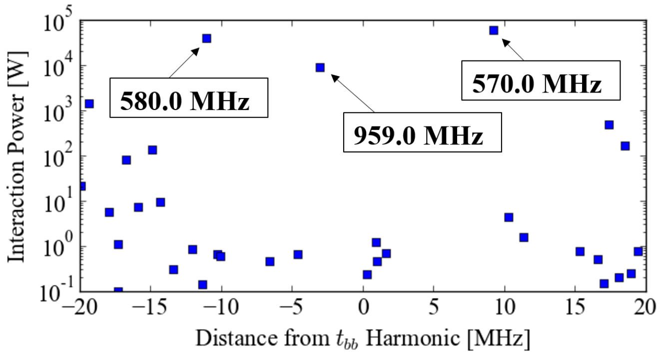

Figure 5.1: Power as a result of a mode interacting with the 24^{th} bunch spacing harmonic as a function of the distance from the harmonic.

For HOM power, it is clear that the most 'at-risk' modes are the longitudinal modes at 570 , 580 and 959 MHz (parameters detailed in Tab. 5.1), but that the two low frequency modes are unlikely to align with a bunch spacing harmonic. The three modes are detailed in Tab. 5.1 and the field profiles are shown in Fig. 5.2.

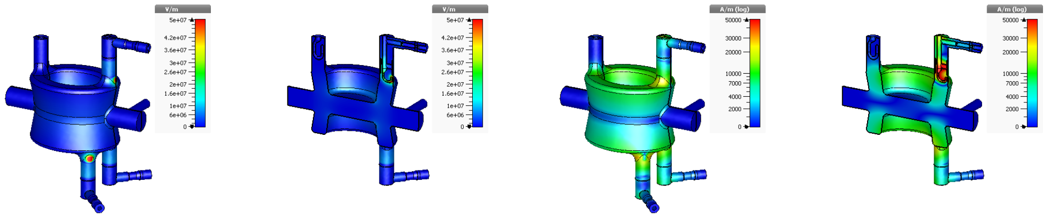

(a) 570 MHz: E-Field.

(b) 570 MHz: H-Field.

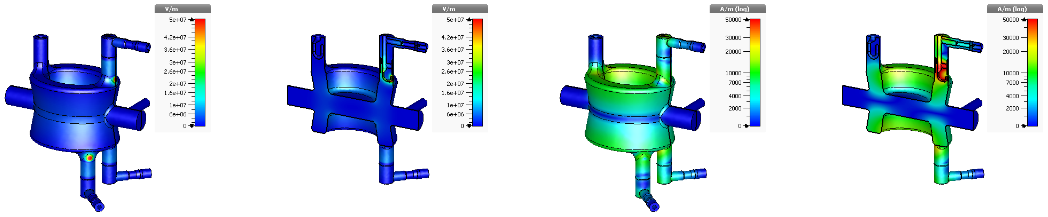

(c) 590 MHz: E-Field.

(d) 590 MHz: H-Field.

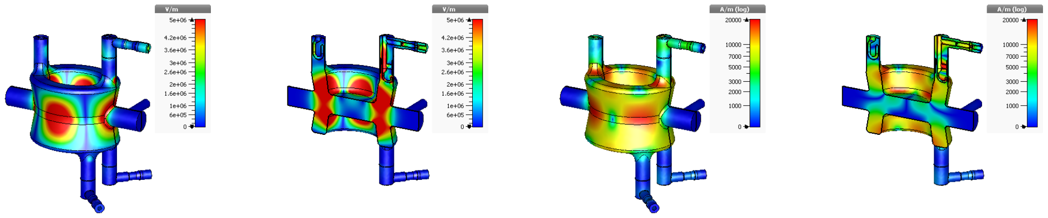

(e) 959 MHz: E-Field.

(f) 959 MHz: H-Field.

Figure 5.2: Field topologies for the modes capable of producing over 1 kW of HOM power as a result of interaction with a bunch spacing harmonic.

As the 580 MHz mode is a high $r/Q_{\|}$ mode (can only be changed with cavity geometry), significant reduction in power is not trivial with transmission alterations of the HOM coupler. However, the other two modes are high Q_e modes and hence, if it is possible to couple to these modes, geometric changes of the coupler could vastly change the longitudinal impedance.

From the manufacture of the SPS DQW HOM coupler (shown in Fig. 5.3), three difficulties were apparent with respect to machining and assembly [114]. The first was the long machining time. The machining time of complex geometries such as couplers is often one of the most expensive steps and hence had to be reduced with the new coupler design[1]. Secondly, welding difficulties were experienced with the area which the 'stub' connects to the capacitive jacket as it was 'non-planar' due to the changing radius of the capacitive jacket's cross-section. This complexity increases the likelihood of not meeting manufacturing tolerances. Finally, the outer conductor was an expensive and time consuming piece to manufacture as currently it has to be machined from a block of niobium. Ideally, the piece would be made from a rolled niobium tube and the perpendicular line would be extruded. This was not possible for the SPS design however, as the bottom of the perpendicular output line is flush with the base of the structure. The welding and extrusion constraints are highlighted in Fig. 5.3.

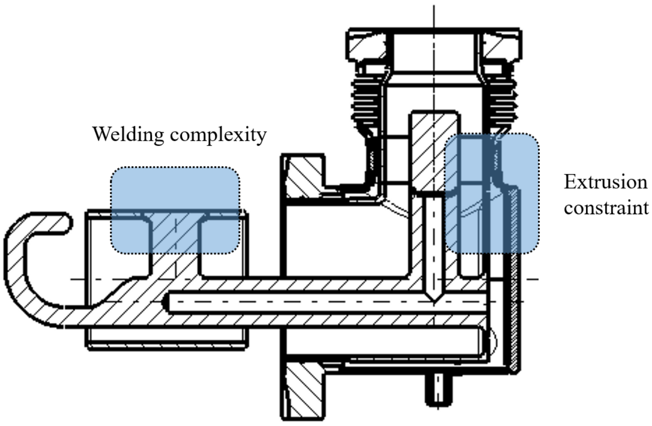

Figure 5.3: Two dimensional schematic of the manufactured SPS DQW HOM coupler geometry with two manufacturing issues highlighted.

---

[1] Whereas six HOM couplers and two spares were required for the SPS tests, at least double are required for the HL-LHC (Appendix Sec. 1).

5.2 Initial Geometry Changes

To provide a base model for RF optimisation, methods to address the manufacturing difficulties were firstly investigated. The methods are depicted in Fig. 5.4 and described hereafter.

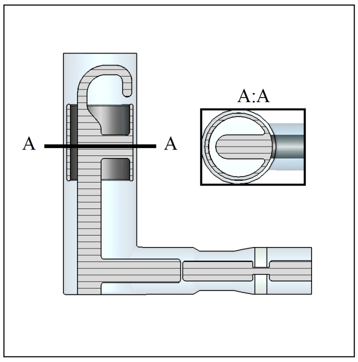

(a) SPS DQW HOM coupler geometry.

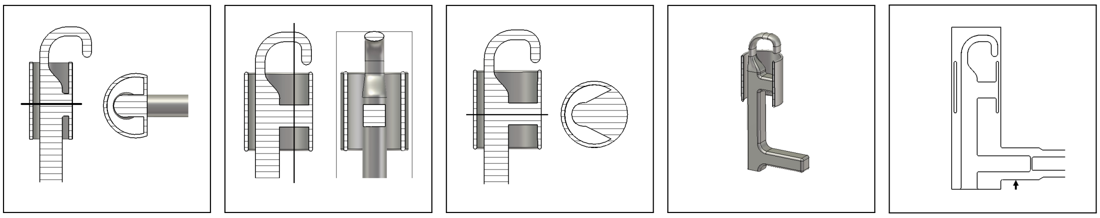

(b) Jacket: flat section.

(c) Stub: square profile.

(d) Stub: tapered.

(e) Profile: rectangular.

(f) Bend: lifted.

Figure 5.4: SPS DQW HOM coupler geometry (top) and the trialled mechanical alterations (bottom) that would simplify manufacturing processes.

To improve the welding ease of the stub to the jacket, a flat section on the jacket was incorporated. This would allow a fully penetrating electron beam weld without difficulties achieving weld uniformity. This concept is shown in Fig. 5.4b. The alteration increases the average distance between the jacket and the outer wall, hence reducing the capacitance of the band-stop filter. Referring to the coupler's equivalent circuit response detailed in Chapter 3, this reduction in capacitance results in an increased stop-band frequency and hence, to compensate, the jacket should be lengthened or the stub inductance increased.

Methods of increasing the stub inductance are shown in Figs. 5.4c and 5.4d. With a rectangular profile inductive stub, the inductance is no longer constrained by the diameter of the central shaft as the cross-sectional height can be varied down to the lower end of the capacitive jacket. The inductance can be further increased by revolving the stub around the central shaft if necessary, but this could add further complications relating to the electron beam welding.

The final two alterations, shown in Figs. 5.4e and 5.4f, were the incorporation of a rectangular profile and lifting of the output line with respect to the lower end of the coupler (where the inner conductor is welded to the outer wall). The square profile significantly reduces the machining time of the coupler, as it is made from a solid block of Niobium and the curvature of a circular cross-section takes a long time to 'shape' using a multi-axis CNC lathe.

For an initial design analysis, all of the alterations detailed in Fig. 5.4 were implemented, except the tapered stub which could be incorporated in the case that a larger band-stop filter inductance is required. The coupler design with the alterations is shown in Fig. 5.5a and the transmission response for the coupler is shown in Fig. 5.5b.

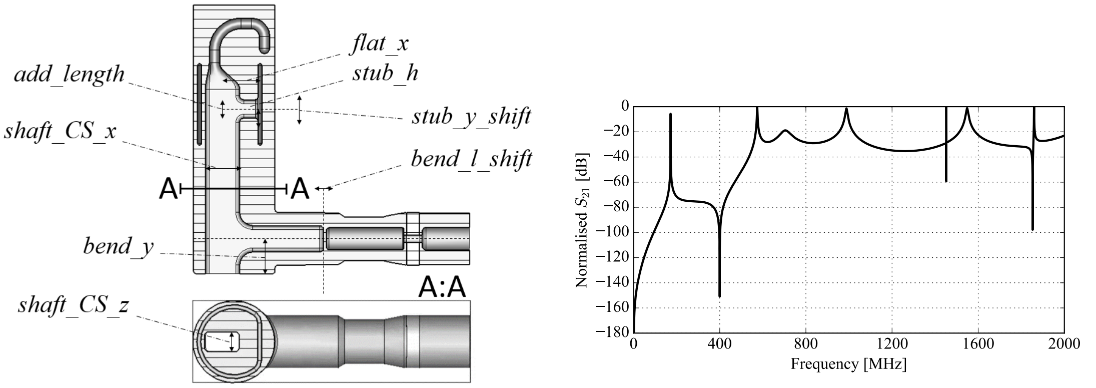

(a) DQW HOM coupler with new features (vacuum geometry) and annotated with the parameters used to alter the geometries in the 3D modelling suite.

(b) Initial response of the altered coupler.

Figure 5.5: Initial response of the altered coupler.

The transmission response is very similar to that of the SPS DQW HOM coupler, with a distinctive stop-band and with four distinctive pass-bands resulting from the transmission lines.

The band-stop filter response was tuned with the length of the stub connecting the central conductor and the capacitive jacket. Lengthening this variable increases both the inductance and capacitance of the band-stop filter. An analytic approximation for the effect of the new jacket geometry on the band-stop filter capacitance is shown in Appendix Sec. 4.

5.3 Parametric Weighting

After conceptualising a base model for the HOM coupler re-design which improved the ease of manufacture and validating that its operation still conformed to that of the previous design, i.e. no spurious resonances were seen, the effect of the coupler's geometries on the transmission response were studied. As this section will refer to the coupler's circuit equivalences and their corresponding stop-band and pass-band frequencies, Fig. 5.6 shows the coupler's equivalent circuit, an annotated schematic and the frequency bands with the circuit elements which most strongly effect them.

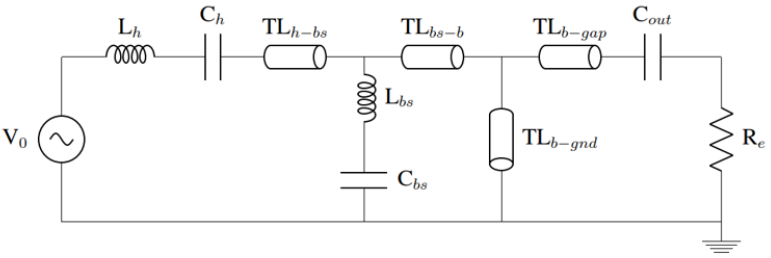

(a) Equivalent circuit.

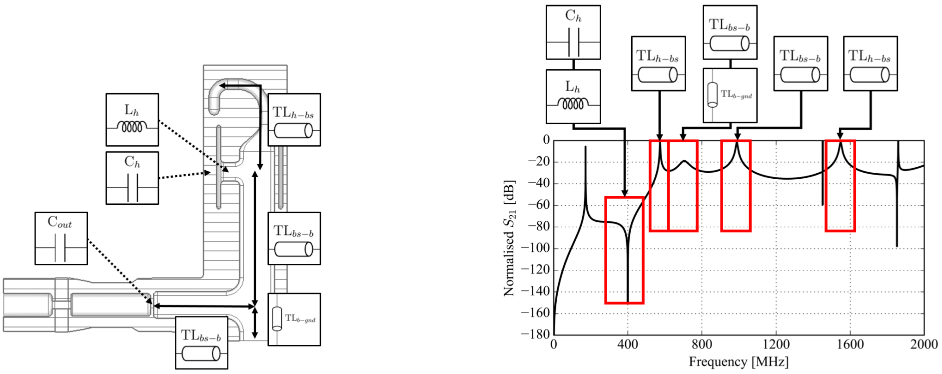

(b) Coupler schematic with annotated transmission line geometries.

(c) Coupler transmission characteristics with annotated frequency bands.

Figure 5.6: HOM coupler equivalent circuit geometries.

For the study, several 3D model parameters were varied. The frequencies of the transmission features were tracked, allowing methods of pass-band optimisation to be established. The results from the analysis are shown in Fig. 5.7. Note, the studies were carried out before tuning of the band-stop filter.

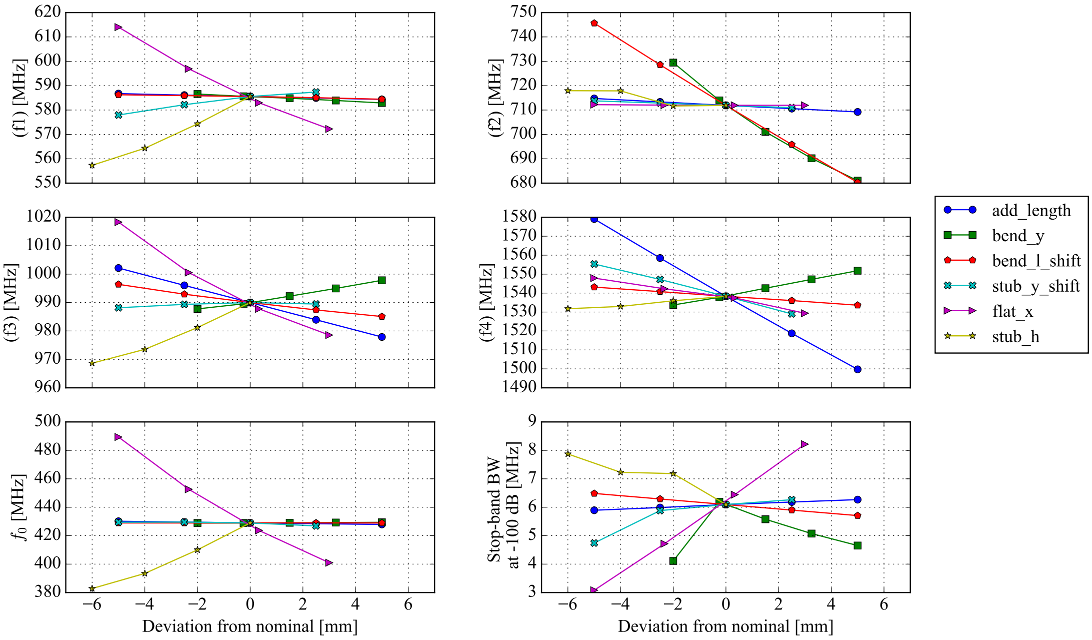

Figure 5.7: Stop-band and pass-band frequency shifts with geometric alterations. The numbered frequencies corresponds to the stop-band and pass-bands detailed in Fig. 5.6c.

Linear fits were applied to each of the trends to quantify the effect of the geometries. Rather than detailing the large array of numerical values, for reference and simplicity, Tab. 5.2 details the geometries altered, their circuit equivalences (Fig. 5.6b) and the features of the coupler's transmission response that they effect. Filled circles show geometries that have the strongest effect on a given transmission feature and empty circles show that the geometry has an effect on the feature but is not the highest. The geometries which were predicted to have the largest effects from the circuit modelling are 'boxed'.

The geometries which alter the band-stop filter reactive elements (L and C) are the only two which effect the stop-band frequency with any significance, as expected. However, from the plots, their effect on the pass-bands is very significant. It should be noted however, that this effect is arbitrary as is is the stop-band interference which effects the pass-bands and, since this will be tuned to the fundamental mode frequency, the parameters are 'locked'.

Geometry	Sim. parameter	Circuit element	SB	PB1	PB2	PB3	PB4
Length from the central conductor to the jacket's flat section.	flat_x	C_{bs}; L_{bs}	$\boxed{\bullet}$				
Height of the stub.	stub_h	L_{bs}	$\boxed{\bullet}$				
Length from band-stop filter to bend.	add_length	TL$_{bs-b}$				$\boxed{\bullet}$	●
Length of the output line before the capacitive gap.	bend_l_shift	TL$_{b-gap}$			$\boxed{\bullet}$	○	○
Length from the hook to the band-stop filter.	stub_y_shift	TL$_{h-bs}$		$\boxed{\bullet}$			$\boxed{\circ}$
Length from bend to connection to outer wall.	bend_y	TL$_{b-gnd}$:↑ TL$_{bs-b}$:↓			$\boxed{\bullet}$	○	○

Table 5.2: How the HOM coupler geometries effect the transmission features. The stop-band (SB) and pass-band (PB) identifiers are shown in Fig. 5.6c. Filled circles show the most strongly weighted and empty circles show parameters which have an effect but less than that of another parameter. The 'boxed' symbols show the parameters predicted to have the highest effect.

Notably, in the equivalent circuit analysis, the highest frequency pass-band was most effected by the distance between the hook and band-stop filter sections. In the 3D simulations the geometry from the band-stop filter to the bend section had a larger effect on this coupler resonance. As discussed in the equivalent circuit modelling section in Chapter 3, this could be the result of smaller geometries not modelled in the circuit equivalence which become more prevalent at high frequencies, interaction with the the stop-band close to this frequency (not modelled by the equivalent circuit) or due to the length of the first transmission line length varying with frequency. This is the only only area which the equivalent circuit did not exactly predict the effect of the geometric changes to the 3D model.

5.4 Optimisation

Following the parametric studies, using both equivalent circuits and 3D electromagnetic simulations, the coupler was optimised to:

- Reduce the impedance of all modes to within the thresholds:
  - Transverse: 1 MΩ/m per cavity.
  - Longitudinal: 200 kΩ per cavity.
- Reduce the longitudinal impedance of the mode at 959 MHz to less than 5 kΩ per cavity.
- Ensure a worst case HOM power of 500 W.

As a reference[1], the modes over the impedance threshold alongside the low frequency, high impedance modes are displayed in Tab. 5.3.

Frequency [MHz]	Q_e	R_v [$k\Omega/m$]	R_h [$k\Omega/m$]	R_l [$k\Omega$]
570.36	3080	3	0	77
590.14	1920	0	0	61
681.62	1160	0	175	0
746.67	6160	$\boxed{1889}$	0	0
926.80	12600	0	$\boxed{4020}$	0
958.87[a]	10300	15	0	100
1620.25	187670	1	$\boxed{2187}$	1
1659.75	106680	0	$\boxed{2911}$	0
1662.25	3377420	2	$\boxed{4542}$	2
1746.23	35440	$\boxed{3132}$	0	3
1754.42[b]	23520	0	$\boxed{2047}$	0
1789.31	104020	$\boxed{1339}$	7	$\boxed{413}$
1840.93	16630	$\boxed{1108}$	0	1
1856.09	126610	1	$\boxed{4013}$	0
1953.89	57330	530	4	$\boxed{227}$

Table 5.3: Modes which are higher in impedance than the design limit (boxed) and low frequency, high impedance modes.

[a] High power mode.

[b] Damped by the pick-up probe on the cavity beam-pipe.

---

[1] Already shown in Chapter 4.

5.4.1 Optimisation 1: Larger Damping to the High Frequency Modes

The first method employed was to move the pass-bands higher in frequency to increase the damping to the high frequency modes above the impedance threshold. The geometric feature chosen for alteration was the length from the bend to the output capacitance. This feature was chosen as its circuit equivalence (TL_{b-gap}) had a strong effect on the passband now at around 700 MHz but also effected the higher frequency pass-bands.

The coupler schematic, with the reduction of the length from the bend to capacitive gap which increases the pass-band frequencies, is shown in Fig. 5.8a alongside the transmission characteristics.

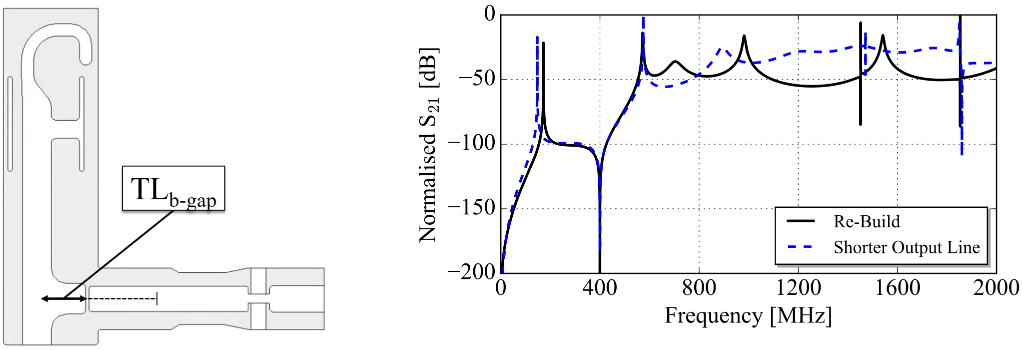

(a) 3D Model.

(b) S_{21} response.

Figure 5.8: Modified HOM coupler for a more broadband response.

Compared to the original transmission response, the new model has a broader response at high frequencies due to the decreased length from the bend to the capacitance. This leaves a damping deficit in the region around 700 MHz. The simulated cavity impedance spectra with these couplers is shown in Fig. 5.9.

Referring to the impedance spectra, the damping is generally better at high frequencies compared to the SPS DQW HOM coupler. All high frequency modes apart from one are now within the threshold. The mode at ∼1.85 GHz is around 40 times the impedance threshold in the vertical plane. This is likely a result of an interaction with the TE coupler resonance acting between the capacitive jacket and outer wall.

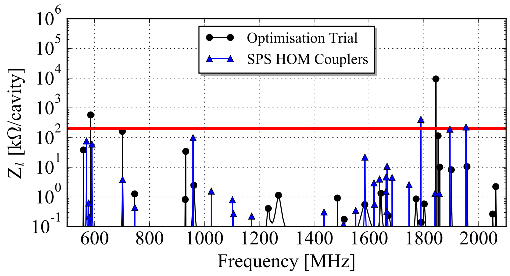

(a) Longitudinal.

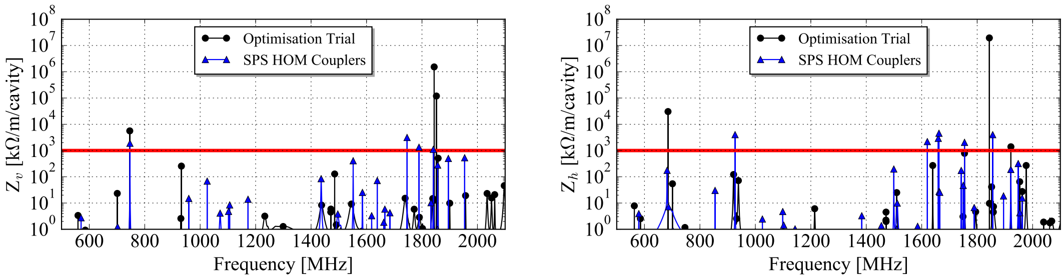

(b) Vertical.

(c) Horizontal.

Figure 5.9: Impedance spectra in each plane for the first modification of the DQW HOM coupler.

With reference to the optimisation goals, this coupler significantly reduces the impedance of the detrimental longitudinal mode at $\sim 959\,\mathrm{MHz}$ from $100\,\mathrm{k\Omega}$ to $2.5\,\mathrm{k\Omega}$. This reduction is mostly due to the external quality factor decrease from 10^4 to 300, but as the HOM couplers now more significantly load this mode, the $r/Q_{\parallel}$ has also been reduced from 9.7 to 9.2 ($\sim 5\%$).

However, the decrease in the HOM coupler's transmission at low frequencies means that the impedance of several low frequency modes have risen above the thresholds in each plane.

The difference in S_{21} between the two couplers is shown in Fig. 5.10. If the vertical mode at 746 MHz is used as an example, the difference in S_{21} is 9.41 dB which is equivalent to a gain of 2.95 computing as a voltage ratio. The Q_e of the mode at this frequency increased from 6160 (using SPS couplers) to 18180 (using coupler shown in Fig. 5.8a) and hence the ratio between them (2.95) exactly matches the reduction in S_{21}.

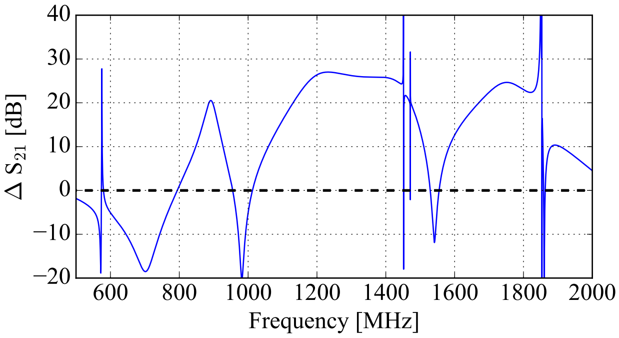

Figure 5.10: Difference in S_{21} from that of the SPS DQW HOM coupler design.

To increase the damping at low frequencies the coupler passband strongly influenced by the length from the bend to the capacitive gap and the length from the bend to the wall-connection (now at around 900 MHz - Fig. 5.8b) was decreased in frequency.

A plot of the S_{21} response for various values of the two parameters which strongly effect this pass-band are shown in Fig. 5.11.

To maintain the damping at high frequencies, the distance from the bend section to the wall-connection (Fig. 5.11b) was altered as the alternative geometry also significantly altered the other pass-bands. Broadband impedance simulations showed that is was possible to reduce the impedance of the low frequency HOMs by increasing this length. However, to reduce them all to within the threshold, the damping deficit left at ~ 1 GHz in the coupler's transmission response meant that modes in this frequency range increased to above the threshold value. The longitudinal mode near to the 24^{th} bunch spacing harmonic was over a factor of five higher than the threshold imposed to avoid HOM power higher than 1 kW. The modes in the 'trade-off' are detailed in the plot.

Trying to achieve a more broadband damping at higher frequencies is not a valid route for optimisation due to the impedance increase of the low frequency modes.

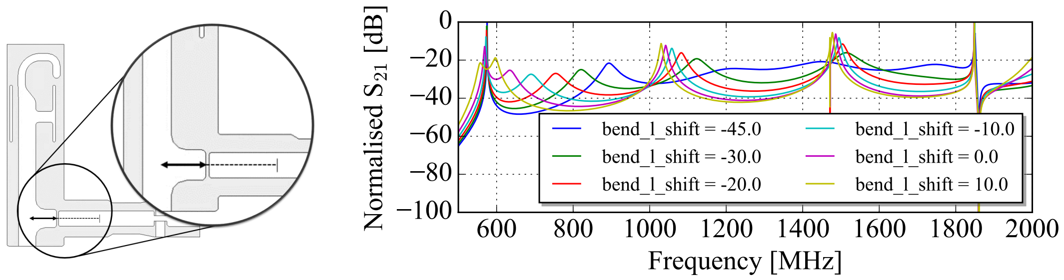

(a) Length from bend to capacitive gap.

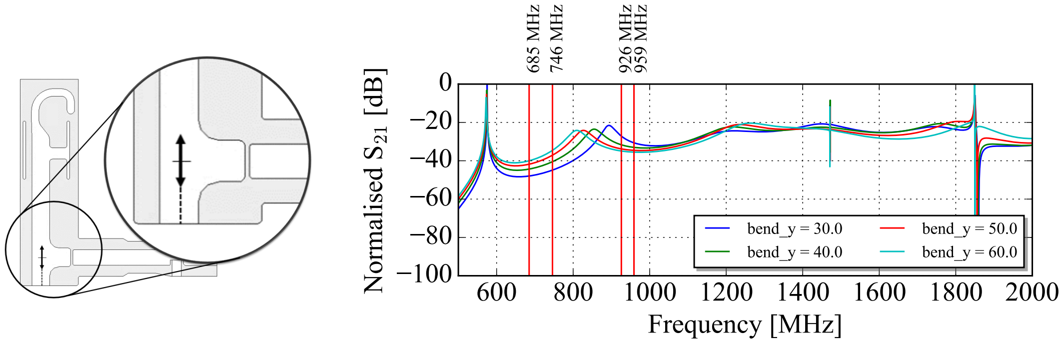

(b) Length from bend to ground.

Figure 5.11: Methods of reducing the pass-band now at 900 MHz to further damp the low frequency modes.

5.4.2 Optimisation 2: Proposed LHC DQW HOM Coupler

As shown, it is not possible to provide the additional damping to the high frequency HOMs by increasing the frequencies of the coupler pass-bands as the impedances of the low frequency modes rise above thresholds in specific bands.

The second route of optimisation was to decrease the coupler pass-band frequencies. Although this could seem like it would act to decrease the damping to the high frequency modes (presented as over the impedance threshold), it would bring the pass-band beyond the beam-pipe cut-off frequency to within the damping range. Conceptually, from equivalent circuit analysis, this pass-band is most strongly affected by the transmission line from the band-stop filter to the bend section (TL_{bs-b}). The transmission line is shorted at both ends and hence the high frequency pass-band above the cut-off frequency acts like the first even harmonic of the first pass-band controlled by this geometry. If the frequency of the harmonic is brought within the damping window, i.e. below the beam-pipe cut-off frequency of 2.1 GHz, this coupler resonance could be used to significantly increase the power flux at the high frequencies. As the other pass-bands will also reduce in frequency, this would also act to increase the damping to the low frequency modes over the thresholds (Tab. 5.3).

To assess the feasibility of this, the length of this section was increased and the resultant S_{21} plots are shown in Fig. 5.12.

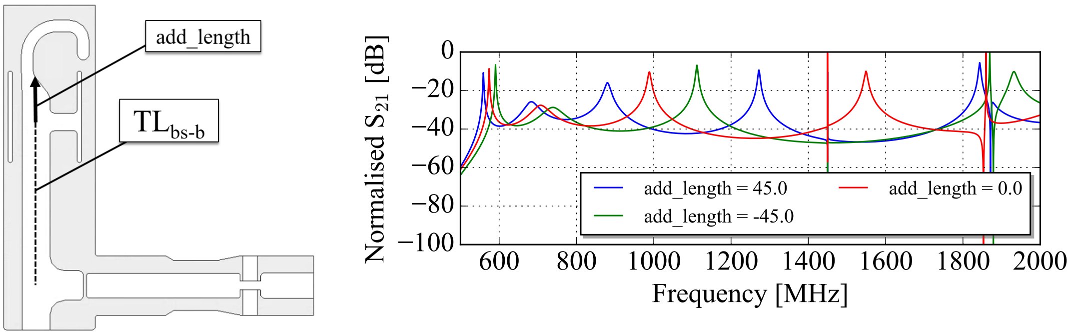

(a) Transmission line lengthened to decrease passband frequency.

(b) Effect on the HOM coupler's S_{21} response.

Figure 5.12: Mechanism to lower the pass-band frequency, bringing the harmonic of the length between the band-stop filter and bend section (TL$_{bs-b}$) into the frequency window.

From the S_{21} plots (Fig. 5.12), the reduction of the pass-band frequencies as a result of the additional length (blue curve) between the band-stop filter and bend is clear. Furthermore, the harmonic of the pass-band most effected by this distance decreases in frequency, becoming lower than the cut-off frequency of the cavity beam-pipes.

After assessing the method works, the coupler was optimised to damp the detrimental HOMs. The S_{21} profiles resulting from the optimisation steps are shown in Fig. 5.13b. The steps are then described in the bulleted list that follows.

Optimisation Procedure (steps correspond to those shown in Fig. 5.13b)

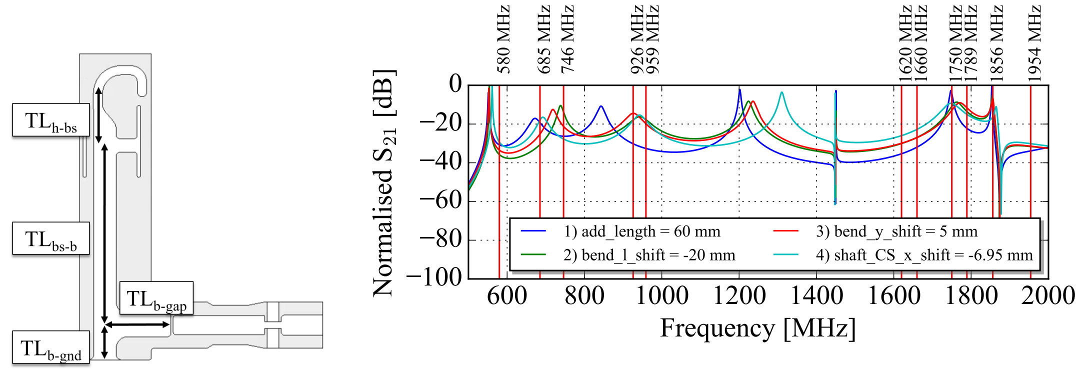

(a) Annotated schematic. (b) Main alterations of the nominal HOM coupler geometry..

Figure 5.13: Main alterations of the nominal HOM coupler geometry.

1. Firstly, the length between the band-stop filter and bend section (TL$_{bs-b}$) was further lengthened to place the second harmonic of it's pass-band (previously above the cut-off frequency of the cavity beam-pipe) at 1.75 GHz. This would provide damping to the high frequency modes over the impedance threshold (Tab. 5.3) in the SPS DQW, i.e. in the range 1.6–1.9 GHz.

2. Secondly, to rectify the decreased transmission at $\sim$ 1 GHz, the length of the line from the coupler's bend section to the capacitive gap was decreased. The pass-band most effected by this geometry (TL$_{b-gap}$) and the adjacent higher frequency pass-band (due to a strong coupling between the two) increased in frequency as a result. The change in length was chosen to efficiently damp the two low frequency detrimental mode pairs, i.e. 685/746 MHz and 926/959 MHz.

3. The two pass-bands described in point 2 were tuned by increasing the height of the output line from the base of the coupler.

4. The pass-band resulting from the second harmonic of the distance from the hook to the band-stop filter (TL$_{h-bs}$) was placed exactly in-between the adjacent pass-bands to provide the most broadband damping achievable in this region.

The frequency shift was achieved by altering the rectangular cross-section of the coupler, since it did not effect any other coupler resonance.

In addition to the alterations detailed, the taper on the output line[1] was also removed. Fig. 5.14 shows the S_{21} as a function of frequency for the SPS DQW HOM Coupler and for the final iteration of the optimisation routine detailed in Fig. 5.14. The difference between the two curves is also shown with the frequencies of the detrimental modes highlighted.

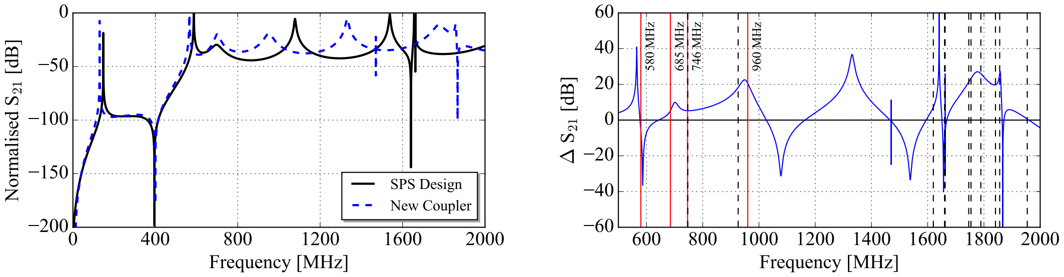

(a) Transmission characteristics for the SPS DQW HOM coupler and the new proposal.

(b) Difference between the SPS DQW HOM coupler and the new proposal. Modes which were over the impedance threshold in the SPS coupler are shown by the vertical dashed lines and the four low frequency detrimental modes are annotated.

Figure 5.14: S_{21} characteristics for the LHC DQW HOM coupler.

Figure. 5.14b shows that for every mode that was above the impedance threshold in the SPS DQW case, there is additional transmission in the case of the new coupler.

5.4.3 Stop-band tuning and heat-load

Before the impedance simulation, the band-stop filter was tuned to reject the fundamental mode. Although the frequency of the band-stop filter was already tuned

---

[1] This was originally incorporated to allow the use of DN40CF flanges however, since the tapers add manufacturing difficulties and RF reflections, the flange type to be used was changed to a DN63CF.

independently, the cavity geometry slightly alters the equivalent circuit parameters of the coupler. As such, the filter was tuned on the cavity to give the lowest dissipation of fundamental mode power. This was done using the length of the capacitive jacket, i.e. the capacitance of the band-stop filter. The dissipated power through the top HOM coupler and the pick-up port as a function of jacket length is shown in Fig. 5.15.

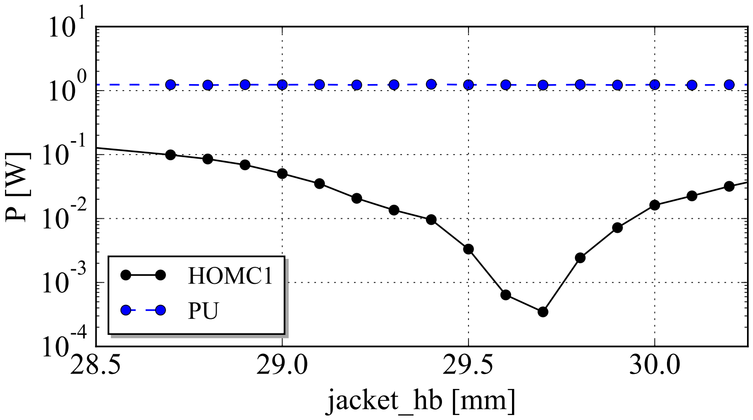

Figure 5.15: Power extracted from the fundamental mode at 3.4 MV as a function of the jacket length (the variable '*jacket_hb*' is the length from the stub of the band-stop filter to the lower side of the capacitive jacket) for the top HOM coupler (HOMC1) and pick-up probe (PU).

Increasing the bottom length of the jacket to 29.7 mm brings the average power per coupler to less than 1 mW. The bandwidth of the stop-band also means that the power is less than 100 mW for the top HOM coupler with an error of ± 0.8 mm on the jacket length. For reference, the pick-up probe was designed to extract 1 W (30 dBm) of fundamental power. This is because the low level RF module minimum input power is 0.01 W (10 dBm) and the cables, attenuators, filters and splitters contribute 20 dB (factor of 100) of attenuation to the signal [115].

It is important to evaluate the dynamic heat load on the HOM coupler's copper gasket, to assess whether the cryogenic system can maintain the required operational conditions. The dynamic heat load limit of the cryomodule is 25 W [17] with each cavity accounting for $\sim$ 7 W each. The total gasket dynamic heat load was specified at less than 1 W for the cavity gaskets, i.e. 0.3 W per gasket.

The dynamic heat load on the gasket can be calculated using

$$P = \int H^2 R_s \, dA \tag{5.1}$$

where H is the magnetic field in A/m and R_s is the surface resistance of the material. The DC resistivity of copper can be calculated using the empirical formula detailed in [116, Section 8-4] as a function of the Residual Resistance Ratio (RRR). This value, at a given temperature and RRR value, can be used with the formula presented in [117] to calculate the surface resistance as a function of frequency. This is shown in Fig. 5.16 for copper at 2 K. The plot is shown for both a 'classical' approach and for one which includes the 'anomalous skin effect' [118, 119]. The latter is an effect which quantifies the increase in surface resistance in metals at high frequencies and low temperatures.

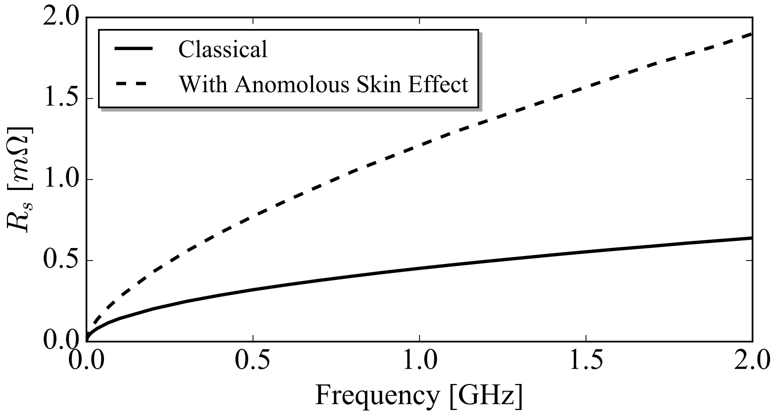

Figure 5.16: Surface resistance of copper at 2 K with a RRR value of 300 as a function of frequency, with and without the anomalous skin effect taken into account.

The anomalous skin effect increases the surface resistance by over a factor of two at 400 MHz and hence should be incorporated in any gasket heat-load simulations.

With a jacket length error, and hence a notch detuning, of ± 1 mm, the simulated dynamic heat load on the gasket is less than 1 mW. This is as a result of the high pass filter section of this coupler design as well as the broadband notch placed before the gasket location (see Fig. 5.3), 'shorting' the fundamental field before it ‘sees’ the gasket.

5.4.4 Impedance Calculations

Following the tuning of the band-stop filter and evaluation of the dynamic heat load on the gasket, the impedance in each plane was calculated. The final coupler model alongside the three impedance spectra is shown in Fig. 5.17.

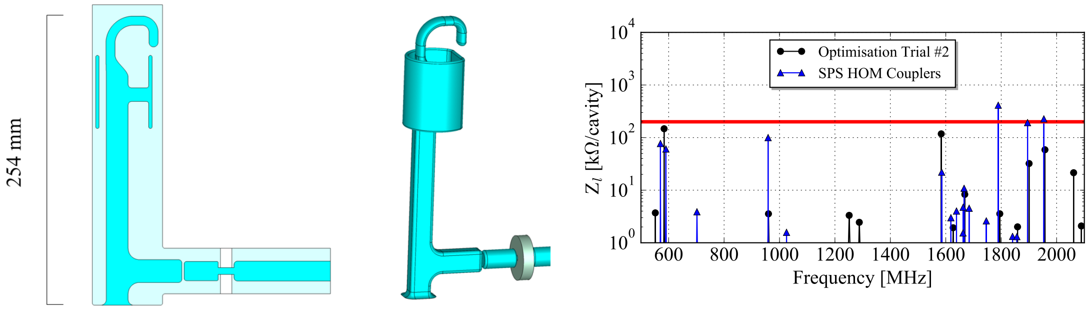

(a) Coupler model.

(b) Longitudinal.

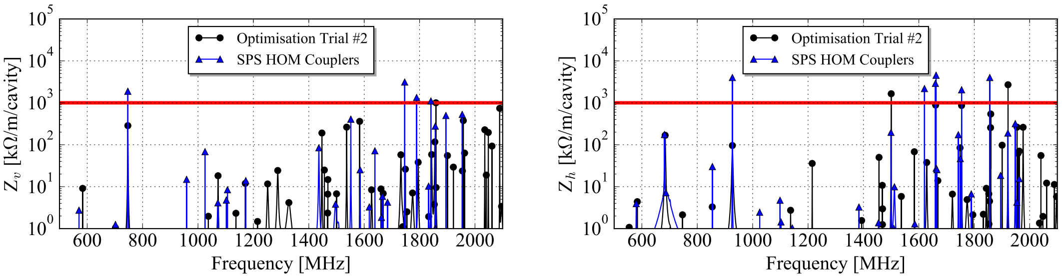

(c) Vertical.

(d) Horizontal.

Figure 5.17: Impedance spectra in each plane for the second modification of the DQW HOM coupler.

All modes apart from two are within the impedance thresholds. The modes which are above the threshold are detailed in Tab. 5.4 and a comparison of the low frequency detrimental modes from the SPS DQW HOM coupler case to that of the HL-LHC version are detailed in Tab. 5.5.

The two modes that are over the impedance threshold are both high frequency, i.e. above 1.5 GHz, and a factor 1.6 and 2.7 larger than the threshold respectively.

Referring to Tab. 5.5, the first two high impedance HOMs have been altered significantly by using the LHC HOM coupler design. Due to the frequency change

Frequency [MHz]	Qe	R_v [$k\Omega$/m]	R_h [$k\Omega$/m]	R_l [$k\Omega$]
1500.23	3.43×10^4	7	$\boxed{1646}$	0
1921.98	8.80×10^4	29	$\boxed{2699}$	0

Table 5.4: Modes over the impedance threshold after the re-design.

SPS DQW HOM Coupler				
Frequency [MHz]	Qe	R_v [$k\Omega$/m][a]	R_h [$k\Omega$/m]	R_l [$k\Omega$][b]
570.36	3.08×10^3	2.75	0.15	$\boxed{77.12}$
590.14	1.92×10^3	0.03	0.03	$\boxed{60.64}$
686.75	2.07×10^1	0.00	$\boxed{7.19}$	0.00
746.67	6.16×10^3	$\boxed{1888.67}$	0.07	0.44
926.80	1.26×10^4	0.01	$\boxed{4019.60}$	0.00
958.87	1.03×10^4	14.95	0.40	$\boxed{99.90}$

LHC DQW HOM Coupler				
Frequency [MHz]	Qe	R_v [$k\Omega$/m]	R_h [$k\Omega$/m]	R_l [$k\Omega$]
551.84	8.18×10^2	0.60	0.13	$\boxed{3.70}$
583.58	2.86×10^3	9.11	4.39	$\boxed{147.34}$
684.12	3.59×10^2	0.04	$\boxed{167.97}$	0.00
746.79	1.05×10^3	$\boxed{285.54}$	2.13	0.06
926.82	3.37×10^2	0.12	$\boxed{95.82}$	0.00
960.12	3.92×10^2	0.71	0.32	$\boxed{3.55}$

Table 5.5: Comparison of low frequency, high impedance modes before and after the HOM coupler re-design.

---

[a] Transverse threshold: 1 MΩ/m/cavity

[b] Longitudinal threshold: 200 kΩ/cavity

of the coupler's first pass-band, the DQW crab cavity HOM is 'split' differently. The first HOM has reduced by over 18 MHz and the longitudinal impedance has decreased by over a factor of 20. The next detrimental HOM has increased by over a factor of two in impedance, but is still within the 200 kΩ impedance threshold. Advantageously, the frequency of this mode has decreased by 6.6 MHz from the case of the SPS DQW HOM coupler design. This means that the mode has gone from being lower than the 15^{th} bunch spacing harmonic frequency by 11.1 to 17.6 MHz. The likelihood of this mode interacting with the bunch spacing harmonic is hence significantly reduced.

As a result of the need to further damp the vertical mode at 747 MHz the, impedance of the horizontal mode at 687 MHz has significantly increased, but has been kept five times lower than the threshold. The mode at 747 MHz has been damped to within the threshold (three times lower).

The two final modes, at 927 and 960 MHz, have been significantly damped, reducing their highest impedances by factors of 42 and 28 respectively. Referring back to the optimisation goals, the high power mode is now at 70% of the new threshold. As a result of stronger coupling to the longitudinal mode at 960 MHz, the frequency has increased by 1.2 MHz and has become closer to the 24^{th} bunch spacing harmonic (at 961.92 MHz). However, if the frequency of this mode increases as it did in the SPS case (Chapter 4, Sec. 4.2.2: + 3.4 MHz) it would be further away from the harmonic compared to the SPS cavities. Since the mode is now significantly damped by the ancillaries, this is difficult to predict. The new maximum power from this mode, using a pessimistic value of J_k, is $\sim$ 350 W.

5.4.5 Power Spectra and Stochastic Analysis

As presented in the case of the longitudinal mode at 960 MHz, the HOM power is not necessarily below the 1 kW threshold just because the longitudinal impedance is less than the 200 kΩ threshold. As with the SPS DQW HOM couplers, the frequencies and quality factors of the simulated modes were stochastically varied by the deviations measured on the SPS cavities.

Rather than modelling the bunch profile with only a Gaussian distribution, it has been shown that the profile of the bunch in the SPS and LHC is is closer to that of a binomial distribution [120, 121]. In the frequency domain, this can be represented [121] as

$$S(f) =_0 F_1 \left(\frac{3}{2} + \mu, -\frac{(\pi \tau_L f)^2}{4} \right) \tag{5.2}$$

where ${}_0F_1(x, y)$ is the hypergeometric function, f is the frequency and τ_L is arrived at from the relationship $\sigma_{rms} = \tau_L / 2\sqrt{3 + 2\mu}$ where σ_{rms} is the root mean square bunch length. The value of μ can be varied to best match the conditions in the respective machines. The variation of J_k (detailed in Chapter 4, Sec. 4.2) is shown in Fig. 5.18a and displays the lobe amplitude dependence and the convergence to a Gaussian function as the value of μ becomes larger. A value of $\mu = 2.0$ gives an accurate representation of the bunch profile in the LHC [120] and a value of 1.5 for the SPS [121].

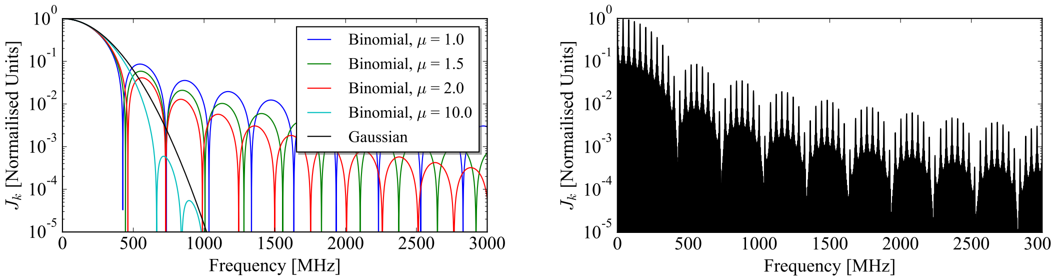

(a) Variation with μ.

(b) 12 bunches, $\mu = 1.5$

Figure 5.18: Examples of J_k as a function of frequency using a binomial bunch profile for one bunch using different values of μ and with 12 bunches for a constant μ value of 1.5. The total bunch length is 3.0 ns.

The lobes of the binomial equation in the frequency domain mean that there are frequencies where the value of J_k (and hence the beam current) is very low. In these areas, here referred to as ‘nodal points’, a small frequency shift can change the amplitude by multiple orders of magnitude. Hence, the excitation of HOMs with frequencies near to a nodal point is very sensitive to bunch length.

Plots of the average and maximum power as a function of stochastic samples, varying the frequency and external quality factor by the tolerances measured and detailed in Chapter 4 (f: $-0.9\% \rightarrow +1.1\%$, Q_e: $50\% \rightarrow 200\%$), are shown in Fig. 5.19 for both a Gaussian and binomial bunch profile.

In each of the four simulation cases, the highest contribution to the power is that of the longitudinal mode at 960 MHz. Additionally, for a bunch length of $\sigma = 1.2$ ns, the Gaussian profile yields a higher power than the binomial.

For the new couplers, the maximum power from the stochastic variations is 500 W for the Gaussian bunch profile and 250 W for the binomial bunch profile. The specifications for the worst case power are hence met for both cases and are lower for the more representative case.

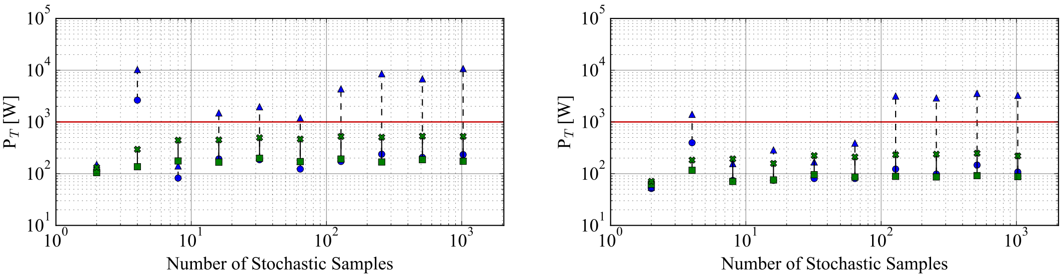

(a) Gaussian.

(b) Binomial.

Figure 5.19: Total HOM power as a function of HOM parameter stochastic deviation samples for the 'SPS DQW' and 'LHC DQW' HOM couplers installed onto the DQW crab cavity. The average and maximum values are given for each stochastic sample set. The 'SPS DQW' HOM couplers are represented by the blue circle to triangle and the 'LHC DQW' by the green square to cross.

As discussed in Chapter 4 Sec. 4.2.1, a continuous train of bunches with equal bunch spacing is assumed to gernerate the form of the current in the frequency domain. Although the form of the current is also modulated by the train spacing, it is the interaction between the cavity HOMs and the bunch spacing harmonics that contrbutes significantly to the HOM power. To verify the extent to which this assumption was correct, the HL-LHC filling scheme was used to evaulate the HOM power stochastically in the same way as that shown in Fig. 5.19. Using a Gaussian beam profile, the same maximum and average power was returned, validating the methods used for analysis and benchmarking. A plot is shown for visualisation in Appendix Sec. 7.

5.4.6 Beam-Pipe Ancillary Changes

During the tests in the Super Proton Synchrotron (which will be detailed in the coming chapters) the 400 MHz signal measured by the pick-up antenna was perturbed as a result of the coupling between the fundamental mode pick-up (field antenna) and charged particle beam. This is detailed in [122].

Referring to Chapter 4 where the dual functionality of the pick-up as a fundamental probe and HOM damper was presented, the section of the pick-up directly coupling to the beam is the 'mushroom' shape designed to damp the 1.75 GHz mode. The geometry was acting as a Beam Position Monitor (BPM).

As such, it was decided to eradicate the dual functionality by adding a second beam-pipe port to the cavity on the FPC side. This would allow two beam-pipe probes where one could act as a High Frequency (HF) damper and the other as a fundamental mode antenna.

To establish the coupling mechanisms and hence geometries necessary for the HF-damper, the modes which the SPS hybrid beam-pipe pick-up damped were evaluated. Figure. 5.20 shows the impedance spectra with the pick-up terminated at 50 Ω and with an electrical short.

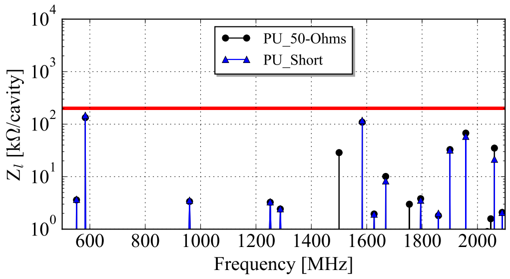

(a) Longitudinal.

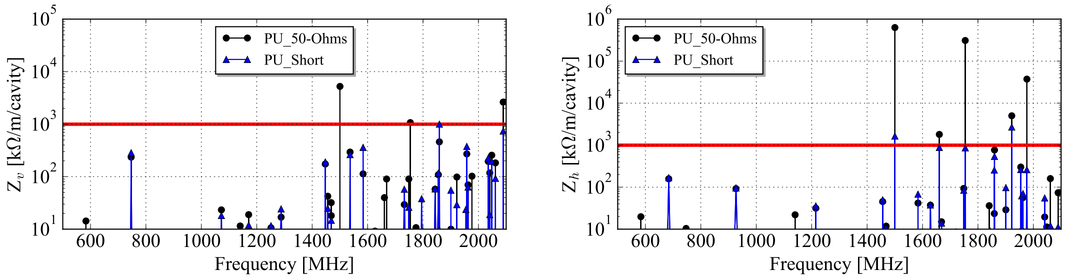

(b) Vertical.

(c) Horizontal.

Figure 5.20: Impedance spectra in each plane with and without the damping of the pick-up probe.

The impedance spectra shows five horizontal HOMs and one vertical which increase significantly in external quality factor and are over the impedance threshold.

In each case, the mode's electric field couples to the perpendicular flat surface of the 'mushroom' and the magnetic field 'flows' around the stem and hook sections. Initially, a simple probe was trialled to only couple electrically to the three modes. However, whilst this could be feasible for the mode at 1754 MHz (the reason the hybrid damper was first designed), the other modes need the accompanying magnetic coupling. Hence an electric coupling element on a ‘stem’ (provides magnetic coupling) was incorporated. The resulting geometry is shown in Fig. 5.21 alongside the new fundamental antenna design [123]. The resulting impedance spectra is displayed in Fig. 5.22 with the difference with that of the hybrid pick-up antenna detailed in Fig. 5.22d for the horizontal modes. The quality factor of the mode significantly over the impedance threshold (1920 MHz) has increased by nearly a factor of two.

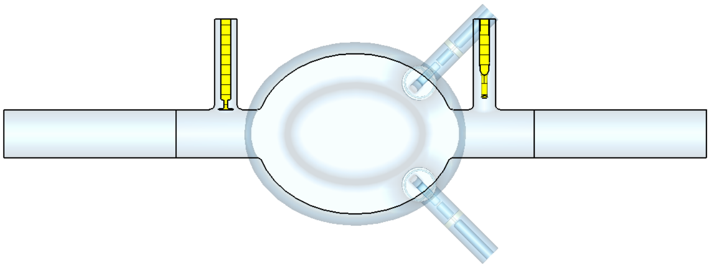

(a) Full cavity view.

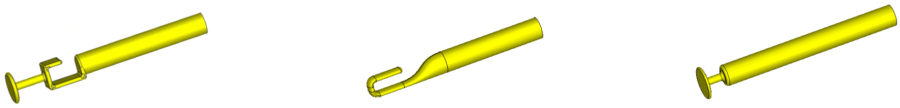

(b) Previously used ‘hybrid’ pick-up.

(c) New fundamental mode pick-up.

(d) New high frequency damper.

Figure 5.21: CAD representation of the new beam-pipe couplers.

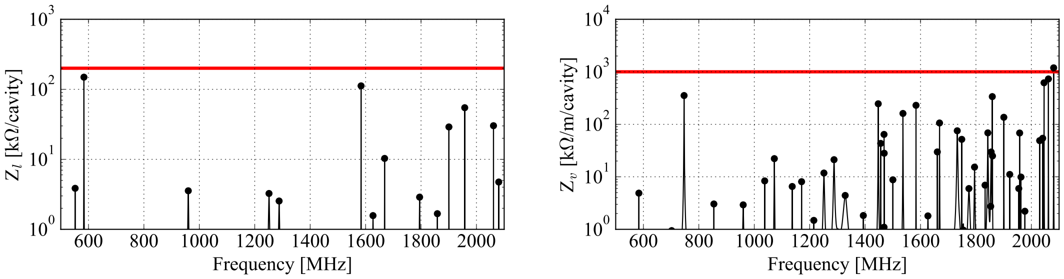

(a) Longitudinal.

(b) Vertical.

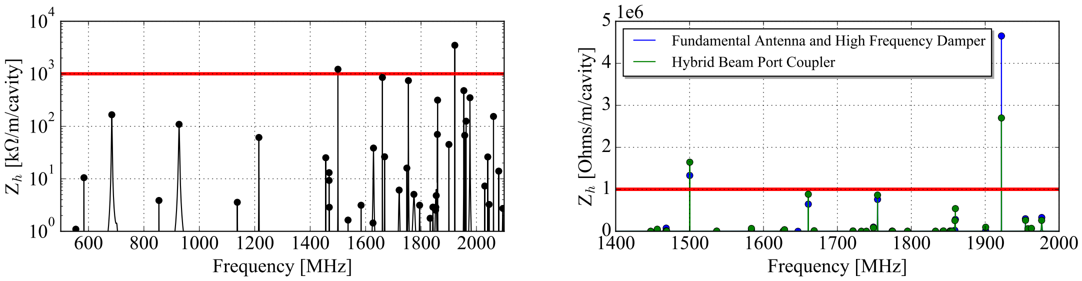

(c) Horizontal.

(d) Horizontal difference.

Figure 5.22: Impedance spectra in each plane with the new fundamental probe and high frequency damper.

5.4.7 Material Changes

Two types of ceramic window (for separating air from vacuum) material are commonly used for RF windows. These are: teflon and alumina. The window material was mistakenly used as teflon. The window geometry (i.e. the ratio of the external to internal diameters) was designed to match the 50 Ω output termination with the dielectric constant of alumina. The spectral transmission for the SPS and LHC HOM coupler output lines is shown in Fig. 5.23 for both teflon and alumina which have dielectric constants of 2.1 and 9.4 respectively.

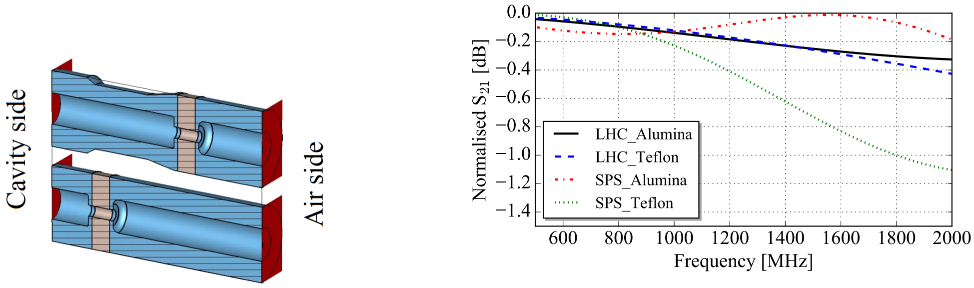

(a) SPS (top) and LHC (bottom) output lines.

(b) Transmission response.

Figure 5.23: Transmission response of the output line before and after the taper removal and with different dielectrics.

The plots show a large difference between the two dielectrics in the SPS output line case but very little difference for that of the LHC design which has a constant output diameter.

Plots of the cavity impedance spectra with the two ceramic window materials are shown in Fig. 5.24. The mode parameter shifts as a result of the material change for high impedance and detrimental modes are shown in Tab. 5.6.

The majority of the modes have reduced in quality factor with the ceramic window material change. Specifically, the horizontal mode significantly above the threshold (at 1920 MHz) has decreased by over a factor of 2.

However, the quality factor of the first high impedance longitudinal mode has increased by a factor of 1.53 and as such is now above the impedance threshold by 13%. Furthermore, the quality factor of the longitudinal mode close to the frequency of the 24^{th} bunch spacing harmonic has increased by a factor of 1.3,

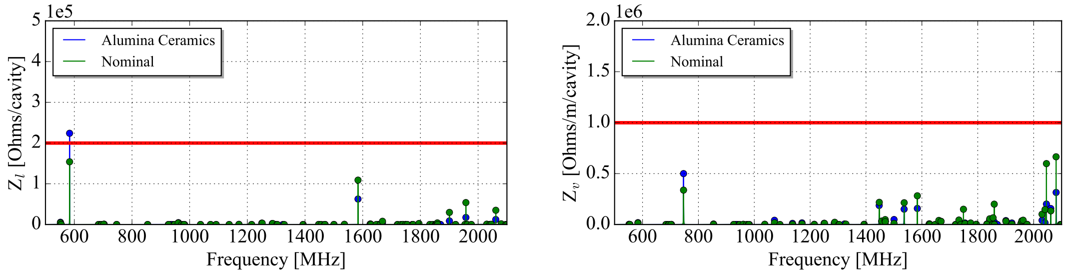

(a) Longitudinal.

(b) Vertical.

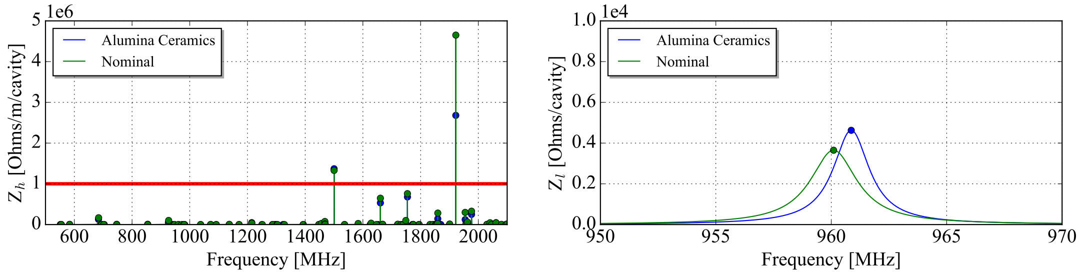

(c) Horizontal.

(d) Longitudinal (960 MHz).

Figure 5.24: Effect of changing the window material on from Teflon to Alumina on the cavity impedance spectra.

bringing the longitudinal impedance to 4.5 kΩ per cavity. This value is still below the impedance threshold of 5 kΩ specifically applied to this mode. The frequency of the mode has increased by 750 kHz and is now closer to the bunch spacing harmonic.

5.5 Geometry Investigations and Mesh Studies

To provide information for further optimisation or tuning in the case of problems or HL-LHC beam parameter changes, several geometric investigations were trialled.

5.5.1 Feed-through Geometry Changes

As shown in Fig. 5.24d, the characteristics of the highly loaded longitudinal mode close to the 24^{th} bunch spacing harmonic of the HL-LHC beam (960 MHz) can be altered by the properties and geometry of the ceramic window. Geometric changes

Frequency [MHz]	Qe	R_v $[k\Omega/\text{m}]$	R_h $[k\Omega/\text{m}]$	R_l $[k\Omega]$	Δf [MHz]	$\frac{Q_e(alumina)}{Q_e(teflon)}$
552.01	815	0.55	0.21	$\boxed{3.79}$	-0.11	1.52
583.58	2857	6.24	7.31	$\boxed{148.00}$	0.01	1.53[a]
684.11	364	0.13	$\boxed{170.00}$	0.00	-0.53	0.80
746.78	1083	$\boxed{289.00}$	1.70	0.07	0.02	1.68
926.81	339	0.36	$\boxed{104.00}$	0.00	-0.80	0.53
960.12	391	3.44	0.13	3.51	0.75	1.29[b]
1500.22	34200	20.20	$\boxed{1680.00}$	0.04	-0.02	0.68
1660.66	67800	6.61	$\boxed{911.00}$	0.04	0.00	0.50
1754.42	16000	2.34	$\boxed{1220.00}$	0.05	-0.01	0.53
1922.00	145000	44.90	$\boxed{5590.00}$	0.06	-0.03	0.42

Table 5.6: Mode parameters for teflon windows and the shifts as a result of the material change.

---

[a] 10% above the threshold.

[b] $3.51 \times 1.29 = 4.53\,\text{k}\Omega$ still within $5\,\text{k}\Omega$ threshold set specifically for this mode.

are often easier to incorporate on the air side of the window and can allow better ‘matching’ to specified modes. The two parameters changed were the position of the ceramic window and the length of the reduced inner diameter section. Figure 5.25 shows the geometries which could be easily varied from a manufacturing point of view. Figures 5.25b–5.25e show the effect of these parameters on the frequency and impedance of the 960 MHz mode.

Referring to the schematic, the effect of the parameter *int_l* is much larger than that of *cap_cyl_l*. Increasing its length decreases the impedance and also allows better access with respect to the electron beam welding of this section. However, with the length increase, the frequency of the mode becomes closer to that of the bunch spacing harmonic (961.9 MHz).

This variation presents a mechanism for an impedance reduction and tuning of the 960 MHz mode. In the case that the mode frequency is exactly that of the nearest bunch spacing harmonic, using a resonator model approximation, a 550 kHz shift would decrease the HOM power at this frequency by 25%. The change in geometry provides a mechanism for mode ‘tuning’ if the power from this mode is too high.

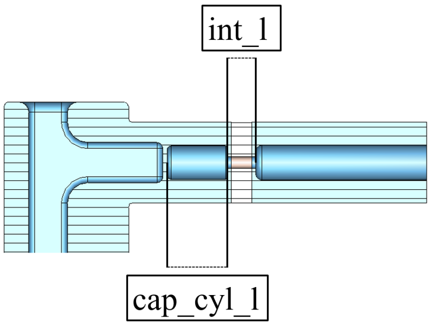

(a) Parameters varied.

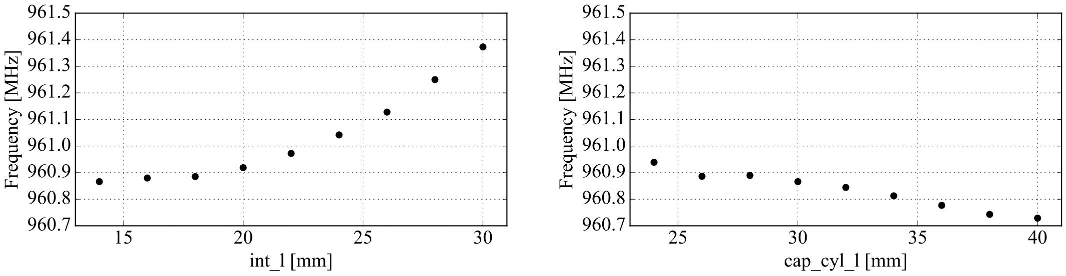

(b) Effect of *int_l* on frequency.
Nominal value = 14 mm

(c) Effect of *cap_cyl_l* on frequency.
Nominal value = 30 mm

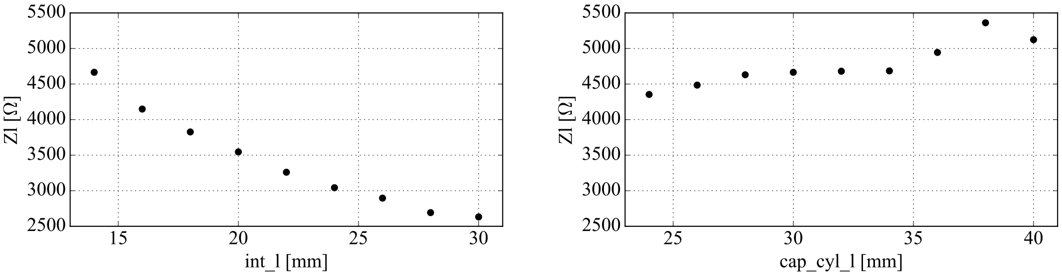

(d) Effect of *int_l* on impedance.
Nominal value = 14 mm

(e) Effect of *cap_cyl_l* on impedance.
Nominal value = 30 mm

Figure 5.25: The effect of output line geometric variations on the frequency and longitudinal impedance of the 960 MHz mode.

5.5.2 Reducing the Impedance of the 580 MHz Mode

If the beam dynamics requirements for the HL-LHC change, i.e. with exotic filling schemes, some modes could become more problematic than others. Specifically, with reference to the HOM power, mechanisms to reduce the mode with the highest longitudinal impedance (580 MHz) were investigated.

Two investigation methods were followed to evaluate by how much the mode could be damped and the detrimental effects on other modes. The methods were:

1. Change the transmission line lengths with pass-bands closest to the mode (TL_{bs-b} and TL_{h-bs} shown in Sec. 5.3, Fig. 5.6). The two transmission line lengths are controlled by the parameters '*bend_l*' and '*stub_y_shift*' respectively.
2. Change the output capacitance (half gap size and remove).

Figure. 5.26 displays the effect of the geometric alterations on the 580 and 960 MHz modes (longitudinal mode capable of producing high HOM powers).

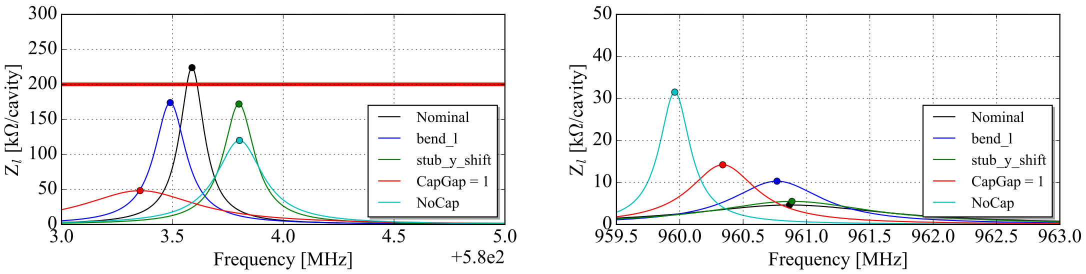

(a) 580 MHz mode.

(b) 960 MHz mode (5 kΩ limit).

Figure 5.26: Investigations to reduce the impedance of the first high-impedance longitudinal mode at 580 MHz.

In all cases the HOM coupler alterations decrease the quality factor of the first longitudinal HOM, but increase that of the 960 MHz HOM. As such, the HOM coupler geometry was kept the same, but the investigations are presented in the case where further damping of the first HOM is necessary. The easiest solution to achieve this would be to increase the output capacitance by reducing the output gap. If the frequency of the 960 MHz mode is known to be far from the bunch spacing harmonic, this is a trivial solution with no further machining requirements.

5.6 Mesh Convergence

For the HOM coupler optimisation and impedance studies presented, the standard meshing ('auto-mesh') was used with the non-linear eigenmode solver (recomended by CST support for broad-band simulations) to generate a tetrahedral mesh based on the cut-off frequency of the cavity beam-pipes. Using a denser mesh added a significant simulation time, slowing the optimisation.

To assess whether the modes were converged, the number of tetrahedra was increased by a factor of 2.5 (the nominal was 200×10^3). High impedance modes with a quality factor variation of greater than 10% were selected for a convergence study (580 MHz and 1500 MHz modes).

For each mode independantly, the external quality factor was simulated using the standard (linear) eigen mode solver as it used 'adaptive mesh refinement' which has an internal convergence test to a user specified accuracy. Here, this is reffered to as a 'narrowband simulation', i.e. only looking at one mode. For these simulations, the number of mesh tetrahedra was increased to evaluate whether the quality factor was converged with respect to the mesh density.

To compare the mesh convergence of each mode on one plot, the ratio between the value from the narrowband simulation (varying with mesh) and that of the broadband simulation (static value calculated once) was used. This is shown in Fig. 5.27. Two other high impedance modes are also shown.

The modes were converged with respect to the number of mesh tetrahedra, but there is an increase in quality factor using the narrow-band simulation method for the two modes seen to be 'mesh-sensitive'. As a pressimistic approach, the higher values were used in the final impedance table.

5.7 Final Impedance Spectra

The final impedance spectra for the cavity with the LHC DQW HOM couplers is shown in Fig. 5.28 on page 149.

Of the three modes over the impedance design threshold (580 MHz(longitundinal), 1500 MHz($\perp$: H) and 1920 MHz($\perp$: H), the first two are so by 10% and 25% and the final mode, at 1920 MHz, is over the horizontal threshold by a factor of 2.5.

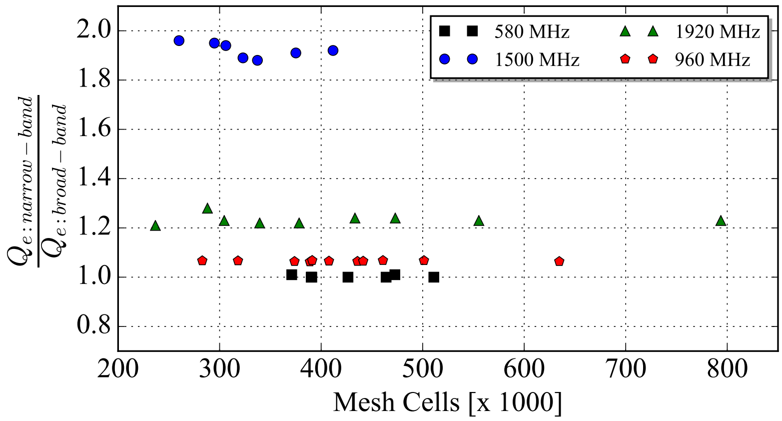

Figure 5.27: Ratio of the external quality factor from single mode simulations with adaptive mesh refinement in the normal eigenmode solver (narrow-band) to the static value from the non-linear eigenmode solver (broad-band) for four high impedance modes.

The impedance spectra was verified as acceptable for beam stability in [124]. As the first two modes over the threshold were so by small amounts, further optimisation was halted as the values were acceptable when investigated. Furthermore, the feedthrough designs and matching impedance for the cavity was not finalised. As the feedthroughs change the coupler's equivalent circuit, they can have a strong effect on the impedance of the modes. As an example, 25 Ω matching is currently being trialled to increase the inner diameter of the feedthrough 'pin'. The impedance of the cavity with a 25 Ω match (and coupler alterations to copensate the decreased transmission at the high power mode) is shown in Appendix Sec. 5. The impedance of the first two modes over the threshold falls to below the design threshold.

For the highest frequency mode over the threshold, at 1920 MHz, it is difficult to damp to this mode because of both its field topology (with respoect to the HOM coupler port locations) and the TE-like resonance between the HOM coupler's capacitive jacket and outer wall. The coupler resonance can be moved by tuning the jacket, but due to the large amount of HOMs at high frequencies, there is always a HOM which is damped insufficiently. This has been seen for every iteration of the DQW HOM coupler design. Since the mode is very high frequency, and the octupole current needed to compensate the transverse impedance reduces with frequency, the mode was accepted but flagged for mode parameter tracking during manufacture. Since the mode is a high quality factor mode, rather then $r/Q_{\perp}$, the likelihook of the modes exactly overlapping in each cavity is also extrememly small. The mode was also benchmarked in ACE3P, resulting in an external quality factor 20% lower than that of the CST calcualtions presented. Finally, the mode is extremely sensitive to beam-pipe boundary conidtions (since it is close to the cut-off frequency) and the presented value represents the worst case.

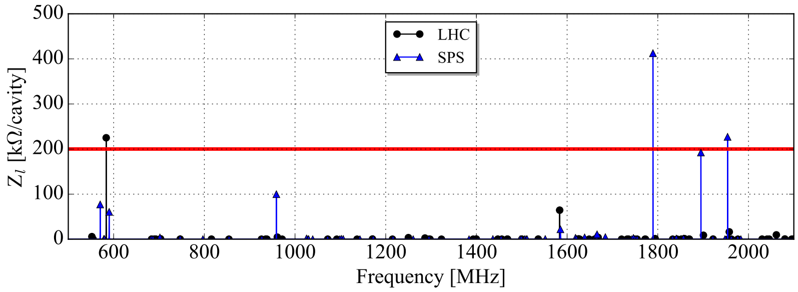

(a) Longitudinal impedance spectra - linear scale.

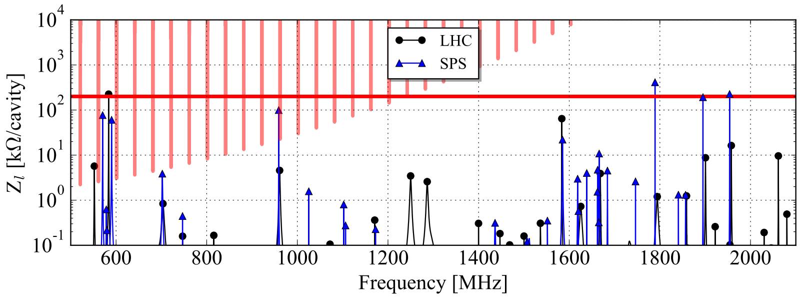

(b) Longitudinal impedance spectra - log scale. Mode impedances which would result in a power of over 1 kW are highlighted in red.

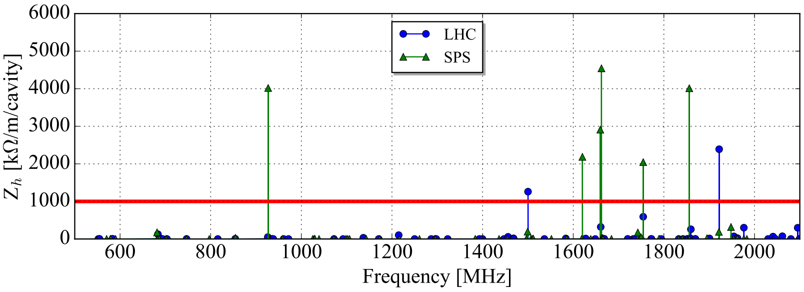

(c) Transverse impedance spectra - horizontal.

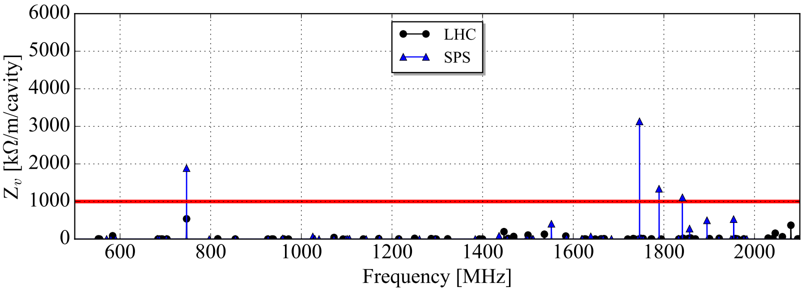

(d) Transverse impedance spectra - vertical.

Figure 5.28: Impedance spectra for the DQW crab cavity with both the SPS and LHC HOM couplers.

5.8 Alternative Coupler Design

A suspected thermal quench[1] during preliminary cold dressed cavity tests launched an investigation into a new HOM coupler design for the DQW crab cavity. The region of the HOM coupler with the highest magnetic field is not hollow which means there is a distance in the order of a few centimetres between this location and the helium bath. For the re-design, it was specified that there should be no physical distance from a high magnetic field region of the coupler to the helium bath. Furthermore, although the manufacturing complexity was reduced for the LHC DQW HOM coupler, it is still a complex geometry with respect to manufacture. A simpler geometry was therefore attractive as this reduces costs in terms of time and materials.

5.8.1 Concept

Conceptually, to provide a stop-band at the frequency of the fundamental mode, a quarter wavelength transmission line was implemented. To centre the rejection filter at 400 MHz, the length of the transmission line should be $\lambda/4 = c/4f = 3 \times 10^8/(4 \times 4 \times 10^6) = 0.75 = 18.75\,\mathrm{cm}$.

Since the general HOM field topology in the DQW crab cavity has a magnetic field which ‘flows’ around the base of the central poles, an inductive coupling mechanism is most efficient (Chapter 2, Sec. 2.3.3) to maximise the coupling to the HOMs. To verify the coupling choice, three coupling mechanisms were modelled on a Quarter Wave Resonator (QWR). The coupling mechanisms evaluated were typical ‘probe’, ‘hook’ and ‘loop’ geometries. To best model the fields of the HOMs in the DQW crab cavity, the couplers were mounted on the magnetic field side of the QWR at the same insertion depth. The S_{11} for each of the couplers is shown in Fig. 5.29. For the same insertion depth, the coupling coefficient (β, Chapter 2, Sec. 2.3.3) for the inductive coupler is significantly higher than for the other two coupling mechanisms.

A disadvantage of an inductive coupling mechanism is that the coupler must be electrically connected to the wall (ground) which means welding the coupling ele-

---

[1] This was solved with further chemistry on the HOM coupler.

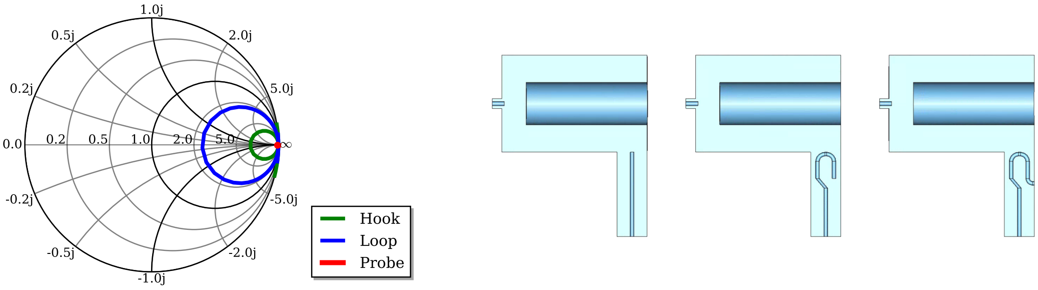

(a) S_{11}.

(b) Probe (left), hook (middle) and loop (right).

Figure 5.29: Comparing coupling mechanisms at a location of high H-field.

ment, as shown in [88]. Welding the coupler to the cavity wall is not practical due to the advantages associated with 'de-mountable' couplers (Chapter 2, Sec. 2.3.4). However, by connecting the coupler far from the field coupling geometry, the couplers can be demounted.

If the distance from the connection to ground to the field coupling geometry is set to 18.75 cm ($\lambda/4$ at 400 MHz), this geometry of the coupler will provide the stop-band response at the frequency of the fundamental mode whilst inductively coupling to the HOMs (albeit less strongly than the loop mechanism shown in Fig. 5.29b). The high field region will be located at the area connected to the helium bath, meaning superfluid liquid helium will 'flow' through this section. As such, there will be no high magnetic field areas conductively cooled over distances greater than a few millimetres. Figure 5.30 shows the alternative coupler design and the S_{21} response.

The high frequency transmission has three distinct areas of rejection which correspond to the odd quarter wave transformer harmonics [69] since the resonator is 'open' at one end. If the coupler was 'shorted' at this end, the harmonics would be at the even multiples of $\lambda/4$. Analytically, the harmonics are at frequencies of 1200, 2000 and 2800 MHz. The coupler response matches this, however since the geometry is not fully representative of an ideal quarter wave transformer, i.e. concentric transmission line without other geometries which act as perturbing lumped elements, some deviation is expected. This deviation was also seen at the fundamental rejection filter which was tuned to 400 MHz by changing the length from the coupling section to the connection of the inner and outer conductors.

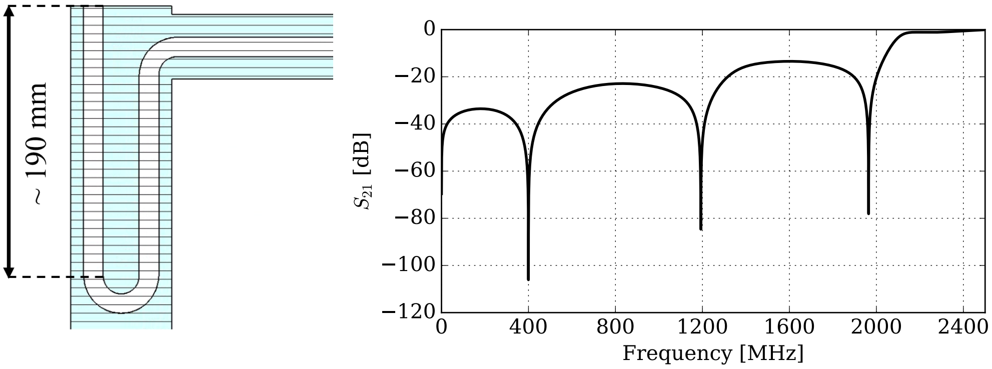

(a) Vacuum model.

(b) Normalised S_{21}.

Figure 5.30: Alternative HOM coupler concept.

5.8.2 Design

A capacitive output coupling was added to relax any mechanical stress imposed on the ceramic window. The capacitance also further reduces the damping at low frequencies as it acts as a first order high-pass ladder filter. Since the high field from the rejection filter at the fundamental mode is now after the gasket location, a 'field-shield' was necessary. Mechanically, this is achieved by reducing the outer diameter of the coupler and inserting an over-length into the cavity port. This feature creates another quarter-wave rejection filter which should be placed at a frequency location where there is no detrimental HOM.

The coupler cross-section is shown in Fig. 5.31 alongside the three impedance spectra (labelled 'Nominal').

Both the longitudinal and transverse impedance spectra are within the specified tolerance. However, the longitudinal HOM (at 960 MHz) close to the 24^{th} bunch spacing harmonic of the HL-LHC filling scheme has a longitudinal impedance of $\sim 35\,\mathrm{k\Omega}$. Referring back to the RF optimisation goals detailed in Sec. 5.4, this value is seven times larger than that of the LHC DQW HOM couplers. Hence, the worst case power would be over the 1 kW threshold. It is difficult to significantly decrease the quality factor of this mode with the coupler geometry. If the bottom couplers were moved to a magnetic maxima of the 960 MHz mode[1], the quality factor could feasibly be decreased by a factor of three, but this would still be ~ 2.5

---

[1] Currently it is only the top coupler which couples to this mode.

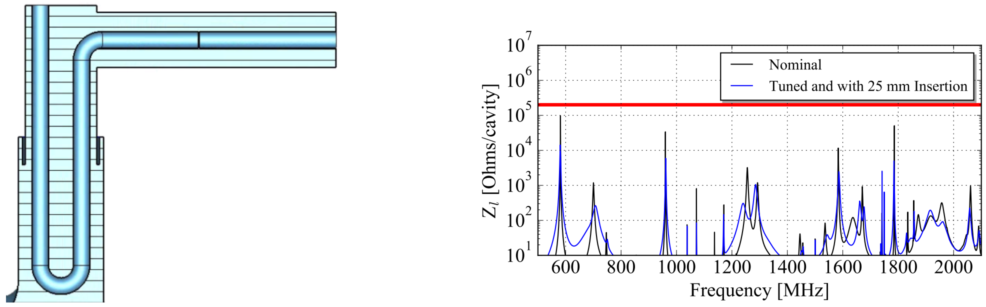

(a) Coupler vacuum geometry with capacitive output.

(b) Longitudinal.

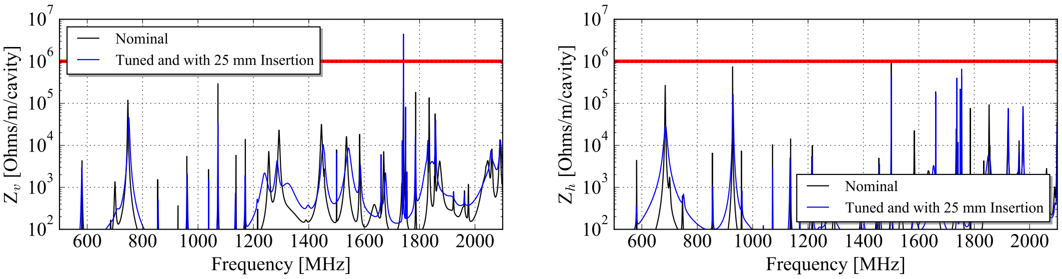

(c) Vertical.

(d) Horizontal.

Figure 5.31: DQW Impedance Spectra with the alternative quarter wave rejection HOM coupler.

times that of the LHC DQW HOM couplers and would sacrifice coupling to other HOMs.

By inserting the couplers further into the cavity, it is possible to increase the coupling. The decrease in longitudinal impedance of the 960 MHz mode as a function of relative insertion depth is shown in Fig. 5.32. A value of 25 mm was chosen to provide a simular damping to the high power mode as the LHC DQW HOM couplers. The broadband impedance spectra with the new insertion is shown in Fig. 5.31.

Note, the rejection filter was also tuned using the length of the quarter-wave resonator and the length of the couplers on the underside of the cavity were made shorter than the top coupler by ~ 0.5 mm. This is because the location at which the fundamental mode couples to the these HOM couplers differs with the angular alignment. Hence, the electrical length of the quarter-wave resonator is slightly different. The impedance spectra is lowered in all cases with the further insertion

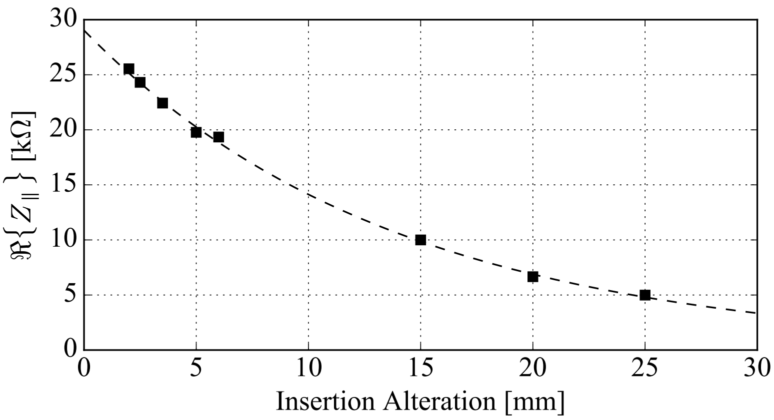

Figure 5.32: Effect of further inserting the alternative HOM coupler on the longitudinal impedance of the 960 MHz mode. The squares are the simulated values and the dashed line is an exponential fit.

except for a vertical mode at ~ 1740 MHz. This is a result of the $\lambda/4$ resonance harmonic shift. The impedance is five times larger that the threshold.

5.9 Coupler Comparison

A contour plot of the field at the fundamental mode frequency is shown in Fig. 5.33.

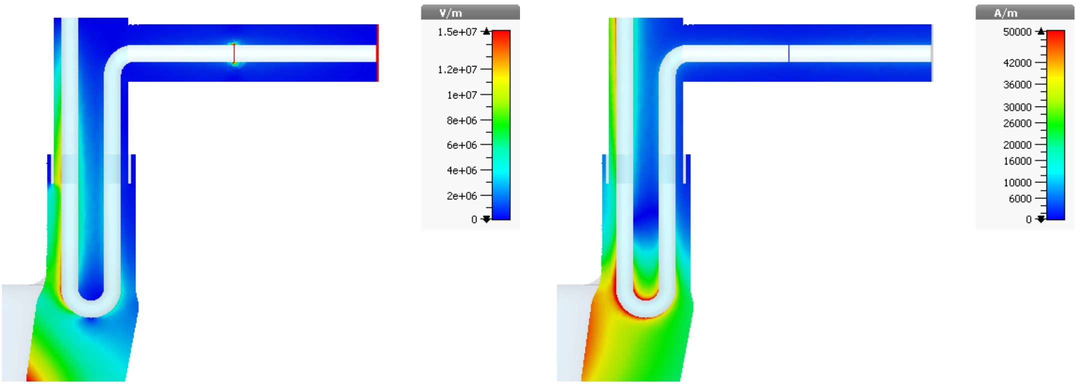

(a) Electric field.

(b) Magnetic Field.

Figure 5.33: Field profile at the fundamental mode frequency at $V_\perp = 3.4$ MV.

The operational characteristics of the DQW with the SPS, LHC and the alternative HOM couplers are shown in Tab. 5.7. Note, the first two couplers are referred to as ‘LC-rejection’ filters and the new design is denoted as the ‘quarter-wave rejection’ filter. The methodology and details of the peak temperature (T_{max}) and sextupole component of the fundamental mode (b_3) are not detailed until later in the thesis. However, to present a full comparative table for reference, they are presented here.

Inserting the alternative coupler loads the fundamental mode, increasing the frequency by $\sim 0.5\,\mathrm{MHz}$ and decreasing the loaded quality factor by over a factor of four. The peak fields move from the cavity wall to the surface of the HOM coupler. The crab cavity peak surface electric and magnetic field limits were set to 50 MV/m and 80 mT respectively [28, 125] to avoid a quench via field emission (E_{pk}) or heating (B_{pk}). The values are conservatively lower than limits achieved experimentally in accelerating cavities due to the lack of knowledge with high field axially asymmetric superconducting cavities operating in the deflecting mode. The LC-rejection couplers meet the specification, i.e. their surface field is less than that of the cavity’s which is within threshold, but for the quarter wave rejection coupler both the electric and magnetic peak fields are above the threshold. To reduce the electric field peak, the output capacitance was reduced by changing the gap from 0.5 mm to 2 mm. The operational characteristics of this coupler is also shown in the table. Increasing the gap reduces the electric peak field to less than that of the peak on the cavity surface. The magnetic peak is still on the coupler and is at the threshold. The loaded quality factor of the fundamental mode is also the same as that of the LC-rejection filter’s with the additional gap length, but the frequency still differs.

The temperature of the quarter-wave rejection coupler is very low due to the small distance from the inductive heating location and helium bath but the dissipated power from the fundamental mode is significantly higher than that of the LC-rejection type. The threshold for this value is 1 W from the technical specification, although in terms of operational efficiency it is feasible to go up to the 10 or even 100 W level. The dissipated power is reduced with the increased gap to around ten times lower than the threshold.

The main drawback of the quarter-wave rejection filter is the dynamic heat load on the gasket. The limit of the two cavity cryomodule is 25 W [17], for which the

Parameter	Unit	SPS Ancillaries	LHC Ancillaries	Alternative Coupler Gap = 0.5 mm	Alternative Coupler Gap = 2.0 mm
Fundamental Mode					
Frequency, f_0	MHz	400.45	400.45	400.97	400.91
Loaded Quality Factor, Q_l	-	5.2×10^5	5.2×10^5	1.2×10^5	5.2×10^5
Deflecting Voltage, $V_\perp$	MV	3.34	3.34	3.34	3.34
$r/Q_\perp$ [†]	Ω/m	424	428	428	427
E_{pk}	MV/m	37	37	71[*]	37
B_{pk}	mT	72	71	81[*]	80[*]
Accelerating Voltage, $V_\parallel$	kV	14.3	15.0	14.9	14.9
Stored Energy	J	10.3	10.2	10.3	10.3
$\Re\{b_3\}$	mT/m^2	496	497	345	N
Coupler Operation					
T_{max} (HOM coupler 1)	K	2.5	2.5	< 2.05	< 2.05
Dissipated Power	W	< 1 mW	< 1 mW	1.0 ± 0.5	< 0.1 W
Gasket heat load (HOM coupler 1)	W	< 1 mW	< 1 mW	4.5 ± 1.0	4.5 ± 1.0
Detrimental HOMs[◊]					
570 MHz: $Z_\parallel$	kΩ	77.1	5.6	‡	‡
590 MHz: $Z_\parallel$	kΩ	60.6	224[††]	16.6	114
686 MHz: $Z_{\perp h}$	kΩ/m	7.2	128	36.7	227
747 MHz: $Z_{\perp v}$	kΩ/m	1888	500	28.9	56.3
927 MHz: $Z_{\perp h}$	kΩ/m	4019	50.1	151	881
958 MHz: $Z_\parallel$	kΩ	99.9	4.6	5.1	22.8
1500 MHz: $Z_{\perp h}$	kΩ/m	197	1680	514	964

[†] Accelerator definition.
[*] On coupler geometry.
[‡] Not applicable, this mode is a result of the 'mode splitting' by the LC-rejection filter.
[††] Significant frequency reduction (~ 6.5 MHz) away from bunch spacing harmonic.
[◊] 200 kΩ and 1000 kΩ/m limits for the longitudinal and transverse impedances respectively.

Table 5.7: Benchmarking the alternative HOM coupler design against that of the SPS and HL-LHC DQW HOM couplers.

cavities account for ~ 5 W each. Hence of the 15 W left, using a factor of safety of 2 and assuming none of the other ancillaries and gaskets have a significant dynamic heat loads, the limit for the HOM coupler gaskets is 1.6 W. It is possible to decrease the heat load with the length of the 'field-shield' and the capacitive output but not in the order of a few Watts. To rectify this issue, indium gaskets could be used which would be superconducting at the operational temperature of 2 K. This would decrease the surface resistance by many orders of magnitude, removing any significant dynamic heat load. Current research into the use of superconducting seals is on-going [126–129], but significant effort into establishing the best implementation of a superconducting seal would be needed.

5.9.1 HOM Power Comparisons

Referring back to the HOM power analysis in Sec. 5.1 (Fig. 5.1) the worst case HOM power for each mode and the frequency shift required to produce this was assessed for the new couplers. This is shown in Fig. 5.34.

As previously discussed, the external quality factor of the 960 MHz mode is significantly reduced with the used of the LHC DQW HOM couplers and the resulting worst case HOM power is now below the threshold. Additionally, the first detrimental mode is reduced by over an order of magnitude in power and, although moving by nearly 20 MHz in frequency, is still $\sim$ 10 MHz away from a bunch spacing harmonic. Furthermore, the second high longitudinal impedance mode has moved 6 MHz further away from its nearest bunch spacing harmonic.

The only problematic mode for the alternative coupler design is the longitudinal mode at 960 MHz mode which is above the power threshold with an output gap of 2 mm. Further insertion would decrease this, but because the dynamic heat load on the gasket is too high, further optimisation of this coupler is limited by this bottleneck. There are no other high impedance longitudinal modes capable of generating over 1 kW within 19 MHz of a bunch spacing harmonic.

5.9.2 Conclusion and Future Work

The quarter-wave rejection filter has a good broadband damping and is much simpler to manufacture than the LC-rejection designs, reducing time and cost constraints. The peak temperature is also significantly lower and the dissipated power, whilst higher than the LC-rejection design and with a narrower stop-band, is within specification. However, the dynamic heat load on the gasket is too large and, although reduced by around four times using a ‘field-shield’, is too high for the cryogenics budget. The use of superconducting seals would alleviate this issue.

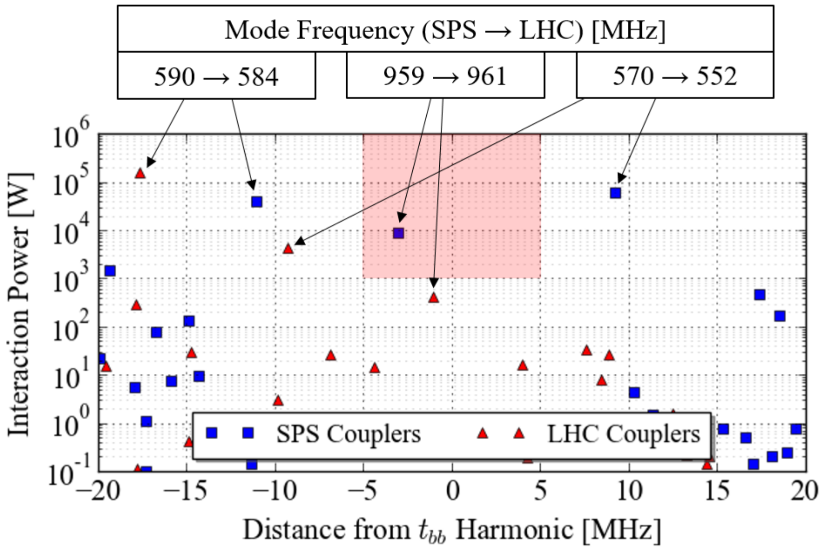

(a) LC Rejection Filters.

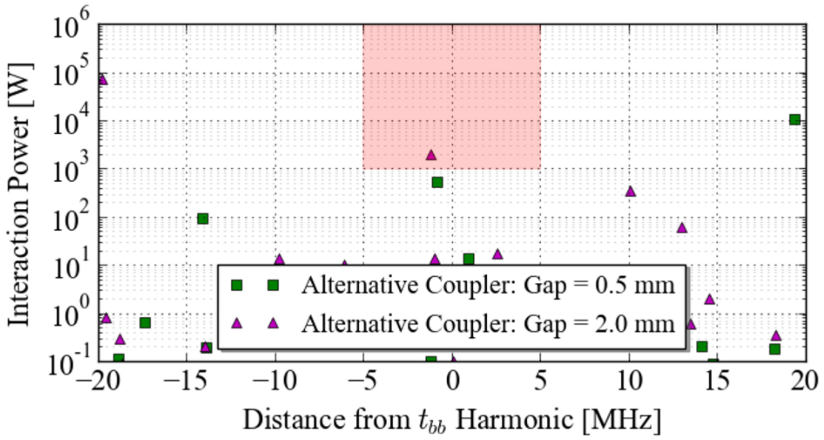

(b) Quarter-Wave Rejection Filters.

Figure 5.34: Power as a result of a mode interacting with the nearest bunch spacing harmonic, using HL-LHC beam parameters, as a function of the distance from the harmonic for both the SPS, LHC and alternative HOM couplers.

With reference to future work and contribution to the RF cavity community, this concept could be applicable for superconducting accelerating cavities. For example, the superconducting LHC accelerating cavities have cylindrical beam-pipes with diameters of 30 cm, tapering down to 10 cm. The cut-off frequency of the beam-pipes is lower than the first odd harmonic (as electrically open) of a

400 MHz quarter-wave transformer, i.e. 1200 MHz. Furthermore, the frequency spacing between the fundamental mode (400 MHz) and first HOM is ~ 300 MHz. The cavity modes and transmission of the coupler are shown in Fig. 5.35.

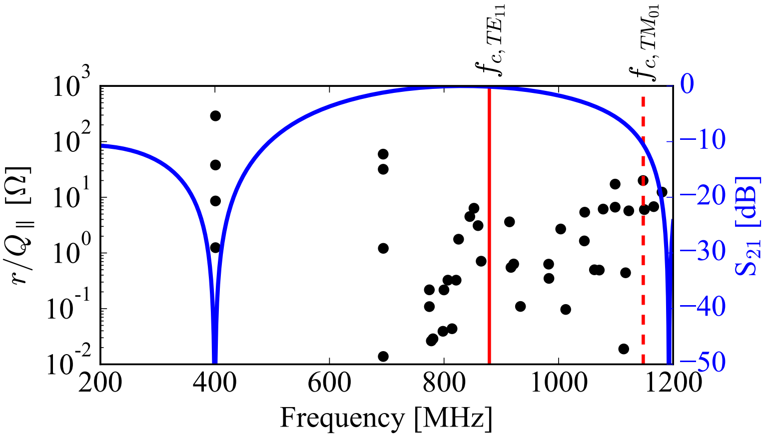

Figure 5.35: LHC accelerating cavity modes (4 single cells in one cryomodule) and coupler transmission characteristics. Cavity parameters provided by R. Calaga and I. Karpov (CERN).

Combining the simple inductive loops with electric probes would allow strong HOM damping with incredibly simple geometries that are both demountable. Furthermore, placing the couplers on the beam pipes would reduce the peak surface magnetic field from the fundamental mode and as such the heating and dynamic heat load would significantly reduce.

5.10 HOM Coupler Re-Design Conclusions

A new HOM coupler design for the HL-LHC DQW crab cavity has been presented in this chapter. The stages to arrive at this design are detailed hereafter.

- From impedance specifications defined in [108] and detailed HOM power simulations conducted in Chapter 4, a set of RF optimisation criteria was established for the DQW crab cavity HOM performance. Additionally, feedback received from the manufacturing of the SPS DQW HOM couplers detailed several mechanical optimisation criterion. For reference, the re-design goals are detailed in Tab. 5.8.

RF	Impedance threshold for transverse modes is 1 MΩ/m per cavity.
	Impedance threshold for longitudinal modes is 200 kΩ per cavity.
	Impedance threshold for the 960 MHz mode is 5 kΩ per cavity.
	Integrated HOM power limit is 500 W.
Mechanical	Reduce machining time by removing circular cross-section.
	Incorporate a planar weld at the joining point of the band-stop filter's inductive stub to its capacitive jacket.
	Lift the output line with respect to the base of the outer conductor.

Table 5.8: HL-LHC DQW HOM coupler design goals.

- Geometric alterations were firstly applied to meet the mechanical design goals. Following this, using the coupler's equivalent circuit detailed in Chapter 3 as well as parametric studies carried out in 3D electromagnetic modelling software (CST MWS [104]), two optimisation routes were trialled to meet the design goals. For the first route, a trade off between two 'bands' of low frequency modes was seen where both could not be sufficiently damped. Optimisation route two provided increased damping to every mode over the threshold using the SPS HOM couplers. Every mode was within the impedance threshold apart from two. The longitudinal mode at 960 MHz was within the specific threshold set for this mode and the integrated power, using stochastic mode sampling, was shown to be below the threshold even for the a pessimistic bunch profile approximation.

- The function of the hybrid beam-pipe pick-up (used to damp a high frequency mode and sample the fundamental mode) was split into two separate beam-pipe ancillaries. The same level of damping was achieved.

- The incorrect material used for the coupler's ceramic window was corrected and the effect of this quantified.

- Two geometric investigations were conducted to provide information on how to alter the frequencies and quality factors of the high power longitudinal mode (960 MHz) and the first high impedance mode (580 MHz). If problems with either of these modes arise in the manufactured cavities, the solutions presented can be incorperated with only the output line of the coupler; Removing machining or tuning efforts.

- An alternative coupler concept was designed and benchmarked with the SPS and LHC DQW crab cavity HOM couplers. The coupler was limited by the dynamic heat-load on the gasket. The applicability of this coupler for superconducting accelerating cavities was discussed and analysed for the LHC accelerating cavity. The applicability of this for CERN's 'Future Circular Collider' (FCC) concept should be examined in the future.

Chapter 6

HOM Coupler Impact on Fundamental Mode Operation

There are several operational considerations at the fundamental mode frequency for which cavity ancillaries, such as HOM couplers, can have a large impact.

6.1 Multipolar Analysis

Due to the geometric asymmetries of the crab cavities, the multipolar components of the fundamental dipole mode can be significant. The formulation of the multipole kick coefficients are defined in [57][1], where a thin lens approximation is used to decompose the electric and magnetic fields in a similar fashion to that done in the case of static magnetic fields. The effect of the HOM couplers and new beam-pipe pick-ups on the multipolar kicks should be quantified.

Here, the Panofsky-Wenzel and Lorentz-force decomposition methods are used to obtain the normal (b_n) and skew (a_n) multipole components. The coefficients can be expressed as

$$a_n = \frac{jn}{\omega\pi}\int_{-\pi}^{\pi}\frac{1}{r^n}sin(n\theta)\int_{-l/2}^{l/2}e^{\left(\frac{j\omega z}{c}\right)}E_z(r,\theta,z)\ dzd\theta \tag{6.1}$$

---

[1] The radial field distribution is approximated as r^n rather than represented as a Bessel function.

$$b_n = \frac{jn}{\omega\pi}\int_{-\pi}^{\pi}\frac{1}{r^n}cos(n\theta)\int_{-l/2}^{l/2} e^{\left(\frac{j\omega z}{c}\right)} E_z(r,\theta,z)\ dzd\theta \tag{6.2}$$

using the Panofsky-Wenzel decomposition method and

$$a_n = \frac{1}{qc\pi}\int_{-\pi}^{\pi}\frac{1}{r^{n-1}}sin(n\theta)\int_{-l/2}^{l/2} F_r(r,\theta,z)\ dzd\theta \tag{6.3}$$

$$b_n = \frac{1}{qc\pi}\int_{-\pi}^{\pi}\frac{1}{r^{n-1}}cos(n\theta)\int_{-l/2}^{l/2} F_r(r,\theta,z)\ dzd\theta \tag{6.4}$$

using Lorentz force decomposition. Note that, as detailed in Chapter 2, the monopole component is denoted by the coefficient 0.

As it is the normal multipole coefficient (b_n) which is of concern [17], Tab. 6.1 details the value of b_n for the quadrupolar, sextupolar and octupolar multipole kick coefficients for several stages of the DQW's design evolution. The RFD crab cavity's kick coefficients are given for comparison between the vertical and horizontal crab cavities.

	PW							
	b_1		b_2		b_3		b_4[a]	
	Re	Im	Re	Im	Re	Im	Re	Im
PoP DQW (Bare)	32	0	0	0	1061	1	63	455
SPS DQW (Bare)	33	0	6	-3	1527	19	521	-350
SPS DQW (Dressed)	33	0	6	-3	1508	23	560	-1027
LHC DQW (Dressed)	33	0	6	-3	1506	27	2106	-539
LHC RFD (Dressed)	33	0	0	0	-522	-56	-914	-36

	LF							
	b_1		b_2		b_3		b_4	
	Re	Im	Re	Im	Re	Im	Re	Im
PoP DQW (Bare)	32	0	0	0	1016	0	155	-238
SPS DQW (Bare)	33	0	6	-3	1486	24	660	-627
SPS DQW (Dressed)	33	0	6	-2	1498	19	1026	-383
LHC DQW (Dressed)	33	0	6	-2	1488	21	1048	-292
LHC RFD (Dressed)	34	0	0	0	-458	-74	128	55

Table 6.1: Evolution of b_n (in units of mTm/m^{n-1}) for the DQW crab cavity using both decomposition methods presented ($V_\perp = 10\,\mathrm{MV}$, $r = 30\,\mathrm{mm}$ and 64 azimuthal points).

---

[a] Not converged.

The multipole coefficients converge with the number of azimuthal points and evaluation radius. Additionally, the Lorentz force decomposition method converges faster than that of the Panofsky-Wenzel method. The results shown in Tab. 6.1 show a good agreement between the two methods for all components apart from b_4 ($\sim 5\%$ deviation). In the case of b_4, only the Lorentz Force decomposition method is converged.

Due to the symmetry planes of the two cavities, the values of the even multipoles are 'naturally' zero. As such, any contribution to these components is a result of either the cavity ports or the ancillaries. This is clear from the increase of b_2 and b_4 seen as a result of the evolution from the 'Proof-of-Principle (PoP) DQW (Bare)' design to the 'SPS DQW (Bare)' design. This step involved widening the HOM coupler ports and changing their locations on the cavity, creating a port asymmetry.

The limit for the sextupole component of the fundamental mode is $1500\,\mathrm{mTm/m^2}$ [17] and as such, the value following the evolution to the SPS design is within 2% of the limit. The HL-LHC ancillaries impose no change on the values and hence the design change with respect to the multipole components of the fundamental mode is acceptable.

For visualisation, the kicks can also be calculated as a function of the distance along the axis of charged particle propagation. The results of this calculation for the dressed HL-LHC DQW crab cavity are shown in Fig. 6.1, which clearly shows the locations of the areas which contribute to the higher order multipole components of the fundamental mode. Note, although still denoted as b_n, the units change as they are not integrated over the length of the cavity. For each component, two profiles are shown which represent the two decomposition methods used (detailed in Eqs. 6.1–6.4).

The $Re\{b_3\}$ value as a function of longitudinal distance is plotted in Fig. 6.2 for each of the DQW crab cavity evolution stages.

It can be seen that the profile of $Re\{b_3\}$ is not significantly effected by the ancillaries, but is most dependant on the cavity geometry.

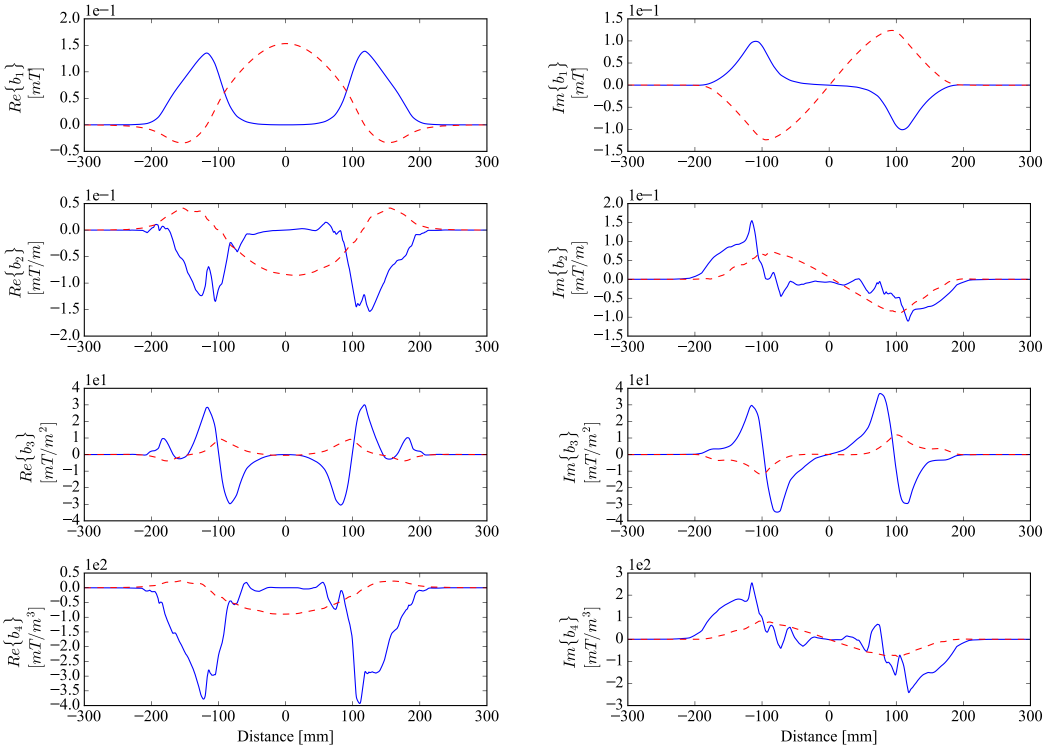

Figure 6.1: Value of b_n at $V_\perp = 10\,\text{MV}$ as a function of longitudinal position for the dressed LHC DQW crab cavity. The results are decomposed using both the Panofsky-Wenzel (blue line) and Lorentz Force (red dashed line) decomposition methods.

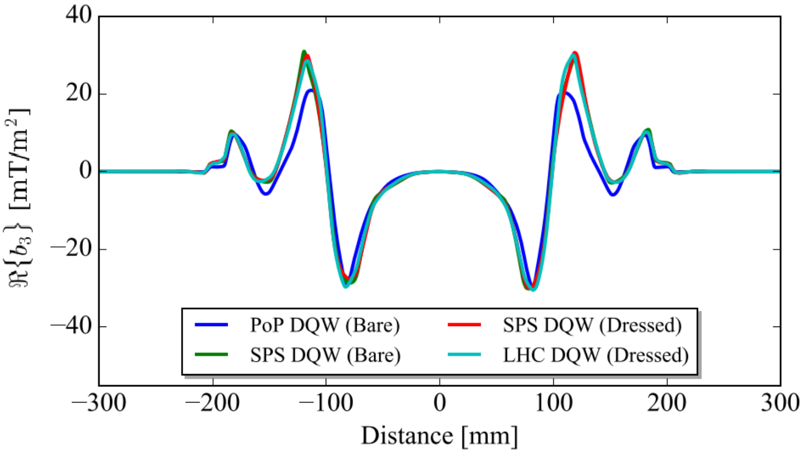

Figure 6.2: $Re\{b_3\}$ as a function of longitudinal distance for each of the DQW crab cavity evolution stages.

6.2 Multipacting

Multipacting as a result of the fundamental electromagnetic field is important to assess whether there are field levels for which the HOM couplers will prevent operation.

6.2.1 Introduction

Multipacting is described as an ‘avalanche-like’ growth of electrons [130]. The increase in electron population is a result of a resonant electromagnetic field which drives cyclical electron trajectories causing electrons to impact with metallic surfaces, which in turn causes electron emission. This phenomena can impose a field (and hence cavity voltage) limitation. An example of superconducting HOM coupler multipacting is presented for the XFEL prototype test stand at DESY [131].

The average number of electrons emitted per incident particle is a function of both the incident electron energy and material. It is quantified by the Secondary Electron Yield (SEY) of the material. Figure. 6.3 shows the SEY value as a function of incident electron energy for niobium with three treatments. The data was extracted from the material library included in CST MWS [104].

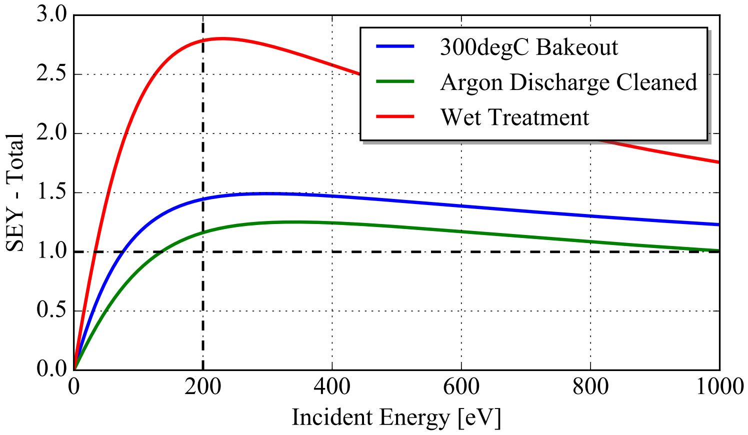

Figure 6.3: Secondary electron yield for niobium with various treatments.

The SEY value for niobium changes significantly with its treatment and is generally highest with incident energies of $\sim 200\,\mathrm{eV}$.

Multipacting is often descibed in two ways. The first is 'soft-multipacting' and the second 'hard-multipacting'. The former contributes to RF conditioning time which, if the multipacting is strong enough, can add multiple hours to the conditioning process. The latter imposes a performance limitation.

6.2.2 LHC DQW Analysis

Multipacting simulations on the top HOM coupler (visualisation shown in Sec. 2.4, Fig. 2.20c) were performed by coupling the Eigenmode and Particle In Cell (PIC) solvers in CST MWS. The solver uses the probabilistic emission Ferman-Pivi model [132]. The electron growth is represented by increasing the number of macro-particles whilst maintaining their charge. The solver varies the angle of emission, the angle of impact and the energies of the secondaries. The SEY value is also altered with respect to the impact angle [133].

The simulations were conducted several times, varying the incident electron emission point and carried out for a time greater than ten times the RF cycle at 400 MHz[1]. The emission faces chosen are shown in Fig. 6.4.

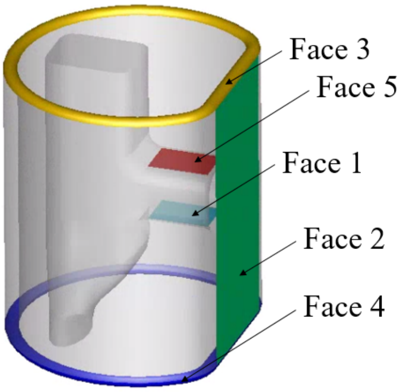

Figure 6.4: Particle area sources used for the multipacting analysis.

Figure. 6.5 shows the 'average SEY' $\langle SEY \rangle$ as a function of the cavity's transverse voltage for the five emission points. This variable is defined as the ratio of

---

[1] A simulation abort was set for the case where the exponential coefficient of the 'particles vs time' exceeded a given threshold.

the emission charge to the collision charge, representing the electron growth rate as a function of field level. The material used for the simulation was Niobium with a 300°C bakeout (see Fig. 6.3).

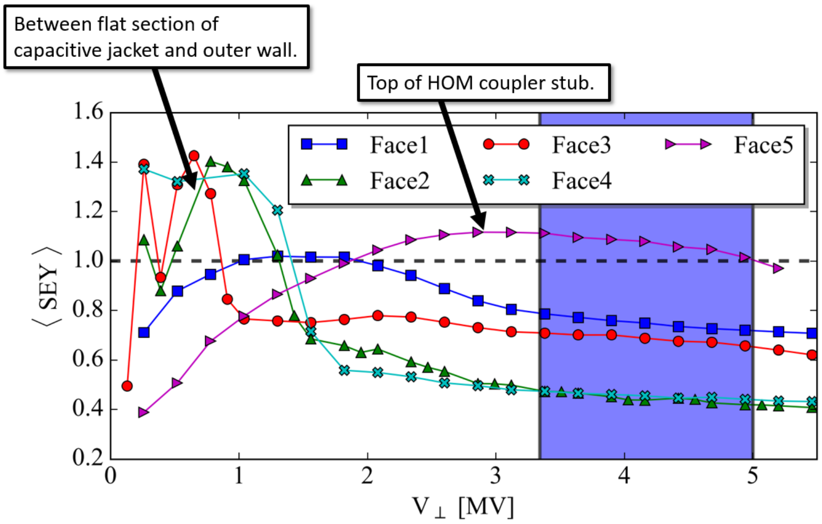

Figure 6.5: Average SEY variation with deflecting voltage for each of the faces detailed in Fig. 6.4 for the top HOM coupler. The transverse voltage range (‘nominal’ to ‘ultimate’ [17]) is highlighted. For reference, the geometric features at which the multipacting acts are described.

Generally, the average SEY is higher at low fields. Emitting the incident electrons from faces two, three and four, results in an avalanche-like growth at around 1 MV transverse deflecting voltage. Using particle position montiors in the simulations, the low field multipacting was seen between the flat section on the capacitive jacket and the outer wall. A visualisation of the periodic trajectory is shown in Fig. 6.6. The higher field multipacting, using ‘face 5’ as an emission point, was seen on the top of the inductive stub. The geometries are annotated in Fig.6.5.

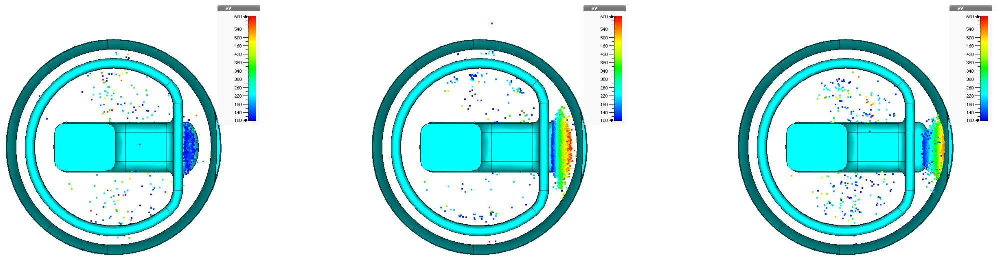

(a) $28ns$. (b) $+t_{RF}/5$. (c) $+2t_{RF}/5$.

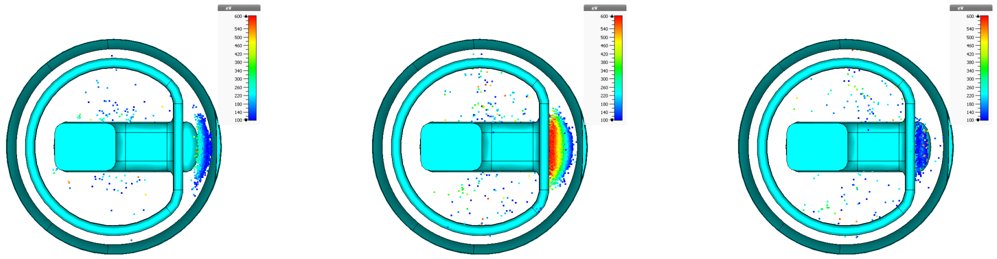

(d) $+3t_{RF}/5$. (e) $+4t_{RF}/5$. (f) $+t_{RF}$.

Figure 6.6: Macro-particle tracking to highlight the area of multipacting at $V_{\perp} = 0.75\,\mathrm{MV}$.

To illustrate the avalanche-like electron growth, the number of particles as a function of time was logged. The results of this are shown in Fig. 6.7 for two emission faces one and four.

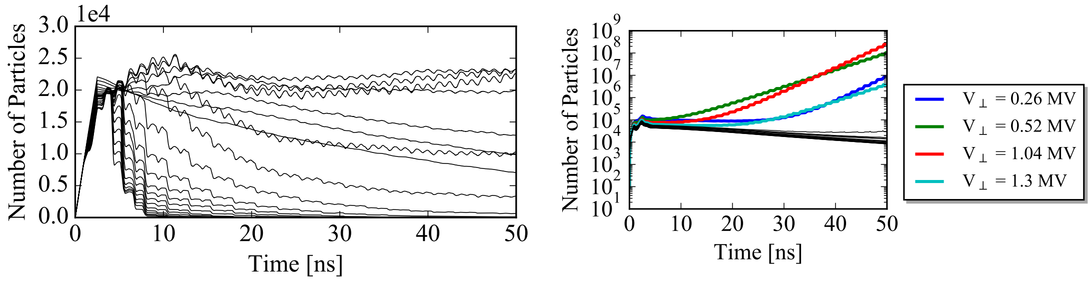

(a) Face 1. (b) Face 4.

Figure 6.7: Number of particles as a function of time for various transverse voltages. The two plots correspond to different emission faces (face one and face four - detailed in Fig. 6.4) on the top HOM coupler. Note, to the y-axis scales differ to highlight the magnitude of the electron growth.

From the average SEY calculations, using face one as an emission point did not return any values above one. Using face four, low field multipacting was seen at from $V_{\perp} = 0.25\,\mathrm{MV}$ to $V_{\perp} = 1\,\mathrm{MV}$. This is observable in the plot of particles against time; Avalanche-like electron growth occurs, and is highlighted, at the voltages where the average SEY is above one.

In addition to the average SEY, the impact energy from low field to the level corresponding to 5.5 MV transverse deflecting voltage was studied for the two coupler areas. This is shown in Fig. 6.8, for the same emission faces detailed in the particle against time plots (Fig. 6.7). The impact energy is shown as a function of transverse voltage using box-and-whisker plots. The standard deviation at each transverse voltage value represents the spread of the impact energies from the simulated data-set.

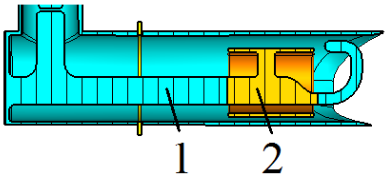

(a) Areas used to evaluate the impact energy.

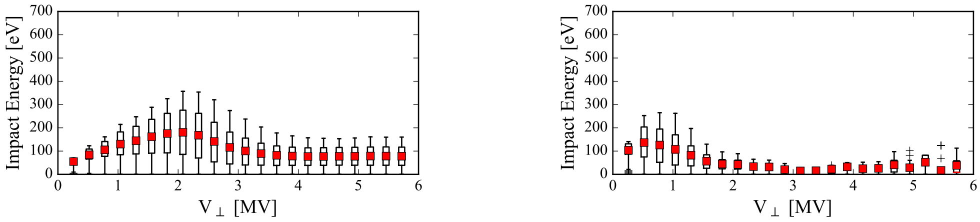

(b) Face 1 - area 1.

(c) Face 1 - area 2.

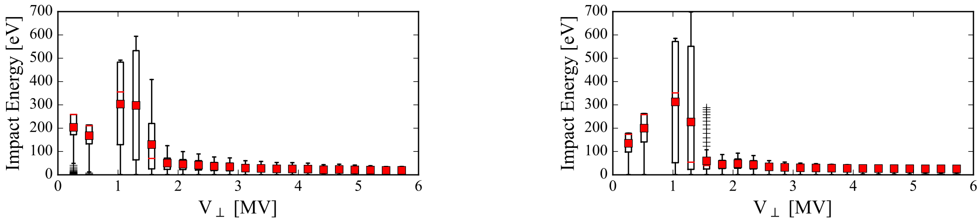

(d) Face 4 - area 1.

(e) Face 4 - area 2.

Figure 6.8: Impact energy on the top HOM coupler as a function of cavity deflecting voltage. The emission face (Fig. 6.4) is labelled in the caption alongside the area for which the impacts were monitored.

The plots show that at around $V_{\perp} = 1\,\text{MV}$ the average incident (or impact) energy of the electrons is between 200 and 300 eV. Referring back to the SEY curves displayed in Fig. 6.3, this incident energy corresponds to the peak SEY range.

6.2.3 Conditioning the Multipacting

To assess whether the multipacting observed on the LHC DQW HOM couplers is ‘hard’ or ‘soft’, i.e. whether it imposes a significant limit to the transverse voltage or whether it can be ‘conditioned’, a material with a lower SEY was used. By doing this, the effect that the RF conditioning process has on the material surface is taken into account, therefore establishing whether the multipacting persists through the conditioning.

This process was proven empirically for the SPS DQW HOM coupler. The coupler had a simulated average SEY higher than one (1.45) at a transverse deflecting voltage of $\sim 2.25\,\text{MV}$. The average SEY decreased to 1.24 (still greater than one) when the material was changed to the more optimistic ‘argon discharge cleaned’ (simulation results detailed in [134]). In the vertical tests of the dressed DQW cavity, multipacting was seen at this voltage, but was ‘conditioned’ away by gradually increasing the RF amplitude and pulse duration (method detailed in [105]) and a transverse voltage of 3.2 MV (i.e. lareger than the voltage at which the high average SEY was observed) was achieved [135].

As such, the material was changed to ‘argon discharge cleaned’ niobium, for which the SEY (shown in Fig. 6.3) reduces by around 25%. A plot comparing the average SEY for the $\sim 1\,\text{MV}$ multipacting and stub multipacting using the two materials is shown in Fig. 6.9.

In both cases, the average SEY drops below one. This suggests that the multipacting can be conditioned away with RF conditioning procedures and as such both cases are classed as ‘soft-multipacting’.

6.2.4 Removing the Low Field Multipacting

Analytically, it is possible to predict the distance between parallel plates for which multipacting is feasible at a given electric field. On the flat section of the jacket,

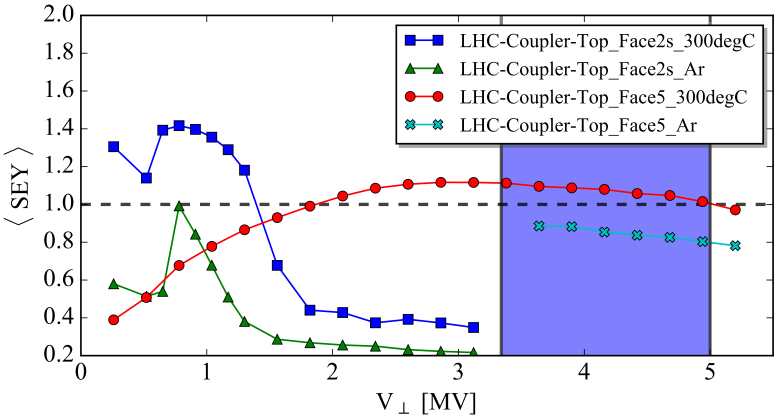

Figure 6.9: Effect of changing to argon discharged cleaned niobium on the multipacting surfaces.

the distance to the outer wall at 2 K is in the range 6.1–9.2 mm. At a cavity stored energy of 1 J, which corresponds to $V_{\perp} = 1.04$ MV, the electric field in the area of multipacting is in the range $\sim$ 100–200 kV/m. Referring to the multipacting tables shown in [136], for which one is shown in Fig. 6.10, the likelihood of multipacting using a parallel plate analogy can be evaluated.

The gap size of 3 mm, annotated as the 'uniform jacket' line on the plot at $f \times gap = 0.4 \times 3 = 1.2$, shows low field multipacting only. The larger gap size, between the flat section on the capacitive jacket and the outer wall has a strong chance of multipacting if the field is between $\sim$ 150 and 250 kV/m. This range corresponds to the field at 1 J and can possibly explain why multipacting is observed around $V_{\perp} = 1$ MV.

To solve the multipacting, one of two options should be explored. The first is to shift the operating point on the 'electric field against gap' plot to a safer area. The best place would be around 5 GHz mm, meaning the gap would have to increase to 12.5 mm. The coupler's band-stop filter frequency would hence have to be tuned back to the frequency of the fundamental mode by increasing the inductance of the stub. Geometrically, these two alterations are feasible. The increased gap length would also reduce the electric field, hence operating in an area with a very small chance of multipacting at 1 J.

However, if the field reached 300 kV/m multipacting would occur. This would

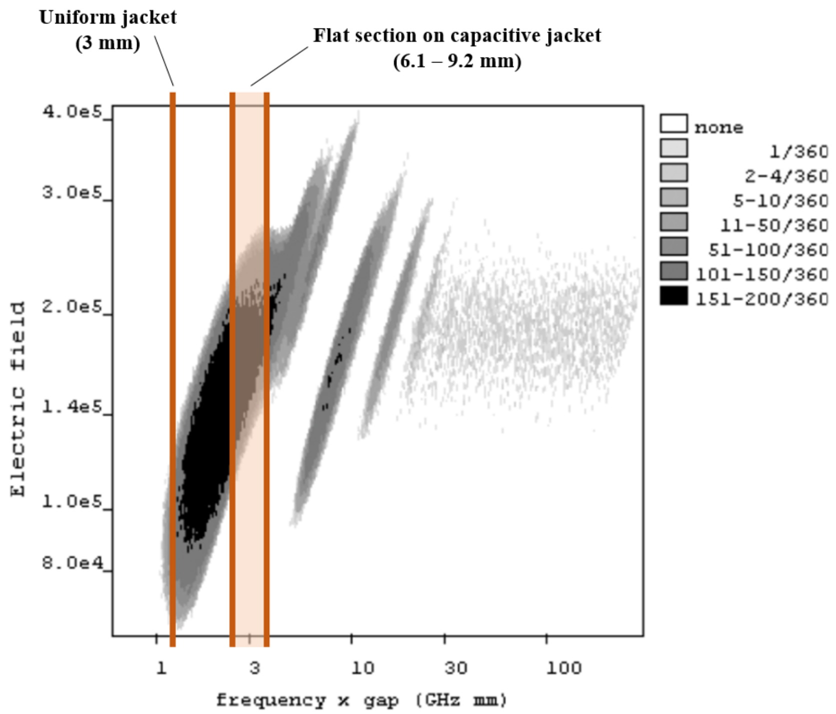

Figure 6.10: Number of starting phases that give multipactor. The plot is taken from [136] and is annotated with the gap lengths seen in both the SPS DQW HOM coupler and the LHC version with the flat section on the capacitive jacket.

be at a higher voltage than before as a result of the lower electric field associated with a 12.5 mm gap. This solution therefore only pushes the multipacting to higher voltage which could be even mode detrimental.

The second option is the use of ‘grooves’ at the multipacting area [137]. Conceptually, this would provide an area where the electric field has a different magnitude and an area which could perturb the trajectory of any emitted electrons as well as the impact angle. This would perturb the resonant behaviour and could stop the avalanche-like electron growth.

Figure. 6.11 shows the electric field on the capacitive jacket with and without grooves.

The resulting average SEY for the $V_\perp = 1\,\mathrm{MV}$ multipacting for each of the three jacket geometries shown in Fig. 6.11 are shown in Fig. 6.12.

Neither of the two types of grooves have a significant effect on the amplitude of

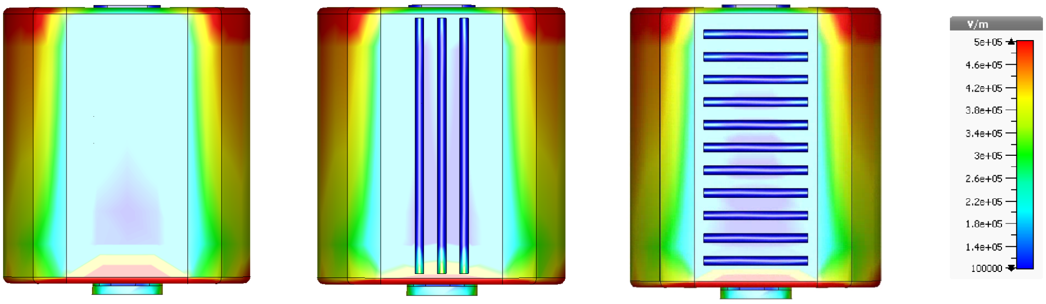

Figure 6.11: Electric field on the capacitive jacket without grooves (left), with vertical grooves (middle) and with horizontal grooves (right).

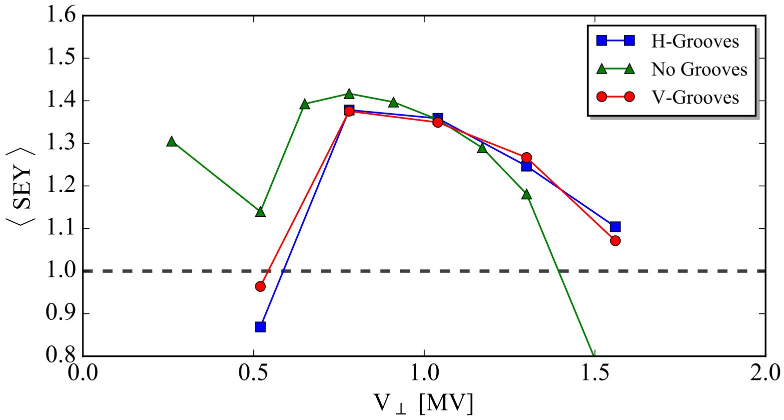

Figure 6.12: Effect of grooves on the low field multipacting.

the average SEY and positively shift the field range over which multipacting occurs. In conclusion, these grooves make little difference to the low field multipacting. A comprehensive study on groove geometry and dimensions could be carried out in order to reduce the multipacting. However, since the multipacting is in the centre of the flat section on the jacket, it is hard to 'deflect' the trajectories of the secondaries outside of this area. Furthermore, as discussed in Sec. 6.2.3 (with evidence from cold test measurements) and shown in Fig. 6.9, the multipacting can be conditioned away.

6.2.5 Comparison with the SPS DQW HOM Coupler

The previous HOM coupler design (SPS DQW HOM coupler) multipacts on the inductive stub, specifically on the bottom HOM coupler[1]. As such, simulations on the bottom LHC DQW HOM coupler were performed and the results compared to that of the SPS DQW HOM coupler[2]. The average SEY is shown in Fig. 6.13.

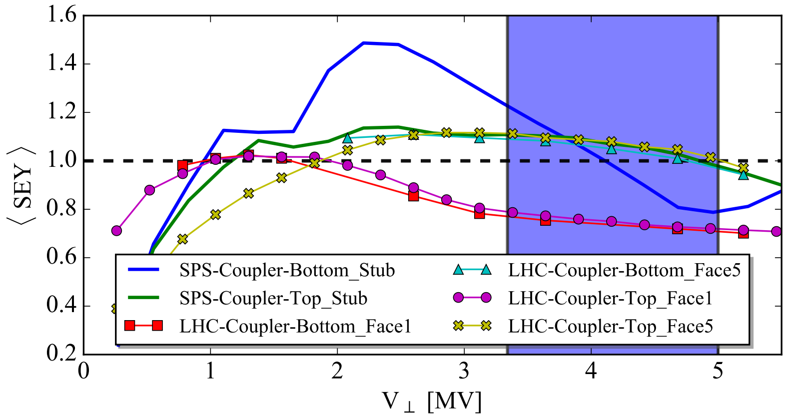

Figure 6.13: Multipacting comparison between the SPS and LHC DQW HOM couplers.

Referring to the top HOM coupler, the average SEY for the SPS and LHC case are very similar. For the bottom HOM coupler, the average SEY has reduced significantly with the use of a square stub section.

A dressed cavity (with SPS DQW HOM couplers) transverse voltage of 3.2 MV was reached at CERN, meaning that the multipacting seen on the bottom HOM coupler in Fig. 6.13 (SEY $>$ 1.4 at 2.5 MV), did not act as a hard barrier to operation. This strengthens the argument that the multipacting seen on the LHC DQW HOM couplers (flat-jacket section at SEY $=$ 1.4) can be ‘conditioned’.

---

[1] Noting that the bottom HOM couplers have slightly different field profiles to the top but have near identical field levels to one another. See Fig. 4.1a for visualisation.

[2] Provided by G. Burt.

6.3 Thermal Behaviour at the Operating Field

Evaluating the thermal behaviour of the coupler as a result of the fundamental field at the operating voltage allowed the risk of a thermal quench to be evaluated.

6.3.1 Introduction

Heating of the coupler occurs due to the magnetic field of the cavity's fundamental mode. It is important to verify that the coupler does not reach a temperature greater than the superconducting transition temperature of niobium ($\sim 9\,\mathrm{K}$). The magnitude of the field varies with the surface resistance (R_s) of the material and the temperature is determined by the thermal conductivity (k) and the distance from the helium bath. Both parameters R_s and k are a function of temperature. The surface resistance of the material can be written as

$$R_s = R_{BCS} + R_{res} \tag{6.5}$$

where the BCS resistance R_{BCS} comes from the BCS theory of superconductivity (Chapter 2, Sec. 2.1.4 and from [39]) and the residual resistance R_{res} is a material specific parameter which is normally between 5 and $50\,\mathrm{n\Omega}$. The BCS resistance is given as

$$R_{BCS} = \frac{0.0002}{T} \times \left(\frac{f_{GHz}}{1.5}\right)^2 \times \exp\left(\frac{17.67}{T}\right) \tag{6.6}$$

and the surface resistance of Niobium as a function of temperature is shown in Fig. 6.14.

The thermal conductivity of niobium as a function of temperature was collected from literature and is shown in Fig. 6.15. This parameter is also dependant on the Residual Resistance Ratio (RRR) [32] value of the niobium. The value of the sample used for all cases was 300[1].

---

[1] Standard 'high-quality' niobium bought for SRF cavities at CERN.

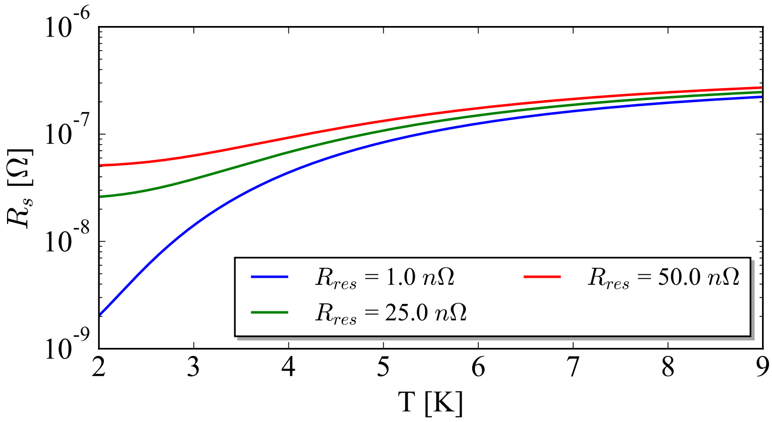

Figure 6.14: Surface resistance of niobium as a function of temperature for various residual resistance values.

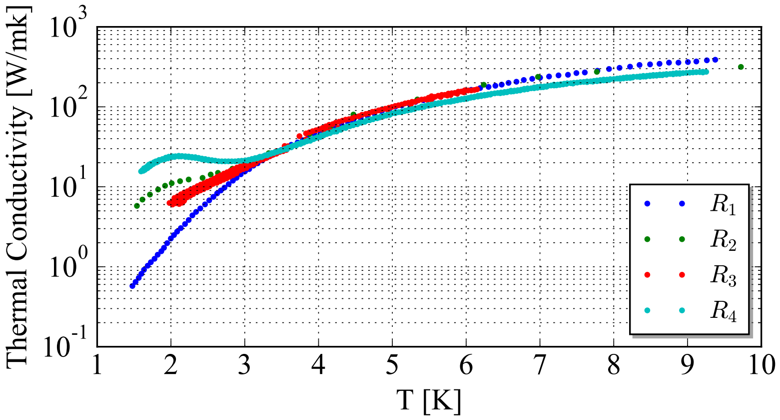

Figure 6.15: Thermal conductivity of niobium (RRR = 300) as a function of temperature. R_1 and R_2 refer to data presented in references [32, 138] respectively and the last two curves are from [139] (R_3 is 'as received' and R_4 is with a 100 µm BCP and baked).

6.3.2 Simulations

Assuming a residual resistance of 50 nOhms, the surface resistance is 51 nΩ (R_{res} is negligible) at 2 K. The normal conducting equation $\sigma = (\mu_0 \pi f) / (R_{BCS}^2)$ was used to change the surface resistance into a quantity for use in CST MWS. The electrical conductivity in units of S/m is given by σ and f is the frequency in Hz. This assumption allows the real part of the losses to be calculated, i.e. heating as a result of the magnetic fields, but neglects the reactive part. The electromagnetic field at the frequency of the fundamental mode was simulated in CST MWS and scaled to that of $V_\perp = 3.4\,\mathrm{MV}$. The resulting heat flux, in $\mathrm{W/m^2}$, was used to simulate the steady state temperature increase in both CST MWS and ANSYS [72]. The thermal conductivity curve labelled as 'R_2' in Fig. 6.15 was used as the curves 'R_2' and 'R_4' corresponded to the Niobium treatments applied to the crab cavity HOM couplers but the prior represented a pessimistic approach. As such, a thermal conductivity of 11 W/mK was assigned.

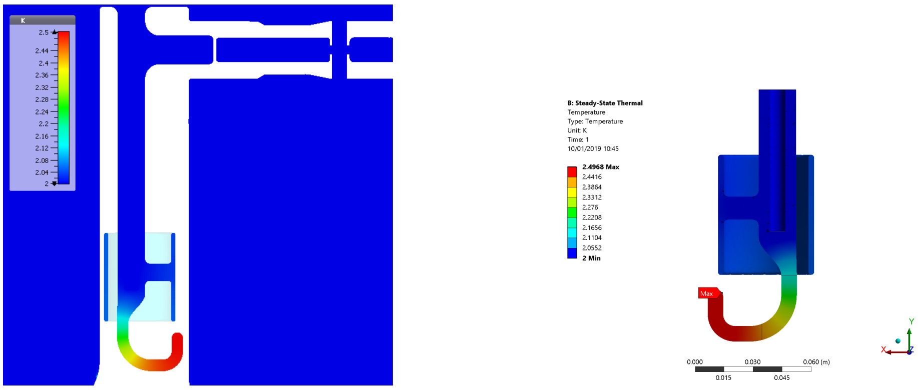

(a) CST MWS.

(b) ANSYS.

Figure 6.16: Temperature contour plots corresponding to a steady state simulation for $V_\perp = 3.4\,\mathrm{MV}$ performed in two solvers for benchmarking purposes.

The ANSYS cross section shows the 'cooling channel' which is filled with 2 K superfluid helium. The temperature profiles from both solvers are very similar and both have maximum temperatures of 2.50 K. Although the highest magnetic field is located on the section of the hook with the large bend radius, the highest temperature is located on the tip of the hook as a result of this being the largest distance from the helium bath and as such the point of least conductive cooling.

As discussed, the increased temperature of the coupler means that the physical properties of the material, i.e. R_s and k, also change. As such, an iterative approach to the thermal analysis is necessary[1]. The peak temperature of the

---

[1] Ideally, the material properties of each of the simulation mesh elements would be altered to reflect the new temperature of that element. However, it was not possible to do this in the current simulation suite and the method presented here represents a pessimistic approach.

coupler could be used to calculate the new properties. However, this approach is too pessimistic as the temperature gradient is only seen on the hook section an decays quickly in the direction of the helium bath. As such, the model was split into four elements, Fig. 6.17, each having different material properties.

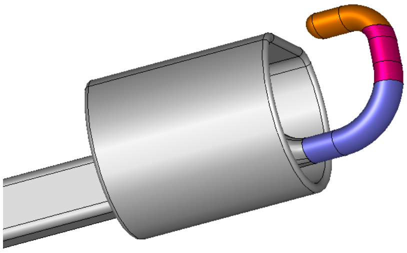

Figure 6.17: HOM coupler sections for the iterative thermal simulations. The jacket and inner conductor section is referred to as 'section 0' progressing to the tip of the hook which is 'section 3'.

The material properties of each section were altered in accordance with the average steady state temperature value. Fig. 6.18 shows temperature evolution of each section until convergence is reached.

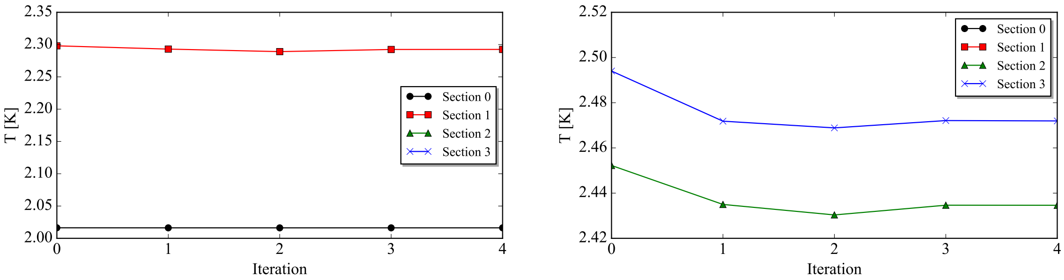

(a) Sections 0 and 1.

(b) Sections 2 and 3.

Figure 6.18: Average section temperature evolution with material property iterations at $V_\perp = 3.4\,\mathrm{MV}$.

Following the first simulation, the temperature of each section decreases. This is a result of the now increased thermal conductivity, allowing more efficient heat extraction to the helium bath. Convergence is met after five steady state simulations.

As the converged temperature is far from 9 K, i.e. the superconducting transition temperature of niobium, with a pessimistic approach to the thermal analysis the HOM couplers are not at risk of causing a thermal quench and as such posing as a field limitation up to $V_\perp = 3.4\,\mathrm{MV}$.

Furthermore, as the power deposited on the hook at the nominal field level is 3.4 mW, the power per unit cross section of the inner liquid helium tube is $6.8\,\mathrm{mW/cm^2}$. This is three orders of magnitude lower than the limit (around $1\,\mathrm{W/cm^2}$ [140]) for which liquid helium can extract the heat load.

6.4 Conclusion

The impact of the LHC DQW HOM coupler on the crab cavity operation at the fundamental mode was evaluated in three main areas:

Multipoles

- The multipolar kicks were evaluated for the DQW and RFD crab cavities. There is no effect of the new DQW HOM couplers on the higher order multipoles of the fundamental mode.

Multipacting

- Multipacting a function of transverse deflecting voltage was evaluated. Multipacting was seen as a result of the newly added ‘flat-section’ on the HOM coupler’s capacitive jacket.
- Using a material with a lower SEY, the multipacting was shown to be ‘soft’ and as such can be removed with RF conditioning.
- The effect of both a change in jacket geometry and the addition of ‘grooves’ was investigated.
- A comparison with the SPS DQW HOM coupler showed that multipacting previously seen on the bottom HOM coupler’s inductive stub was removed with the square profile.

Thermal

- For pessimistic values of the surface resistance and thermal conductivity, the temperature of the couplers was shown to be far from the critical temperature of Niobium (9 K).

Chapter 7

DQW Test in the SPS

As discussed in Chapter 3, the DQW crab cavity was scheduled for tests in the Super Proton Sychrotron[1] (SPS). The test aims were to identify any unforeseen risks and to demonstrate operational reliability, machine protection and cavity transparency [17]. Overviews of the tests with the main results are shown in [141, 142]. Images of the installation are shown in Fig. 7.1.

As part of the tests, since it was the first time that superconducting crab cavities would be used for proton bunches, the HOM performance was of significant interest. Specifically, the main areas for investigation and measurement were:

- To identify any unforeseen operational issues arising from the HOMs.
- To quantify the effect of the geometric deviations arising from manufacture on the HOM characteristics and performance.
- Ensure HOM performance with proton beam is predictable, thus validating the HOM simulations for the HL-LHC.

To validate the performance, measurements of the power coming from each of the HOM couplers for various beam parameters were taken. Two main beam parameter categories were used: Single bunch and multi-bunch.

The single bunch measurements were taken over large frequency bandwidths (broadband) to evaluate the form of the HOM spectra and over small bandwidths (narrowband) to evaluate high impedance modes in detail.

---

[1] CERN's 7 km proton synchrotron.

For the multi-bunch measurements, the predictability of the HOM characteristics with different ‘filling schemes’ was assessed.

Finally, transverse modes were investigated by taking ‘off-axis’ measurements to evaluate whether the assumptions made in simulations are valid.

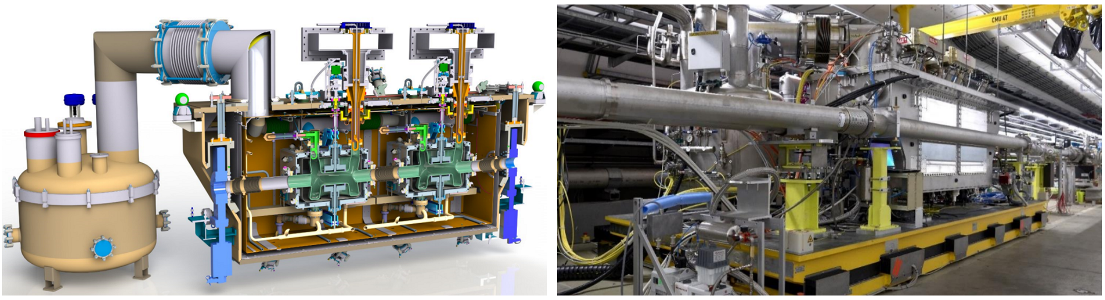

(a) CAD render. (b) Photograph of the installation.

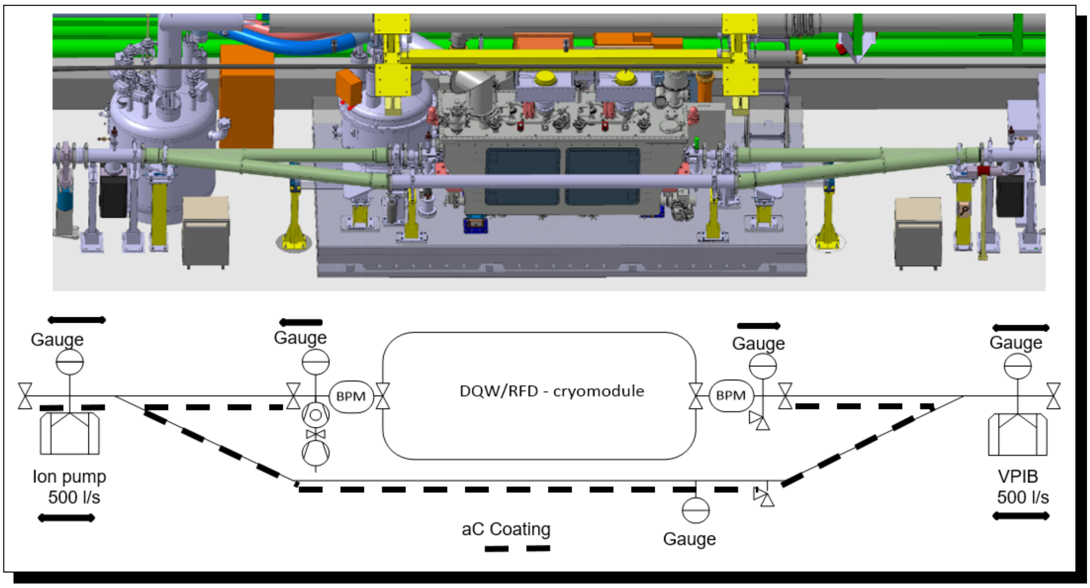

(c) Schematic of the installation. Image from [143]

Figure 7.1: DQW crab cavity cryomodule installed in the SPS tunnel for tests.

7.1 HOM Measurement Set-Up

To measure the HOM characteristics, a test stand in the ‘BA6’ Faraday cage[1] was developed. An image of the test stand is shown in Fig. 7.2.

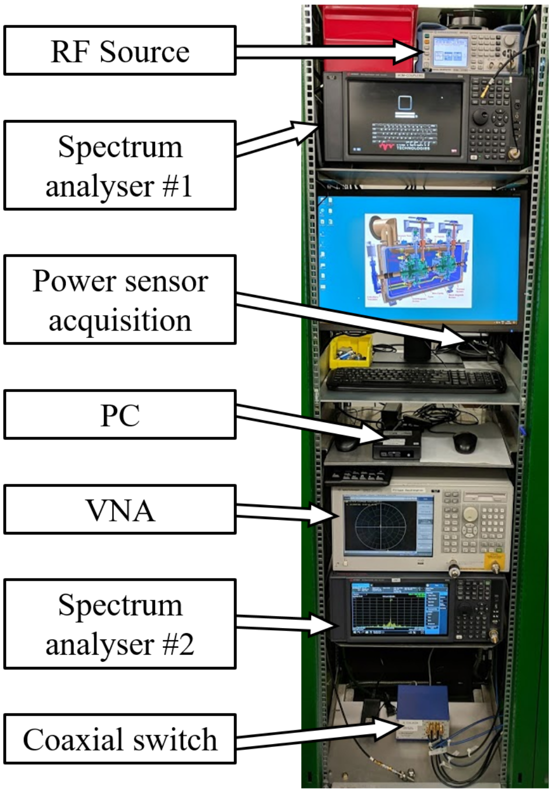

Figure 7.2: HOM measurement rack in the ‘BA6’ Faraday cage.

Spectrum analysers and Vector Network Analysers (VNAs) were the main instruments used for the HOM measurements. They are situated over 150 m above the cavities located in the SPS tunnel. Coaxial cables connect each of the HOM couplers, pick-ups and RF drive signals (forward and reflected) to a patch panel on the Faraday cage wall. The HOM coupler signal is split using 20 dB directional couplers, where the ‘through line’ is connected to a patch panel inside the Faraday cage and the ‘coupled line’ is sent to a fast acquisition power sensor to provide an interlock in the case that the integrated power rises above 250 W. The six HOM coupler patch panel signals were connected to a coaxial switch with six inputs and

---

[1] Faraday cage located at point ‘BA6’ of the SPS.

one output. The single output could hence be connected to a measurement device and the signal shifted between the six HOM couplers. All inactive ports on the coaxial switch are terminated at 50 Ω.

To accurately measure the HOM characteristics at the cavity, the cable attenuations were measured up to each of the measurement points located in the Faraday cage. For the HOM coupler cable measurements, an RF signal of known frequency and amplitude was sent from the point at which the cable connects to the cryomodule's HOM coupler output, through all of the cabling infrastructure (including the RF switch) and measured on the spectrum analyser. The calibration was performed at multiple frequencies and the resulting cable attenuations are shown in Fig. 7.3.

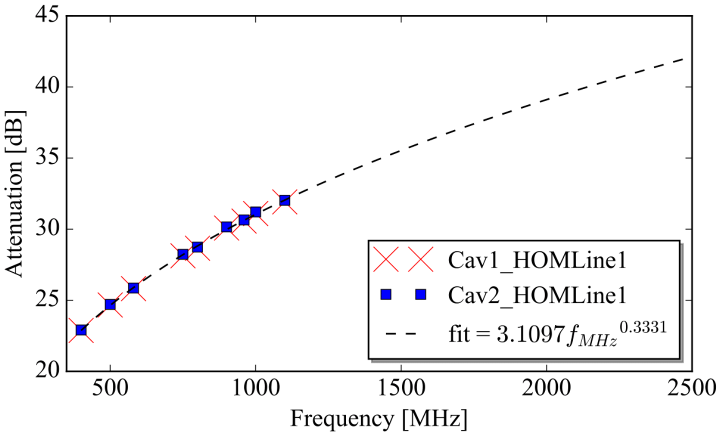

Figure 7.3: Attenuation measurements and fit.

7.2 Generating a 'Measured' Impedance Spectra

As discussed, the method employed to characterise the higher order mode parameters was to measure the power from each HOM coupler over various frequency ranges using a spectrum analyser. To provide an analytic power spectra for comparison, the equation for power, presented in Chapter 4, should be referenced. This is given by

$$P_{\|} = J_A^2 \sum_{-\infty}^{\infty} Re\left\{Z_{\|}(k\omega_0)\right\} |J_k|^2 \tag{7.1}$$

where J_A is the average beam current, k the integer value representing the revolution harmonic, ω_0 the angular revolution frequency and J_k[1] the normalised Fourier harmonic of the beam current. From the machine parameters and filling scheme, the values of J_A and J_k can be computed. For the longitudinal impedance however, although the simulated HOM parameters could be used to form the impedance spectra, the HOM frequency and quality factors had already been measured (detailed in Chapter 4). As such, the longitudinal impedance spectra was computed for each cavity, using the measured HOM parameters. The resultant spectra are shown in Fig. 7.4 and compared to the simulated case.

Referring to the broadband impedance spectra shown in Fig. 7.4a, the deviations of the measured HOM parameters from the simulated were evaluated extensively in Chapter 4. The main conclusions made were:

- Large increases in the frequencies of the first four HOMs and a number of HOMs around 1.65 GHz.
- Large increases in quality factors for the modes at 685 and 701 MHz (vertical and hybrid mode respectively).
- A shift in the frequency of the longitudinal mode at 960 MHz could result in a large power if 25 ns bunch spacing is used.

The low frequency modes and the high power mode are highlighted in Fig. 7.4b and 7.4c respectively.

---

[1] In literature, J_k is also referred to as the 'time structure' of the beam.

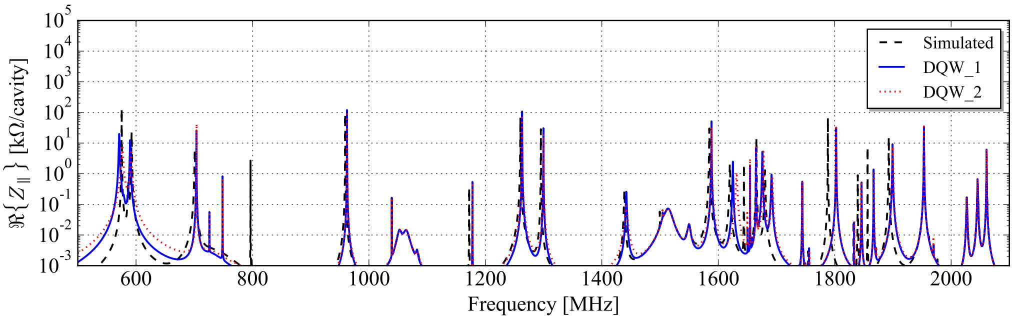

(a) Broadband.

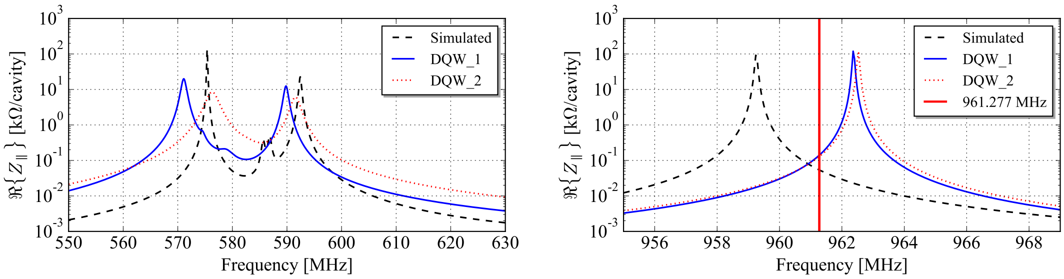

(b) Fist two high impedance modes.

(c) 960 MHz mode annotated with closest bunch spacing harmonic.

Figure 7.4: Simulated and altered impedance spectra for both cavities.

Notably, the longitudinal mode at 960 MHz has increased in frequency by 3.12 and 3.27 MHz respectively for cavity one and cavity two from that of the simulated values. Although a small sample size, the frequency increase is seen to be systematic. The increase is more than the spacing from the simulated frequency (959.3 MHz) to the frequency of the 24^{th} bunch spacing harmonic (961.3 MHz in the SPS, annotated in Fig. 7.4c). This shows that it is feasible for the mode to increase in frequency by the amount necessary for the worst case HOM power (+2 MHz).

7.3 Single Bunch Measurements

For the single bunch measurements, one bunch was circulated for multiple hours around the SPS. This method, referred to as ‘coasting’, provided very stable and reproducible conditions for HOM measurements.

Before detailing the measurements, the dressed DQW crab cavity is shown again, for reference and nomenclature, in Fig. 7.5.

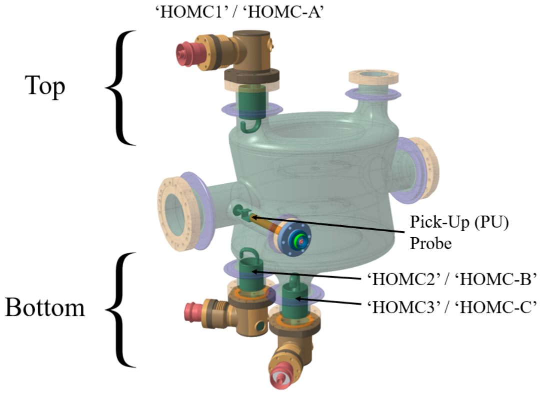

Figure 7.5: DQW crab cavity dressed with the HOM couplers and pick-up probe.

7.3.1 Broadband Measurements

Power spectra for cavity one and two, using the HOM coupler located on the top of the cavity, were measured using a spectrum analyser. Careful consideration of the analyser settings is necessary to return an accurate measurement. The set-up of the analyser is described hereafter.

The HOM power spectra is comprised of many discrete points at multiples of the revolution frequency (43 kHz for the SPS).

The spectrum analyser measures the integrated power after passing through a band-pass filter centred at a given frequency. The bandwidth of the filter is defined by the resolution bandwidth (RBW), set by the user. To ensure that the discrete samples are measured accurately, the RBW should be smaller than the signal spacing. As such, the RBW was set to a maximum of four times smaller than the revolution frequency (i.e. to ~ 10 kHz).

Reducing the RBW has a positive impact on the signal quality as it also acts to reduce the noise floor of the measurement. The noise floor is often referred to as the ‘Displayed Average Noise Level’ (DANL). The DANL reduces by $\sim 10\,\mathrm{dB}$ with a reduction in the RBW by a factor of 10. However, this comes at the expense of sweep time which is inversely proportional to the square of the RBW. Hence, there is a lower threshold dictated by the measurement time available.

The point spacing was set to equal the RBW to ensure that each discrete signal was within a measurement ‘bin’. Due to the sharp ‘shape-factors’ of modern sampling filters (detailed in [144]), the accurate amplitude of the discrete impulse is measured, regardless of its position within the ‘bin’. This concept was proved experimentally in the laboratory by measuring a 30 dBm signal from a vector signal generator (calibrated to the end of the SMA coaxial cable) and varying the frequency over two resolution bandwidths. At each frequency, the measured power was 30.00 dBm ± 0.01 dBm. With reference to the discrete signal within the filter, there is a maximum frequency error equal to half that of the resolution bandwidth, as the measured power is returned at the centre of the ‘bin’ (i.e. the signal is only seen in one bin regardless of its relative position within the bin).

To compare the measured spectra to the predicted power level, an analytical power spectra (Eq. 7.1) was generated for both cavities using a binomial bunch profile and the bunch parameters used in the coast. The binomial profile, detailed in Sec. 5.4.5 of Chapter 5, is shown in Fig. 7.6 for reference. The bunch length and μ-coefficient are varied to best represent the profile of the bunch in the SPS/LHC. The two variables are co-dependant. For the SPS, the value of μ is nominally 1.5 [121].

For the measurements, the bunch length was taken from CERN’s SPS bunch length measurement system (ABWLM[1]) [145]. To represent the measurement taken at the Faraday cage, the cable attenuation (Fig. 7.3) and a factor three ($10 \times log_{10}(1/3) = 4.77\ dB$) were subtracted from the analytic data-set. This makes the assumption that each cavity mode couples equally to each HOM coupler (i.e. the power is split equally between the three HOM couplers at each resonance). The measured and analytic spectra are shown in Fig. 7.7.

The plots show that for both cavities, the form of the power spectra and the

---

[1] ‘A (for RF) Beam Wideband Longitudinal Measurement’.

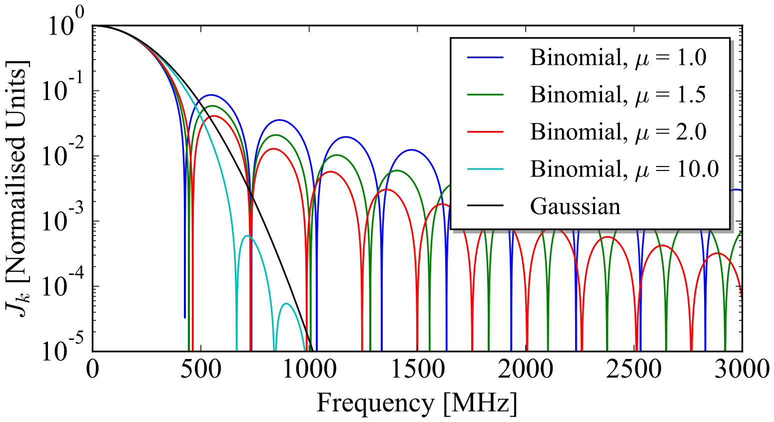

Figure 7.6: Binomial profile for different values of μ. An arbitrary bunch length (total) of 3 ns is used.

frequencies at which the high power modes are expected can be well predicted.

Referring specifically to the first seven high power modes seen in the plots (at $\sim$ 570, 590, 700, 750, 960, 1250 and 1300 MHz), there is an under-representation of the power from the analytic calculation for the first five modes whereas the last two match very well. In addition to the high impedance mode under-representation, there is a large, broadband impedance at $\sim$ 1.75 GHz. Even though this is relatively low in power, the disparity between the simulated and measured is an area of concern and the frequency is also close to the mode damped by the beam pipe pick-up (detailed in Chapter 4) and hence should be investigated further.
The four causes for lower power could be:

1. A misrepresentation of the form of the proton bunch (J_k, Eq. 4.3).
2. An error in the assumption that one third of the HOM power is seen at each HOM coupler (up to a 4.8 dB underestimation).
3. An underestimation of the impedance spectra ($\Re\{Z_{\|}\}$).
4. An error in the measurement signal (e.g. perturbation due to an RF filter).

Misrepresentation of J_k

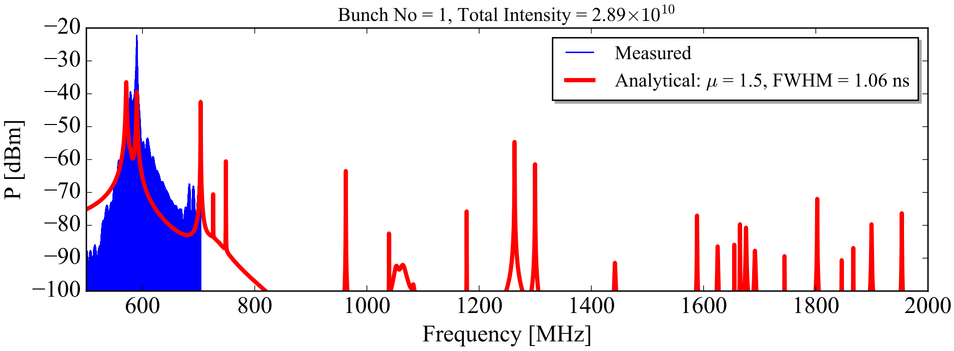

(a) Cavity one, HOM coupler one.

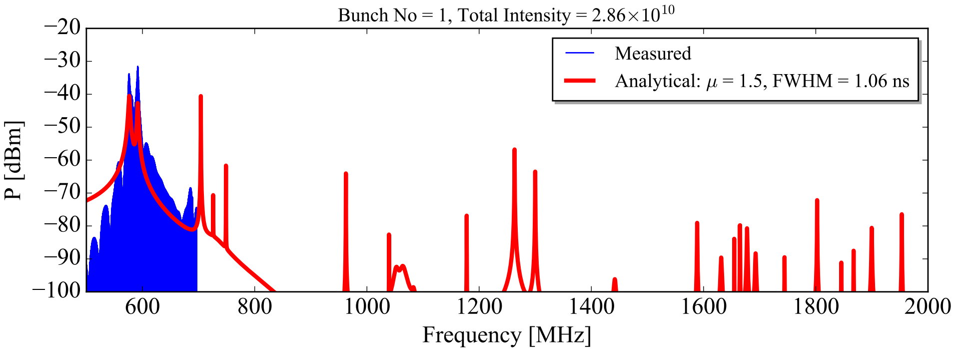

(b) Cavity two, HOM coupler one.

Figure 7.7: Measured and analytic broadband spectra at the Faraday cage (i.e. with cable attenuations and power splitting between ancillaries) for both cavities on the top HOM coupler, assuming that each mode couples equally to each of the three HOM couplers per cavity. The Full Width Half Maxima (FWHM) and μ values for the analytical binomial equation are shown.

With reference to the four possible reasons for an underestimation, the first (J_k underestimation) could be a result of the coefficients which alter the binomial form (bunch length and μ) or the profile itself could be inaccurate. The equation for calculating the value of J_k was detailed in Chapter 4 (Eq. 4.3). This parameter is multiplied by the beam current to give the form of the current in the frequency domain. With a single bunch, the value of J_k is simply the binomial equation shown in Fig. 7.6.

As the bunch length can vary by ± 10% [145, 146] with respect to the nominal value, the effect of decreasing the bunch length is shown in Fig. 7.8.

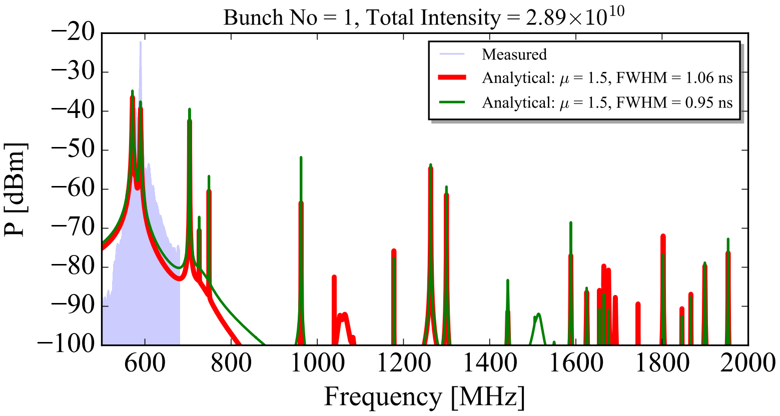

Figure 7.8: Effect of decreasing the bunch length by 10% on the analytic spectra for cavity 1.

Each of the lower frequency modes increases in power with a smaller bunch length. Specifically, the mode at 960 MHz increases by over 12 dB as a result of its close proximity to the 'node' of the binomial profile and hence increased sensitivity to bunch length. To illustrate the movement of the node, Fig. 7.9 shows the binomial bunch profile for the two bunch lengths. The large increase in J_k at the frequency of the high power mode is highlighted.

The small changes in J_k in the range 1.2–1.3 GHz explain why the measured modes here match the analytic values; They are insensitive to bunch length changes.

The main conclusion of the analysis is that small deviations in the form of the bunch can have significant effects on the HOM power. The effect of this is greater at certain frequencies, as seen for longitudinal mode at 960 MHz with a bunch length FWHM of ~ 1 ns.

Mode coupling

To assess the validity of the assumption that the power at each resonance is equally split between the three HOM couplers, the power from the low frequency (500–1000 MHz) section was measured from each of the three ancillaries and averaged. The comparison of the measurement taken from the top coupler and the

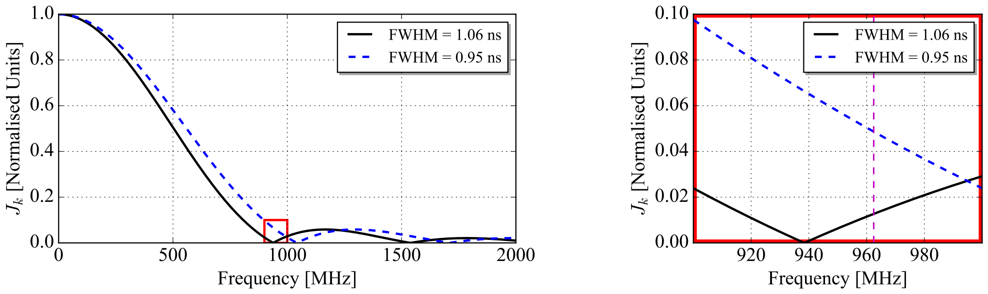

(a) (b)

Figure 7.9: J_k as a function of frequency for the nominal measured bunch length and with a 10% decrease.

average of the three couplers is shown in Fig. 7.10. The analytic profiles are shown for the nominal bunch length and with a reduction of 10%.

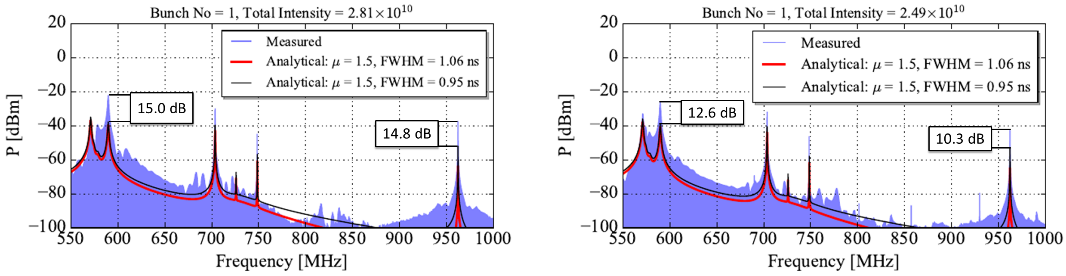

(a) Measured from the top HOM coupler (H1).

(b) Average measured from the three HOM couplers.

Figure 7.10: Evaluation of the effect inter-mode coupling differences.

Although the measured power is still higher than the simulated, two modes clearly couple more strongly to the top HOM coupler as they become much closer to the analytic value when the measurements are averaged. From the plots, these are the modes at 590 and 960 MHz. The difference highlights the need to investigate the individual mode coupling ratios to accurately compare the measured and simulated data-sets.

Misrepresentation of $\Re\{Z_{\parallel}\}$

For the third point, it is unlikely that the impedance is underestimated due to incorrect mode frequencies or quality factors, as they were measured. As such, for an incorrect value of $\Re\{Z_{\|}\}$, it would be the value of $r/Q_{\|}$ that was underestimated (Chapter 2, Sec. 2.1.2). This could be a result of a deviation of a change in the cavity geometry from the simulated, or from an offset of the beam with respect to the mechanical centre of the cavity in the transverse planes.

As the geometry of the cavity met the manufacturing tolerances, it is unlikely that the $r/Q_{\|}$ of the high power HOMs varies by more than 10%. Since the power deviates by significantly more than this, this is probably not the main cause of the discrepancy.

To evaluate the effect of a beam offset on the magnitude of the HOM power error, the simulated normalised mode impedance variation as a function of offset in both planes was assessed for the high power modes. This is shown in Fig. 7.11.

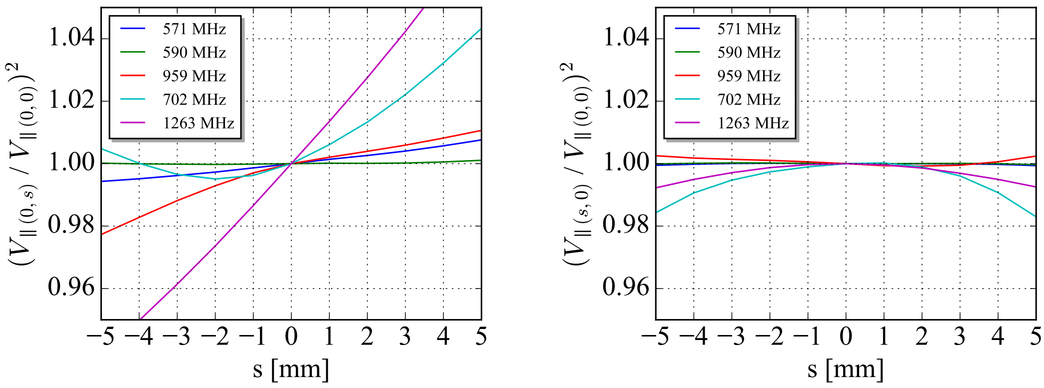

(a) Vertical. (b) Horizontal.

Figure 7.11: Impedance variation with offset.

The relationships show that for an error of ± 3 mm, the maximum change in mode impedance (and therefore HOM power) is less than 5% (∼ 0.2 dB). As this is extremely small compared to the error observed in Fig. 7.7, its effect was not taken into account.

Measurement Signal

Post measurement evaluation showed no issues with the HOM coupler cabling. However, an RF filter centred at 400 MHz was installed on the pick-up probe. This probe is mounted on the beam pipe and, in addition to sampling the fundamental mode signal, damps a mode at 1.75 GHz (detailed in Chapter 4). As such, this mode was perturbed by the filter, explaining the deviation at this frequency in the measured response (referring back to Fig. 7.7).

Figure 7.12 shows the single bunch power spectra measured from cavity one, HOM coupler one, before and after the bandpass filter was added to the beam-pipe pick-up cabling. Although the traces correspond to different bunch intensities and use different spectrum analyser parameters, the addition of the high frequency impedance as a result of the band-pass filter is clearly visible at 1.75 GHz.

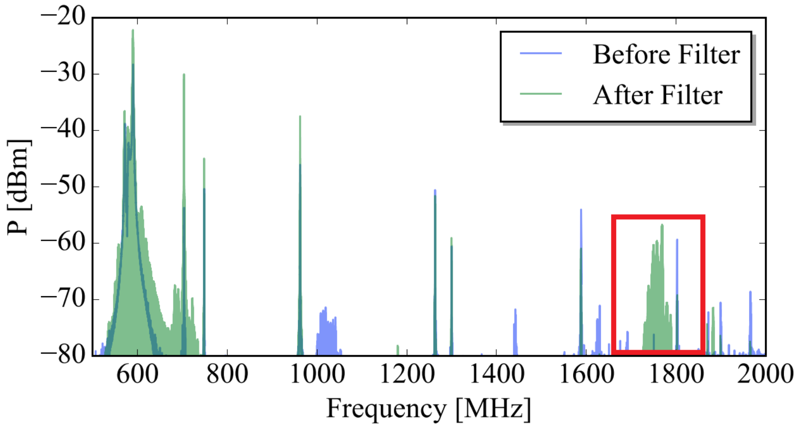

Figure 7.12: Power spectra measured from the top HOM coupler with and without a bandpass filter on the beam-pipe pick-up cabling. Note, different beam parameters and analyser sampling are used.

Additionally, a design error meant that the RF ‘feedthroughs’ used for this probe were actually 33 Ω, whereas all of the RF infrastructure had an impedance of 50 Ω. Hence, the matching of the coupler to the load was not as designed.

The problems detailed here form part of the motivation for the beam-pipe ancillary changes presented in Chapter 5.

7.3.2 Narrowband Measurements

Following the broadband analysis, narrowband measurements were taken for more accurate, high resolution information on the mode power and inter-mode coupling differences. A selection of these measurements are shown in Fig. 7.13.

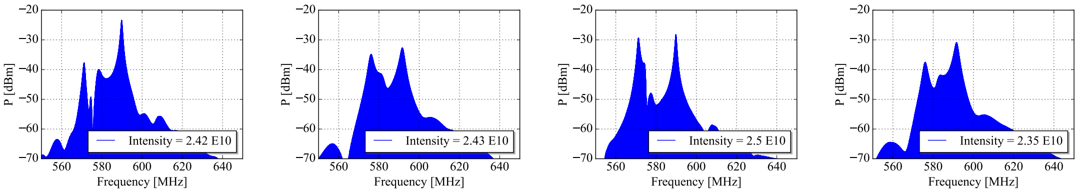

(a) C1H1
First modes

(b) C2H1
First modes

(c) C1H2
First modes

(d) C2H2
First modes

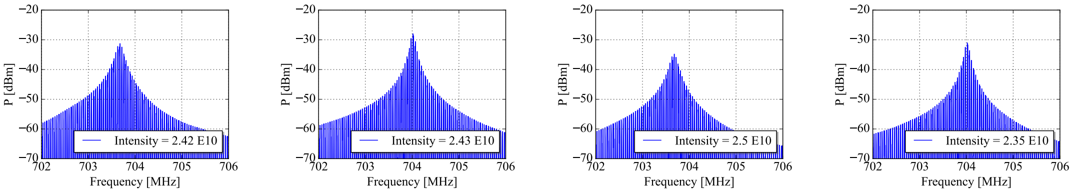

(e) C1H1
704 MHz

(f) C2H1
704 MHz

(g) C1H2
704 MHz

(h) C2H2
704 MHz

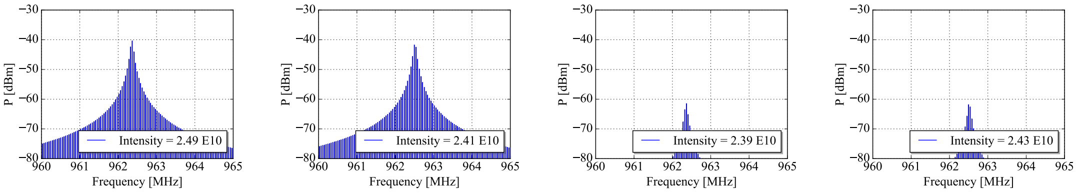

(i) C1H1
960 MHz

(j) C2H1
960 MHz

(k) C1H2
960 MHz

(l) C2H2
960 MHz

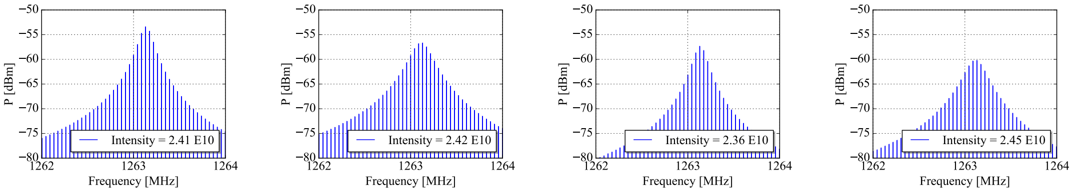

(m) C1H1
1253 MHz

(n) C2H1
1263 MHz

(o) C1H2
1263 MHz

(p) C2H2
1253 MHz

Figure 7.13: HOM power for high longitudinal impedance modes. Nomenclature is use such that ‘C1H1’ refers to Cavity 1, HOM Coupler 1.

The measurements clearly show the difference in frequency and quality factor between the two cavities. This is particularly prevalent for the first HOMs for which the deviations are quantified and discussed in Chapter 4. In addition to the inter-cavity differences, the deviations in the magnitude differs between each coupler as shown in Fig. 7.10. This is due to the fact that for a given mode, there is a different coupling coefficient to each HOM coupler. For the high power modes, Tab. 7.1 gives the maximum power measured for each mode and the coupler through which this was measured.

Cavity One			Cavity Two		
f_0 [MHz]	P_{max} [dBm]	Coupler	f_0 [MHz]	P_{max} [dBm]	Coupler
571.1	-3.53	HOMC2	576.3	-5.42	HOMC3
589.8	$\boxed{2.69}$	HOMC1	591.5	-4.85	HOMC2
703.7	-3.25	HOMC3	704	$\boxed{-0.37}$	HOMC1
962.4	-9.73	HOMC1	962.5	-11.09	HOMC1
1263.1	-19.85	HOMC1	1263.1	-23.12	HOMC1

Table 7.1: Maximum power measured with single bunch with an intensity of 2.4×10^{10} and with a bunch length of FWHM = 1.06 ns. The power is increased by the frequency dependant cable attenuation to represent the power at the HOM coupler.

The maximum power values show that, for single bunch with a FWHM of ~ 1.06 ns and an bunch intensity of 2.4×10^{10}, the largest contribution to the HOM power differs for the two cavities. For cavity one, this contribution comes from the mode at 590 MHz and for cavity two, the largest contribution is at 704 MHz. The power at each of these modes is 6 and 4.5 dB higher than the next highest power mode.

Referring back to the analysis of the cavity mode parameter deviations from simulations (Chapter 4, Sec. 4.2.2), the 704 MHz mode in cavity two had the second highest quality factor shift measured, increasing by a factor of five. This is hence the reason why this mode has the highest power measured.

7.3.3 Coupling Ratios

As a result of the large intra-coupler power deviations detailed (see Fig. 7.10), the ‘coupling-ratios’ (i.e. the percentage of the HOM power at each resonance seen at each coupler) were quantified for the high power modes.

Eigenmode cavity simulations were firstly launched, where each simulation had only one HOM coupler terminated at $50\,\Omega$ and the other two were shorted. The ratio of the external quality factors, remembering to sum in parallel, gave the coupling ratios of each mode. These ratios are shown in Fig. 7.14 for the high longitudinal impedance modes referenced. The cavity schematic is displayed again for nomenclature.

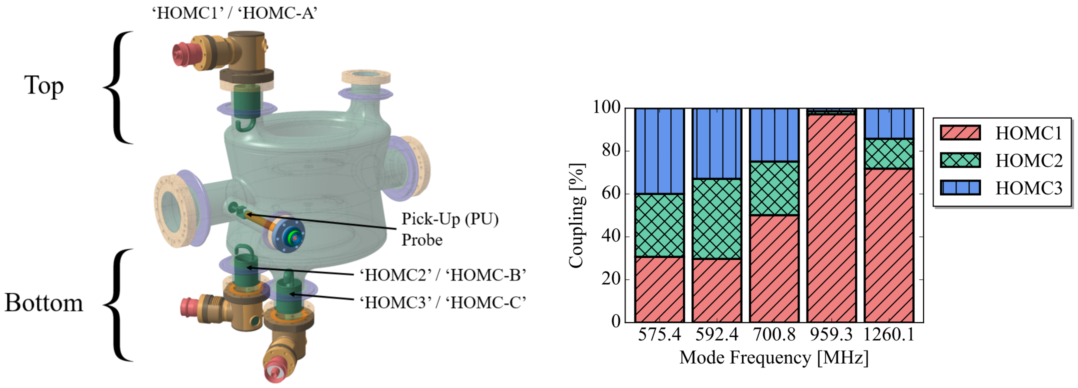

(a) Dressed cavity schematic.

(b) Simulated coupling.

Figure 7.14: Simulation of the coupling ratios for the high power modes.

The ratio of the measured power was used to calculate the measured coupling ratios for the HOMs. These ratios are shown in Fig. 7.15.

The largest deviations in coupling ratios, from simulated to measured, are for the first HOMs (575 and 592 MHz). The deviations are not systematic. The reason that these modes deviate in coupling is due to geometric differences between the manufactured HOM couplers. As presented in Chapter 3, the HOM coupler’s S_{21} has a sharp pass-band at this frequency, most significantly effected by the distance from the coupling hook to the band-stop filter. The bandwidth of this pass-band is smaller than that of the two HOMs. As presented in Chapter 4, the inter-coupler spread of the sharp pass-band changes the coupling and damping significantly at these cavity modes. To illustrate this, the HOM coupler transmission

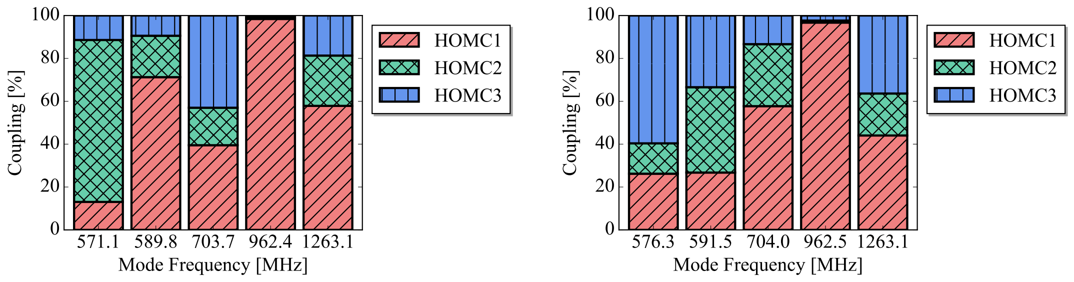

(a) Cavity One. (b) Cavity Two.

Figure 7.15: Measured coupling ratios.

characteristics measured with the 'test-boxes' detailed in Chapter 3 are shown in Fig. 7.16 with the cavity one impedance spectra on the second y-axis to show the mode frequencies. The deviation in transmission due to the differences between the couplers is hence significant.

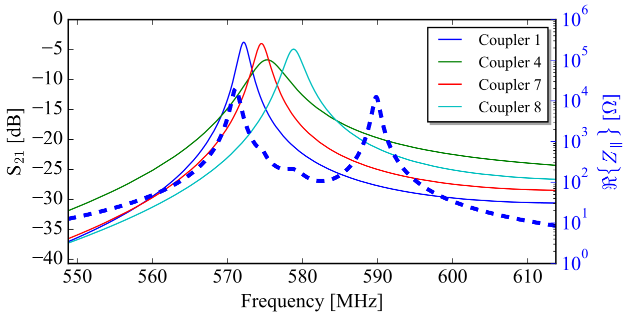

Figure 7.16: SPS DQW HOM coupler transmission measured on the test-box. The frequency range around 580 MHz is displayed to illustrate the intra-coupler transmission differences due to manufacturing deviations.

The coupling ratios of the three higher frequency modes (Fig. 7.15) are closer to the simulated. The deviations are likely a result of HOM coupler insertion depth, alignment errors and small transmission differences due to manufacture.

Notably, the 960 MHz mode couples only to the top HOM coupler (insignificant coupling on the lower two couplers). This is due to the field configuration of this mode; magnetic field nodes are present at 45° and hence the hook type coupling mechanism on the bottom HOM couplers do not couple to the field. The top coupler is at an H-field maxima.

As the 960 MHz mode is the mode which can produce the most power with the HL-LHC filling scheme (Chapter 4), this means that the HOM line and ceramic window on the top HOM coupler will be subjected to the full cavity HOM power at this frequency.

7.3.4 Single-Bunch Conclusions

Broadband measurements

Broadband measurements were taken from the top HOM coupler of both cavities. An under-representation of the power spectra was seen from the analytical calculations. Additionally, a disparity between the simulated and measured power spectra was observed at 1.75 GHz. Possible reasons for the underestimations are numbered below with the main conclusions from each of the investigations bulleted.

1. A misrepresentation of the form of the proton bunch (J_k, Eq. 4.3).
    - The form of the J_k (i.e. form of the beam current as a function of frequency) was seen to be very sensitive to variations in bunch length.
    - Specifically, at the bunch length used, the value of J_k at 960 MHz was very sensitive to bunch length errors, contributing to why the form of the bunch is underestimated at this frequency.
2. An error in the assumption that one third of the HOM power is seen at each HOM coupler (up to a 4.8 dB underestimation).
    - The average of the traces from each of the three HOM couplers brought the modes closer to the analytic form, suggesting that the modes do not couple equally to each of the HOM couplers.
3. An underestimation of the impedance spectra ($\Re\{Z_\parallel\}$).
    - The impedance variation with offset for the high power modes was evaluated. This was seen to have little effect with respect to the large differences in HOM power observed.

4. An error in the measurement signal (e.g. perturbation due to an RF filter).
    - A 400 MHz band-pass filter was used on the beam-pipe pick-up cabling. The filter caused a reflection at the 1.75 GHz mode and was the reason for the discrepancy at this frequency.

Narrowband measurements

Narrowband measurements further highlighted the inter-cavity differences. As a result of the power differences seen between the couplers in the broadband measurements, the narrowband measurements were used to assess the mode 'coupling ratios' (i.e. the percentage of power that couples to each port). The ratios differed between the cavities and from that of the simulations. The notable conclusions were:

- The coupling ratios of the first high-power HOMs differed significantly from the simulations. This was shown to be a result of the geometric differences between the HOM couplers. The 'test-box' measurements in Chapter 3 were used to describe this.
- The high power mode (960 MHz) only couples to the HOM coupler. Referring back to Chapter 4, the power of this mode contributes to the vast majority ($> 90\%$) of the HOM power using the HL-LHC filling scheme. The coupling ratios mean that all of this power must be supported by one HOM coupler and therefore one ceramic window and RF line.

7.4 Bunch Profile Measurements

The deviations between the measurements and the analytic calculations shown in Sec. 7.3 prompted an investigation into the bunch profile distribution.

7.4.1 Time Domain Measurements and Analysis

Time-domain measurements of the bunch profile using an oscilloscope connected to a Wall Current Monitor (WCM) [147] were taken, with the timings provided by a fibre-optic link. Fourier transforms of the time domain bunch profiles into the frequency domain would allow comparison of the measured bunch profile with the analytic. To measure the profiles, four bunches spaced with 105 RF buckets circulated the SPS with the crab cavities 'turned off' (no RF power). The time domain traces taken are shown in Fig. 7.17.

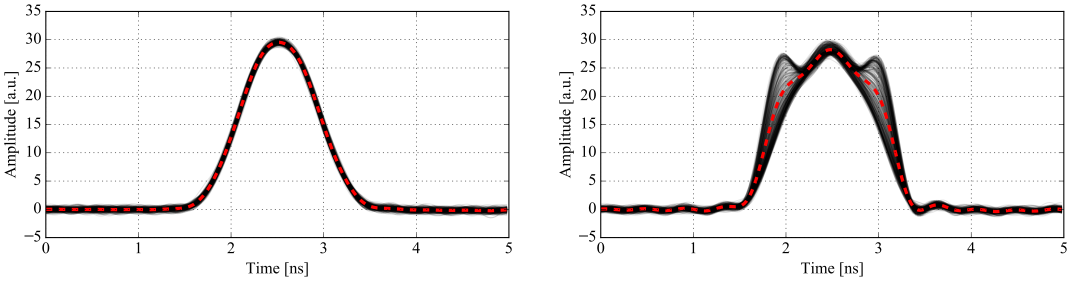

(a) Bunch 0.

(b) Bunch 1.

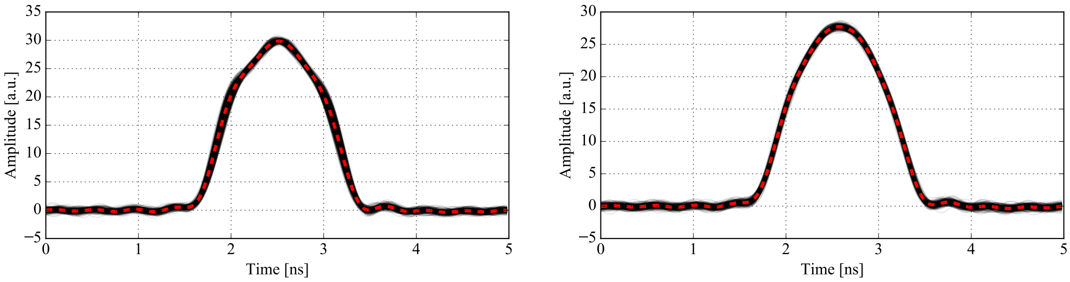

(c) Bunch 2.

(d) Bunch 3.

Figure 7.17: Bunch profile measurements. The black lines show all of the traces taken and the average is shown by the red dashed line. Measurements courtesy of M. Schwarz.

All profiles for the first bunch (bunch 0) are similar in shape and hence have little deviation from the average profile shown by the dashed red line. Bunch 1 on the other hand has an instability which varied over the acquisition time. Hence, the average profile differs from each of the individual traces. Bunch 2 and 3, like bunch 0, have little variation over the acquisition time. From the average of the measured traces, the FWHM for each bunch was 0.99, 1.30 (instability), 1.23 and 1.21 ns respectively.

To evaluate the bunch profiles in the frequency domain, the Fourier transform of each bunch was computed. The resulting traces are shown in Fig. 7.18. The order of the transformations was varied:

1. Fourier transform of each time domain trace → averaged: RED

2. Average of time domain traces → Fourier transformed: DASHED BLUE

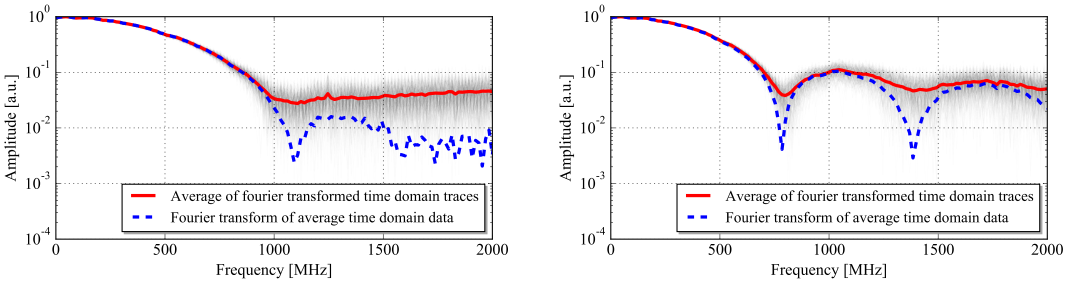

(a) Bunch 0. (b) Bunch 1.

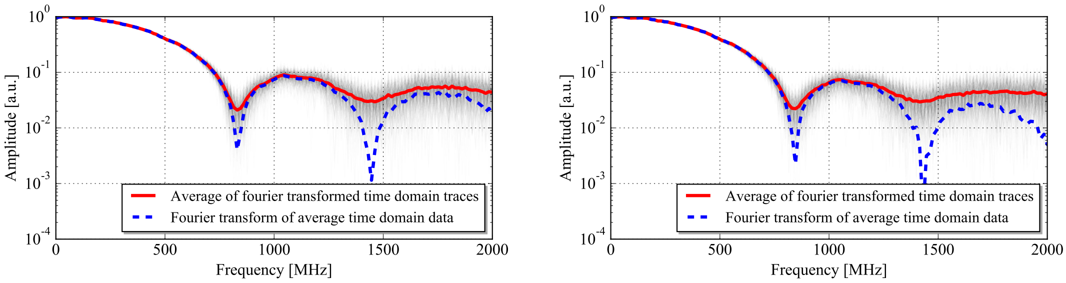

(c) Bunch 2. (d) Bunch 3.

Figure 7.18: Fourier transforms of the bunch profile measurements shown in Fig. 7.17.

Referring to Fig. 7.18, the first 'lobe' of the bunch profile is clearly measurable with little variation between acquisitions. The smaller bunch length of the first bunch means that it's profile is 'longer' in the frequency domain with respect to the other bunches and hence the first node is above 1 GHz whereas this is at $\sim$ 800 MHz for the other bunches. The subsequent 'lobes' are apparent in the measured data-sets for the last three bunches, however these are not seen in the first.

For the average of the Fourier-transformed time-domain traces (red line), the multiple lobes are not apparent for the first bunch but are clearly visible for the following three. These traces do not show the very low amplitude nodal points presented by the binomial equation.

For the Fourier transform of the average time domain trace (dashed blue trace), the multiple lobes of the bunch profile are much more visible and the trace looks very similar to that of the binomial function. Performing an average of the time domain traces removes the effect of the small intra-acquisition deviations which can have a large effect at high frequencies. Hence, the high frequency spread between the individual bunches is removed. This means that the bunches vary in profile over time. Hence, although the Fourier transform of the average time-domain profile gives a result which is very close to that of the binomial function, the value of J_k at a discrete frequency varies with time. As the sweep time of the spectrum analyser is much longer than the time needed for one bunch to circulate the full circumference of the SPS, the bunch profile changes during the acquisition time. This could contribute to the difficulties in matching the analytic and measured broadband signals in Sec. 7.3.1.

To evaluate the accuracy of the binomial function, a least squares fit was applied to the Fourier transform of the average time-domain traces. The best combination of bunch length and μ was returned. This is shown in Fig. 7.19.

The fits show that the first bunch in the four bunch train is closer to a Gaussian than any of the others, i.e. has a much larger μ coefficient, and has a shorter bunch length. Although the fit is a much better representation of the measured data than that of the nominal parameters, there are still large discrepancies which start before the first node of the profile. This could explain the lower approximation in power shown in the broadband measurements in Sec. 7.3.1; The shorter bunch

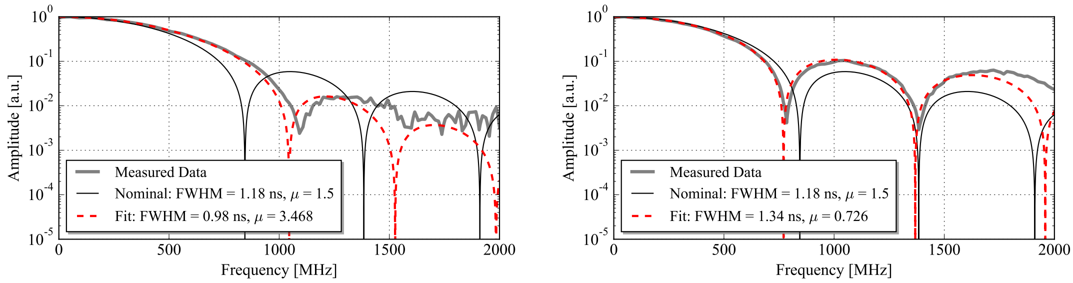

(a) Bunch 0. (b) Bunch 1.

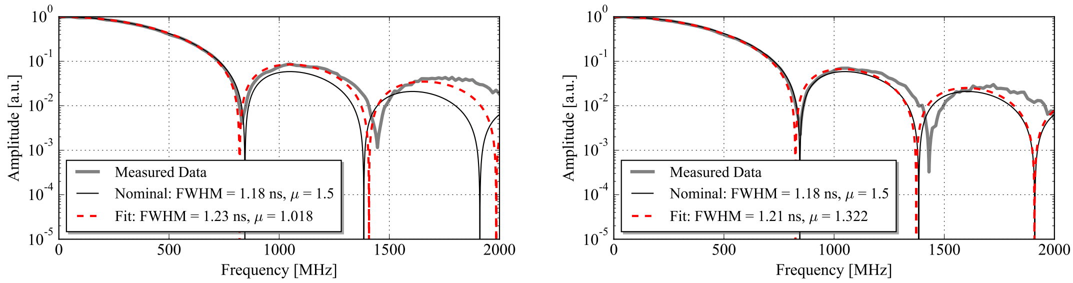

(c) Bunch 2. (d) Bunch 3.

Figure 7.19: Fits to Fourier transform of the average time-domain trace for each bunch.

length and higher μ coefficient means there is a higher current at low frequencies. If this is the case when a single bunch is injected into the machine, a higher power than that of the predicted will result. However, due to the lack of bunch profile information in the single bunch measurements and the possible profile oscillation over the analyser sweep time, it is difficult to conclusively attribute the higher measured power to this, but it highlights the need for bunch profile measurements in future tests.

The following three bunches are better represented by the binomial profile, with the fits allowing a good match to the measured data. The fit for bunch two is very close to the measured data and only starts to deviate after $\sim 1.8\,\mathrm{GHz}$. The deviation seen from the second two bunches starts slightly earlier but both are still representative up to $\sim 1.3\,\mathrm{GHz}$.

Referring to the last three bunches only, as the first bunch is much shorter and 'typical' of the first bunch in a train in the SPS [146], in all cases the μ coefficient is less than the nominal 1.5 used for the single and multi-bunch analytic calculations. The average bunch parameter deviations for the last three bunches are:

Bunch length: 9.9%
μ: 0.48

Therefore, variations of ± 10% and ± 0.5 should be applied to the analytic power at discrete frequencies to compare the measured to the predicted powers.

7.4.2 Beam Variations

The deviation between the analytic and measured power shown in Sec. 7.3.1, Fig. 7.7 as a result of unrepresentative beam parameters (bunch length and μ) was further investigated. Using the measured bunch parameter tolerances, the value of J_k was assessed with a variation of both the bunch length and μ. Note, their values are co-dependant. The plots, for a bunch length variation of ± 10% and a μ variation of ± 0.5, are shown in Fig. 7.20.

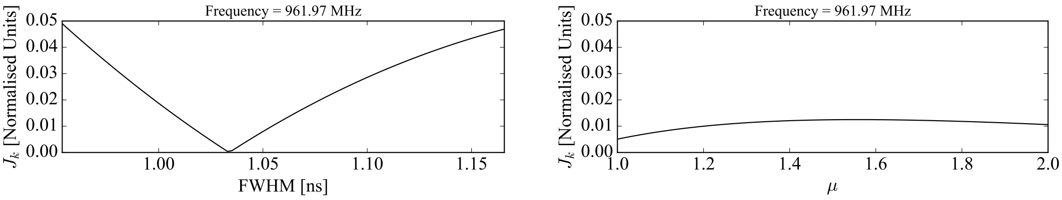

(a) J_k as a function of bunch length.

(b) J_k as a function of μ.

Figure 7.20: Value of J_k as a function of both bunch length and μ for a single bunch at the frequency of the 960 MHz mode in cavity one.

As previously seen, the value of J_k, and hence the beam current at this frequency, varies significantly with a small change in bunch length. However, it does not change with a variation in μ.

This is not the case at all frequencies. Figure. 7.21 shows the effect of the two parameters at 1200 MHz.

The effect of μ at this frequency is significantly larger than that of the bunch length. As such, the main conclusion regarding variations in bunch profile parameters is that, depending on the frequency, the power at a given mode can change

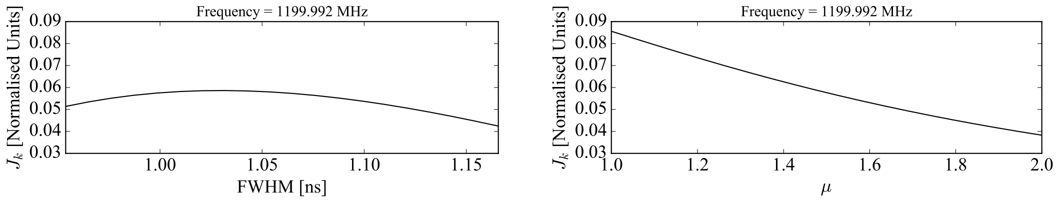

(a) J_k as a function of bunch length.

(b) J_k as a function of μ.

Figure 7.21: Value of J_k as a function of both bunch length and μ for a single bunch at 1200 MHz.

significantly. As such, bunch parameter tolerances should be used to provide a ‘power window’ for further analysis and for analysis of the DQW in the HL-LHC.

7.5 Multi-Bunch

In order to verify that the HOM power could be predicted with more than one bunch, and that the relationship between HOM power and the number of bunches is well understood, the HOM power as a function of the number of bunches was investigated.

As presented with the single bunch measurements, the value of J_k at a given frequency can change significantly with bunch parameters. In the case of multiple bunches, the bunch profiles will never exactly conform to the analytic case and each bunch in the train will be slightly different. For visualisation, the average profile of a 72 bunch train was plotted for the case where each bunch matched exactly and for the case where each bunch has a random error in bunch length (up to 10%). The result of this is shown in Fig. 7.22.

The variation of bunch lengths removes the nodes, increasing the excitation at these frequencies by many orders of magnitude. Similarly, the peak excitation at the lobes of the binomial is reduced. With a large number of bunches, the amount of bunch length configurations means it is computationally expensive to stochastically evaluate each of the possible average bunch profiles.

However, since the main interest is to evaluate the evolution of power with bunch number at discrete frequencies, i.e. cavity modes or bunch spacing harmon-

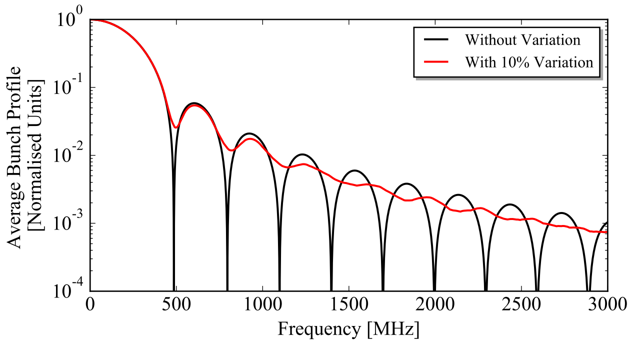

Figure 7.22: Effect of intra-bunch, bunch-length variation on the average bunch profile for an arbitrary nominal bunch length and μ.

ics, the range of J_k can be calculated at the frequency of interest to define a power range.

As an example, Fig. 7.23 shows the value of J_k at 962 MHz for 72 bunches with a bunch spacing of 25 ns, as a function of both bunch length and μ. The ranges used for the analysis correspond to those presented in Sec. 7.4 and, as discussed in Sec. 7.4.2, the values of bunch length and μ are co-dependant.

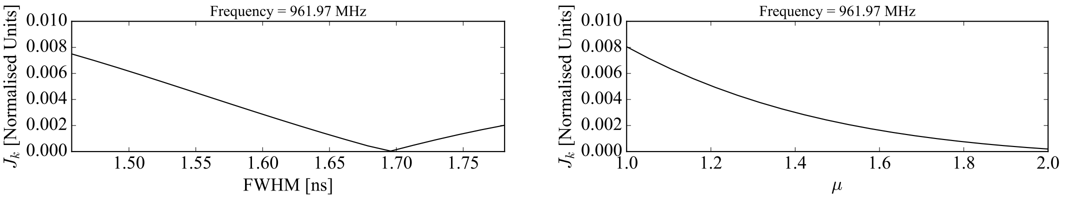

(a) J_k as a function of bunch length.

(b) J_k as a function of μ

Figure 7.23: Value of J_k as a function of both the bunch length and μ at 962 MHz for 72 bunches with a bunch spacing of 25 ns.

Deviations are observed in the order of a factor of three from the nominal. This corresponds to nine times the power.

The lower limit for J_k at is often close to zero due to the nodes of the binomial profile and hence the range between the nominal and maximum was used for the analytic window. The power against the number of bunches (M) was calculated at 962 MHz using cavity one's longitudinal impedance spectra, for a train of 1 to

200 bunches with a 25 ns bunch spacing. At each value of M, the nominal and upper limit of J_k was used to create the HOM power ‘window’. The resulting plot is shown in Fig. 7.24.

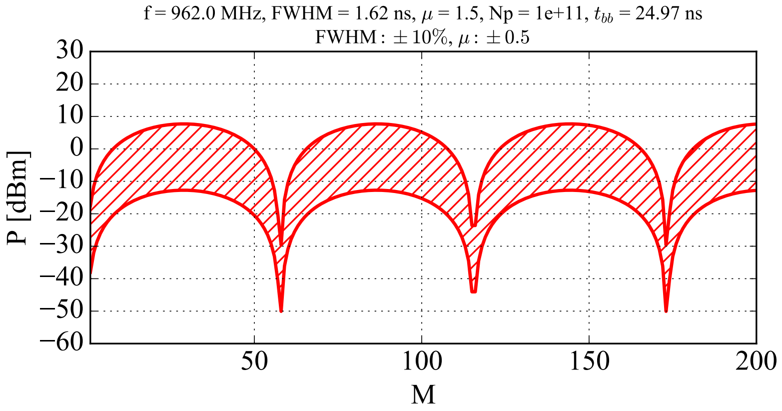

Figure 7.24: HOM Power as a function of bunch number (M) at 962 MHz using cavity one’s impedance spectra.

Notably, the power is periodic with the number of bunches. This is due to the modulation of the form of J_k. Assuming the same bunch spacing, the period of the power as a function of the number of bunches decreases, i.e. acts over a lower range, as the frequency at which it is evaluated moves further from a bunch spacing harmonic. As a reference, the bunch spacing harmonics and modulation due to the number of bunches are shown again in Fig. 7.25.

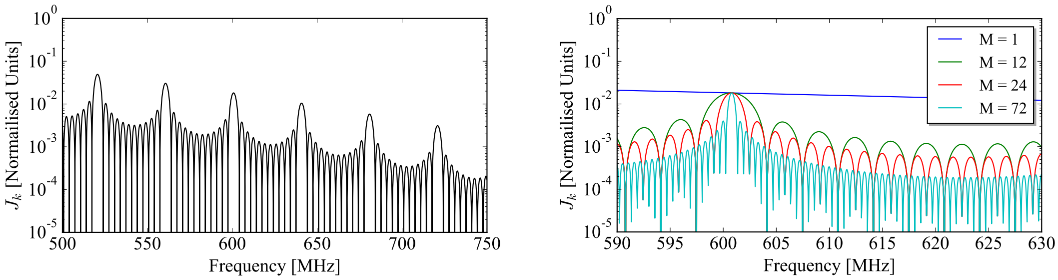

(a) 12 bunches, narrow frequency range. (b) Modulation with bunch number (M).

Figure 7.25: J_k as a function of frequency.

The form of J_k for different bunch trains was measured using the Wall Current Monitor (WCM) [147]. As a precaution (to protect the analyser), a large attenuation was used and hence the spectral composition at the HOM frequencies was not measured at high frequency. However, the form of the modulation conformed to that of the analytic. The measurements are shown in Fig. 7.26.

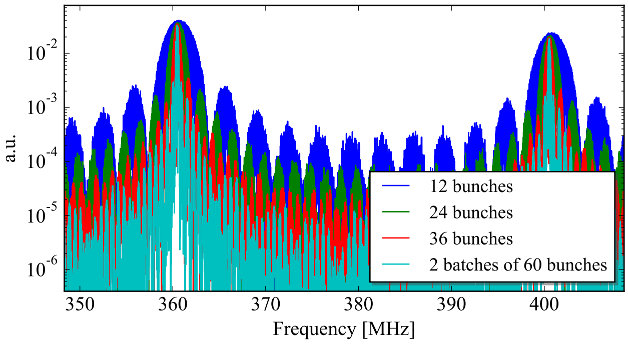

Figure 7.26: Measured profile example for different bunch numbers.

The variation of J_k with the number of bunches (M) is shown in Fig. 7.27 for various frequencies. The frequencies are presented with respect to their distance from a bunch spacing harmonic multiple (i.e. $1/t_{bb}$). The decrease in period can be seen as the frequency moves further from away from these multiples.

Although the value of J_k has a general quadratic reduction as the number of bunches increases, the intensity as a result of this increases linearly. As such the current, and hence HOM power, increases quadratically. The cancellation of these two relationships explains why the HOM power at a discrete frequency as a function of bunch number (shown in Fig. 7.24) is periodic.

7.5.1 Measurements at the bunch spacing harmonics

Filling every fifth RF bucket in the SPS (25 ns bunch spacing) with bunches with intensities of $\sim 1 \times 10^{11}$, the bunch number was increased from 12 to 60 in steps of 12 bunches. Due to the limited acquisition time, the power in the frequency range from 500 MHz–1000 MHz was measured to allow analysis of the most detrimental high longitudinal impedance modes whilst maintaining a sufficient measurement

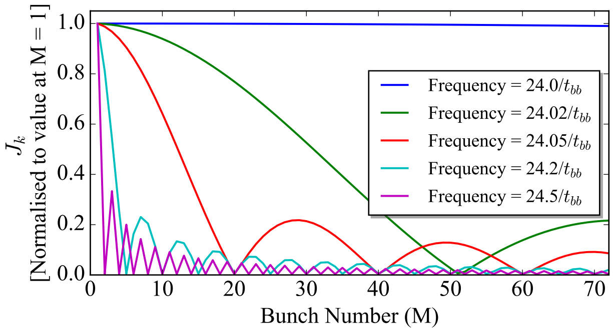

Figure 7.27: J_k as a function of bunch number (M) and normalised to the value at M = 1. The plot is shown at five frequencies to illustrate the change in periodicity depending on the distance from a bunch spacing harmonic.

resolution. An example of one of the measurements taken from the top HOM coupler of cavity one, is shown in Fig. 7.28.

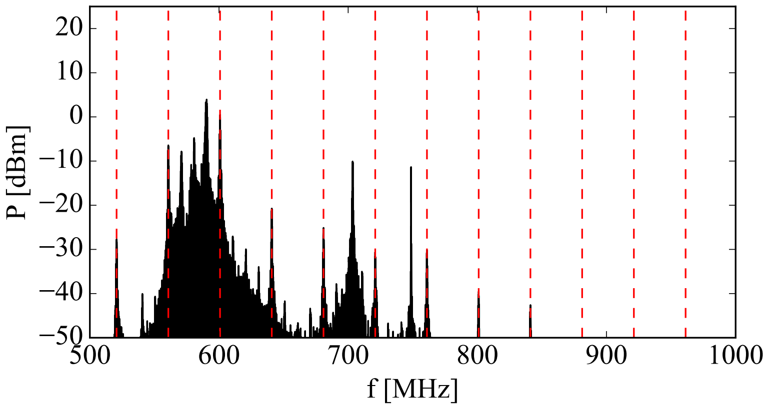

Figure 7.28: Measurement of HOM power from cavity one, HOM coupler one with 60 bunches with a bunch intensity of 1×10^{11} spaced by 25 ns. The measurement is increased by the measured cable attenuation and is annotated with the frequencies of the multiples of the bunch spacing harmonics ($1/t_{bb}$).

The bunch spacing harmonics are visible on the HOM power spectra, and conform to the predicted frequencies. Furthermore, unlike with the single bunch measurements, the power is now highest at 960 MHz due to the interaction of the longitudinal mode with the 24^{th} bunch spacing harmonic.

For the frequencies of the bunch spacing harmonics, as the HOM coupler specific coupling coefficient was difficult to quantify, the measured result was increased by a factor of three (4.77 dB) to represent the total HOM power and hence assumes that the power is split equally between each coupler. The resulting plots are shown in Fig. 7.29.

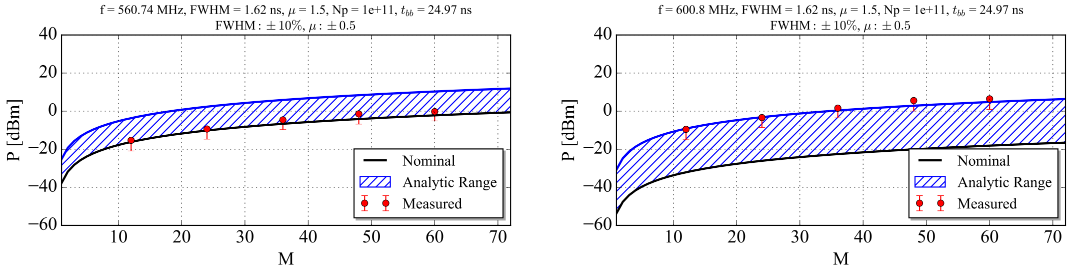

(a) Harmonic 14. (b) Harmonic 15.

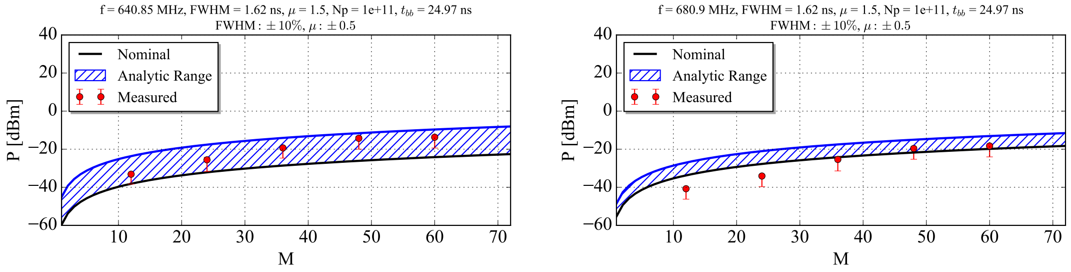

(c) Harmonic 16. (d) Harmonic 17.

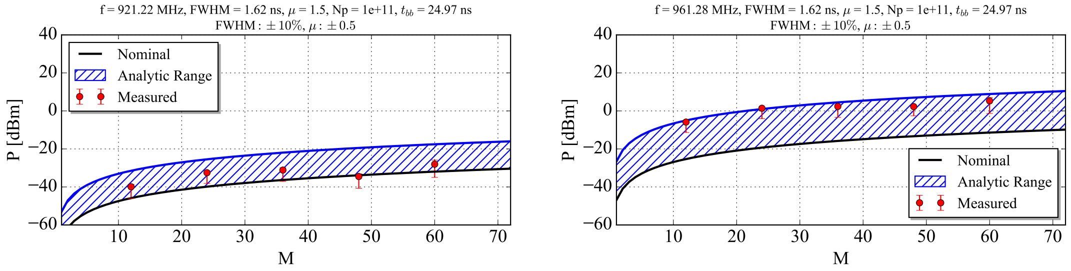

(e) Harmonic 23. (f) Harmonic 24.

Figure 7.29: HOM Power as a function of bunch number (M) for several bunch spacing harmonics ($t_{bb} = 25\,\text{ns}$). Measurements are from cavity one, HOM coupler one and are normalised to the analytic intensity and increased by 4.77 dB to represent the cavity HOM power assuming equal coupling to each HOM coupler.

For each case, there is a good agreement between the analytic and measured data. The quadratic relationship is only expected at these frequencies, i.e. multiples of $1/t_{bb}$, as there is no significant modulation of J_k from a variation in M (Fig. 7.27). Furthermore, the measured data generally falls within the analytic range.

For the case of the 15^{th} and 24^{th} bunch spacing harmonics, the measured values are at the upper limit. However, the coupling calculations in Sec. 7.3.3 show that $>$ 70% of the power extracted at the 590 MHz mode and $>$ 98% of the power extracted at the 960 MHz mode is transmitted through the top HOM coupler (coupler one). Hence, as the frequencies of the 15^{th} and 24^{th} bunch spacing harmonics are close to these modes, a similar coupling ratio is expected. As such, the increase of 4.77 dB is too high and, if it assumed that the power at these harmonics splits in the same way as the adjacent HOMs, the value added to the measurement to reflect the power at the cavity should be 1.47 and 0.07 dB respectively. To reflect the coupling uncertainty, each of the measured data points has the lower error increased by 4.77 dB.

7.5.2 Measurements at the cavity modes

In addition to the bunch spacing harmonic frequencies, the evolution of the power at the frequencies of several high impedance longitudinal modes was also monitored. Referring to the example measurement shown in Fig. 7.28, the four highest power modes were chosen. The resulting plots are shown in Fig. 7.30. The measured power at the mode frequencies was increased by the frequency dependant cable attenuation and mode dependant measured coupling coefficient to represent the cavity HOM power.

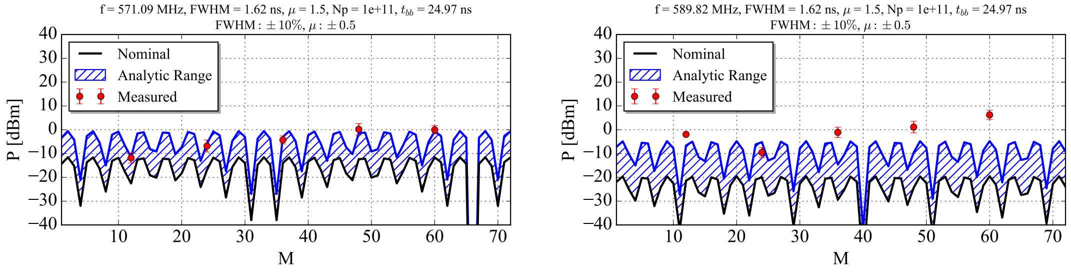

(a) 571 MHz.

(b) 590 MHz.

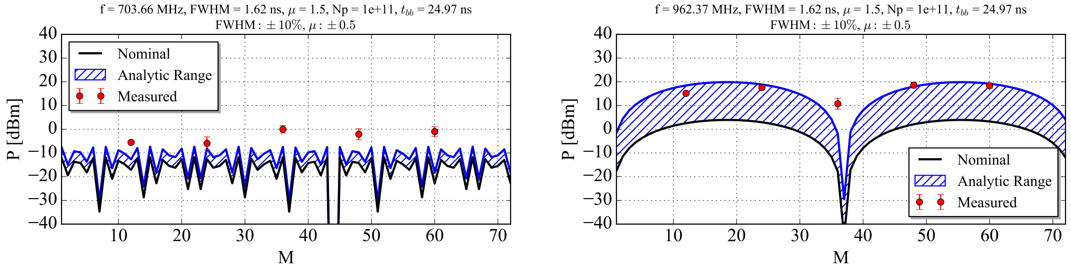

(c) 704 MHz.

(d) 962 MHz.

Figure 7.30: HOM Power as a function of bunch number for several modes with high longitudinal impedance. Measurements are from cavity one, HOM coupler one, and are normalised to the analytic intensity and increased by the mode specific measured coupling ratio and cable attenuation to represent the cavity HOM power.

As discussed previously, the analytic dependence of the mode power with the number of bunches is periodic. The period is determined by the distance from a multiple of a bunch spacing harmonic in the frequency domain. For the four modes plotted, the absolute distance from the nearest bunch spacing harmonic frequency

(n/t_{bb}) as a percentage of half the harmonic spacing ($0.5/t_{bb}$ =20.03 MHz) is 52%, 55%, 86% and 5.4% respectively.

This is seen in the measurements for the mode at at 962.4 MHz. Because it is very close to the 24^{th} bunch spacing harmonic, the period of the power as a function of the number of bunches is very long compared to that of the other modes. With reference to the measured data sets, the trend of the measured power matches that of the analytic.

In two cases, 590 and 704 MHz, the power is higher than the calculated nominal value. To check that this was not isolated to cavity one, the corresponding data for cavity two was analysed. This is shown in Fig. 7.31.

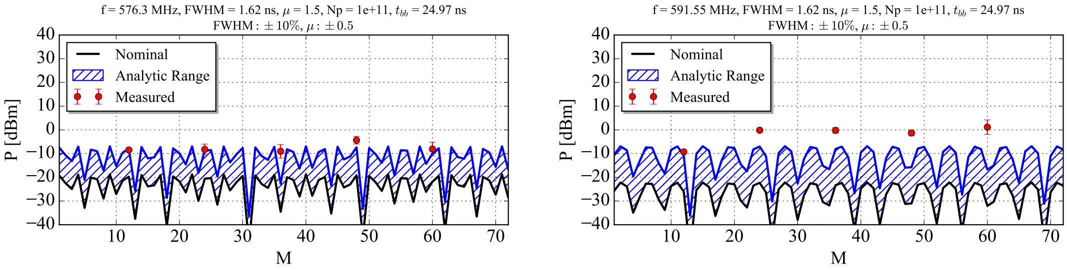

(a) 576 MHz.

(b) 592 MHz.

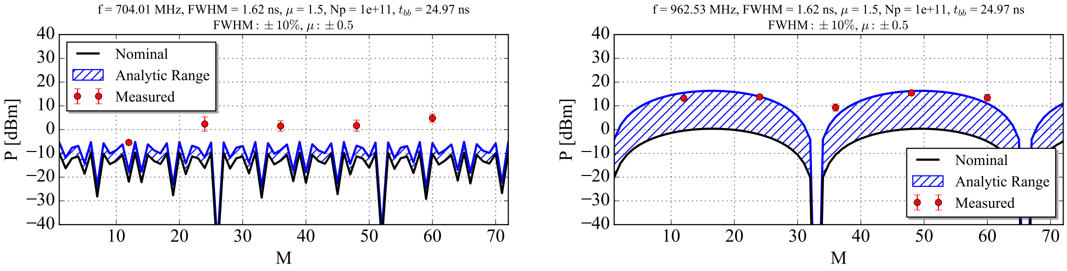

(c) 704 MHz.

(d) 962 MHz.

Figure 7.31: HOM Power as a function of bunch number for several modes with high longitudinal impedance. Measurements are from cavity two, HOM coupler one, and are normalised to the analytic intensity and increased by the mode specific measured coupling ratio and cable attenuation to represent the cavity HOM power.

Analytically, very similar relationships between the HOM power and the number of bunches are observed for each of the modes in the respective cavities, with the periodicity slightly changing due to inter-cavity mode frequency deviations.

As with cavity one, the measured results for cavity two are higher for the modes at 592 and 704 MHz when compared to the analytic data. The average increase from the analytic calculations is detailed for each mode in Tab. 7.2.

f [MHz]	$P_{meas} - P_{sim}$ [dB (Linear)]			
	Cavity One		Cavity Two	
	From Nominal	From Maximum	From Nominal	From Maximum
571	10.92 (12.36)	-0.07 (0.98)	15.53 (35.73)	3.73 (2.36)
590	21.88 (154.17)	7.12 (5.15)	24.98 (314.77)	9.71 (9.35)
704	12.81 (19.10)	8.34 (6.82)	15.49 (35.40)	11.03 (12.68)
962	17.47 (55.85)	1.56 (1.43)	16.59 (45.60)	0.64 (1.16)

Table 7.2: Measured increase in power from both the average and maximum analytic values for four low frequency high longitudinal impedance modes from multi-bunch measurements.

The measured values for the 571 and 962 MHz modes are similar to the upper threshold in both cavities. However the 704 and 590 MHz modes are at least a factor of five higher in both cavities, with a larger deviation seen in cavity two.

It is difficult to attribute the increase in observed power of these to modes to the $r/Q_{\parallel}$ (for which the simulated value is used in the analytic calculations). However it is unlikely that the values change more than 10%. Even for the 590 MHz mode, for which the $r/Q_{\parallel}$ is effected by the HOM coupler geometry, a large geometric error (few mm in simulations) has an effect in the order of 5%.

As such, it is more likely that the form of the beam current is the source of the deviation. The modes which deviate more significantly from the analytic calculations are in frequency areas where the Fourier harmonic of the beam current (J_k) is very low. The bunch spacing harmonic frequencies and the mode close to the 24^{th} bunch spacing harmonic are within or negligibly above the analytic window. As such, the conclusion made here is that: Even with the analytical power windows used as a result of the measured bunch parameter deviations, the power for modes far from the frequency of a bunch spacing harmonic is difficult to predict. Since the HOM power is only detrimental at or close to the harmonics, the highest power is hence predictable.

Irrespective of the deviation from analytical calculations the main contribution to the HOM power is both predicted and measured at the frequency of the mode near to the 24th bunch spacing harmonic at 25 ns bunch spacing. Table. 7.3 shows the maximum HOM power at each mode for the two respective cavities.

Mode Frequency [MHz]	Cavity 1 [dBm]	Cavity 2 [dBm]
571	-2.49	-7.22
590	4.28	-1.71
700	-2.63	3.55
960	17.39	14.05

Table 7.3: Maximum HOM power at the frequency of each mode in both cavities.

The power at the frequency of the 962 MHz mode is larger than any of the other mode frequencies by over 10 dB in both cavities. The power in cavity 1 at this frequency is double that of cavity 2 as the mode frequency is closer to the bunch spacing harmonic and the Q_e is higher. The measurements hence conform to the analytic predictions that the highest HOM power is a result of the HOM near to the 24th bunch spacing harmonic at that this mode could be detrimental in the HL-LHC case.

7.5.3 Transverse Mode Characterisation

In addition to the assessing the trend of the HOM power with the number of bunches, the effect of a beam offset was evaluated.

The mode chosen for the measurements was that of the 748 MHz mode as it is a low frequency mode with the highest transverse impedance in the vertical plane. Furthermore, it also has a high longitudinal impedance meaning that the power induced at this frequency is relatively high and as such, can be easily measured.

The power as a function of vertical beam offset was hence measured with fixed beam parameters (two batches of 60 bunches). A quadratic fit was applied to the measured data-set and both the measurements and fit were normalised by the value at the mechanical centre of the cavity, resulting in the squared ratio of the offset voltage to the voltage at the aperture centre. As discussed in the previous sections, the impedance of the mode cannot be plotted with accuracy due to uncertainties in the form of the bunch profile. The results are shown in Fig. 7.32, plotted alongside the simulated function.

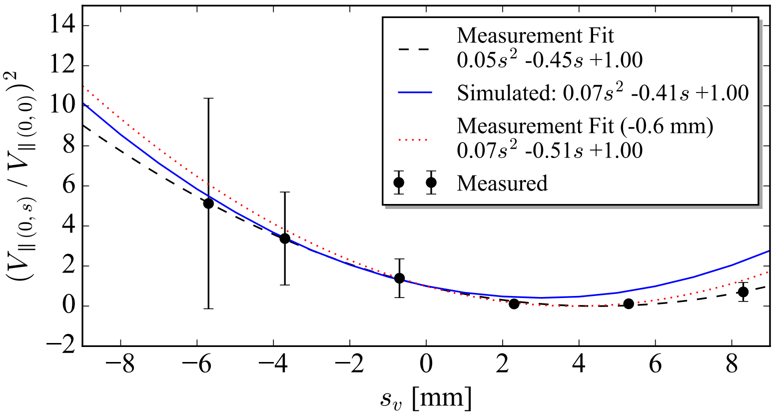

Figure 7.32: Simulated and measured impedance variation as a function of vertical offset for the 748 MHz mode.

The quadratic function fits well to the measured data-set and the fit is very similar to that of the simulated dataset.

By shifting the measurement fit by -0.6 mm (shown in plot) the measured fit is very close to the simulated. This suggests that the mode topology has shifted with manufacturing processes, moving the electrical centre at this frequency. This means that it is not only a beam offset that could induce a higher transverse impedance, but also deviations in cavity manufacture that alter the field topology of the mode and hence the impedance could increase with the beam in the same X-Y position.

7.5.4 Multi-Bunch Conclusions

Measurements at the bunch spacing harmonics (multiples of $1/t_{bb}$)

- A quadratic increase of the power with the number of bunches was predicted at multiples of $1/t_{bb}$.
- Measurements were taken with trains of 12 to 60 bunches in steps of 12 bunches.

- The measurements are within the analytic window which used the bunch parameter variations measured in Sec. 7.4.

Measurements at HOM frequencies

- The periodic relationship between HOM power and the number of bunches was presented. The period changes with the frequency distance from a bunch spacing harmonic.
- Measurements of four high impedance modes were taken for cavity one and cavity two with varying bunch train lengths.
- Even with the analytic power window, two modes were higher than the predicted.
- The high power mode (960 MHz) was generally within the predicted window (at the upper limit).
- From the measurements it was seen that the power (form of the bunch current) is difficult to predict for modes where there is a low beam spectral content.

Transverse mode characterisation

- The relationship between the impedance and offset for a verticle mode was measuered.
- The measured data had a good agreement with the simulations.
- A shift of the measured fit by -0.6 mm resulted in a curve very simular to the simulatied. This suggested that the mode's field topology had shifted with cavity manufacture.
- The field shift prompted a study into the effect of beam offset on HOM power.

7.6 Studies from Lessons Learnt

7.6.1 Bunch Parameter Variation

The main conclusion from the SPS DQW tests with regards to higher order mode measurements was that the bunch parameters can have a significant impact on the form of the beam current. As a result, the HOM power was calculated in the same way as shown in Sec. 4.2.7 but with a stochastic error in the bunch parameters. The results are displayed in Tab. 7.4. The analysis was also performed for the Radio Frequency Dipole (RFD - crab cavity for horizontal crabbing).

	P_{max} (P_{av}) [kW]			
	Nominal Bunch Parameters		Bunch Length: ±10%, μ: ±0.5	
	Gaussian	Binomial	Gaussian	Binomial
DQW	0.66 (0.17)	0.28 (0.08)	1.10 (0.19)	0.62 (0.08)
RFD	5.09 (0.90)	3.60 (0.65)	6.68 (0.92)	5.12 (0.64)

Table 7.4: Maximum HOM power from ten thousand stochastic simulations. The mode frequency and Q deviation used is that of the values returned from the DQW measurements.

For both cavities, the Gaussian bunch profile yields a higher power than that of the binomial. Using stochastic bunch parameter variations increases the power by a larger factor for the binomial profile for both cavities, but is still higher for the Gaussian profile.

Referring to the HOM power threshold of 1 kW, the DQW is below this value in all cases except for that of the 'Gaussian profile with bunch parameter variations' where the maximum power that could be seen is 10% over the threshold. The highest contributor (by at least one order of magnitude) is the longitudinal mode at 960 MHz with a frequency shift measured to be feasible. The majority of this power ($> 98\%$) couples to the top HOM coupler.

For the RFD, the maximum power from each of the four stochastic simulations is over the design threshold due to the interaction of the 752 MHz mode with the 19^{th} bunch spacing harmonic. It should be noted that even with the worst case frequency shift simulated, the mode is still 2.75 MHz from the bunch spacing harmonic. If the mode frequency lined up with the harmonic, the worst cast power would be over 20 kW, however this frequency shift is unrealistic.

For the simulations, the quality factor stochastic error range used was $0.5\ Q_{e:sim} \rightarrow 2.0\ Q_{e:sim}$. The DQW measurements show that the quality factor reduced from simulations by factors of 1.2 and 1.4 respectively for cavity one and two. For the RFD, although for a slightly different cavity geometry, the measured quality factor was 1.3 times higher than that of the simulated [148, 149].

As there is one mode in each cavity which is by far the most detrimental in terms of HOM power, the frequencies of these modes were swept and the power from this mode alone, using a Gaussian bunch profile, was returned. Bunch parameter and quality factor errors were used to define a range at each mode frequency shift. The power as a function of frequency shift is shown in Fig. 7.33.

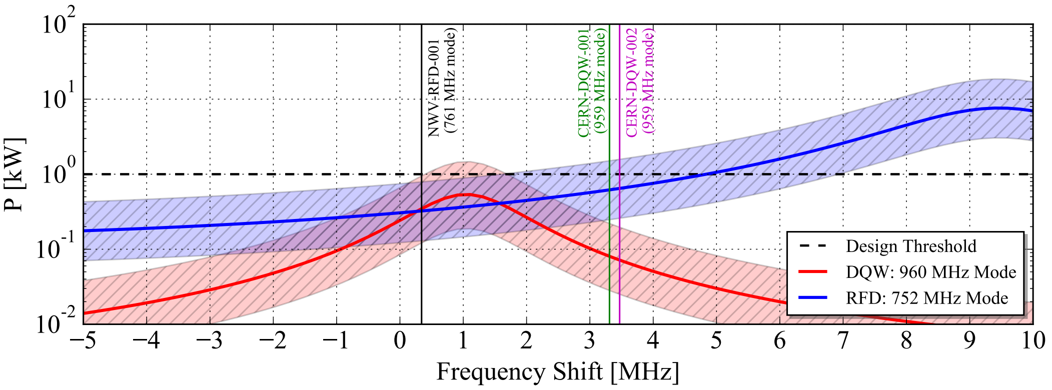

Figure 7.33: HOM power for the detrimental modes in the two crab cavities as a function of the mode frequency with HL-LHC parameters (modelled as a continuous train of bunches) and assuming a Gaussian bunch profile (pessimistic). Ranges represent the effect of a variation in mode quality factor and bunch length. The vertical annotated lines show the mode shifts from existing cavity measurements.

For the DQW, the highest power feasible for the detrimental mode is shown as ~ 1.5 kW. This is higher than the stochastic maximum returned as the perfect alignment of the bunch spacing harmonic and resonant mode is modelled. The stochastic samples are used to return an indicative, probabilistic figure and allow detrimental mode identification for further study.

It should be noted that, with the bunch lengths used in the SPS test, the high power mode was close to a ‘node’ of the binomial function, meaning that small changes in the bunch profile parameters had a large effect excitation current at the frequency of the high power mode. However, the shorter bunch length proposed for the HL-LHC means that the first node is much higher in the frequency domain. Henceforth, for the HL-LHC bunch, the deviation in mode quality factor is now the dominant factor in the predicted power range for this mode.

Nominally, the RFD is below the power threshold for up to a + 4.5 MHz from the simulated value. However, with bunch parameter and mode quality factor tolerances, the worst case power is over the threshold for any positive frequency shift greater than 1.5 MHz.

An acceptance criteria should hence be applied to each of the LHC crab cavities for the detrimental longitudinal modes. This is shown in Tab. 7.5.

Cavity	Mode	f_{max} [MHz]	$Q_{nominal}$	Q_{max}
DQW	960.87 MHz	-	500	650
RFD	752.06 MHz	753.0	220	310

Table 7.5: Detrimental longitudinal mode acceptance criteria for the LHC series cavities, ensuring that the individual mode HOM power does not exceed 1 kW.

Procedurally, if the if the mode shifts are larger than those shown in the table, the HOM power should be calculated at the measured parameters for qualification.

7.6.2 Load on Each Ancillary

The SPS measurements highlighted the difference in power observed at each of the HOM couplers at a given mode frequency. This is due to the differing coupling coefficients resulting from the field topology of the resonant mode with respect to the HOM coupler port locations. The highest power at each coupler was henceforth of interest, to assess the power handling requirements of each coupler and the associated infrastructure (i.e. coaxial lines and RF loads).

Using the global mode frequency shift technique shown in Chapter 4, the three modes identified as capable of generating powers of greater than 10 W are detailed in Tab. 7.6.

The power of the modes, assuming a Gaussian bunch profile and perfect alignment with the bunch spacing harmonic, was calculated using the bunch profile tolerances measured in the SPS tests. The mode quality factors were doubled to reflect the mode parameter deviations quantified in Chapter 4, Sec. 4.2.2.

Mode Frequency [MHz]	Closest bunch spacing harmonic [MHz]	$Z_{\parallel}$ [Ohms]	J_k[a]	P [W]	HOM Coupler		
					1 [W]	2 [W]	3 [W]
690.27	681.36 [b]	62	0.31→0.51	7.5→79	26	26	26
960.94	961.92	4576	0.03→0.26	5→1497	**1452**	22	22
1250	1242.48	3455	0.00→0.11	0→202	**144**	28	28

Table 7.6: Maximum feasible HOM power of modes capable of generating high power (> 10 W) and the ratio extracted by each HOM coupler.

---

[a] At the bunch spacing harmonic frequency.

[b] Beyond the measured frequency shift range and hence unlikely to align.

As discussed, the highest foreseeable power results from the longitudinal mode at 960 MHz for which over 95%, using the simulated coupling ratios, is extracted by the top HOM coupler (coupler 1). Using both punch parameter and mode parameter tolerances, this value increases to 1.5 times the threshold. Furthermore, the high frequency mode in the table (1250 MHz) is capable of generating 20% of the HOM power budget, and again, the majority of the power is extracted by the top HOM coupler.

For the HL-LHC infrastructure, the coaxial lines and RF loads connected to the top HOM coupler should be validated for the powers shown and the need for higher power handling evaluated.

7.6.3 HOM Power at Offsets

Referring to the measurements of the 748 MHz mode, it is clear that for modes which have a high longitudinal and transverse impedance, the contribution to the HOM power generally increases as a function of offset. This increase is quadratic for a dipole mode. As such, the HOM power variation as a result of an offset for each mode was investigated. The magnitude of the relationship between the longitudinal impedance and offset could be calculated knowing the axial longitudinal and transverse impedance in the plane of interest because, as defined by the Panofsky-Wenzel theorum [34], the transverse voltage is proportional to the gradient of the longitudinal voltage with offset. However, the relationship defined by the transverse impedance (or $r/Q_\perp$) is the square of this relationship and hence, unless the mode is a dipole mode with a voltage minima on the mechanical centre, the relationship between the voltage and offset is not representative of polarity. The axial voltage at several offsets was hence evaluated and the relationships between these and the on-axis voltage was used to scale the impedance tables.

The cumulative power was plotted against frequency for various ‘fills’. For Figs. 7.34a and 7.34b, an infinitely short pulse was applied, so that the entire impedance spectra is subjected to the same current. The plots show that the main deviation with respect to offsets is from that of the longitudinal mode at ∼581 MHz, increasing with negative and positive offsets in the vertical and horizontal planes respectively. Using a Gaussian bunch profile would reduce the power along the frequency range and hence the 581 MHz mode would still be the main contributor.

The case for multiple bunches is shown in Figs. 7.34c–7.34f. Here, a single train of 1000 bunches is used at both 25 and 50 ns bunch spacing respectively. It is clear that for 25 ns operation, the mode at 962 MHz is by far the largest contributor to power using the nominal impedance spectra. This mode varies quadratically in both directions with the larger deviation in the vertical plane.

If a 50 ns bunch spacing is used for the same number of bunches, the 581 and 701 MHz modes contribute more significantly to the power due to the bunch spacing harmonics near to these modes.

The main contributors to the HOM power using the nominal impedance spectra and 25 ns bunch spacing, is the 962 MHz mode. The $r/Q_\parallel$ of the high power mode increases quadratically as a function of offset in all directions (vertical/horizontal, +/-). The increase is around 10% for offsets less than 5 mm.

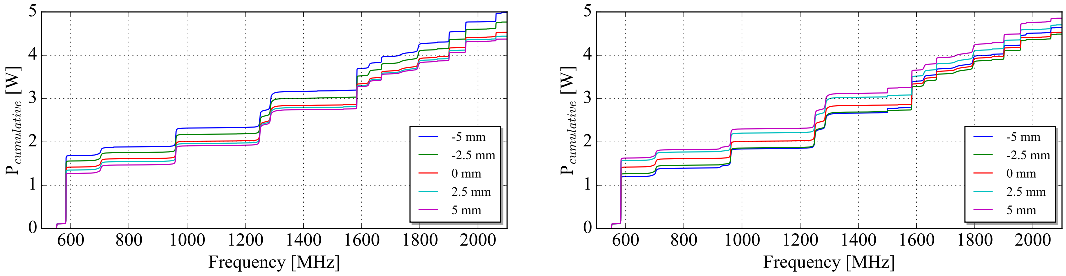

(a) Pulse - vertical offset (b) Pulse - horizontal offset

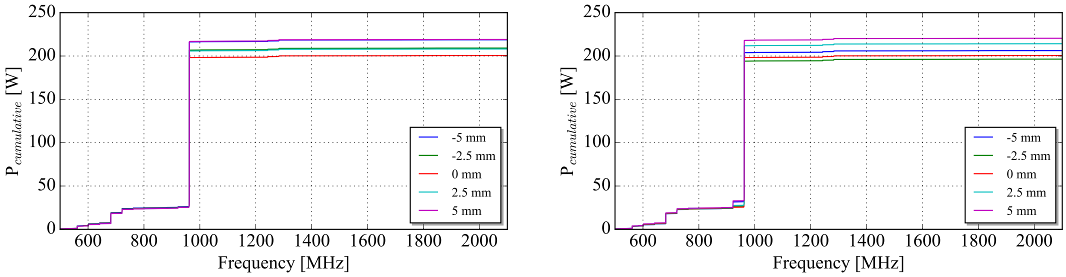

(c) Multi-bunch ($t_{bb} = 25ns$) - vertical offset. (d) Multi-bunch ($t_{bb} = 25ns$) - horizontal offset

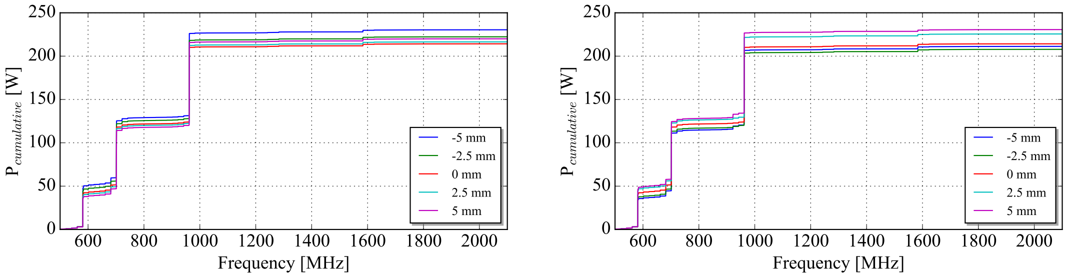

(e) Multi-bunch ($t_{bb} = 50ns$) - vertical offset (f) Multi-bunch ($t_{bb} = 50ns$) - vertical offset

Figure 7.34: Cumulative power for various filling schemes with offsets in both the vertical and horizontal planes.

7.7 SPS Crab Cavity Test Summary, Conclusions and Outlook

As discussed in the chapter introduction, the purpose of the HOM measurements was to asses the validity of the analytic calculations and simulations. The main conclusions and outcomes are presented hereafter.

As already found from the cold test measurements, the frequency of the high power mode at 960 MHz increased by $\sim$ 3.3 and 3.5 MHz for cavity one and two respectively. This measurement shows that it is possible, due to manufacturing and tuning procedures, for this mode to increase in frequency to that of the 24^{th} bunch spacing harmonic. The impedance spectra at this frequency is again shown to present the mode shift with respect to the frequency of the bunch spacing harmonic.

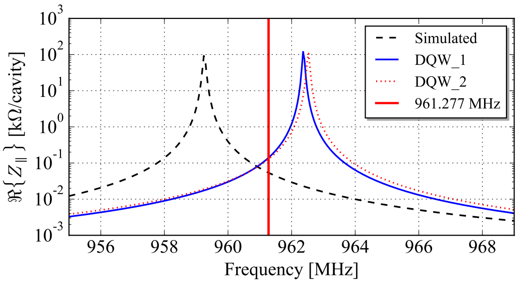

Figure 7.35: Simulated and altered impedance spectra for both cavities: 960 MHz mode annotated with closest bunch spacing harmonic. Note, the vertical line represents the 24^{th} bunch spacing harmonic in the SPS. The frequency of the harmonic in the LHC is 961.92 MHz and as such is closer to the 'manufactured' frequenies.

Single-bunch measurements

Broadband and narrowband measurements were compared with analytic calculations. This showed that it is possible to have large disagreements between the simulated and measured HOM power, with small errors on the charged particle bunch parameters. Deviations from the nominal to the maximum of over 12 dB were shown to be feasible for the high power mode. In following tests, measurements of the bunch profile showed that the first bunch in a multi-bunch train had a higher low frequency content that expected (shorter bunch length and higher μ coefficient) This could in-part explain the discrepancies between the analytic and measured data-sets, but the bunch profile was not measured in the single bunch tests and hence it is difficult to conclusively attribute the discrepancy to a shorter 'more-Guassian' profile associated with the first bunch injected. The need for profile measurements in every test was highlighted.

A broadband discrepancy was measured at the frequency of a transverse mode (horizontal) at $\sim 1.75\,\text{GHz}$ which is only damped by the hybrid beam-pipe pick-up (fundamental pick-up and HOM damper). Measurements verified that the discrepancy was due to a mismatch on the hybrid damper resulting from the use of a band-pass filter centred at the fundamental mode frequency. Additionally, a discrepancy in the feed-through and load impedance was found. Alterations and re-designs for HL-LHC infrastructure have ensued from the observations.

Mode 'coupling ratios' were simulated and quantified in measurements. For the first two longitudinal modes, the simulated coupling varied drastically from the measured. This was attributed to the location of the sharp peak of the HOM coupler's transmission profile at this frequency range which is very sensitive to manufacturing tolerances. Furthermore, the mode capable of producing the most HOM power (960 MHz) couples only to the top HOM coupler in both simulations and measurements.

Bunch profile measurements

The large variations in predicted HOM power at certain frequencies due to bunch parameter variations prompted a study to quantify the bunch profile. Bunch proile measuremesnts were taken and the deviation from the nominal was quantified as: μ: ±0.5, bunch-length: ±10%.

Multi-bunch measurements

Measurements were taken at the frequencies of the bunch spacing harmonics and at four high power modes. The measured data was compared to an analytic window, using the bunch parameter deviations quantified, in each case. The general conclusion made was that the closer the frequency of evaluation to a bunch spacing harmonic, i.e. where there is high spectral content of the beam, the more predictable the HOM power is. As such the bunch spacing harmonic frequencies were predictable and the high power mode, although at the upper limit, was generally within the window.

The power, and hence $r/Q_{||}$, variation as a function of offset was measured for a low frequency transverse (vertical) mode. The variation was compared to simulations with good agreement. Applying an offset of -0.6 mm to the measured data-set gave a much better agreement to the simulated. This deviation suggests that the mode topology has changed which challenges the current beam offset limitations which do not take this possibility into account.

Studies

Two studies resulted from the analysis:

1. HOM power evaluation taking into account bunch parameter variations for HL-LHC.
    - Both of the HL-LHC crab cavities (DQW and RFD) were assessed.
    - Stochastic variations on the mode and bunch parameters showed the increase in the simulated worst-case power to be 70% and 30% for the DQW and RFD respectively.
    - A plot of the HOM power as a function of frequency of the detrimental mode in each cavity was evaluated, with ranges corresponding to mode and bunch parameter deviations. The frequency shifts measured thus far were annotated.
    - As both cavities could produce over the threshold in the worst case, mode frequency shift limits were proposed for assessment during the manufacturing stages.
2. Maximum power for each HOM coupler.
    - The worst case power for three ‘high-power’ modes was evaluated.
    - The highest power results from the interaction of the 960 MHz mode and the 24^{th} bunch spacing harmonic and, using both bunch profile and

mode parameter tolerances, the highest foreseeable power is 1.5 times the threshold.

- A high frequency mode at 1250 MHz is also capable of producing 20% of the power threshold for which 70% of this power is extracted by the top HOM coupler.
- The studies prompt infrastructure evaluation for the higher power handling seen by the top HOM coupler for the HL-LHC cavities.

3. HOM power variations with offset.
    - The effect of mode offset on the nominal HL-LHC DQW impedance spectra was evaluated.
    - With 25 ns bunch spacing, the $r/Q_{\|}$ of the high power mode (960 MHz) increases as a function of offset in all directions (vertical/horizontal, +/-). The increase is around 10% for offsets less than 5 mm.

Outlook

The main piece of information from the SPS tests with respect to the higher order modes, was the magnitude of the effect of bunch tolerances. Currently, whilst the mode parameters are shifted, the bunch parameters are 'static' for the simulations of HOM power. The bunch parameter, profile and tolerances for the HL-LHC should hence be further investigated in the future, applying the foreseen deviations from the nominal in simulations. With respect to the measurement goals in the opening of this chapter, the magnitude of the high power modes and bunch spacing harmonics can be predicted analytically, but only if the bunch profile tolerances are taking into account.

Notably, for the high power mode in the DQW crab cavity, the resonant frequency is close to a 'node' in the SPS bunch profile used for testing. However, since the bunch length in the HL-LHC is much smaller, the node moves higher in frequency. This means that although the current will be higher at the high power mode frequency ($\sim$ 960 MHz) with the HL-LHC bunch, the magnitude of the current will change significantly less with bunch parameter changes. However, the node will be closer to higher frequency modes and as such, studies into the effect of bunch parameter tolerances are still necessary.

For future measurements, i.e. RFD in SPS and HL-LHC measurements, although the individual coupler measurements were useful in detailing the load associated with each ancillary, the signals should be ‘combined’ to have a constant measurement of the cavity HOM power.

Chapter 8

Conclusion

8.1 Overview of the Work Presented in this Thesis

8.1.1 Crab Cavity Impedance and Power

The operation of the Higher Order Mode (HOM) coupler designed for the preliminary beam tests of the Double Quarter Wave (DQW) crab cavity in CERN's Super Proton Synchrotron (SPS) was analysed in detail, using both equivalent circuit modelling and 3D electromagnetic simulations. The dressed cavity impedance, in both the transverse and longitudinal planes, was calculated. For installation into the LHC as part of the HL-LHC upgrade, some modes did not meet the impedance threshold.

Prior to installation on the cavity, each HOM coupler was characterised using a 'test-box' designed to replicate the transmission response of the HOM coupler in the frequency domain. The deviations from the simulated response were quantified for the 400 MHz stop-band and pass-band sections. It was concluded that the test-box was not capable of accurately measuring the stop-band frequency, but the frequency and amplitude of the pass-bands could be accurately measured. One pass-band was identified as deviating from the simulated case.

Dressed cavity HOM parameter measurements were compared to simulations and the HOM parameter shifts were quantified. Notably, two modes at 685 and

701 MHz were seen to increase in quality factor significantly from that of the simulations. Using the measured mode parameter deviations, the expected average and worst case HOM power was calculated. A HOM at $\sim$ 960 MHz was identified as capable of generating multiple kilowatts due to its large longitudinal impedance and frequency close to that of the 24^{th} bunch spacing harmonic.

The measured HOM parameter deviations from the simulations were compared to the change in transmission of the HOM couplers quantified by the test-box measurements. The test-box measurements predicted the 'under-damping' of the modes at 685 and 701 MHz. The feasibility of pre-installation damping analysis is hence verified. It was not possible to calculate the exact value of the mode's quality factor as the location of each HOM coupler (i.e. which port it was installed on) was unknown.

8.1.2 HOM Coupler Re-Design

A HOM coupler re-design was launched to improve damping to the high-power HOM as well as HOMs above the impedance threshold. Coupled with geometric alterations to reduce difficulties associated with manufacture, a new design was proposed (Fig. 8.1).

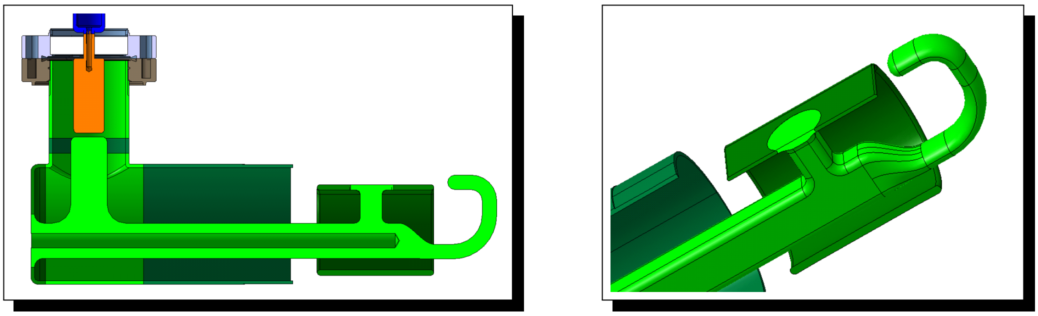
(a) (b)

Figure 8.1: CAD renders of the DQW HOM coupler re-design for the HL-LHC. CAD model by F. Eriksson.

The modified design damps all modes apart from three to within the threshold value. The modes over the threshold are confirmed as acceptable for stability [124]. The impedance of the high power 960 MHz mode was altered to result in no more than 1 kW of power in the worst case, taking into account mode parameter shifts.

Fundamental operation, multipacting, thermal and impact on mutlipolar components were quantified and accepted.

In parallel, a new HOM damping concept was proposed. The design uses a quarter wave resonance to provide a rejection at the frequency of the cavity's operational mode. The filter then acts as a pass-band until the next odd-harmonic of the coupler's resonance. The coupler is very simple to manufacture and as such would reduce costs and machining time. The coupler was benchmarked against that of the SPS and LHC DQW HOM couplers. Whilst the broadband damping and rejection of the fundamental mode was sufficient, the main drawback of the design is the dynamic heat load on the copper gasket. Unless a superconducting gasket is used, it is very difficult to design a HOM coupler without a rejection filter placed before the gasket location for the case of 'on-cell' damping (defined in Chapter 2).

8.1.3 First test of a Crab Cavity with Proton Bunches

To identify unforeseen risks, and demonstrate operation, the crab cavities for the HL-LHC upgrade were scheduled for tests in the SPS. Tests of the Double Quarter Wave (DQW) crab cavity (two cavity cryomodule) took place in 2018. A test stand for taking HOM measurements was set-up.

To provide the analytical reference for comparison, the simulated impedance spectra were altered using the measured frequency and quality factor values from the cryomodule 'cold-test'. Broadband measurements showed the power spectra as expected, with the mode frequency and quality factors well predicted for the two cavities. However, disparities between the measured and analytic amplitudes were observed. It was later found that this could be a result of a 'more-Gaussian' profile associated with the first bunch injected, but there was not enough information on the bunch profile in the single bunch tests.

Single mode measurements from each of the six HOM couplers allowed a more detailed analysis of low frequency, high impedance modes. It became evident that there was a deviation in power between each of the three HOM couplers on each cavity for the same beam conditions. The coupling ratios for each of the low frequency modes were hence evaluated in both simulations and measurements. Tolerances on the HOM coupler geometries, alignments and insertion depths meant deviations from the simulations were observed as well as inter-cavity differences. All of the power from the 960 MHz mode was seen through the top HOM coupler in both simulations and measurements.

The dependence of HOM power with the number of bunches was simulated and measured. If the mode lies at any frequency apart from that of a bunch spacing harmonic, the power has a periodic dependence with the number of bunches. Hence, the highest power does not necessarily correspond with the highest intensity.

The variation of voltage as a function of offset was measured and compared with simulations. This verified the methods used to assess the impedance as a function of offset, but raised the notion that the electrical centre of a transverse mode could move, meaning a higher contribution to beam instabilities than predicted at the same beam X-Y position. The power as a function of offset for the HL-LHC case was checked and quantified.

The major conclusion from the tests in the SPS was that small variations in the bunch parameters can have a significant affect on the HOM power. For example, by applying the measured bunch parameter tolerances of ± 10% to the bunch length and ± 0.5 to the μ coefficient of the binomial profile, the expected power for the 960 MHz mode can vary by over 15 dB with the SPS bunch used for cavity testing. Therefore, with reference to the measurement goal of predicting the HOM power analytically, the magnitude of the high power modes and bunch spacing harmonics can be predicted analytically, but only if the bunch profile tolerances are taking into account. Although the bunch profile deviation at the frequency of the DQW's high power mode is significantly less with the HL-LHC bunch characteristics, future HOM analysis should still include bunch tolerance studies for the full frequency spectrum, especially near 'nodes' of the binomial profile.

A plot of the power generated by the most detrimental longitudinal modes in both the DQW and RFD crab cavities as a function of frequency offset from the simulated was generated, showing a range at each frequency representing bunch parameter and mode quality factor deviations. An acceptance criteria for these two modes in all future crab cavities was defined.

8.2 Future Work

8.2.1 Further Analysis

The conclusions and lessons learnt from the SPS tests should be incorporated into further analysis for HOM performance with the HL-LHC beam. This should not only include the bunch parameter tolerances as discussed, which should be evaluated from LHC data and expertise, but also should explore the effect of different filling schemes (for example the filling 8b+4e filling scheme shown in Fig. 8.2). The effect of the different filling schemes used in commissioning, e.g. 50 ns bunch spacing, should also be investigated.

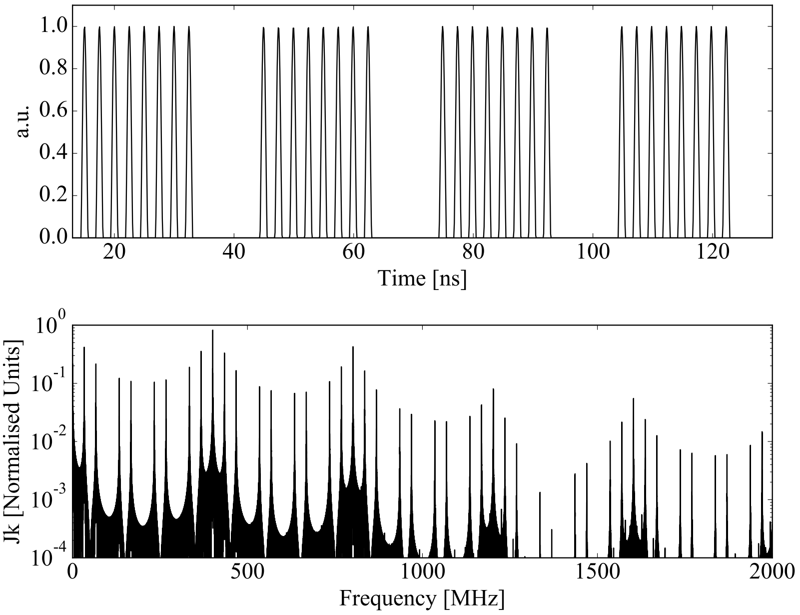

Figure 8.2: 8b+4e filling scheme.

8.2.2 Radio Frequency Dipole

The Radio Frequency Dipole (RFD) is the horizontal crabbing design proposed for HL-LHC. This cavity will be tested in the SPS in 2022. The same higher order mode analysis as that done for the DQW in this thesis should be applied in order to verify that the analytic predictions for the HL-LHC are accurate. As already presented, there is a mode with a high longitudinal impedance at 752 MHz which could produce multiple kilowatts with a frequency shift of over 1 MHz. Impedance analysis was started with benchmarking between solvers (ACE3P and CST [104, 150]) (Appendix Sec. 6). Additionally, the same pre-installation coupler characterisation using 'test-boxes' should be used. The proposed test box for the RFD HOM coupler is shown in Fig. 8.3.

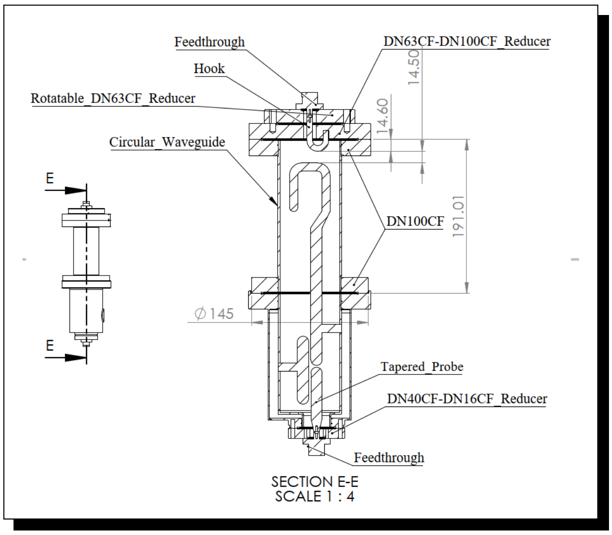

Figure 8.3: RFD low power transmission response test box. Image from the collection of drawing sheets included (page 255).

8.2.3 DQW HOM Coupler

Due to the impedance variation as a result of the feed-through ceramic window material, the window geometry and material should be investigated further alongside an effort to reduce the impedance of the longitudinal mode at 590 MHz. This should be done in parallel with matching the impedance to 25 Ω. The current status of these investigations are shown in Appendix Sec. 5. The choice of 25 Ω allows a bigger inner conductor through the ceramic window. This acts to decrease the mechanical stress on this piece and hence reducing the risk of damage in assembly, transport and installation[1].

For the SPS DQW HOM couplers, the low power test boxes were able to predict HOM quality factor deviations from the nominal simulated values. In the future, this measurement should be made part of the procedural qualification of the Higher Order Mode couplers. Furthermore, the port for which each coupler is installed onto should be optimised. For example, the high power mode at 960 MHz only couples to the top HOM coupler of the DQW. As such, the coupler with the highest transmission at this frequency should be used on the top of the cavity.

8.2.4 Applications of the Quarter-Wave Rejection Filter

The quarter wave rejection filter was shown to be a simple and cost-effective method of damping higher order modes. It's limitation is that it is not possible to use it in a high H-field region, i.e. as an 'on-cell' damper. The feasibility of using the quarter-wave rejection filter with other cavities should be explored. Superconducting accelerating cavities, in addition to having couplers installed onto the beam-pipes (lower H-field) have large beam pipe diameters, bring the cut-off frequency down to below the frequency of the first harmonic of the quarter wave resonance.

8.2.5 HOM Coupler Conditioning

Fundamental Power Coupler (FPC) and cavity RF conditioning at the frequency of the operational mode is routinely exercised across a wide range of accelerator systems. The conditioning involves steadily increasing the RF power level (pulse length and amplitude) whilst monitoring a dependant variable (e.g. vacuum level). Once the dependant variable reaches a threshold value, the RF drive is stopped and the power is again increased. This process is often coupled with the use of Amplitude and Frequency Modulation (AM and FM) and is carried out until the

---

[1] Problems have been seen with cryomodule transport for other accelerator systems such as that of LCLS-II [125].

required RF input power is achieved for a sustained time at the given duty cycle (may be specified as continuous wave). FPC conditioning [105, 151] is often done outside of the cavity on a ‘test-box’, validating their power handling capability and saving conditioning time in the machine (can take several days). In addition to reaching the operational RF power, the conditioning process reduces the amount of metallisation and avoids electrical discharge (and multipactor) and out-gassing. These phenomena can be particularly detrimental near to the coupler’s ceramic window.

For HOM couplers with a band-stop filter, the geometry after the filter, including the ceramic window, is not subjected to any power until beam enters the cavity. When beam enters the cavity, the power resulting from interaction with the cavity’s higher order modes is extracted by the couplers. The higher beam-currents ($\sim 1.1\,\mathrm{A}$ for HL-LHC) mean that the power extracted can be in the order of several kilowatts. For such high power HOMs, there is a strong case for pre-conditioning of HOM couplers before installation. The effects seen for the FPCs, i.e. metallisation, electrical discharge and out-gassing, could be apparent with the HOM couplers as soon as beam is injected. If a coupler fails, the whole cryomodule is off-line and as such the crabbing to one beam is removed. Furthermore, the finite lifetime of FPCs, presented in [105], can be lengthened with the correct conditioning procedure.

As discussed, applying a 400 MHz drive to the couplers would be shorted by the band-stop filter. It would still be possible to condition the couplers using the operational mode frequency, but it would have to be done so in ‘reflection’, i.e. by injecting RF power into one side of the coupler, and using a circulator to send the reflected power (a very large percentage of the input - only reduced by losses in the coupler and wall material) to a load. This would not allow the usual ‘transmission’ conditioning which is advantageous as it allows multiple couplers to be conditioned and a phase modulation to be easily applied by an RF trombone (ensuring every section of the coupler ‘sees’ the maxima of the RF drive signal).

Whilst broadband conditioning remains a challenge due to the cost of broadband RF amplifiers and the complexity of the ‘test-boxes’ required, conditioning at a single HOM frequency is feasible. As such the frequency of the mode responsible for the highest power generation in the DQW (960 MHz) was chosen. The

FPC test box, design shown in Appendix Sec. 8, uses a quarter wave resonator with a resonant mode at 400 MHz. The FPCs are installed and aligned to couple to the resonant mode and hence a high transmission between the two is possible. A similar concept was used for the HOM couplers. The quarter wave resonator and transmission characteristics are shown in Fig. 8.4. Following the conditioning at a single frequency, the need to condition at other HOM frequencies should be evaluated.

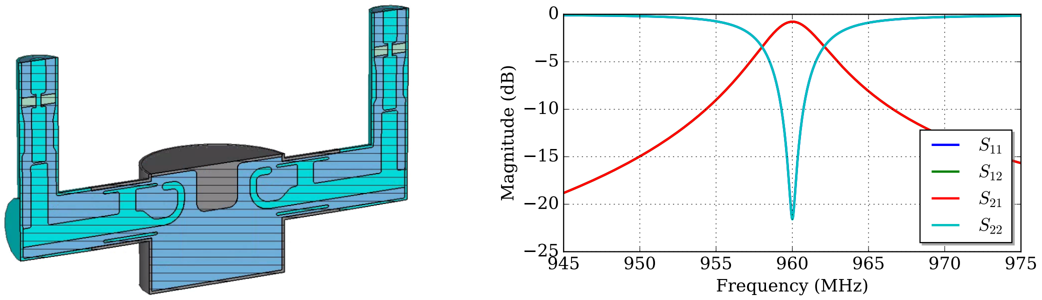

(a) CST MWS model. (b) S-Parameters.

Figure 8.4: 960 MHz QWR for HOM coupler RF conditioning.

As a proof-of-principle, a single HOM coupler conditioning system was designed and built. The set-up uses a simple cylindrical waveguide where one side had one of the spare SPS DQW HOM couplers mounted and the other had a coupling hook to allow RF transmission. Transmission frequencies were limited to those of the HOM coupler resonances (referred to as pass-bands) as any resonances associated with the waveguide would be too high in frequency. One advantage of conditioning in such a regime is that the majority of the RF losses are on the coupler geometries. The disadvantage is that it is not at the frequency of the cavity mode which will generate the highest power in the machine. The test-box design and S-Parameters are shown in Fig. 8.5.

The transmission characteristics of the test box show that conditioning in transmission is feasible. The conditioning system [105], will be implemented using a 500 W broadband amplifier. In addition to the location of any arcing and temperature rise, the time taken to condition the couplers to high power will indicate whether pre-installation HOM coupler conditioning is necessary.

If a long conditioning time is needed to reach an unperturbed vacuum level,

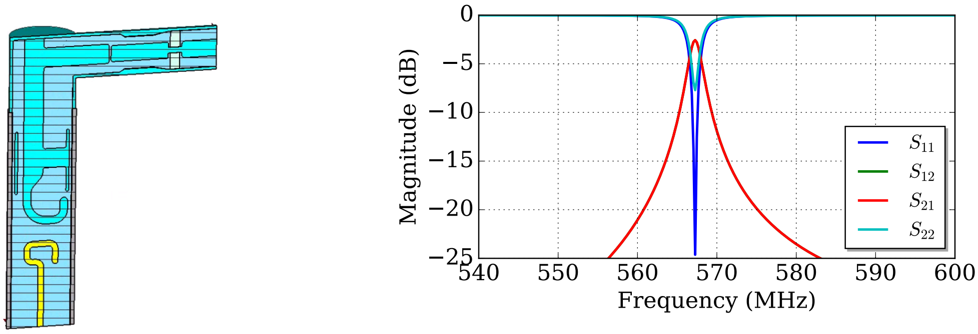

(a) CST MWS Model.

(b) Simulated transmission characteristics at the first pass-band.

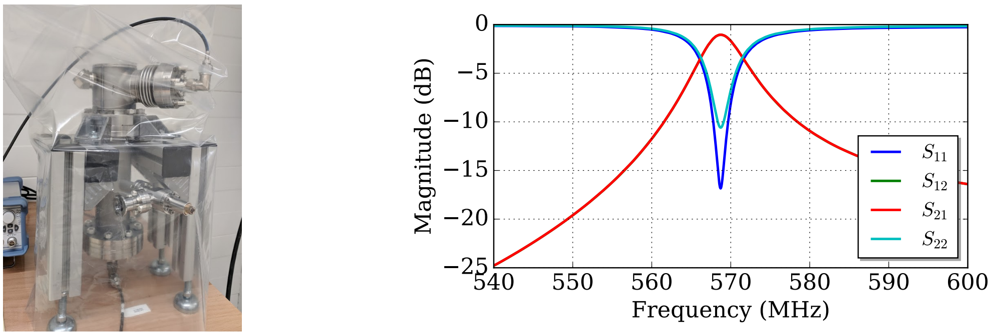

(c) Manufactured test-box.

(d) Measured transmission characteristics at the first pass-band.

Figure 8.5: Proof-of-Principle (PoP) HOM coupler conditioning test-box.

then the excitation of high impedance higher order modes by the beam (i.e. the first time the HOM couplers would see field without pre-conditioning) would cause vacuum break-down. The filling scheme could be gradually changed to condition the HOM couplers, however, depending on the time that this takes, it could be a costly procedure, adding additional commissioning time to the HL-LHC. The proof-of-principle HOM coupler conditioning will hence provide an insight into the necessity of the pre-installation conditioning of higher order mode couplers when dealing with high beam currents and high impedance HOMs.

Appendix

1 Crab Cavity Layout

Figure 6 shows the layout evolution for the crab cavities. Note, the figure is not to scale and does not include any other infrastructure.

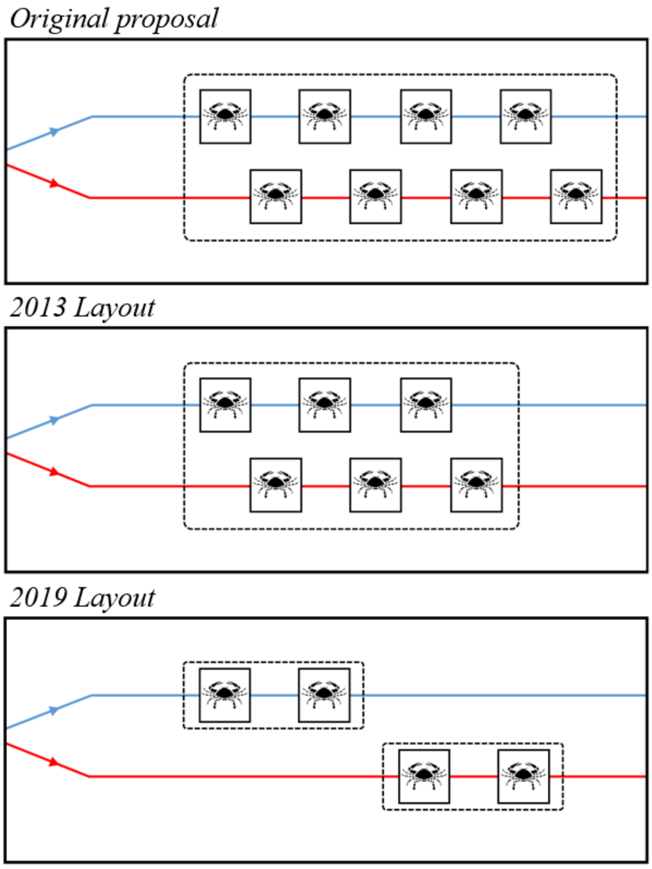

Figure 6: Crab cavity layout evolution at one side of the IP.

2 Superconductivity History

The crab cavities are made from niobium and are cooled to operate in the superconducting regime. For this reason, the concept and history of superconductivity is presented here. The application of superconductivity to the RF cavity will be discussed, presenting advantages and disadvantages, and a selection of superconducting RF cavities in operation will be shown.

For a selection of materials, with subjection to a DC source, it is possible to observe zero electrical resistance and the expulsion of magnetic flux when cooled below a certain (critical) temperature. This phenomenon is called superconductivity and was discovered by Heike Kamerlingh Onnes in 1911 [35, 36]. The discovery was twinned with the discovery of the superfluid transition of helium at 2.2 K. Like superconductivity it is a zero-resistance phenomena, but rather than zero opposition to electron flow, superfluidity is the frictionless flow of liquid through a channel [37, 38].

Following Onnes' discovery, a first insight into understanding superconductivity was made when Meissner and Ochsenfeld in 1933 with the discovery of the Meissner effect [152]. The effect is the expulsion of magnetic flux observed by a superconductor.

An explanation for the Meissner effect was arrived upon in 1935 by the London theory [153]. The theory presents two core equations. The first equation defines the collision-less propagation of a super-electron in a perfect conductor and the second defines the Meissner effect. The equations are used to represent the electrodynamic behaviour of a superconductor. The ability of these equations to fully and accurately achieve this is a topic of dispute in the materials science community. Although this is too in-depth for this thesis, more information can be found in [154] and [155].

'Conventional' theories for superconductivity were brought about in the 1950's in the form of the Ginzburg-Landau theory and the BCS theory. The prior, originally documented in [156] with English versions published later in [157] and [158], gives a theory to the macroscopic behaviour of superconductors. The theory gave a basis for A. Abrikosov to separate superconducting materials into two categories [159, 160]: Type I and type II.

To detail type I and type II superconductors, the differences in their responses to an applied magnetic field should be evaluated. If applied to a type I superconductor, the field is fully repelled up to a material specific critical field H_c. Above this field level the material no longer operates in the superconducting regime. For the case of a type II superconductor, the field is again fully repelled up to a critical field. However unlike the type I superconductor, the ability to repel magnetic flux does not stop at this field level and hence is denoted as H_{c1}. After this level, due to magnetic vortices in the superconductor [161] creating localised areas of normal conductivity, the metal's ability to repel magnetic flux reduces, but it stays in the superconducting state until field level higher then H_c, denoted H_{c2}. Figure. 7 shows the magnetisation of the two types of superconductors as a function of applied magnetic field.

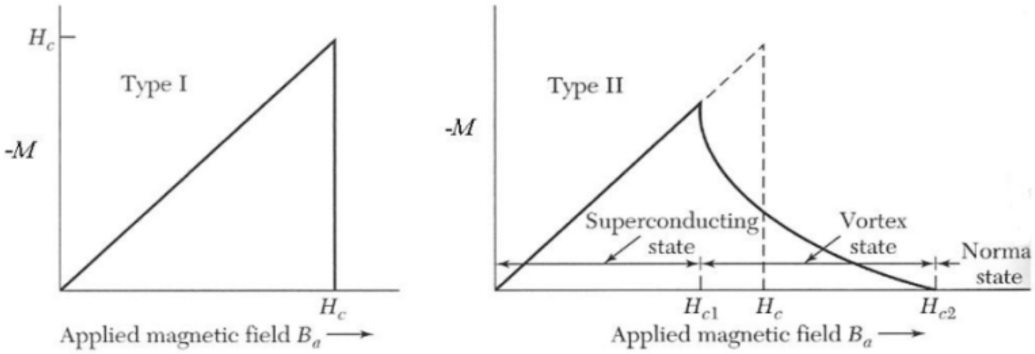

Figure 7: Magnetisation of type I (left) and type II (right) superconductors as a function of applied magnetic field. Image from [161].

The second conventional theory, the BCS theory, is named after it's founders *Bardeen*, *Cooper* and *Schrieffer* and provided a microscopic theory into the electron behaviour in the superconducting regime. The theory [39] describes the unperturbed superconducting current as a super fluid of pairs of electrons (Cooper pairs) interacting through phonon exchanges. The Cooper pairs separate at the critical temperature of the superconductor T_c when the material enters the normal conducting state.

3 SPS DQW HOM Vector Plots

Figure 8 shows the low frequency, high impedance mode field patterns for the DQW crab cavity.

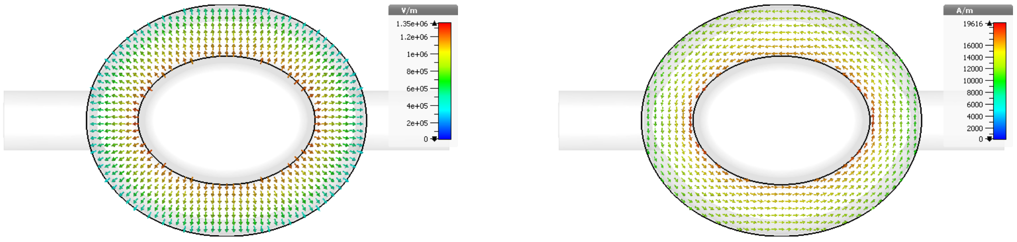

(a) 592 MHz - E-Field. (b) 592 MHz - H-Field.

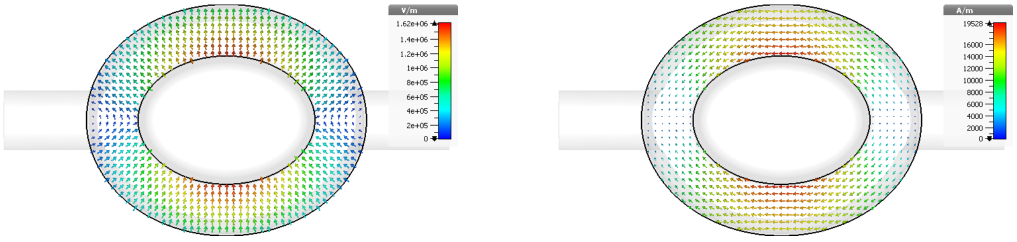

(c) 685 MHz - E-Field. (d) 685 MHz - H-Field.

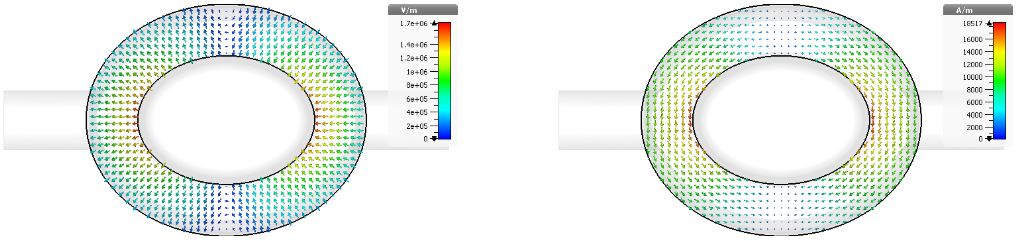

(e) 748 MHz - E-Field. (f) 748 MHz - H-Field.

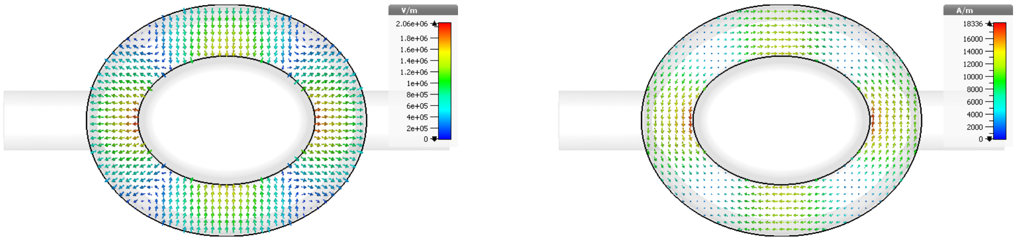

(g) 960 MHz - E-Field. (h) 960 MHz - H-Field.

Figure 8: Field profiles for high impedance higher order modes in the bare SPS DQW crab cavity.

4 Effect of the New Jacket Geometry on the Band-Stop Filter Capacitance

As an approximation, the jacket was split into two sections represented by ‘C1’ and ‘C2’. Parallel plate approximations for both capacitances were calculated where the average distance between C1 and the outer wall was used as in the parallel plate approximation for this variable. The capacitance was calculated as a function of the angle at which C1 intersected with C2 and is shown in Fig. 9.

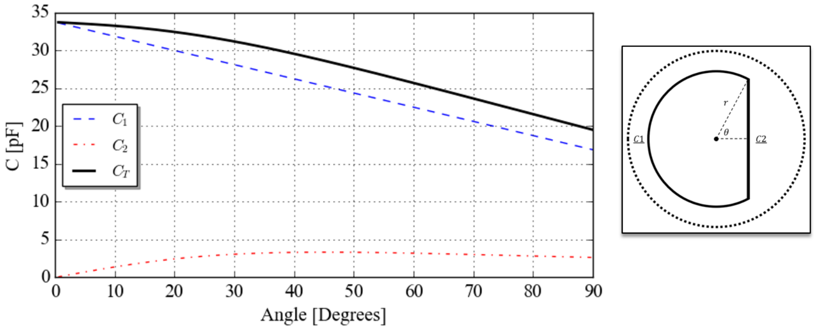

Figure 9: Dependence of the band-stop filter capacitance on the angle of intersection with the flat face.

At an angle of 0° the capacitance is only determined by C1 and is hence the same as that of the nominal SPS DQW HOM coupler. As the angle increases, the capacitance decreases and as a result, the band stop frequency also decreases. Furthermore, as the angle increases, the length of the inductive stub also decreases which also acts to decrease the notch frequency.

5 Matching to 25 Ohms

In an effort to increase the strength of the inner conductor at the feedthrough ceramic locations, studies into matching the crab cavity ancillaries at 25 Ω are on-going. The impedance spectra for the DQW is shown in Fig. 10.

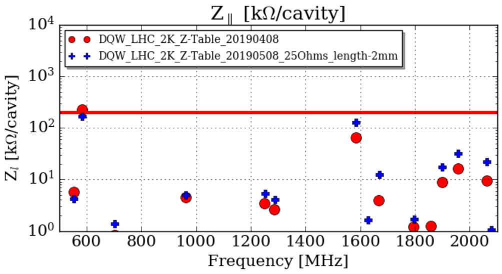

(a) Longitudinal.

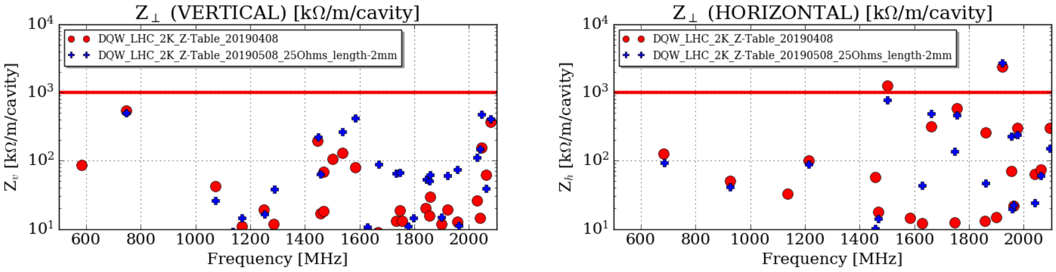

(b) Vertical.

(c) Horizontal.

Figure 10: DQW impedance spectra with 25 Ω matching.

6 Benchmarking ACE3P and CST

Benchmarking the RFD crab cavity shows strong agreement between both solvers. Any disagreements are generally a result of high quality factor modes for which the lower meshed CST simulation was not converged.

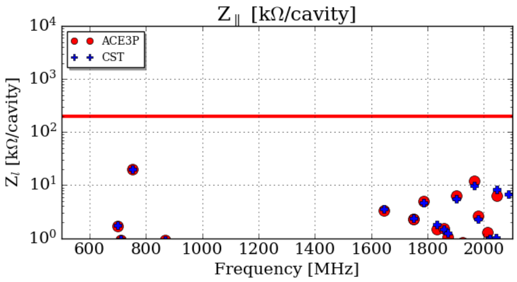

(a) Longitudinal.

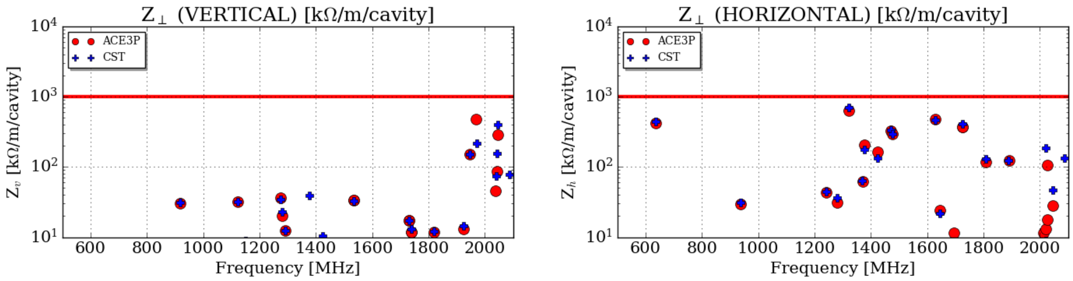

(b) Vertical.

(c) Horizontal.

Figure 11: RFD impedance spectra in both CST MWS and ACE3P.

7 HOM Power Assessment using the HL-LHC Filling Scheme

To evaluate whether the assumption that modelling the beam as a continuous train of bunches is a valid assumption for the HOM power, the stochastic power (moving the frequency and quality factor of each mode) was compared for a case with a continuous train and using the HL-LHC filling scheme [111]. The comparison is seen in Fig. 12 and a negligible difference was seen between the two models.

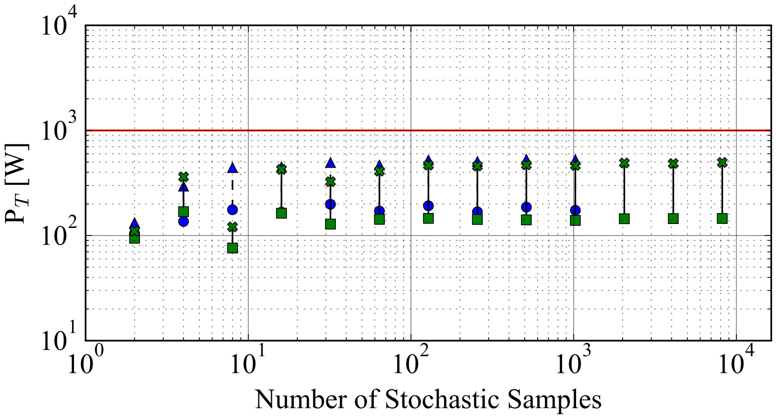

Figure 12: Total HOM power as a function of HOM parameter stochastic deviation samples for the 'LHC DQW' HOM couplers installed onto the DQW crab cavity. The average and maximum values are given for each stochastic sample set. The blue circle to triangle do not take into account the filling scheme, i.e. use a continuous train of bunches, and the green square to cross use the HL-LHC filling scheme.

8 FPC Test Box

The FPC test box is used to condition the FPC's for the crab cavities. Without detail, images and plots are shown for reference.

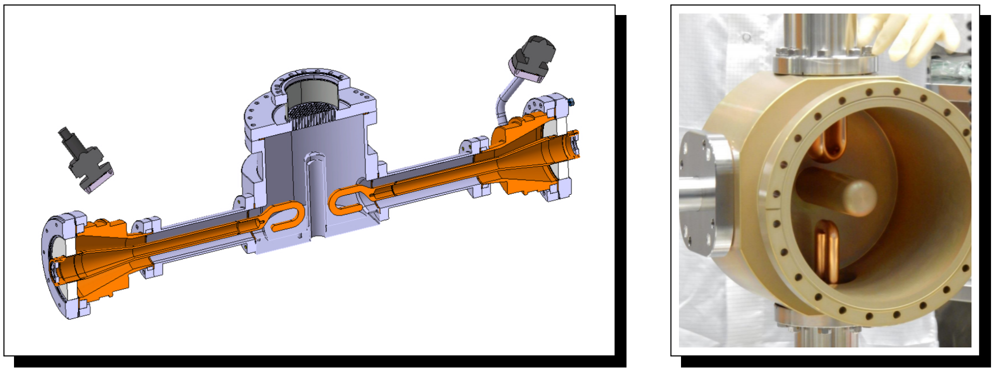

(a) CAD Render.

(b) Photo.

Figure 13: QWR test box designed for RF conditioning of the crab cavity Fundamental Power Couplers FPCs. Images from [162].

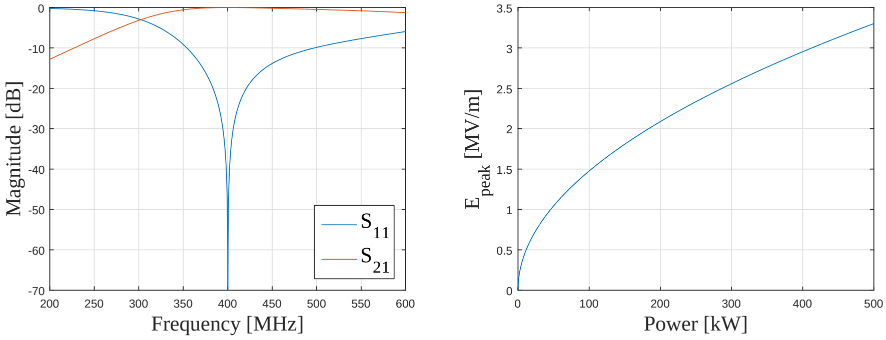

Figure 14: S_{11}, S_{21} (left) and the electric peak field value corresponding to a power range of 0 - 500 kW (right) for the DQW FPC conditioning test box.

Drawing Sheets

The following pages detail mechanical drawing sheets referenced throughout the thesis. DQW LHC HOM ancillary drawings are provided by BE-RF-PM (S. Calvo and F. Eriksson – 07/03/2019). Due to the continued design evolution, the drawings are not in their final state, but rather represent a reference for visualisation and discussion.

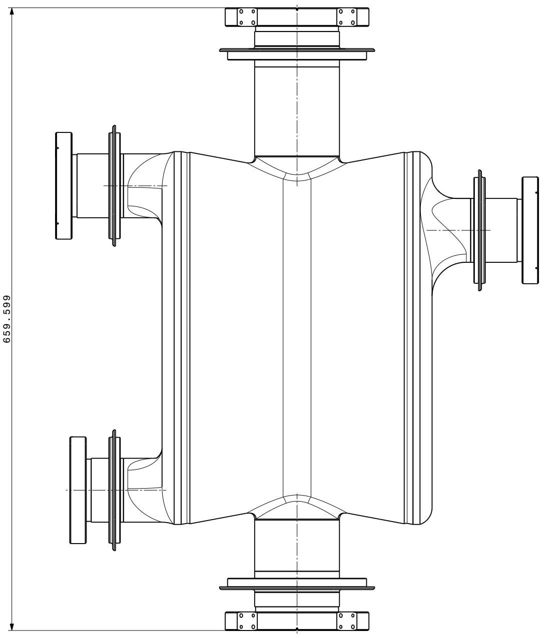
659.599

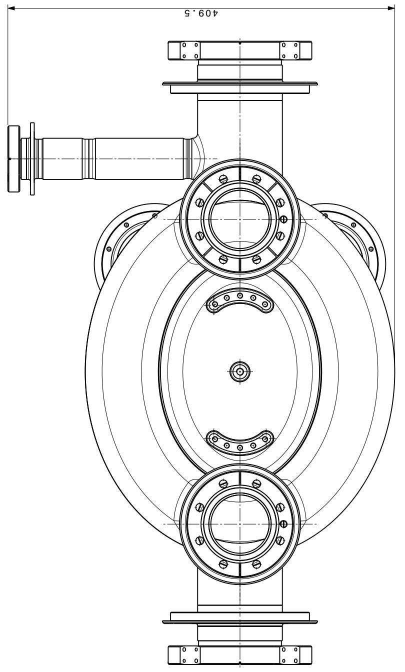
409.5

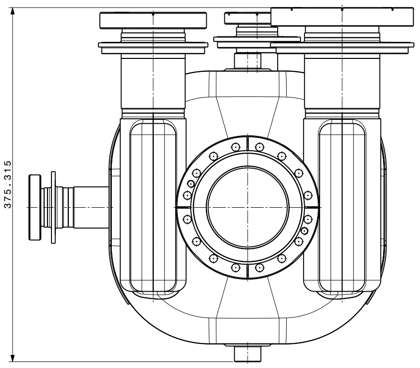
375.315

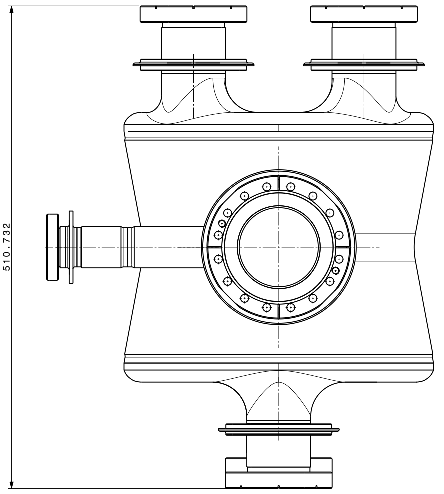
510.732

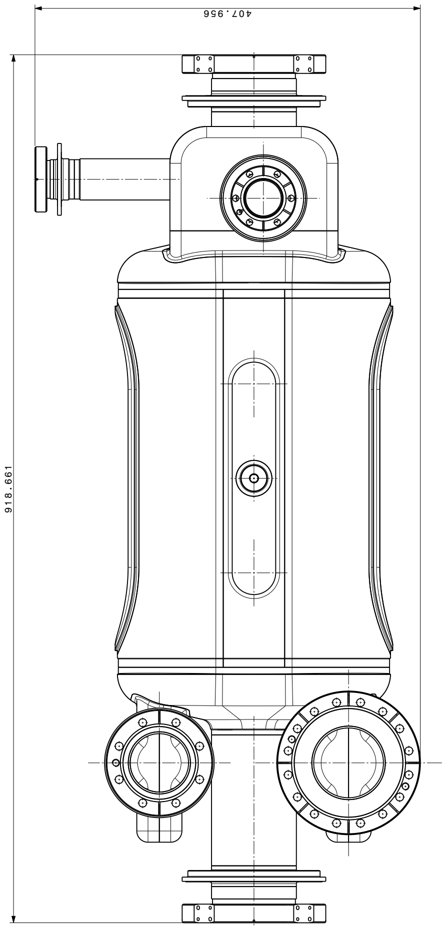
407.956
918.661

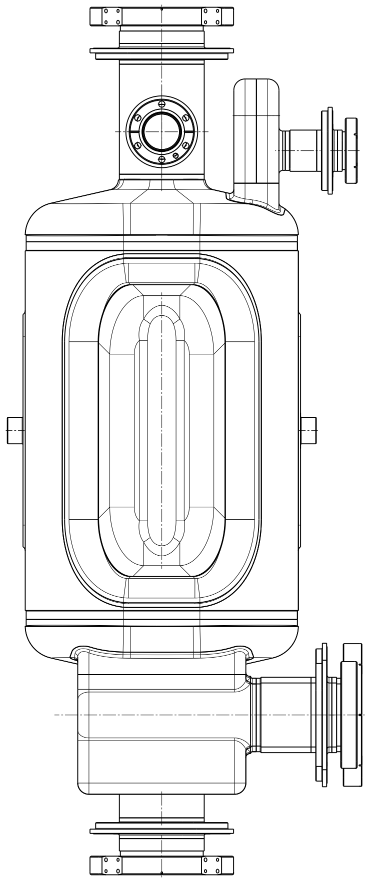

RFD
HOM coupler test box

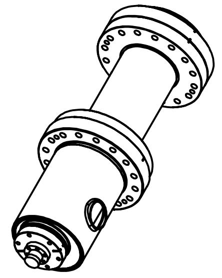

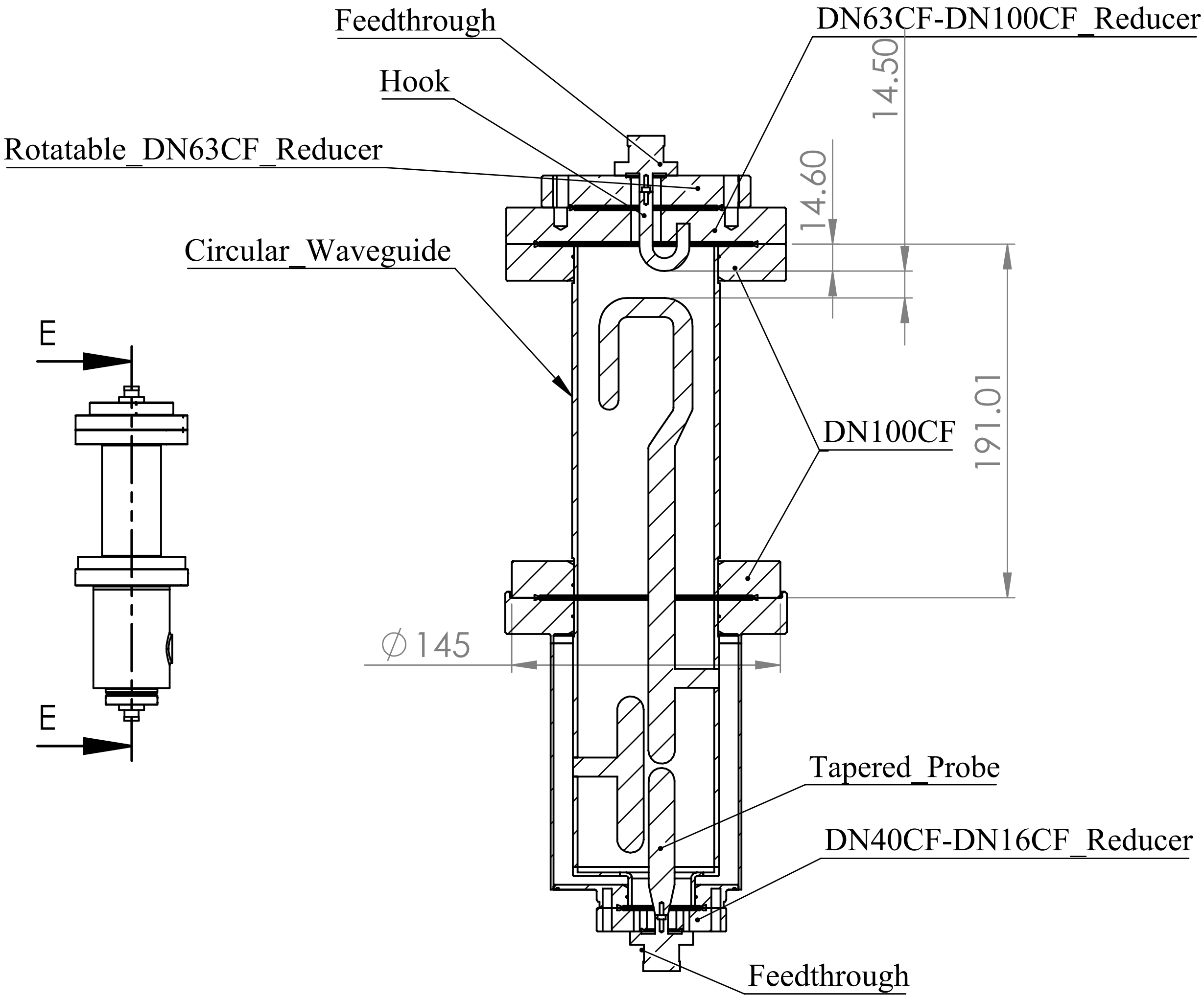

SECTION E-E
SCALE 1 : 4

UNLESS OTHERWISE SPECIFIED:
DIMENSIONS ARE IN MILLIMETERS
SURFACE FINISH:
TOLERANCES:
LINEAR:
ANGULAR:

FINISH:

DEBURR AND
BREAK SHARP
EDGES

DO NOT SCALE DRAWING

REVISION

	NAME	SIGNATURE	DATE
DRAWN			
CHK'D			
APPV'D			
MFG			
Q.A			

MATERIAL:

TITLE:

DWG NO.
RFD_Test_Box

A4

WEIGHT:

SCALE:1:10

SHEET 1 OF 1

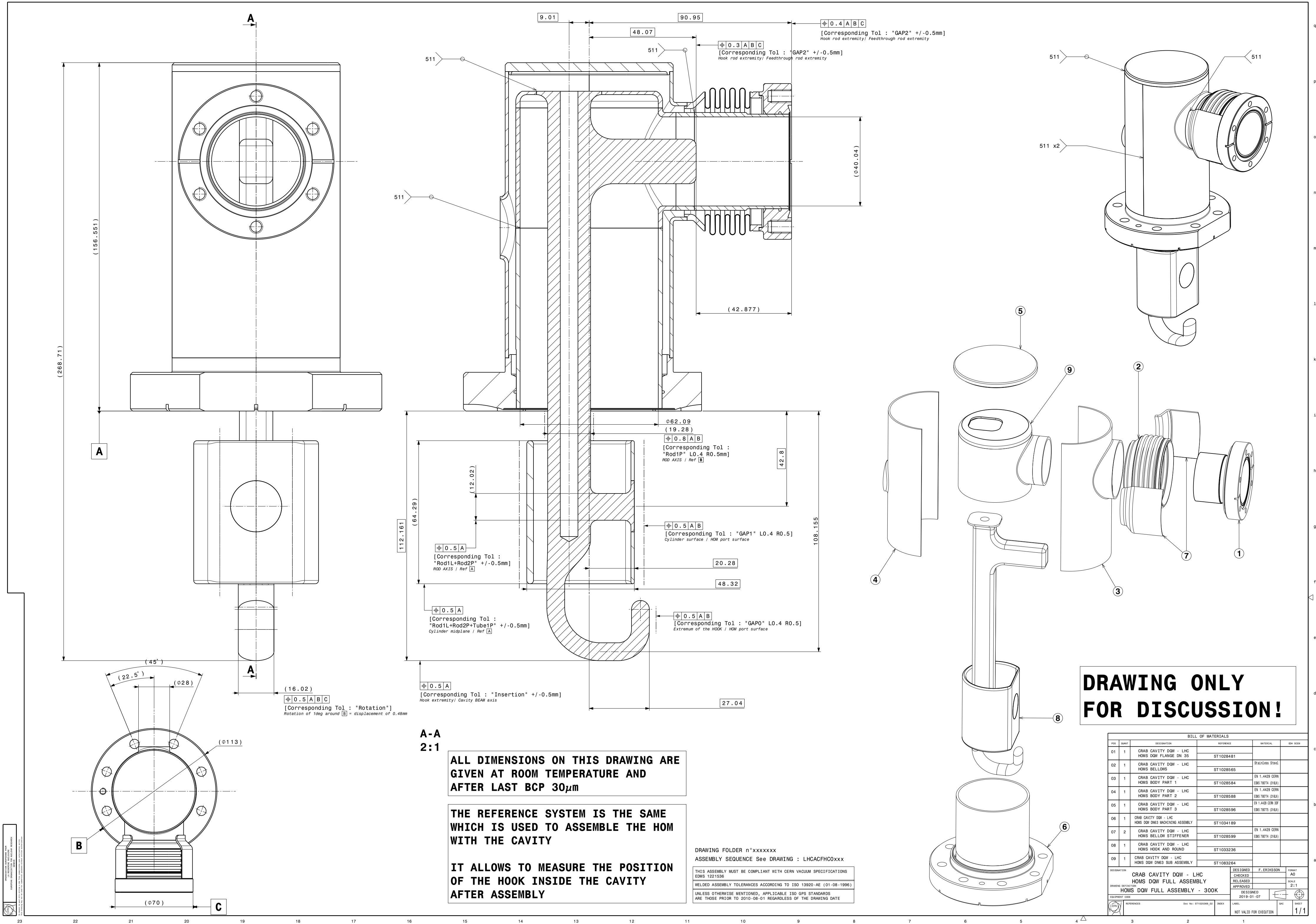

A-A
2:1

ALL DIMENSIONS ON THIS DRAWING ARE GIVEN AT ROOM TEMPERATURE AND AFTER LAST BCP 30μm

THE REFERENCE SYSTEM IS THE SAME WHICH IS USED TO ASSEMBLE THE HOM WITH THE CAVITY

IT ALLOWS TO MEASURE THE POSITION OF THE HOOK INSIDE THE CAVITY AFTER ASSEMBLY

DRAWING FOLDER n°xxxxxxx
ASSEMBLY SEQUENCE See DRAWING : LHCACFHCOxxx

THIS ASSEMBLY MUST BE COMPLIANT WITH CERN VACUUM SPECIFICATIONS EDMS 1221536

WELDED ASSEMBLY TOLERANCES ACCORDING TO ISO 13920-AE (01-08-1996)

UNLESS OTHERWISE MENTIONED, APPLICABLE ISO GPS STANDARDS ARE THOSE PRIOR TO 2010-08-01 REGARDLESS OF THE DRAWING DATE

DRAWING ONLY FOR DISCUSSION!

BILL OF MATERIALS

POS	QUANT	DESIGNATION	REFERENCE	MATERIAL	EDH SCEM
01	1	CRAB CAVITY DQW - LHC HOMS DQW FLANGE DN 35	ST1028481		
02	1	CRAB CAVITY DQW - LHC HOMS BELLOWS	ST1028565	Stainless Steel	
03	1	CRAB CAVITY DQW - LHC HOMS BODY PART 1	ST1028584	EN 1.4429 CERN EDMS 790774 (316LN)	
04	1	CRAB CAVITY DQW - LHC HOMS BODY PART 2	ST1028588	EN 1.4429 CERN EDMS 790774 (316LN)	
05	1	CRAB CAVITY DQW - LHC HOMS BODY PART 3	ST1028596	EN 1.4429 CERN 3DF EDMS 790775 (316LN)	
06	1	CRAB CAVITY DQW - LHC HOMS DQW DN63 MACHINING ASSEMBLY	ST1034189		
07	2	CRAB CAVITY DQW - LHC HOMS BELLOW STIFFENER	ST1028599	EN 1.4429 CERN EDMS 790774 (316LN)	
08	1	CRAB CAVITY DQW - LHC HOMS HOOK AND ROUND	ST1033236		
09	1	CRAB CAVITY DQW - LHC HOMS DQW DN63 SUB ASSEMBLY	ST1083264		

DESIGNATION
CRAB CAVITY DQW - LHC
HOMS DQW FULL ASSEMBLY
DRAWING DEFINITION
HOMS DQW FULL ASSEMBLY - 300K
EQUIPMENT CODE

DESIGNED	F.ERIKSSON	FORMAT	A0
CHECKED		SCALE	2:1
RELEASED			
APPROVED			

DESIGNED
2019-01-07

CERN
REFERENCES
Doc No: ST1025369_02
INDEX
LABEL
NOT VALID FOR EXECUTION
QAC
SHEET
1/1

A-A
1:1

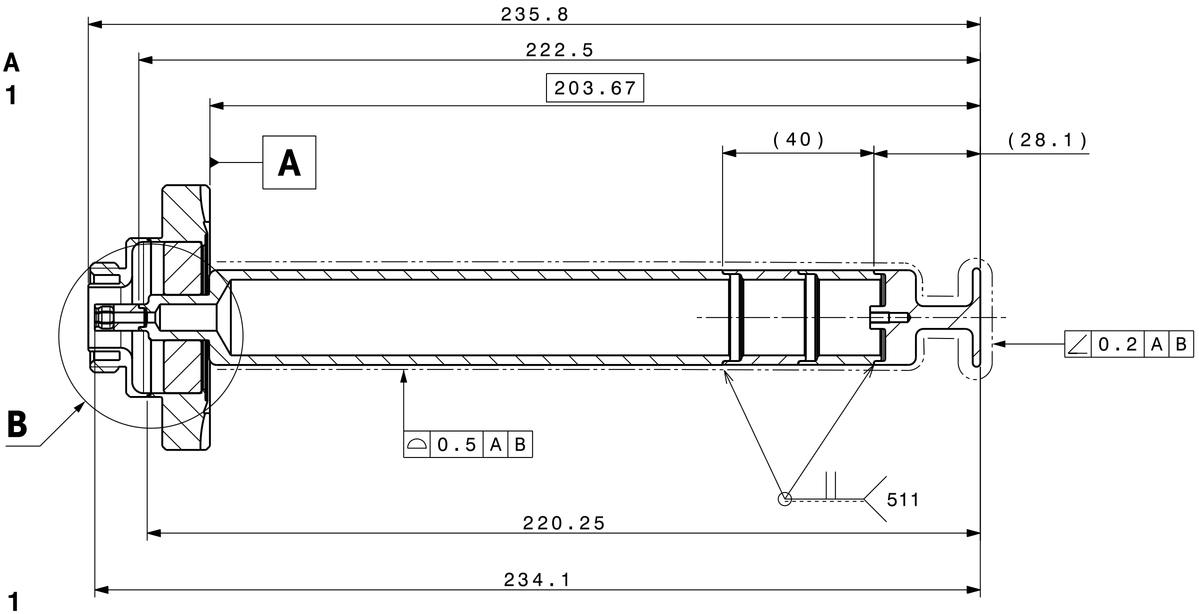

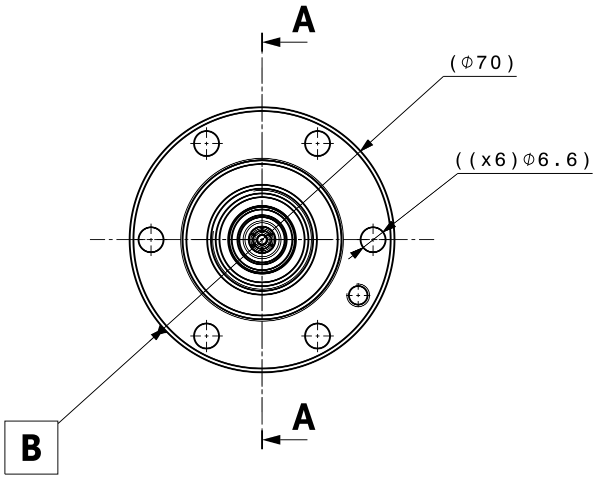

B
4:1

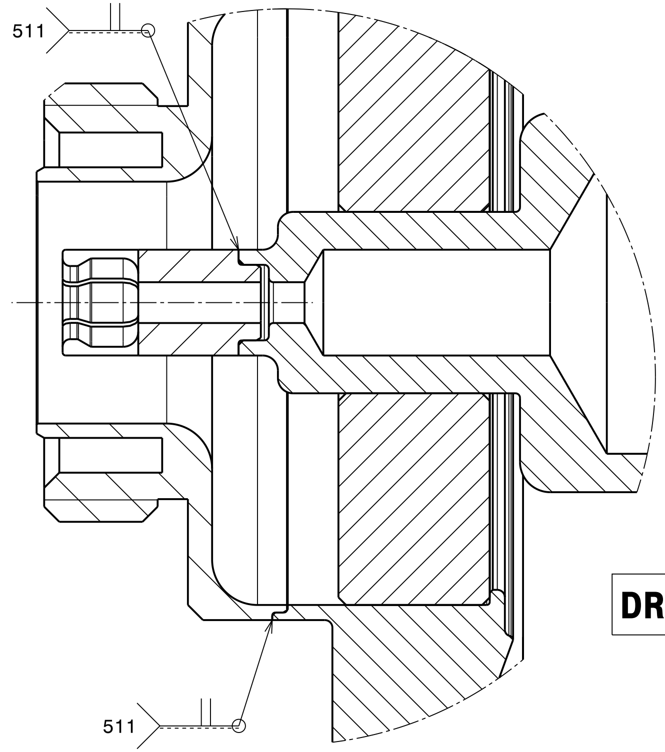

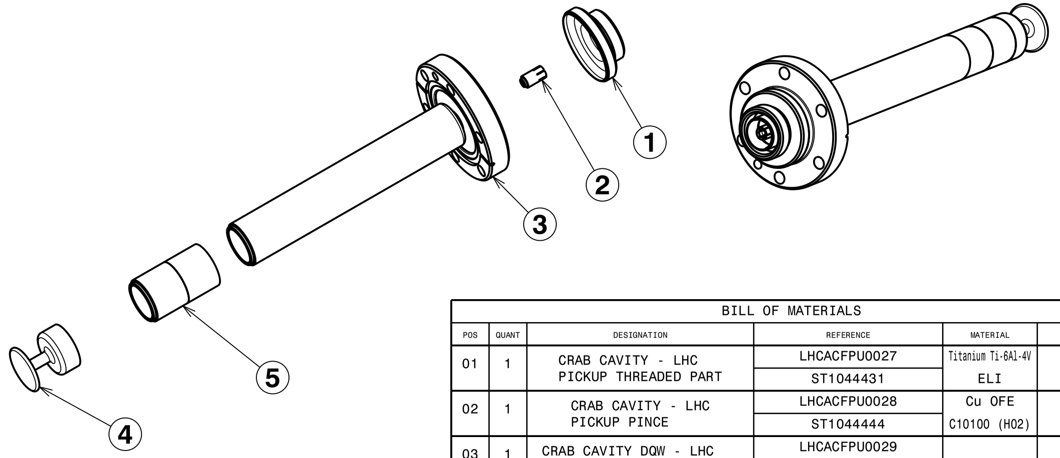

DRAWING FOR DISCUSSION ONLY!

DRAWING FOLDER SEE EDMS N°xxxxxxx

UNLESS OTHERWISE MENTIONED, APPLICABLE ISO GPS STANDARDS ARE THOSE PRIOR TO 2010-08-01 REGARDLESS OF THE DRAWING DATE

WELDED ASSEMBLY TOLERANCES ACCORDING TO ISO 13920-AE (01-08-1996)

BEAM VACUUM SPECIFICATIONS : SEE EDMS 1221536

BILL OF MATERIALS

POS	QUANT	DESIGNATION	REFERENCE	MATERIAL	EDH SCEM
01	1	CRAB CAVITY - LHC PICKUP THREADED PART	LHCACFPU0027 ST1044431	Titanium Ti-6Al-4V ELI	
02	1	CRAB CAVITY - LHC PICKUP PINCE	LHCACFPU0028 ST1044444	Cu OFE C10100 (H02)	
03	1	CRAB CAVITY DQW - LHC PICKUP ANTENNA INNER ROD	LHCACFPU0029 ST1080122		
04	1	CRAB CAVITY DQW - LHC PICKUP ANTENNA Nb END	LHCACFPU0033 ST1082605	Niobium RRR 300 CERN EDMS 1095252	
05	1	CRAB CAVITY - LHC Nb-Cu TRANSITION	ST1103397		

DESIGNATION
CRAB CAVITY DQW - LHC
PICK UP ANTENNA ASSEMBLY
DRAWING DEFINITION
PICK UP ANTENNA DQW - ASSEMBLY 300K
EQUIPMENT CODE LHCACFPU CRAB CAVITIES - Dressed cavity - Pick-up antenna

DESIGNED	F.ERIKSSON	FORMAT	A2
CHECKED		SCALE	1:1
RELEASED			
APPROVED			

DESIGNED
2019-02-22

CERN
REFERENCES
Doc No: ST1080125_03
LHCACFPU0026
INDEX
LABEL
NOT VALID FOR EXECUTION
QAC -
SHEET 1/1

CERN
ORGANISATION EUROPEENNE POUR
LA RECHERCHE NUCLEAIRE
EUROPEAN ORGANIZATION FOR NUCLEAR RESEARCH
GENEVE

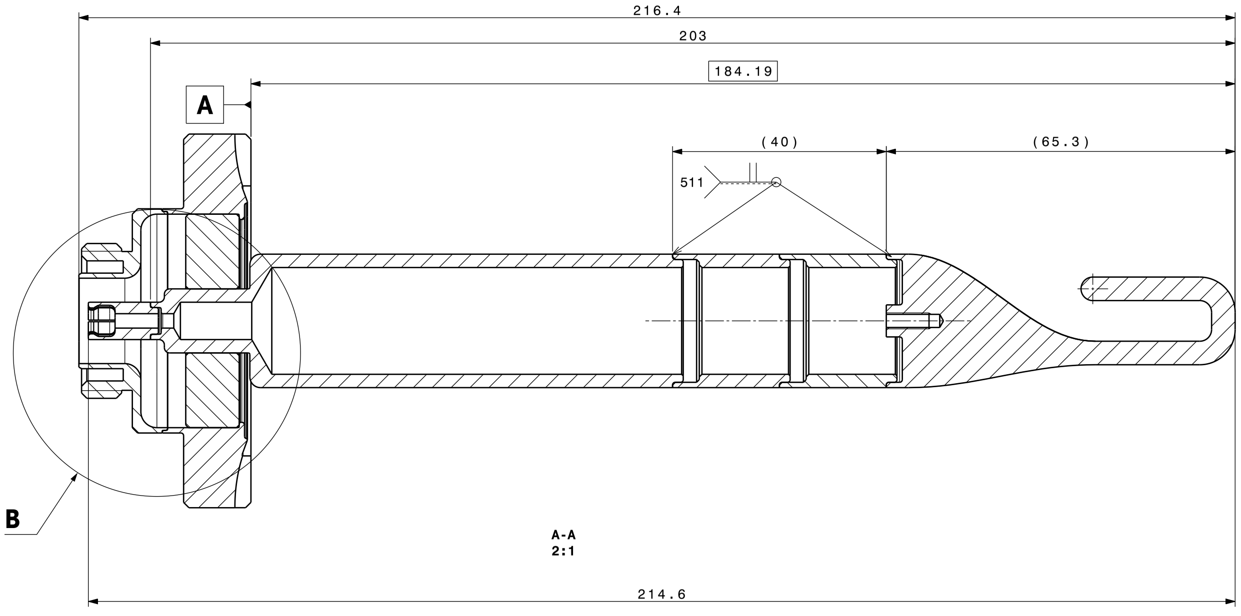

A-A
2:1

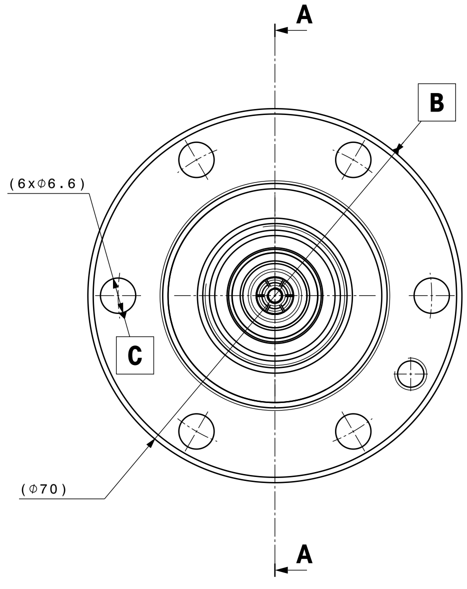

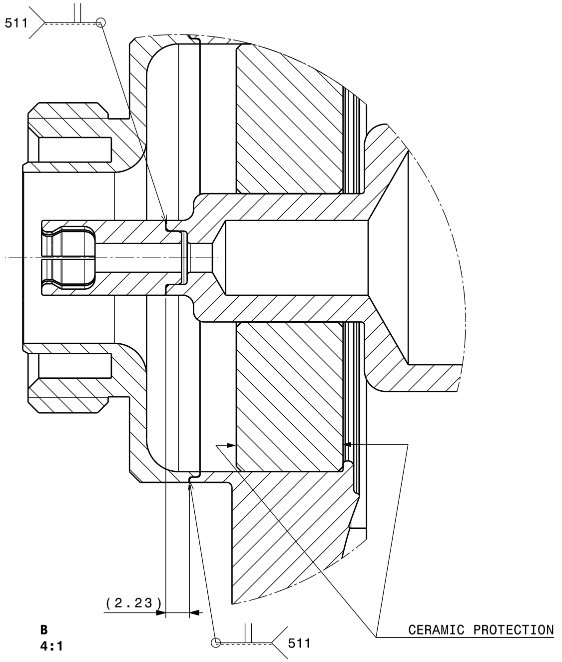

B
4:1

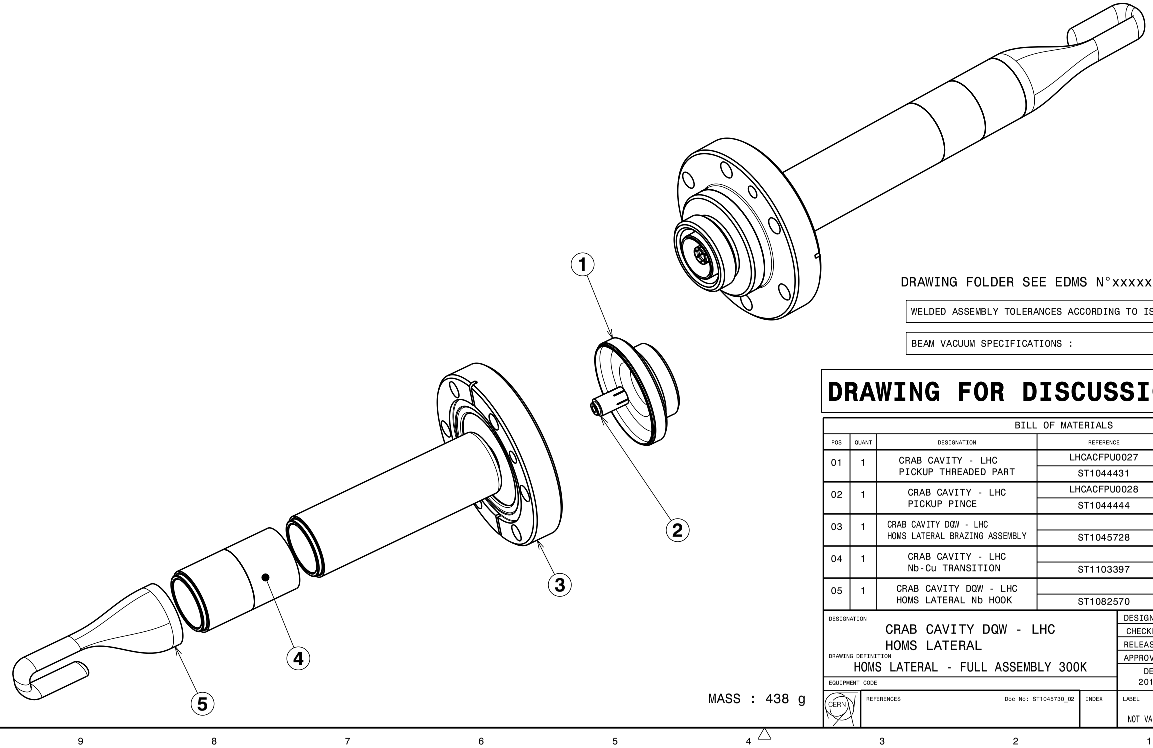

DRAWING FOLDER SEE EDMS N°xxxxxxx

WELDED ASSEMBLY TOLERANCES ACCORDING TO ISO 13920-AE (01-08-1996)

BEAM VACUUM SPECIFICATIONS : SEE EDMS 1221536

DRAWING FOR DISCUSSION ONLY!

BILL OF MATERIALS

POS	QUANT	DESIGNATION	REFERENCE	MATERIAL	EDH SCEM
01	1	CRAB CAVITY - LHC PICKUP THREADED PART	LHCACFPU0027 ST1044431	Titanium Ti-6Al-4V ELI	
02	1	CRAB CAVITY - LHC PICKUP PINCE	LHCACFPU0028 ST1044444	Cu OFE C10100 (H02)	
03	1	CRAB CAVITY DQW - LHC HOMS LATERAL BRAZING ASSEMBLY	ST1045728		
04	1	CRAB CAVITY - LHC Nb-Cu TRANSITION	ST1103397		
05	1	CRAB CAVITY DQW - LHC HOMS LATERAL Nb HOOK	ST1082570	Niobium RRR 300 CERN EDMS 1095252	

MASS : 438 g

DESIGNATION
CRAB CAVITY DQW - LHC
HOMS LATERAL
DRAWING DEFINITION
HOMS LATERAL - FULL ASSEMBLY 300K
EQUIPMENT CODE

DESIGNED	F.ERIKSSON
CHECKED	
RELEASED	
APPROVED	

FORMAT A1
SCALE 2:1
DESIGNED 2019-02-22

REFERENCES Doc No: ST1045730_02
INDEX
LABEL NOT VALID FOR EXECUTION
QAC
SHEET 1/1

ORGANISATION EUROPEENNE POUR
LA RECHERCHE NUCLEAIRE
EUROPEAN ORGANIZATION FOR NUCLEAR RESEARCH
GENEVE

References

[1] O. Bruning *et al.*, “Building a behemoth,” *Nat. Insight*, vol. 448, no. 7151, pp. 285–289, 2007. [Online]. Available: https://www.nature.com/articles/nature06077 1, 2, 3

[2] P. Higgs, “Broken Symmetries, Massless Particles and Gauge Fields,” *Phys. Lett.*, vol. 12, no. 2, pp. 132–133, 1964. [Online]. Available: https://www.sciencedirect.com/science/article/pii/0031916364911369?via{%}3Dihub 1

[3] ——, “Broken Symmetries and the Masses of Gauge Bosons,” *Phys. Rev. Lett.*, vol. 13, no. 16, pp. 508–509, 1964. [Online]. Available: https://journals.aps.org/prl/abstract/10.1103/PhysRevLett.13.508 1

[4] LEP Collaboration, “LEP Design Report: Volume II,” CERN, Geneva, Tech. Rep., 1984. [Online]. Available: http://cds.cern.ch/record/102083/files/cm-p00047694.pdf?version=1 1

[5] Nature Publishing Group, “Here we go. . . ,” *Nat. Phys.*, vol. 4, no. 8, p. 581, 2008. [Online]. Available: https://doi.org/10.1038/nphys1040 1

[6] M. Beech, *The Large Hadron Collider: Unraveling the Mysteries of the Universe.* Springer Science & Business Media, jul 2010. 1

[7] ATLAS Collaboration, “Observation of a new particle in the search for the Standard Model Higgs boson with the ATLAS detector at the LHC,” *Phys. Lett. B*, vol. 716, no. 1, pp. 1–29, 2012. [Online]. Available: https://doi.org/10.1016/j.physletb.2012.08.020 1

[8] CMS Collaboration, “Observation of a new boson at a mass of 125 GeV with the CMS experiment at,” *Phys. Lett. B*, vol. 716, no. 1, pp. 30–61, 2012. [Online]. Available: https://doi.org/10.1016/j.physletb.2012.08.021 1

[9] R. Wolf, *The Higgs Boson Discovery at the Large Hadron Collider.* Springer International Publishing, 2015. 1

[10] K. Foraz *et al.*, “CERN-ACC-2014-0223: LS1 ”First Long Shutdown of the Accelerator and its Injector Chains”,” CERN, Geneva, Switzerland, Tech. Rep. [Online]. Available: http://cds.cern.ch/record/1956664/files/CERN-ACC-2014-0223.pdf?version=1 2

[11] F. Bordry *et al.*, “The First Long Shutdown (LS1) for the LHC,” in *IPAC’13*, Shanghai, China, 2013, pp. 44–48. [Online]. Available: https://accelconf.web.cern.ch/accelconf/IPAC2013/papers/mozb202.pdf 2

[12] CERN, “The Large Hadron Collider — CERN Timelines European Organization for Nuclear Research (CERN), [Online].” [Online]. Available: https://timeline.web.cern.ch/timelines 2

[13] F. Gerigk *et al.*, “Linac4 Technical Design Report,” CERN, Geneva, Switzerland, Tech. Rep., 2006. [Online]. Available: http://cds.cern.ch/record/1004186/ 2

[14] CERN, “CERN Accelerator Complex.” [Online]. Available: https://cds.cern.ch/record/2197559 3

[15] The LHC Collaboration, “The Large Hadron Colider - Conceptual Design,” CERN, Geneva, Switzerland, Tech. Rep., 1995. [Online]. Available: http://cds.cern.ch/record/291782/files/cm-p00047618.pdf?version=1 2

[16] A. Schaeffer, “CERN Bulletin BUL-NA-2012-089: The LHC and its Successors,” no. 12 & 13, pp. 1–2, mar 2012. [Online]. Available: http://cds.cern.ch/record/1431013/?ln=en 2

[17] The HiLumi LHC Collaboration, “HL-LHC Preliminary Design Report,” The European Organization for Nuclear Research (CERN), Geneva, Switzerland, Tech. Rep., 2014. [Online]. Available: https://cds.cern.ch/record/1972604/files/CERN-ACC-2014-0300.pdf 2, 4, 5, 7, 23, 55, 131, 155, 164, 165, 170, 185

[18] F. Zimmerman *et al.*, “High-Energy LHC Design,” in *IPAC’2018*, Vancouver, BC, Canada, 2018, pp. 269–272. [Online]. Available: https://cdsweb.cern.ch/record/2647706/files/mopmf064.pdf 2

[19] O. Brüning, “LHeC-Note-2013-001: The Large Hadron Electron Collider,” Geneva, Switzerland, Tech. Rep., 2013. [Online]. Available: http://cds.cern.ch/record/1546382/files/BKarX.pdf?version=1 3

[20] W. Herr and B. Muratori, “CAS Report: Concept of Luminosity,” in *Cern Accel. Sch.*, Zeuthen, Germany, 2003. [Online]. Available: http://cds.cern.ch/record/941318/files/p361.pdf?version=1 3

[21] L. Rossi, “HiLumi Conference Presentation: HL-LHC Status at CM # 8,” in *HiLumi 2018*, Geneva, Switzerland, 2018. [Online]. Available: https://indico.cern.ch/event/742082/contributions/3072115/attachments/1733884/2803534/HL-LHC{_}Status{_}Rossi{_}v1.pdf 4

[22] E. Métral *et al.*, “Update of the HL-LHC Operational Scenarios for Proton Operation,” 2018. [Online]. Available: http://cds.cern.ch/record/2301292/files/CERN-ACC-NOTE-2018-0002.pdf?version=1 5

[23] The LIU Collaboration, “LHC Technical Design Report - Volume I: Protons,” Tech. Rep. December, 2014. [Online]. Available: http://cds.cern.ch/record/1976692/files/CERN-ACC-2014-0337.pdf?version=1 5

[24] ——, “LHC Technical Design Report - Volume II: Ions,” Geneva Switzerland, Tech. Rep., 2000. [Online]. Available: http://cds.cern.ch/record/2153863/files/CERN-ACC-2016-0041.pdf?version=2 5

[25] R. Palmer, “SLAC-PUB-4707: Energy Scaling, Crab Crossing, and the Pair Problem,” *Slac-Pub-4707*, 1988. [Online]. Available: http://slac.stanford.edu/pubs/slacpubs/4500/slac-pub-4707.pdf 6

[26] S. Verdú-Andrés *et al.*, “Crab cavities for colliders: past, present and future,” *Nucl. Part. Phys. Proc.*, vol. 273-275, pp. 193–197, 2016. [Online]. Available: https://doi.org/10.1016/j.nuclphysbps.2015.09.025 6

[27] R. Calaga, “Crab Caivties for the LHC Upgrade.” Chamonix, France: Proceedings of Chamonix 2012 workshop on LHC Performance, 2012, pp. 363–372. [Online]. Available: http://cds.cern.ch/record/1493034/files/RC{_}9{_}04.pdf?version=1 6, 7

[28] B. Hall, “Designing the Four Rod Crab Cavity for the High-Luminosity LHC Upgrade,” PhD Thesis, Lancaster University, 2014. [Online]. Available: https://cds.cern.ch/record/1742051/files/EuCARD-BOO-2014-007.pdf 6, 155

[29] R. Calaga, “Comments on Crab Cavity Voltage,” CERN, Geneva, Switzerland, Tech. Rep., 2014. [Online]. Available: https://espace.cern.ch/HiLumi/WP4/SharedDocuments/Reports/crabvolt.pdf 7

[30] F. Gerigk, “Cavity types,” 2011. [Online]. Available: http://arxiv.org/abs/1111.4897 11

[31] T. Wangler, *RF Linear Accelerators*, 2008. 14, 49

[32] H. Padamsee, J. Knobloch, and T. Hays, *RF Superconductivity for Accelerators.* John Wiley & Sons, 1998. 11, 178, 179

[33] R. Wanzenberg, “Monopole, Dipole and Quadrupole Passbands of the TESLA 9-Cell Cavity,” DESY, Hamburg, Germany, Tech. Rep., 2001. [Online]. Available: http://cds.cern.ch/record/533324 16, 29

[34] W. Panofsky and W. Wenzel, “Panofsky-Wenzel Theorum,” *Rev. Sci. Instrum.*, vol. 27, no. 967, 1956. 19, 226

[35] H. K. Onnes, *Research Notebooks 56-57, Kamerlingh Onnes Archive, Boerhaave Museum*, Liden, the Netherlands, 1911. 21, 246

[36] D. Van Delft and P. Kes, “The Discovery of Superconductivity,” *Phys. Today*, vol. 63, no. 9, pp. 38–43, 2010. [Online]. Available: https://physicstoday.scitation.org/doi/10.1063/1.3490499 21, 246

[37] R. J. Donnelly, “The Discovery of Superfluidity,” vol. 48, no. 7, pp. 30–36, 1995. [Online]. Available: https://physicstoday.scitation.org/doi/10.1063/1.881467 21, 246

[38] D. R. Tilley and J. Tilley, *Superfluidity and Superconductivity*, 3rd ed. Bristol, UK: CRC Press, 1990. 21, 246

[39] J. Bardeen, L. Cooper, and J. Schrieffer, “Theory of superconductivity,” *Phys. Rev.*, vol. 108, no. 5, pp. 1175–1204, 1957. [Online]. Available: https://journals.aps.org/pr/abstract/10.1103/PhysRev.108.1175 22, 178, 247

[40] D. Broun, “Introduction to Solid State Physics,” Tech. Rep. [Online]. Available: http://www.sfu.ca/cifarqmss2015 22

[41] P. Bramham *et al.*, “The CERN Radio Frequency Particle Seperator - Fist Operation,” *Phys. Lett.*, vol. 15, no. 3, pp. 290–291, 1965. [Online]. Available: https://www.sciencedirect.com/science/article/pii/0031916365912527 23

[42] C. Leeman and C. Yao, “A Highly Effective Deflecting Structure,” in *LINAC’90*, Albuquerque, New Mexico, USA, 1990, pp. 232–234. [Online]. Available: https://accelconf.web.cern.ch/AccelConf/l90/papers/mo465.pdf 23

[43] KEKB Collaboraion, “KEKB B-Factory Design Report,” KEK, Tsukuba, Ibaraki 305, Japan, Tech. Rep., 1995. [Online]. Available: http://inspirehep.net/record/401380/files/27045036.pdf?version=1 23

[44] Y. Funakoshi, “Operational Experience with Crab Cavities at KEKB,” in *ICFA Mini-Workshop Beam-Beam Eff. Hadron Colliders*, Geneva, Switzerland, 2014. [Online]. Available: https://cds.cern.ch/record/1955812/files/27-36-Funakoshi.pdf 23

[45] T. Berenc, “ANL/APS/LS-324: An Equivalent Circuit Model and Power Calculations for the APS SPX Crab Cavities,” Tech. Rep., 2011. [Online]. Available: https://www.aps.anl.gov/files/APS-sync/lsnotes/files/APS{_}1428680.pdf 23

[46] Bor *et al.*, “Planned Use of Pulsed Crab Cavities for Short X-Ray Pulsed Generation at the Advanced Photon Source,” in *PAC’07*, Albuquerque, New Mexico, USA, 2007, pp. 1127–1129. [Online]. Available: https://accelconf.web.cern.ch/accelconf/p07/PAPERS/TUPMN091.PDF

[47] H. Wang, “Crab Cavity and Cryomodule Prototype Development for the Advanced Photon Source,” 2011. [Online]. Available: https://www.researchgate.net/profile/Houfeng{_}Wang/research 23

[48] C. Adolphsen *et al.*, “FERMILAB-TM-2388/EUROTeV-Report-2007-010: Design of the ILC Crab Cavity System,” Tech. Rep., 2007. [Online]. Available: http://slac.stanford.edu/pubs/slacpubs/12750/slac-pub-12751.pdf 23

[49] G. Burt *et al.*, “Progress Towards Crab Cavity Solutions for the ILC,” in *EPAC’06*, Edinburgh, Scotland, UK, 2006, pp. 724–726. [Online]. Available: https://accelconf.web.cern.ch/accelconf/e06/PAPERS/MOPLS075.PDF 23

[50] J. Shi *et al.*, “A 3-cell deflecting RF cavity for emittance exchange experiment at ANL,” *Nucl. Instruments Methods Phys. Res. A*, vol. 598, pp. 388–393, 2009. [Online]. Available: https://www.sciencedirect.com/science/article/pii/S0168900208014654 23

[51] L. Xiao and Z. Li, “LHC-CC09 Presentation: 800MHz Elliptical-shape Crab Cavity RF Design For LHC Upgrade,” 2009. [Online]. Available: https://indico.cern.ch/event/55309/contributions/2040236/attachments/980832/1394269/ZLI-LCC-CC09-800MHz-Crab-Cavity.pdf 23

[52] L. Ficcadenti and J. Tuckmantel, “sLHC Project Note 0036: Slim Elliptical cavity at 800 MHz for Local Crab Crossing,” Geneva Switzerland, Tech. Rep., 2011. [Online]. Available: http://cds.cern.ch/record/1385886/files/project-note-0036.pdf?version=1 23

[53] Y. P. Sun *et al.*, “Beam dynamics aspects of crab cavities in the CERN Large Hadron Collider,” *Phys. Rev. Spec. Top. - Accel. Beams*, vol. 12, no. 10, pp. 1–18, 2009. [Online]. Available: https://doi.org/10.1103/PhysRevSTAB.12.101002 23

[54] B. Xiao *et al.*, “Design, prototyping, and testing of a compact superconducting double quarter wave crab cavity,” *Phys. Rev. Spec. Top. - Accel. Beams*, vol. 18, no. 4, 2015. [Online]. Available: https://journals.aps.org/prab/abstract/10.1103/PhysRevSTAB.18.041004 23, 59

[55] J. Delayen and S. U. De Silva, “Design of Superconducting Parallel-Bar Deflecting Crabbing Cavities with Improved Properties,” in *IPAC’11*, New York, NY, USA, 2011, pp. 1021–1023. [Online]. Available: https://accelconf.web.cern.ch/accelconf/IPAC2011/papers/mopc120.pdf 23

[56] Z. Li, J. Delayen, and S. U. De Silva, “RF Modeling Using Parallel Codes ACE3P for the 400-MHz Parallel-bar/Ridged-waveguide Compact Crab Cavity for the LHC HiLumi Upgrade,” in *IPAC’12*, New Orleans, Louisiana, USA, 2012, pp. 2185–2187. [Online]. Available: http://accelconf.web.cern.ch/Accelconf/IPAC2012/papers/weeppb010.pdf 23

[57] J. Barranco García *et al.*, “Long term dynamics of the high luminosity Large Hadron Collider with crab cavities,” *Phys. Rev. Accel. Beams*, vol. 19, no. 10, pp. 1–9, 2016. [Online]. Available: http://cds.cern.ch/record/2261122/files/10.1103{_}PhysRevAccelBeams.19.101003.pdf?version=1 25, 59, 163

[58] R. Tomas, “26th HL-LHC TCC Presentation: Parameter update for the nominal HL-LHC : Standard, BCMS and 8b + 4e,” in *26th HL-LHC TCC*, no. March, Geneva Switzerland, 2017. [Online]. Available: https://indico.cern.ch/event/590415/contributions/2511517/attachments/1429118/2194441/2017-03-16{_}HLLHC-TC.pdf 25

[59] R. Calaga, “Linear Beam Dynamics and Ampere Class Superconducting RF Cavities @ RHIC,” PhD Thesis, 2006. 26, 27

[60] J. Delayen, “USPAS Lecture: Instabilities and Higher Order Modes,” in *USPAS’15*, Hampton, VA, USA, 2015. [Online]. Available: http://uspas.fnal.gov/materials/15Rutgers/HOMs.pdf 27

[61] F. Marhauser, “USPAS Presentation: Higher Order Modes,” in *USPAS’15*, Hampton, VA, USA, 2015. [Online]. Available: https://www.jlab.org/indico/event/98/contribution/3/material/slides/0.pdf 27, 35

[62] B. Zotter, *Impedances and Wakefields.* World Scientific, 1998. 29

[63] F. Gerigk, “Status and Future Strategy for Advanced High Power Microwave Sources for Accelerators,” in *IPAC’18 Present.*, Vancouver, BC, Canada, 2018. [Online]. Available: https://accelconf.web.cern.ch/AccelConf/ipac2018/ 31

[64] R. F. Hoeberling and P. J. Tallerico, “The RF Modulator Design and Phase Amplitude Control for a High-Power Free-Electron Laser Linac,” in *LINAC’81*, Santa Fe, New Mexico, USA, 1981, pp. 290–292. [Online]. Available: https://accelconf.web.cern.ch/accelconf/l81/papers/h11.pdf 31

[65] G. Caryotakis, “SLAC-PUB-10620: High power Klystrons: Theory and Practice at the Stanford Linear Accelerator Center,” *Slac-Pub-4707*, no. August 2004, pp. 0–138, 2004. [Online]. Available: http://slac.stanford.edu/pubs/slacpubs/10500/slac-pub-10620.pdf

[66] M. V. Hoover, “Grid-Controlled Power Tubes in Particle Accelerator Applications,” *IEEE Trans. Nucl. Sci.*, pp. 76–85, 1965. [Online]. Available: https://ieeexplore.ieee.org/document/4323600

[67] H. Obata, K. Furumoto, and H. Miyamoto, “State of the Art Advanced Magnetrons for Accelerator RF Power Source,” in *LINAC’16*, East Lansing, MI, USA, 2016, pp. 405–407. [Online]. Available: http://accelconf.web.cern.ch/AccelConf/linac2016/papers/tuop09.pdf

[68] J. Jacob, “CAS Report: Radio Frequency Solid State Amplifiers,” in *Cern Accel. Sch.*, ESRF, Grenoble, 2015, pp. 197–216. [Online]. Available: https://arxiv.org/abs/1607.01570 31

[69] D. M. Pozar, *Microwave Engineering*, 4th ed. Wiley New York, 2012. 31, 32, 34, 38, 44, 151

[70] D. Alesini, “CAS Report: Power Coupling,” in *Cern Accel. Sch.*, Ebeltoft, Denmark, 2010. [Online]. Available: http://arxiv.org/abs/1112.3201 33

[71] J. Sekutowicz, “HOM Damping and Power Extraction From Superconducting Cavities,” in *LINAC’06*, Knoxville, Tennessee, USA, 2006, pp. 506–510. [Online]. Available: https://accelconf.web.cern.ch/accelconf/l06/PAPERS/WE2005.PDF 35

[72] F. Marhauser, “Next Generation HOM-Damping,” *Supercond. Sci. Technol.*, vol. 30, no. 6, pp. 1–38, 2017. [Online]. Available: https://iopscience.iop.org/article/10.1088/1361-6668/aa6b8d 47, 180

[73] H. Padamsee, “CAS Report: Design Topics for Superconducting RF Cavities and Ancillaries,” in *Cern Accel. Sch.*, Erice, Italy, 2013. [Online]. Available: https://arxiv.org/abs/1501.07129 35, 49

[74] F. Gerigk, “Design of Higher-Order Mode Dampers for the 400 MHz LHC Superconducting Cavities,” PhD, Institut für Nachrichtentechnik and Theoretische Elektrotechnik, Technische Universität, 1997. [Online]. Available: https://www.researchgate.net/profile/Frank{_}Gerigk/publications 36, 38, 39, 45

[75] E. Haebel, “Couplers for Cavities,” CERN, Geneva, Switzerland, Tech. Rep. [Online]. Available: https://cds.cern.ch/record/308016/files/p231.pdf 36

[76] J. Sekutowicz, “HOM Couplers at DESY,” in *SRF'87*, Argonne National Lab, Illinois, USA, 1987, pp. 597–604. [Online]. Available: https://accelconf.web.cern.ch/accelconf/srf87/papers/srf87e09.pdf 41

[77] A. Mosnier, “Saclay Report: Developments of HOM Couplers for Superconducting Cavities,” Tech. Rep., 1989. [Online]. Available: https://inis.iaea.org/collection/NCLCollectionStore/{_}Public/21/049/21049942.pdf 41

[78] P. Legendre *et al.*, “Coupler Developments at CERN,” in *SRF'87*, Argonne National Lab, Illinois, USA, 1987, pp. 565–588. [Online]. Available: http://accelconf.web.cern.ch/accelconf/srf87/papers/srf87e07.pdf 41

[79] D. Boussard and T. Linnecar, “The LHC Superconducting RF System,” Tech. Rep., 1999. [Online]. Available: https://cds.cern.ch/record/410377/files/lhc-project-report-316.pdf 41

[80] K. Papke, F. Gerigk, and U. Van Rienen, “Comparison of coaxial higher order mode couplers for the CERN Superconducting Proton Linac study,” *Phys. Rev. Accel. Beams*, vol. 20, no. 6, pp. 1–19, 2017. [Online]. Available: https://journals.aps.org/prab/pdf/10.1103/PhysRevAccelBeams.20.060401 41

[81] G. Y. France *et al.*, “Hom Damping in Soleil Superconducting Cavity,” in *EPAC'98*, Stockholm, Sweeden, pp. 1864–1866. [Online]. Available: http://accelconf.web.cern.ch/AccelConf/e98/PAPERS/TUP05C.PDF 41

[82] E. Chiaveri *et al.*, “Demountable E-H Field Higher Oorder Mode Couplers for the Niobium Sputtered 4-Cell LEP Cavity,” in *SRF'91*, DESY, Hamburg, Germany, 1991, pp. 956–962. [Online]. Available: https://accelconf.web.cern.ch/accelconf/SRF91/papers/srf91g05.pdf 41

[83] S. Noguchi, E. Kako, and K. Kubo, “Couplers - Experience at KEK,” in *SRF'89*, KEK, Tsukuba, Japan, 1989, pp. 397–412. [Online]. Available: http://accelconf.web.cern.ch/Accelconf/SRF89/papers/srf89e04.pdf 41

[84] Q. Wu and I. Ben-Zvi, “Simulation of the High-Pass Filter for 56 MHz Cavity for RHIC,” in *IPAC'10*, Kyoto, Japan, 2010, pp. 3078–3080. [Online]. Available: https://accelconf.web.cern.ch/accelconf/IPAC10/papers/wepec085.pdf 41

[85] W. Xu *et al.*, “New HOM Coupler Design for High Current SRF Cavity,” in *Pac2011*, New York, NY, USA, 2011, pp. 925–927. [Online]. Available: http://accelconf.web.cern.ch/accelconf/pac2011/papers/tup060.pdf 41

[86] Q. Wu *et al.*, “BNL-PUB: Operation of the 56 MHz Superconducting RF Cavity in RHIC During Run 14,” *BNL-108416-2015-IR*, no. September, 2015. [Online]. Available: https://www.bnl.gov/isd/documents/89316.pdf 44, 50

[87] BNL Collider-Accelerator Department, “RHIC Design Manual,” BNL, Tech. Rep. November, 2006. [Online]. Available: https://www.bnl.gov/cad/accelerator/docs/pdf/rhicconfmanual.pdf 44, 50

[88] J. Sekutowicz, "Higher Order Mode Coupler for TESLA," in *Sixth Work. RF Supercond.*, CEBAF, Newport News, VA, USA, 1993, pp. 426–439. [Online]. Available: https://accelconf.web.cern.ch/accelconf/SRF93/papers/srf93g04.pdf 45, 151

[89] ——, "Private Communication." 45

[90] F. Marhauser *et al.*, "Status and results of High Current 5-Cell SRF Cavities Developed at JLAB," in *EPAC'08*, Genoa, Italy, 2008, pp. 886–888. [Online]. Available: https://accelconf.web.cern.ch/accelconf/e08/papers/mopp140.pdf 47

[91] R. A. Rimmer *et al.*, "The JLAB Ampere-Calss Cryomodule Conceptual Design," in *EPAC'06*, Edinburgh, Scotland, UK, 2006, pp. 490–492. [Online]. Available: https://accelconf.web.cern.ch/AccelConf/e06/PAPERS/MOPCH182.PDF 47

[92] E. Chojnacki and W. J. Alton, "Beamline RF Load Development at Cornell," in *PAC'99*, New York, NY, USA, 1999, pp. 845–847. [Online]. Available: https://ieeexplore.ieee.org/document/795375 48

[93] H. Podlech, "CAS Report: Superconducting Versus Normal Conducting Cavities," in *Cern Accel. Sch.*, Bilbao, Spain, 2011. [Online]. Available: https://cds.cern.ch/record/1533028/files/CERN-2013-001-p151.pdf 49

[94] R. Pendleton *et al.*, "PEP-II B-Factory Prototype Higher Order Mode Load Design," in *PAC'95*, Dallas, TX, USA, 1995, pp. 1800–1802. [Online]. Available: https://ieeexplore.ieee.org/document/505366 49

[95] K. Ko *et al.*, "Design of a High-Power Test Model of the PEP-II RF Cavity," in *PAC'93*, Washington, DC, USA, 1993, pp. 1039–1041. [Online]. Available: https://ieeexplore.ieee.org/document/308691 49

[96] R. A. Rimmer *et al.*, "High-Power Testing of the RF Cavities for PEP-II," in *PAC'97*, Vancouver, BC, Canada, 1997, pp. 3004–3006. [Online]. Available: https://ieeexplore.ieee.org/document/753089 49

[97] M. Allen *et al.*, "An RF Cavity for the B-Factory," in *PAC'91*, San Francisco, CA, USA, 1991, pp. 819–821. [Online]. Available: https://accelconf.web.cern.ch/accelconf/p91 49

[98] V. Serrière *et al.*, "352.2 MHz HOM Damped Normal Conducting ESRF Cavity Design and Fabrications," in *IPAC'11*, San Sebastián, Spain, 2011, pp. 68–70. [Online]. Available: http://www-linac.kek.jp/mirror/IPAC2011/papers/mopc004.pdf 49

[99] SLAC, "PEP II Photographs." [Online]. Available: https://www.slac.stanford.edu/BFROOT/www/doc/public/ 50

[100] H. Wang *et al.*, "Design, Prototype and Measurement of a Single-Cell Deflecting Cavity for the Advanced Photon Source," in *PAC'09*, Vancouver, BC, Canada, 2009, pp. 2138–2140. [Online]. Available: https://accelconf.web.cern.ch/accelconf/pac2009/papers/we5pfp059.pdf 50, 51

[101] Z. Li *et al.*, "FPC and Hi-Pass Filter HOM Coupler Design for the RF Dipole Crab Cavity for the LHC HiLumi Upgrade," in *IPAC'15*, Richmond, VA, USA, 2015, pp. 3492–3495. [Online]. Available: https://cds.cern.ch/record/2114082/files/CERN-ACC-2015-0184.pdf 52

[102] R. Apsimon *et al.*, "Design and testing of a four rod crab cavity for High Luminosity LHC," *Phys. Rev. Accel. Beams*, vol. 20, no. 1, pp. 1–17, 2017. [Online]. Available: https://journals.aps.org/prab/abstract/10.1103/PhysRevAccelBeams.20.012001 55

[103] F. W. Grover, *Inductance calculations: working formulas and tables.* Courier Corporation, 2004. 61

[104] Computer Simulation Technology, "CST Microwave Studio," Bad Nauheimer Str. 19, D-64289 Darmstadt, Germany. [Online]. Available: http://www.cst.com 62, 67, 86, 160, 168, 240

[105] E. Montesinos and G. Trento, "CERN-ATS-Note- 2013-031TECH: Optimal RF Conditioning of Advanced Photon Source (APS) Fundamental Power Coupler," CERN, Geneva, Switzerland, Tech. Rep., 2013. [Online]. Available: http://cds.cern.ch/record/1551741/files/ 80, 173, 242, 243

[106] J. Jackson, *Classical electrodynamics.* John Wiley & Sons, 2007. 86

[107] CST, "Private Communication," 2018. 86

[108] B. Salvant *et al.*, "CERN-ACC-NOTE-2018-0087: HL-LHC impedance," CERN, Geneva, Switzerland, Tech. Rep., 2018. [Online]. Available: http://cds.cern.ch/record/2652401/files/ 87, 95, 113, 160

[109] K. Sang-ho, "Presentation: HOM Experiences at the SNS SCL," in *SPL HOM Work.*, CERN, Geneva, Switzerland, 2009. [Online]. Available: https://indico.cern.ch/event/57247/contributions/1212326/ 90

[110] I. Karpov, R. Calaga, and E. Shaposhnikova, "CERN-ACC-NOTE-2018-0005: HOM power in FCC-ee cavities," Tech. Rep., 2018. [Online]. Available: https://cds.cern.ch/record/2302276 91

[111] Work Package 2 (WP2), "Filling Schemes HL-LHC." [Online]. Available: https://espace.cern.ch/HiLumi/WP2/SharedDocuments/Forms/AllItems.aspx?RootFolder={%}2FHiLumi{%}2FWP2{%}2FSharedDocuments{%}2FFillingSchemesHL-LHC{&}FolderCTID=0x012000D3C091270D48B94AA66DB4BE9594B203 93, 252

[112] J. Chambrillon *et al.*, "CERN SRF Assembling and Test Facilities," in *SRF'11*, Chicago, IL, USA, 2011, pp. 530–532. [Online]. Available: https://accelconf.web.cern.ch/accelconf/SRF2011/papers/tupo058.pdf 95

[113] P. F. Menendez, "CERN EMDS 1759686: Non Conformity Report - HOM Coupler Ports," CERN, Geneva, Switzerland, Tech. Rep., 2016. [Online]. Available: https://edms.cern.ch/ui/file/1759686/1/NCR-EXTRALENGHT{_}HOM-FPC{_}PORTS.pdf 97

[114] S. Atieh, P. Naisson, and T. Tardy, "Private communication and internal meetings." 116

[115] P. Baudrenghien, "Private communication." 131

[116] N. Simon, E. Drexler, and R. Reed, *Properties of Copper and Copper Alloys at Cryogenic Temperatures.* NIST, 1992. [Online]. Available: https://nvlpubs.nist.gov/nistpubs/Legacy/MONO/nistmonograph177.pdf 132

[117] W. Singer, A. Ermakov, and X. Singer, "TTC-Report-2010-02: RRR-Measurement Techniques," Tech. Rep., 2010. [Online]. Available: https://bib-pubdb1.desy.de/record/91801/files/TTC-Report2010-02.pdf 132

[118] R. Chambers, "Anomalous Skin Effect in Metals," *Nature*, vol. 165, no. 4189, pp. 239–240, 1950. [Online]. Available: https://www.nature.com/articles/165239b0 132

[119] W. Chou and F. Ruggiero, "LHC Project Note 2 (SL/AP): Anomalous Skin E ect and Resistive Wall Heating," CERN, Geneva, Switzerland, Tech. Rep., 1995. [Online]. Available: http://cds.cern.ch/record/691905/files/project-note-2.pdf 132

[120] J. Müller, "Longitudinal Intensity Effects in the CERN Large Hadron Collider PAR," PhD Thesis, EPFL, 2016. [Online]. Available: https://cds.cern.ch/record/2196930/files/CERN-THESIS-2016-066.pdf 135, 136

[121] A. Lasheen, "Beam Measurements of the Longitudinal Impedance of the CERN Super Proton Synchrotron," PhD Thesis, Universite Paris-Saclay, 2017. [Online]. Available: http://cds.cern.ch/record/2270190/files/CERN-THESIS-2017-068.pdf?version=1 135, 136, 192

[122] P. Baudrenghien, "HiLumi Conference Presentation: Measurements and Lessons Learned," in *HiLumi 2018*, Geneva, Switzerland, 2018. [Online]. Available: https://indico.cern.ch/event/742082/contributions/3084929/attachments/1734377/2804530/HL-LHC18v5.pdf 137

[123] S. Verdú-Andrés and R. Calaga, "HiLumi Conference Presentation: Evaluation of RF Pickup Antennas for Crab Cavity (DQW and RFD) LHC-Series," in *HiLumi 2018*, Geneva, Switzerland, 2018. [Online]. Available: https://indico.cern.ch/event/742082/contributions/3085085/ 139

[124] S. Antipov, J. Mitchell, and B. Salvant, "Update on DQW crab cavity HOMs Crab cavity HOMs," in *140th HiLumi WP2 Meet.*, CERN, Geneva, Switzerland. [Online]. Available: https://indico.cern.ch/event/788818/contributions/3277284/ 147, 236

[125] R. Calaga, "Private communication." 155, 241

[126] P. Kneisel *et al.*, "Development of a Superconducting Connection for Niobium Cavities," in *PAC'07*, Albuquerque, New Mexico, USA, 2007, pp. 2484–2486. [Online]. Available: https://ieeexplore.ieee.org/document/4441291 157

[127] ——, "Progress on the Development of a Superconducting Connection for Niobium Cavities," *IEEE Trans. Appl. Supercond.*, vol. 19, no. 3, pp. 1416–1418, 2008. [Online]. Available: https://ieeexplore.ieee.org/document/5109618

[128] R. Sundelin *et al.*, "Application of Superconducting RF Accelerating Sections to an Electron Synchrotron - A Progress Report," Tech. Rep., 1974. [Online]. Available: http://inspirehep.net/record/94004/files/HEACC74{_}149-153.pdf

[129] K. Saito, "Application of Mo Sealing for SRF Cavities," in *IPAC'10*, Kyoto, Japan, 2010, pp. 3359–3361. [Online]. Available: http://accelconf.web.cern.ch/AccelConf/IPAC10/papers/wepe009.pdf 157

[130] W. Henneberg, R. Orthuber, and E. Steudel, "Zur Wirkungsweise des Elektronenvervielfachers," *Zeitschrift für Tech. Phys.*, vol. 4, pp. 115–120. 168

[131] D. Kostin *et al.*, "Multipacting in HOM Couplers at the 1.3 GHz 9-Cell TESLA Type SRF Cavity," in *SRF'11*, Chicago, IL, USA, 2011, pp. 691–694. [Online]. Available: https://accelconf.web.cern.ch/accelconf/SRF2011/papers/thpo003.pdf 168

[132] M. A. Furman and M. Pivi, "Probabilistic model for the simulation of secondary electron emission," *Phys. Rev. Spec. Top. - Accel. Beams*, vol. 5, no. 12, pp. 82–99, 2002. [Online]. Available: https://journals.aps.org/prab/abstract/10.1103/PhysRevSTAB.5.124404 169

[133] G. Burt, "Private Communication." 169

[134] ——, "Simulation Report: Multipactor DQW," Lancaster University, Lancaster, Tech. Rep., 2017. [Online]. Available: https://espace.cern.ch/HiLumi/WP4/SharedDocuments/Forms/AllItems.aspx 173

[135] S. Verdú-Andrés *et al.*, "HiLumi Conference Presentation: US Cold RF Test Program of DQW Prototype Cavities," *HiLumi 2018*, 2018. [Online]. Available: https://indico.cern.ch/event/742082/contributions/3084937/ 173

[136] A. Dexter and R. Seviour, "Rapid Generation of Multipactor Charts by Numerical Solution of the Phase Equation," *J. Phys. D. Appl. Phys.*, vol. 38, pp. 1383–1389, 2005. [Online]. Available: https://iopscience.iop.org/article/10.1088/0022-3727/38/9/009/meta 174, 175

[137] P. Goudket, "A Study of Multipacting in Rectangular Waveguide Geometries," Ph.D. dissertation, Lancaster University, 2004. [Online]. Available: http://eprints.lancs.ac.uk/76622 175

[138] F. Koechlin and B. Bonin, "Parametrization of the Niobium Thermal Conductivity in the Superconducting State," *Supercond. Sci. Technol.*, vol. 9, no. 6, pp. 453–460, 1996. [Online]. Available: https://iopscience.iop.org/article/10.1088/0953-2048/9/6/003/pdf 179

[139] P. Dhakal *et al.*, "Superconducting DC and RF Properties of Ingot Niobium," in *SRF'11*, Chicago, IL, USA, 2011. [Online]. Available: http://accelconf.web.cern.ch/accelconf/SRF2011/papers/thpo057.pdf 179

[140] C. Zoller, "Experimental Investigation and Modelling of Incidents in Liquid Helium Cryostats," PhD, Karlsruher Instituts für Technologie (KIT), 2018. [Online]. Available: https://publikationen.bibliothek.kit.edu/1000082999 182

[141] L. Carver, "CERN MSWG Meeting 2018 #7: SPS Crab Cavity MDs First results with beam SPS-BA6 Installation," in *MSWG 2018 #7*, Geneva, Switzerland, 2018. 185

[142] ——, "CERN MSWG Meeting 2018 #13: SPS Crab Cavity MDs Latest Results," in *MSWG 2018 #13*, 2018. [Online]. Available: https://indico.cern.ch/event/747394/contributions/3130411/ 185

[143] R. Calaga, "Presentation: First Crabbing of Proton," in *TTC'19*, UBC, Vancouver, Canada, 2019. [Online]. Available: https://indico.desy.de/indico/event/21337/session/9/contribution/7/material/slides/1.pdf 186

[144] Agilent, "Spectrum Analyser Basics," Agilent Technologies, Tech. Rep., 2004. [Online]. Available: https://www.keysight.com/upload/cmc{_}upload/All/5952-0292EN.pdf 192

[145] G. Papotti, "ABWLM Wiki Page." [Online]. Available: https://wikis.cern.ch/pages/viewpage.action?pageId=99716677 192, 194

[146] E. Shaposhnikova, "Private communication," 2018. 194, 208

[147] T. Bohl and J. F. Malo, "CERN-BE-2009-006: The APWL Wideband Wall Current Monitor," Geneva, Switzerland, Tech. Rep., 2009. [Online]. Available: https://cds.cern.ch/record/1164165/files/CERN-BE-2009-006.pdf 205, 213

[148] S. U. De Silva *et al.*, "Room Temperature Measurements of Higher Order Modes for the SPS Prototype RF-Dipole Crabbing Cavity," in *IPAC'18*, Vancouver, BC, Canada, 2018, pp. 3805–3807. [Online]. Available: http://accelconf.web.cern.ch/AccelConf/ipac2018/papers/thpal067.pdf 224

[149] P. Berrutti, "Private communication." 224

[150] SLAC, "ACE3P," SLAC National Accelerator Laboratory, 2575 Sand Hill Rd, Menlo Park, CA 94025, USA. [Online]. Available: https://confluence.slac.stanford.edu/display/AdvComp/ACE3P+-+Advanced+Computational+Electromagnetic+Simulation+Suite 240

[151] E. Montesinos, "LHC Project Report 1054: Construction and Processing of the Variable Rf Power Couplers for the Lhc Superconducting Cavities," Tech. Rep. 2007. [Online]. Available: https://cds.cern.ch/record/1080548/files/lhc-project-report-1054.pdf 242

[152] W. Meissner and R. Ochsenfeld, "Ein neuer Effekt bei Eintritt der Supraleitfähigkeit," *Naturwissenschaften*, vol. 21, no. 44, pp. 787–788, nov 1933. [Online]. Available: https://doi.org/10.1007/BF01504252 246

[153] F. London and H. London, "The Electromagetic Equations of the Supraconductor," *Proc. R. Soc. London A Math. Phys. Eng. Sci.*, vol. 149, no. 866, pp. 71—-88, 1935. [Online]. Available: http://rspa.royalsocietypublishing.org/content/149/866/71 246

[154] J. E. Hirsch, "Electrodynamics of superconductors," *Phys. Rev. B*, vol. 69, dec 2004. [Online]. Available: https://arxiv.org/abs/cond-mat/0312619 246

[155] M. Tinkham, *Introduction to Superconductivity.* Courier Corporation, 2004. 246

[156] V. L. Ginzburg, “On the Theory of Superconductivity,” *Zh. Eksp. Teor. Fiz. 20*, pp. 1064–1082, 1950. 246

[157] ——, “On the theory of superconductivity,” *Nuovo Cim.*, vol. 2, no. 6, pp. 1234–1250, 1955. [Online]. Available: http://dx.doi.org/10.1007/BF02731579 246

[158] L. D. Landau, “On the Theory of Superconductivity,” *Collect. Pap. L. D. Landau*, pp. 546–568, 1965. [Online]. Available: https://www.sciencedirect.com/science/article/pii/B978008010586450078X 246

[159] A. A. Abrikosov, “On the Magnetic Properties of Superconductors of the Second Group,” *Sov. Phys. Jetp*, vol. 5, no. 6, pp. 1174–1182, 1957. [Online]. Available: http://www.jetp.ac.ru/cgi-bin/e/index/e/5/6/p1174?a=list 246

[160] ——, “Nobel Lecture: Type II Superconductors and the Vortex Lattice,” 2003, pp. 59–67. [Online]. Available: https://journals.aps.org/rmp/abstract/10.1103/RevModPhys.76.975 246

[161] A. Orthacker, “Superconductivity,” in *Lect. Notes.* [Online]. Available: http://lampx.tugraz.at/ 247

[162] E. Montesinos, “WWFPC Presentation: CERN FPC Status and Perspectives,” in *WWFPC #4*, Geneva, Switzerland, 2018. [Online]. Available: https://indico.cern.ch/event/733100/contributions/3023502/ 253